UNIVERSITY OF CALIFORNIA,
IRVINE

Ice core records of ethane and acetylene for use as biomass burning proxies

DISSERTATION

submitted in partial satisfaction of the requirements
for the degree of

DOCTOR OF PHILOSOPHY

in Earth System Science

by

Melinda Renee Nicewonger

Dissertation Committee:
Professor Eric Saltzman, Chair
Professor Ellen Druffel
Professor Donald Blake
Professor Michael Prather

2019

DEDICATION

To

my mother Colleen & her mother Marjorie

for being fearless women and my heroes.

"It's not the load that breaks you down, it's the way you carry it."
– Lena Horne

TABLE OF CONTENTS

Page

LIST OF FIGURES **v**

LIST OF TABLES **vii**

ACKNOWLEDGMENTS **x**

CURRICULUM VITAE **xi**

ABSTRACT OF THE DISSERTATION **xiv**

1 Introduction **16**
1.1 Overview of thesis 16
1.2 Background 18
1.2.1 Ethane 19
1.2.2 Acetylene 22
1.2.3 Methane 25
1.2.4 Archive of ancient air in polar ice sheets 28
1.2.5 Biomass burning proxy records 31

2 Analytical methods for analysis of trace gases in ice cores **38**
2.1 Overview 38
2.2 Analysis of trace gases 38
2.2.1 Gas chromatology/mass spectrometry instrumentation 38
2.2.2 Automatic sample preparation 39
2.2.3 Internal and external standards 40
2.2.4 Gas chromatography 41
2.2.5 Mass spectrometric detection 42
2.3 Ice core gas extraction method 43
2.3.1 Wet extraction apparatus 43
2.3.2 Wet extraction procedure 46
2.3.3 Extraction system cleaning procedure 49
2.3.4 Decontamination of ice core samples prior to analysis 49
2.4 Blank correction and determination 50
2.5 Solubility effect during wet extraction 53
2.6 Ice core sites and chronologies 59

3 Modeling methods for interpreting ice core records **62**
3.1 Overview 62
3.2 The six-box steady state model 62
3.2.1 Six-box steady state model: preindustrial simulation 66
3.2.2 Six-box steady state model: modern simulation 66
3.4 Chemistry transport model 68

3.4.1 CTM perturbations and sensitivity calculations 69
3.4.2 Simulating atmospheric levels with CTM sensitivities 73
3.5 One-box steady-state methane model 74
3.5.1 Simulating atmospheric methane levels 76

4 Polar ice core records of ethane 79
4.1 Overview 79
4.2 Results and discussion 79
4.2.1 Procedure 1 results 79
4.2.2 Procedure 4 results 82
4.2.3 Comparison of procedure 1 and 4 ethane results 85
4.3 Implications for the preindustrial ethane budget 88
4.3.1 Ethane budget with no Cl sink 89
4.3.2 Ethane budget with Cl sink 93

5 Polar ice core records of acetylene 99
5.1 Overview 99
5.2 Results and discussion 99
5.2.1 Procedure 1 results 99
5.2.2 Procedure 4 results 101
5.2.3 Comparison of procedure 1 and 4 acetylene results 105
5.3 Implications for the preindustrial acetylene budget 108

6 Comparison of biomass burning histories from ethane, acetylene, and methane 116
6.1 Overview 116
6.2 Preindustrial methane biomass burning histories 116
6.3 Impact of atmospheric oxidative changes on the preindustrial budgets 119
6.4 Biomass burning histories from ethane, acetylene and methane 121
6.5 Conclusions 133

7 Conclusion 137
7.1 Overview 137
7.2 Biomass burning trends 138
7.3 Do the ethane, acetylene, and methane records indicate a single fire history? 139
7.4 Modeling past and future fire 144
7.5 Future work 145

BIBLIOGRAPHY 146

APPENDIX A: MATLAB codes 161
APPENDIX B: Ice core data 182
APPENDIX C: UCI-CTM sensitivities versus lifetime 195
APPENDIX D: UCI-CTM perturbation sensitivities 203

LIST OF FIGURES

		Page
Figure 1.1	Three-dimensional representation of the latitudinal distribution of atmospheric ethane (in ppt) from 2005-2014 based on data from the NOAA/ESRL air sampling network	20
Figure 1.2	Atmospheric histories of ethane over Greenland and Antarctica derived from firn air measurements	22
Figure 1.3	Surface flask measurements of acetylene from Summit, Greenland and South Pole, Antarctica	24
Figure 1.4	Atmospheric histories of acetylene over Greenland and Antarctica derived from firn air measurements	25
Figure 1.5	Ice core and surface flask atmospheric methane over the last 2,000 years	27
Figure 1.6	Schematic diagram of an idealized firn column (adapted from Figure 1 *Battle et al.*, 2011)	30
Figure 1.7	Atmospheric methane over the last 800,000 years from the EPICA Dome C ice core	31
Figure 1.8	Spatial and temporal scales of biomass burning proxies (adapted from *Kehrwald et al.*, 2013)	32
Figure 1.9	Compilation of biomass burning proxy records for the last 2,000 years (adapted from *van der Werf et al*., 2013)	37
Figure 2.1	Ethane and acetylene calibration curves. File: CAL primary 17Oct2018	41
Figure 2.2	Sample chromatogram from a Greenland sample and post-melt analytical blank.	43
Figure 2.3	Schematic diagram of the wet extraction system	45
Figure 2.4	Photo of the wet extraction vacuum line with an ice core sample in the extraction chamber. Photo by M. Nicewonger.	45
Figure 2.5	Photo of the extraction chamber with an exploded ice core sample. Photo by M. Nicewonger.	46
Figure 2.6	Photo of the flat glass flange connection with indium o-rings and the Derlin clamp. Photos by M. Nicewonger	47
Figure 2.7	Ethane post-melt analytical blanks through time	52
Figure 2.8	Acetylene post-melt analytical blanks through time	52
Figure 2.9	Dry-extraction and wet-extraction results of carbonyl sulfide, methyl chloride, and methyl bromide from the South Pole Ice Core	58

Figure 2.10	Observed versus calculated equilibrium solubility depletion between the wet- and dry-extraction mixing ratios measured for carbonyl sulfide (COS), methyl chloride (CH_3Cl), and methyl bromide (CH_3Br) from measurements in the South Pole Ice Core.	59
Figure 3.1	Schematic diagram depicting the six-box steady-state model used in *Nicewonger et al.* (2016)	64
Figure 3.2	Results from the six-box model for the preindustrial and modern simulation (*Nicewonger et al*., 2016)	68
Figure 3.3	UCI-CTM global biomass burning emissions and the resulting global annual mean ethane mixing ratios in the tracer simulation	71
Figure 4.1	Atmospheric ethane from Greenland and Antarctica using wet-extraction procedure 1	81
Figure 4.2	Ethane ice core data from procedure 4 excluded from analysis and interpretation	83
Figure 4.3	Atmospheric ethane from Greenland and Antarctic using wet-extraction procedure 4	84
Figure 4.4	Greenland and Antarctic ethane from procedure 1 and procedure 4	86
Figure 4.5	Trends in Greenland ethane data from procedure 1 and procedure 4	87
Figure 4.6	Trends in Antarctic ethane data from procedure 1 and procedure 4	88
Figure 4.7	Modeled ethane boreal and non-boreal biomass burning and geologic emission scenarios for the Medieval Period and Little Ice	90
Figure 4.8	Biomass burning emission scenarios for ethane with geologic emissions fixed and the resulting ethane mixing ratios over Greenland and Antarctica	92
Figure 4.9	Modeled ethane boreal and non-boreal biomass burning and geologic emission scenarios for the Medieval Period and Little Ice Age assuming a 60% Cl sink	97
Figure 4.10	Biomass burning emission scenarios for ethane with geologic emissions fixed and a 60% Cl sink and the resulting ethane mixing ratios over Greenland and Antarctica	98
Figure 5.1	Ice core acetylene measurements from Greenland and Antarctica measured with procedure 1	101
Figure 5.2	Ice core acetylene data from procedure 4 excluded from analysis	102
Figure 5.3	Atmospheric acetylene from Greenland and Antarctic using wet-extraction procedure 4	103
Figure 5.4	Trends in the procedure 4 Greenland acetylene ice core data	104
Figure 5.5	Trends in the procedure 4 Antarctic acetylene ice core data	105

Figure 5.6	Greenland and Antarctic ethane from procedure 1 and procedure 4	106
Figure 5.7	Trends in Greenland acetylene data from procedure 1 and procedure 4	107
Figure 5.8	Trends in Antarctic acetylene data from procedure 1 and procedure 4	107
Figure 5.9	Biomass burning acetylene emission scenarios and the resulting Greenland and Antarctic acetylene mixing ratios	110
Figure 5.10	Modeled acetylene boreal, rest of world, and South American emissions scenarios for the Medieval Period and Little Ice Age	113
Figure 6.1	Modeled preindustrial methane emissions scenarios for the Medieval Period and Little Ice Age assuming a 5% Cl sink	118
Figure 6.2	Modeled preindustrial methane emissions scenarios for the Medieval Period and Little Ice Age assuming a 0% Cl sink	119
Figure 6.3	Biomass burning emission scenarios for ethane, acetylene, and methane.	126
Figure 6.4	Dry matter burned scenarios inferred from ethane, acetylene, and methane.	134
Figure 7.1	Inferred dry matter burned from scenario 2 and dry matter burned from methane that results from changing the $\delta^{13}C$ end-members of biogenic and biomass burning methane sources	143

LIST OF TABLES

		Page
Table 1.1	Ethane, acetylene, and methane sources	27
Table 1.2	Proxies used for reconstructing past biomass burning	34
Table 2.1	Temperature profile scheme for the Agilent 6890 gas chromatograph	41
Table 2.2	Masses and retention times of analytes detected by the GC/MS	42
Table 2.3	Differences between the various wet extraction procedures	47
Table 2.4	Ethane and acetylene levels in the post-melt N_2 blanks	51
Table 2.5	Ethane blank during procedure 4	51
Table 2.6	Acetylene blank during procedure 4	51
Table 2.7	Henry's law constants used for the solubility calculation	57
Table 3.1	Transport and flow rate coefficients used in the six-box steady-state model	64
Table 3.2	Average k_{OH} for each box in the steady state model	64
Table 3.3	Latitudinal distribution of ethane sources in the six-box model	65
Table 3.4	Emission factors used in the UCI-CTM simulations to calculate emissions of ethane and acetylene from dry matter emissions	69
Table 3.5	UCI-CTM sensitivities for ethane and acetylene for Greenland and Antarctica from different tracer simulations	72
Table 3.6	Description of UCI-CTM tracer model runs	73
Table 3.7	Methane isotopic source end-member signatures used in the box model	77
Table 3.8	Kinetic isotope effect for the methane losses used in the box model	77
Table 3.9	Ice core methane mixing ratio and $\delta^{13}CH_4$ used in the box model	78
Table 4.1	Ethane levels in the post-melt N_2 blanks from procedure 1	95
Table 4.2	UCI-CTM sensitivities for ethane assuming a 60% Cl sink strength	94
Table 4.3	Preindustrial ethane budget with no Cl sink	98
Table 4.4	Preindustrial ethane budget with a 60% Cl sink	98
Table 5.1	Acetylene levels in the post-melt N_2 blanks from procedure 1	100
Table 5.2	Preindustrial acetylene budget from boreal and non-boreal emissions	111

Table 5.3	Biomass burning regions and their Greenland and Antarctic acetylene sensitivities used for the South American scenario	112
Table 5.4	Preindustrial acetylene budget for the South American simulation	115
Table 6.1	Modeled methane emissions from biomass burning and microbial sources during the Medieval Period and Little Ice Age for scenarios of geologic emissions and Cl sink strength	124
Table 6.2	Modeled ethane emissions from non-boreal and boreal sources during the Medieval Period and Little Ice Age for scenarios of geologic emissions and Cl sink strength	125
Table 6.3	Dry matter burned emission for different biomes from GFED4.1 and biome-specific emissions factors for ethane, acetylene, and methane	129
Table 6.4	Boreal dry matter emissions from the GFED4 inventory and the regionally-weighted emission factors for ethane and acetylene	135
Table 6.5	Non-boreal dry matter emissions from the GFED4 inventory and the regionally-weighted emission factors for ethane and acetylene	135
Table 6.6	Dry matter burned during the Medieval Period and Little Ice Age inferred from the ethane, acetylene and methane ice core records	136

ACKNOWLEDGMENTS

I would like to extend my upmost appreciation to my advisor Dr. Eric Saltzman. Your enthusiasm and passion for science has inspired me and you have taught me how to be a confident and level-headed scientist. Your dedication to your students and their success is highly respected. Thank you to my co-advisor and Antarctic field work companion Dr. Murat Aydin. Your patience and knowledge in the lab are extraordinary, and I am forever thankful for the skills you have taught me. Thank you for trusting my abilities and giving me the opportunity to participate in the South Pole Ice Core project. The experience has forever shaped my life and my perspective of scientific research. Thank you to my committee members Dr. Ellen Druffel, Dr. Donald Blake, and Dr. Michael Prather. Your comments, guidance, and support helped make this work possible.

I would like to thank the entire Saltzman/Aydin lab group members past & present: Tom Bell, Mike Lawler, Kristal Verhulst, Jack Porter, Sarah Aarons, Mackenzie Grieman, John Patterson, and Kaden Martin. Thank you all for being fantastic lab mates, colleagues, and friends outside of work. Thank you to the numerous undergraduate students who helped in the lab and contributed to the measurements in this project including Tara Harder, Kyle Callahan, Gaby Garcia, and Christopher Lee. Thank you to Cyril McCormick and Ricky Jimenez for ensuring our precious samples stayed frozen. Xin Zhu, thank you for your patience and assistance with the UCI-CTM. Special thanks to Jorg Meyer and the UCI Glass Shop for your support of science.

Thank you to my first-year cohort for the support during the first year and beyond. Scot Parker, thanks for the countless messages and encouragement. Thank you to my close friends who live far but have given me the strength to persevere. Ashley, Marcel, Madeline (& baby "M"), Bryanne, Stephanie, and Erik. I love you all so much. Thank you to my ESS friends who have reminded me to take time for myself and to find joy. I'm especially grateful to Morgan Gorris, Jessica Wang, Emily Kane, Dianne Sanchez, and Daniel Ruiz. Thank you to the whole ESS department both past, present, and future for creating an inclusive work environment and always being down to have fun. Thank you to the "Anomalous SpikESS" volleyball team members for many great memories: "BATTLE!"

Thank you to the NSF's Ice Core Facility for many years of assistance in obtaining samples used for this project. As I witnessed first-hand in Antarctica, the behind-the-scenes of scientific research is immense. Thank you to the countless people who help make science possible at the bottom of the world and elsewhere. We, scientists, appreciate your dedication and commitment. Portions of this dissertation are reproduced with permission from the American Geophysical Union and the National Academy of Science. This research was made possible through the support of several fellowships: an NSF GRFP (DGE-1321846) and a UCI Chancellor's Club Dissertation Fellowship. The ice core studies were supported by the National Science Foundation (OPP-1204248, OPP-1043780, OPP-1644245).

I would not have made it where I am today without the love, support, and guidance of my family: my parents Colleen and Michael, my grandparents Marjorie, Don, Janet, and Husky, my brother Christopher, and my aunt Kristen. Thank you to my extended family: Ellen, Jay, and Alice for your support. Thank you to Dr. Julie Ferguson, the most wonderful roommate and most caring person I know. Thank you for sharing your home with me, Sallie, and Nova. Finally, thank you to my sweet love Matthew for your patience, kindness, and compassion and your willingness to indulge with me. Our Stricklands dates will always be some of my favorite memories at UCI.

CURRICULUM VITAE

Melinda Renee Nicewonger

EDUCATION

Doctor of Philosophy in Earth System Science, *University of California, Irvine*, 2019
Master of Science in Earth System Science, *University of California, Irvine,* 2016
Bachelor of Science in Meteorology, *Texas A&M University, 2013*

HONORS AND AWARDS

Most Promising Future Faculty Award, 2019
UCI Chancellor's Club Dissertation Fellowship, 2019
Outstanding Contributions to the ESS Department Award, May 2018
Associated Graduate Student Symposium Judges' Award, 2018
National Science Foundation Graduate Research Fellowship, 2014-2019
National Science Foundation REU Fellow, 2012
Jesse Jones and Mary Gibbs Scholarship, 2009-2013

PUBLICATIONS

Nicewonger, M. R., M. Aydin, M. J. Prather, and E. S. Saltzman (2018), Large changes in biomass burning over the last millennium inferred from paleoatmospheric ethane in polar ice cores, *Proc Natl Acad Sci.,* 115 (49), 12413-12418, doi.org/10.1073/pnas.1807172115

Nicewonger, M. R., K. R. Verhulst, M. Aydin, and E. S. Saltzman (2016), Preindustrial atmospheric ethane levels inferred from polar ice cores: A constraint on the geologic sources of atmospheric ethane and methane, *Geophys. Res. Lett*., 43, 214–221, doi:10.1002/2015GL066854.

Aydin, M., J. E. Campbell, T. J. Fudge, K. M. Cuffey, **M. R. Nicewonger**, K. R. Verhulst, and E. S. Saltzman (2016), Changes in atmospheric carbonyl sulfide over the last 54000 years inferred from measurements in Antarctic ice cores. *J. Geophys. Res. Atmos*., 120, doi: 10.1002/2015JD024235.

Aydin, M., T. J. Fudge, K. R. Verhulst, **M. R. Nicewonger**, E. D. Waddington, and E. S. Saltzman (2014), Carbonyl sulfide hydrolysis in Antarctic ice cores and an atmospheric history for the last 8000, *J. Geophys. Res. Atmos*., 119, doi:10.1002/2014JD021618.

RESEARCH EXPERIENCE

University of California, Irvine

Graduate Student Researcher, 2013-2019
Dissertation title: "Ice core records of ethane and acetylene for use as biomass burning proxies"

NSF REU Fellow, June – August 2012
Developed analytical methods for corrected ice core carbonyl sulfide measurements for in situ hydrolysis loss

FIELD EXPERIENCE

South Pole, Antarctica

South Pole Ice Core Drilling Project, Nov 2014 – Feb 2015 and Nov – Dec 2015
Assisted with the drilling, processing, logging, handling, and shipment of the South Pole Ice Core.

National Science Foundation Ice Core Facility (NSF-ICF), Lakewood, CO

Collected ice core samples and assisted with core processing lines of the South Pole Ice Core during five yearly visits.

TEACHING EXPERIENCE

Teaching Assistant, *University of California, Irvine*

ESS 17: Catastrophes, Sep – Dec 2018, Class size: 380
ESS 5: The Atmosphere, Mar – Jun 2017, Class size: 400
ESS 7: Physical Geology, Jan – Mar 2017, Class size: 190
ESS 21: On Thin Ice, Mar – Jun 2014, Class size: 250

Teaching Associate (Instructor), *University of California, Irvine*

ESS 5: The Atmosphere, Aug-Sep 2017, Class size: 45

PRESENTATIONS

Nicewonger, M.R., Aydin, M., Prather M. J, Saltzman E.S. (2018) *Ice core measurements of ethane and acetylene over the last 2000 years and implications for biomass burning variability*, oral presentation at the AirUCI Internal Symposium, University of California, Irvine. Jan 14

Nicewonger, M.R., Aydin, M., Prather M. J, Saltzman E.S. (2018) *Ice core measurements of ethane and acetylene over the last 2000 years and implications for biomass burning variability*, oral presentation at the American Geophysical Union Fall Meeting, Washington, DC. Dec 14.

Nicewonger, M.R., Aydin, M., Saltzman E.S. (2018) *Holocene measurements of ethane and acetylene from the SPC14 core*, oral presentation at the South Pole Ice Core Meeting, Seattle, WA. Sep 12

Nicewonger, M.R. (2018) *Fire and ice: quantifying preindustrial fire emissions through ice core gas measurements*, oral presentation at the Associated Graduate Students Research Symposium, Irvine, CA. Apr 20.

Nicewonger, M.R., Aydin, M., Prather M. J, Saltzman E.S. (2017) *Measuring ethane and acetylene in Antarctica ice cores to reconstruct biomass burning emissions over the last 1,000 years*, poster presentation at the American Geophysical Union Fall Meeting, New Orleans, LA. Dec 11.

Nicewonger, M.R., Aydin, M., Saltzman E.S. (2017) *SPICEcore and WAIS Divide measurements of ethane and acetylene over the last 2,000 years*, oral presentation at the South Pole Ice Core Meeting, Seattle, WA. Sep 20.

Nicewonger, M.R., Aydin, M., Montzka S., Saltzman E.S. (2017*) Measurements of acetylene in air extracted from polar ice cores*, poster presentation at the 1st NSF GRFP Training for Tomorrow Symposium, Irvine, CA. May 26.

Nicewonger, M.R., Aydin, M., Montzka S., Saltzman E.S. (2016) *Measurements of acetylene in air extracted from polar ice cores*, poster presentation at the American Geophysical Fall Meeting, San Francisco, CA. Dec 12.

Nicewonger, M.R., Aydin, M., Saltzman E.S. (2016) *Measuring ethane and acetylene in polar ice cores to quantify long-term biomass burning and geologic hydrocarbon emissions*, oral presentation at the South Pole Ice Core Science Meeting, La Jolla, CA. Sep 21.

Nicewonger, M.R., Aydin, M., Saltzman E.S. (2015) *Ethane measurements in polar ice cores and preindustrial ethane emissions from biomass burning and geologic sources*, oral presentation at the WAIS Divide/South Pole Ice Core Science Meeting, La Jolla, CA. Sep 22.

Verhulst, K.R., Aydin, M., Nicewonger, M.R., Saltzman E.S. (2015) *Pre-industrial ethane levels inferred from polar ice cores*, poster presentation at the American Geophysical Union Fall Meeting, San Francisco CA.

Nicewonger, M.R., Aydin, M., Saltzman, E.S., Fudge, T.J., Waddington, E.D., Verhulst, K.R. (2012) *Carbonyl sulfide hydrolysis in polar ice cores and the feasibility of recovering a paleoatmospheric history*, poster presentation at the American Geophysical Union Fall Meeting, San Francisco CA.

ABSTRACT OF THE DISSERTATION

Ice core records of ethane and acetylene for use as biomass burning proxies

By

Melinda Renee Nicewonger

Doctor of Philosophy in Earth System Science

University of California, Irvine, 2019

Professor Eric Saltzman, Chair

Biomass burning plays a major role in atmospheric chemistry, carbon cycling, and climate. To understand and better predict how biomass burning may change in the future, it is important to investigate how biomass burning has varied in the past. Proxy records of biomass burning over long time periods are necessary to identify the link between biomass burning and climate. This information is needed by Earth system models to make accurate projections about future climate change and biomass burning.

In this dissertation, new ice core measurements are used to reconstruct biomass burning variability over the last 2,000 years. The trace gases ethane and acetylene are released to the atmosphere during biomass burning events. New analytical techniques utilizing a wet-extraction method coupled with gas-chromatography and high-resolution mass spectrometry analysis were developed to measure these gases in polar ice cores. The abundance of ethane and acetylene were measured in ice cores from Summit, Greenland, West Antarctic Ice Sheet (WAIS) Divide, Antarctica, and South Pole, Antarctica.

The ice core ethane and acetylene records exhibit similar temporal variability over the 2,000-year period. Over Greenland, little variability is observed in the ethane and acetylene levels. Over Antarctica, they both decline substainitally after 1500 CE, ethane by roughly 30% and acetylene by 50%. Using chemistry transport modeling, this decline in Antarctic ethane and acetylene was attributed to a decline in biomass burning emissions in the non-boreal (tropical) biome, rather than the boreal forests, from the warmer Medieval Period to the cooler Little Ice Age.

My study presents the first millennial scale record of these trace gases in polar ice cores and demonstrates that long-term paleo-climate records from these reactive, trace-level gases are attainable. The results show spatial and temporal variability in biomass burning emissions which were likely driven by climate. More work is needed to extend these records further back in time to periods where there is less influence by human activity and where there is a broader range of climatic variation in order to fully tease apart and quantify the climatic, rather than human, controls over fire in order to aid in validation of Earth system models.

CHAPTER 1

Introduction

Includes excerpts from:

M. R. Nicewonger, K. R. Verhulst, M. Aydin, E. S. Saltzman, "Preindustrial atmospheric ethane levels inferred from polar ice cores: A constraint on the geologic sources of atmospheric ethane and methane," *Geophysical Research Letters*, (2016)

M. R. Nicewonger, M. Aydin, M. J. Prather, E. S. Saltzman, "Large changes in biomass burning over the last millennium inferred from paleoatmospheric ethane in polar ice cores," *Proceedings of the National Academy of Sciences*, (2018).

1.1 Overview of this thesis

Fires emit large amounts of carbon-containing gases to the atmosphere. These include the two most radiatively important gases, carbon dioxide (CO_2) and methane (CH_4), as well as many other reactive trace gases such as carbon monoxide (CO) (*Andreae and Merlet*, 2001; *Agaki et al.*, 2011). CO and CH_4 both react readily with the hydroxyl radical (OH) thus reducing the overall oxidative capacity of the atmosphere. Additional gases released from fires, including nitric oxide and hydrocarbons, react and lead to high levels of tropospheric ozone, a pollutant with serious health effects for humans (*Crutzen and Andreae*, 1990). Globally, fire emissions released on average roughly 2.2 Pg C (10^{15} g) to the atmosphere each year during the 1997-2016 period based on burned area measurements from the MODIS satellite (*van der Werf et al.*, 2017). This is roughly ¼ as much carbon as is emitted to the atmosphere from fossil fuel use (*Ciais et al.*, 2013).

Fires are not well represented in climate models because of limited knowledge of the climatic factors and feedbacks controlling fires over long-time periods (*Solomon et al.*, 2007; *Hantson et al.*, 2016). Most climate models scale fire emissions positively with human population density, but there is a debate about the ways in which humans have influenced fire emissions over time. It is thought that humans have increased fire activity and emissions through ignitions and deforestation practices, but humans may also decrease fires through fragmenting landscapes and using fire suppression (*Archibald et al.*, 2009; *Bowman et al.*, 2009, 2011; *Hantson et al.*, 2016; *van Marle et al.*, 2017; *Andela et al.*, 2017). Recent modeling work and analysis of satellite-derived global burned area shows a negative correlation between burned area and human population density, contrary to the positive relationship used in fire models (*Bistinas et al.*, 2014; *Knorr et al.*, 2014; *van der Werf et al*., 2017). Historical reconstructions of biomass burning over long-time periods would aid in understanding what the climatic controls on fires are, how much humans have impacted fires, and help in predicting how biomass burning will change in the future.

The most commonly used tools to investigate paleo-biomass burning trends in are charcoal in lake sediments and fire scars on tree rings. Both methods are temporally and spatially limited, leading to only local or regional fire activity reconstructions. Neither of these methods can quantify the magnitude of emissions from biomass burning which is necessary to constrain the preindustrial budgets of CO_2 and CH_4, as well as tropospheric ozone.

A few studies have used the abundance of trace gases (CH_4 and carbon monoxide, CO) and their stable isotopes ($\delta^{13}CH_4$, $\delta^{13}CO$, $\delta C^{18}O$) in ice core air bubbles to reconstruct biomass burning emissions over the last few millennia (*Ferretti et al.*, 2005; *Mischler et al.*, 2009; *Wang et al.*, 2010; *Sapart et al.*, 2012; *Bock et al*., 2017; *Beck et al.*, 2018). These records disagree on

the magnitude and timing of biomass burning trends in the past and are limited in their spatial and temporal coverage. These discrepancies between the proxy records have made it difficult to ascertain how the climate controls biomass burning and how biomass burning feeds back on climate.

This study uses a new approach to reconstruct historical biomass burning emissions by measuring ultra-trace gases, ethane (C_2H_6) and acetylene (ethyne, C_2H_2) in air bubbles from polar ice cores. This study presents the first measurements of ethane and acetylene in ice cores from Greenland and Antarctica over the last two millennia. These gases are emitted to the atmosphere today through leakage and combustion of fossil fuel and biofuels and open biomass burning. In the preindustrial atmosphere, these gases are emitted mainly by biomass burning. Therefore, preindustrial records of ethane and acetylene from ice cores can inform us about biomass burning emission variability through time.

Biomass burning emissions of these gases is also linked to those from methane. As a result, reconstructing the burning emissions from ethane and acetylene should provide an estimate for the biomass burning emissions of methane. The goals of this study were to: 1) develop an analytical technique to measure ethane and acetylene in ice core air bubbles, 2) reconstruct an atmospheric record of these gases from Greenland and Antarctic ice cores for the last 2,000 years, 3) explore the implications of the preindustrial levels of ethane and acetylene in terms of biomass burning emissions and 4) explore the implications of this new biomass burning emission proxy record on the preindustrial budget of methane.

1.2 Background

This section provides background information necessary to understand 1) the atmospheric budgets of ethane, acetylene, and methane and why they are useful tracers for paleo-biomass

burning, 2) how ancient air is trapped and preserved in polar ice sheets and 3) biomass burning proxy records and their limitations.

1.2.1 Ethane

Ethane is emitted to the modern atmosphere primarily from the production, processing, transmission and use of oil and natural gas, burning of biofuels and biomass, and natural geologic seeps (*Rudolph*, 1995; *Xiao et al.*, 2008; *Etiope and Ciccioli*, 2009; *Pozzer et al*., 2010; *Simpson et al.*, 2012; *Helmig et al*., 2016; *Tzompa-Sosa et al*., 2017). Minor emissions from oceanic and terrestrial ecosystems have been suggested but are highly uncertain (*Plass-Dülmer et al*., 1995; *Clarkson et al*., 1997; *Stein and Rudolph*, 2007). Total global emissions of ethane have been estimated at 10-20 Tg y^{-1} with roughly two-thirds of the budget from human use of fossil fuels and biofuels (*Rudolph*, 1995; *Xiao et al*., 2008; *Etiope and Ciccioli*, 2009; *Aydin et al*., 2011; *Simpson et al*., 2012, *Nicewonger et al*., 2016; *Franco et al.*, 2016; *Helmig et al*., 2016; *Tzompa-Sosa et al*., 2017*; Dalsøren et al*., 2018). The largest natural sources of ethane are from biomass burning and geologic emissions. Ethane emissions from biomass burning are estimated at around 3.4 Tg y^{-1} during the satellite era (1997-2017) (*Giglio et al*., 2013; *van der Werf et al*., 2017), while geologic ethane emissions in the modern atmosphere are 2-4 Tg y^{-1} (*Etiope and Ciccioli*, 2009). Table 1.1 summarizes the ethane global budget.

The major sink of atmospheric ethane is via oxidation with the hydroxyl radical (OH) resulting in a global mean lifetime of roughly two months (*Rudolph*, 1995; *Poisson et al*., 2000; *Xiao et al*., 2008, *Burkholder et al*., 2015). Ethane is also oxidized by chlorine atoms (Cl) which are produced in the marine boundary layer by reactions involving marine aerosols and polluted air (*Knipping and Dabdub*, 2003; *Lawler et al*., 2009; *Wang et al.*, 2019). The reaction rate constant with chlorine occurs at a rate roughly 230 times faster than the reaction rate constant

with OH (*Burkholder et al*., 2015). This reaction has been omitted from most budget analyses of ethane (ex: *Xiao et al.*, 2008; *Pozzer et al*., 2010; *Tzompa-Sosa et al*., 2017) because the distribution and magnitude of Cl atoms is not well known. Recent analysis by *Wang et al*. (2019) shows the reaction with Cl may constitute a significant portion (~20%) of the ethane sink. Ethane levels in surface air exhibit a strong seasonal variation with maximum levels occurring during austral winter and minimum levels occurring during austral summer. This seasonal cycle reflects wintertime buildup and summertime depletion driven by the loss to OH and possibly Cl.

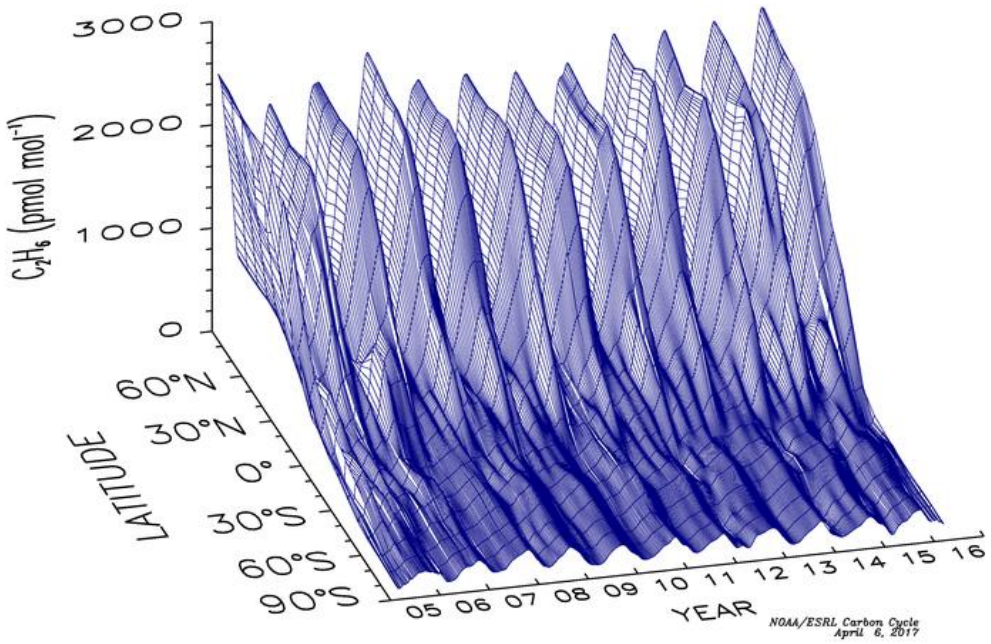

Figure 1.1: Three-dimensional latitudinal distribution of atmospheric ethane (in pmol mol^{-1} = parts per trillion [ppt]) from March 2005 – April 2016 based on data from the NOAA/ESRL air sampling network from *Helmig et al*. (2009) with updates at: http://instaar.colorado.edu/arl/Global_VOC.html. The "flying carpet" represents many flask measurements with data smoothed by time and latitude.

The N/S asymmetry in ethane sources results in a strong interhemispheric gradient in atmospheric ethane levels with significantly greater ethane levels over the high northern latitudes (60-90°N) than the high southern latitudes (60-90°S). From 2005-2015 CE, the mean ethane level over Greenland and Antarctica measured in surface flasks from the NOAA Global

Monitoring Division was roughly 1300 parts per trillion (ppt = pmol mol^{-1}) and 210 ppt, respectively (*Helmig et al*., 2009). During this time, the interpolar ratio of ethane, measured as the ratio between high northern latitude ethane levels and high southern latitude ethane levels was roughly 6:1. Figure 1.1 shows a three-dimensional time series plot of the global distribution of atmospheric ethane.

Observations show that ethane levels have declined globally by roughly 30% from 1984-2008 (*Simpson et al*., 2006, 2012). Other studies utilizing surface air and firn air measurements also confirmed this strong decline in ethane from the early 1980s to 2000 and attributed the decline to reduced fossil fuel emissions (*Helmig et al*., 2009; 2014; *Aydin et al*., 2011; *Worton et al*., 2012). Recently, ethane levels have begun to rise again. Several studies have credited the rise in atmosphere ethane levels starting around 2009 to increased natural gas exploration in shale regions via hydraulic fracking (*Peischl et al*., 2016; *Helmig et al*., 2016; *Hausmann et al*., 2016, *Kort et al*., 2016, *Franco et al*., 2016; *Tzompa-Sosa et al*., 2017).

Ethane has been measured in Antarctic firn air from South Pole and WAIS Divide and in Greenland firn from Summit, NGRIP and NEEM (*Kaspers et al*., 2004; *Aydin et al*., 2011; *Worton et al*., 2012; *Helmig et al*., 2014) (Figure 1.2). All these records show ethane levels rising in the atmosphere until around 1980 when levels peaked and quickly declined.

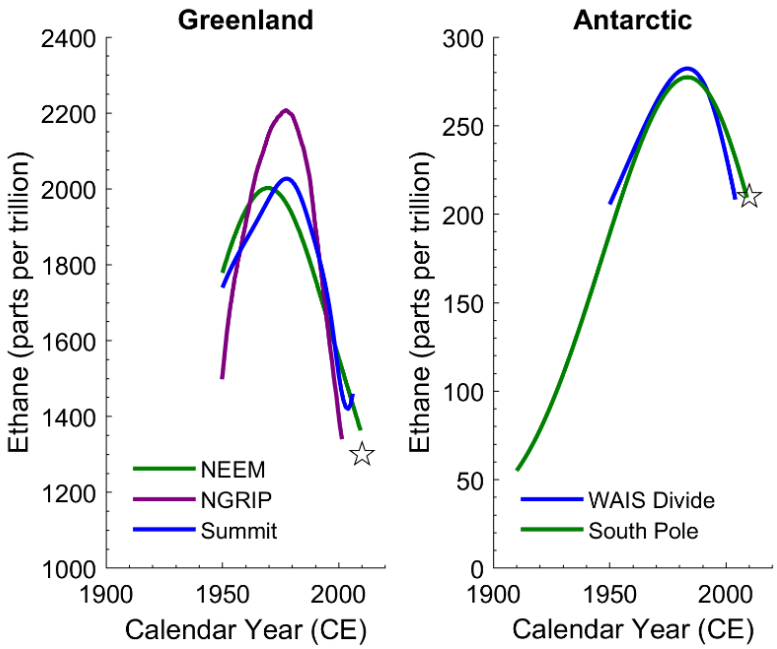

Figure 1.2: Atmospheric histories of ethane inferred from Greenland (left) and Antarctic (right) firn measurements. For Greenland, data is from NEEM (green line; *Helmig et al*., 2014), NGRIP (purple line; *Worton et al*., 2012) and Summit (blue line; *Aydin et al*., 2011). For Antarctic data is from WAIS Divide (blue line) and South Pole (green line; *Aydin et al*., 2011).

1.2.2 Acetylene

Acetylene is emitted to the atmosphere via incomplete combustion process, including biomass and biofuel burning and fossil fuel use (mainly through vehicle exhaust) (*Whitby and Altwicker*, 1978; *Rudolph and Ehhalt*, 1981; *Singh and Zimmerman*, 1992; *Xiao et al*., 2007). Small but uncertain sources from oceanic and terrestrial systems and from geologic sources have also been suggested (*Kanakidou et al*., 1988; *Plass-Dülmer et al*., 1995; *Blake et al*., 2001; *Xiao et al*., 2007; *Gunther and Musgrave*, 1971, *G. Etiope*, personal communication). Geologic emissions of acetylene have been measured in geothermal-magmatic gas (*Gunther and Musgrave*, 1971) and are theoretically predicted to be emitted in mud volcanos and burning gas seeps through the partial combustion of methane (*Watt*, 1951; *Anderson*, 1958; *Lui et al*., 2017;

G. Etiope, personal communication). There is limited data on the location and magnitude of this potential geologic acetylene source. *Xiao et al.* (2007) estimated the fossil fuel source of acetylene at 1.7 Tg y^{-1}, the biofuel source at 3.3 Tg y^{-1}, and the biomass burning source at 1.6 Tg y^{-1} for a total atmospheric source of 6.6 Tg y^{-1}. Modern acetylene biomass burning emissions are estimated at 1.2 Tg y^{-1} (*Akagi et al*., 2011; *van der Werf et al*., 2017). Acetylene emissions are mainly located in the northern hemisphere. Table 1.1 summarizes the global acetylene budget.

Acetylene is removed from the atmosphere via oxidation with OH, resulting in an annual mean lifetime of roughly 2-3 weeks (*Burkholder et al*., 2015; *Xiao et al*., 2007). Acetylene also has a small sink (<5%) with Cl (*Burkholder et al*., 2015; *Wang et al.*, 2019). The asymmetric distribution of sources combined with the short atmospheric lifetime results in a large interhemispheric ratio and a strong seasonal cycle that is amplified in the high latitude regions. Mean acetylene levels over Greenland and Antarctica during the 2012-2018 period measured in surface flasks from the NOAA Global Monitoring Division are roughly 160 ppt and 15-20 ppt, respectively (Figure 1.3) (*Helmig*, 2017; *D. Helmig, personal communication; S. Montzka, personal communication; this study*). The resulting interhemispheric of acetylene is roughly 8-10.

Greenland firn air indicates a large increase in northern hemispheric acetylene levels during the beginning of the 20th century until 1980 CE (peaking around 600 ppt), followed by a sharp decline from 1980-2000 CE to a mean level less of than 300 ppt (Figure 1.4) (*Worton et al*., 2012). This trend in 20th century acetylene is similar to that of other hydrocarbons and is likely due to reduced fossil fuel emissions and more stringent air quality controls (i.e. catalytic converters in vehicles) (*Aydin et al*., 2011; *Worton et al*., 2012). There have been few reconstructions of southern hemisphere acetylene. *Kaspers et al*. (2004) made measurements of

acetylene in firn air from Donning Maud Land, Antarctica. Acetylene levels varied between 20-30 ppt in the firn column. South Pole firn air shows a peak in atmospheric acetylene levels around 1980 CE (Figure 1.4) (*E. Atlas, personal communication*).

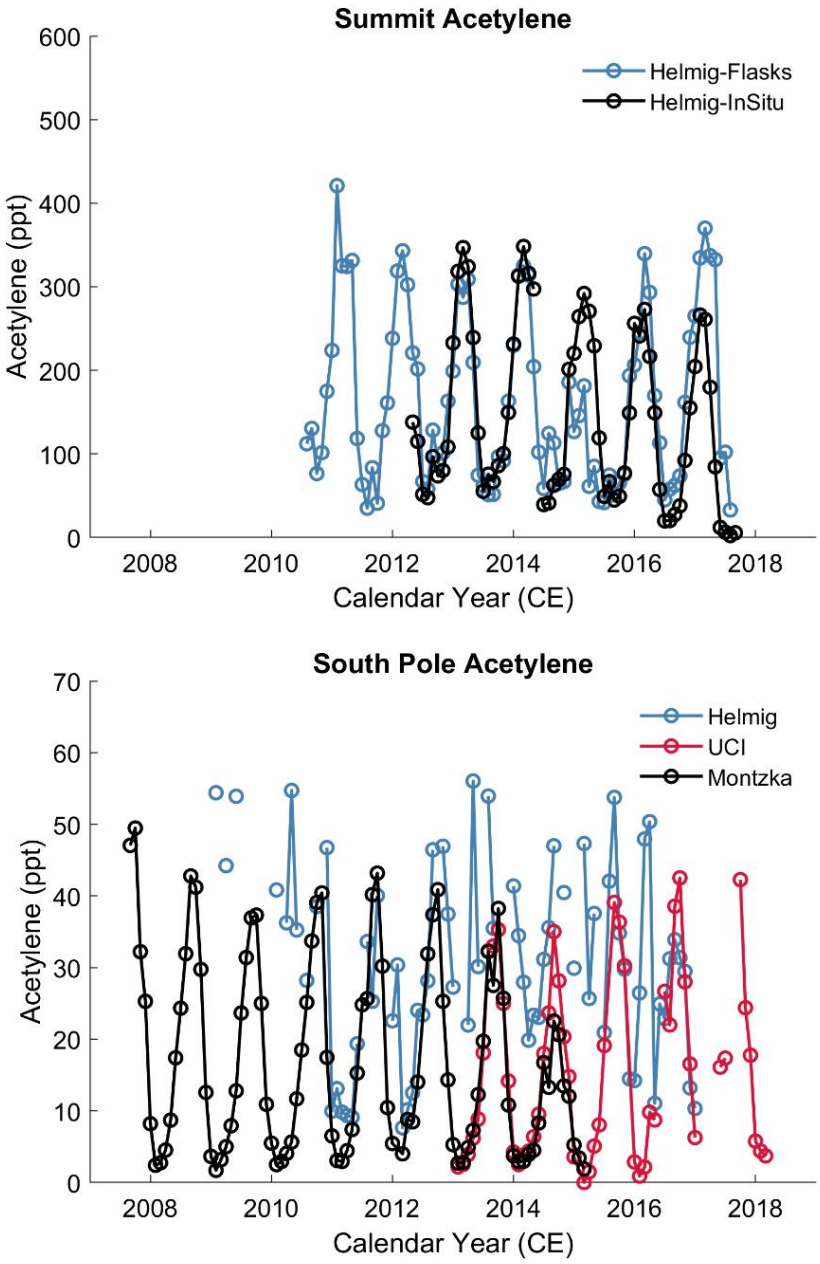

Figure 1.3: Surface flask measurements of acetylene from Summit, Greenland (top) and South Pole, Antarctica (bottom). Data are from the NOAA GMD network (*S. Montzka, personal communication*), INSTAAR at CU Boulder (*D. Helmig, personal communication*), *Helmig et al*. (2009, 2017) and UCI (this research).

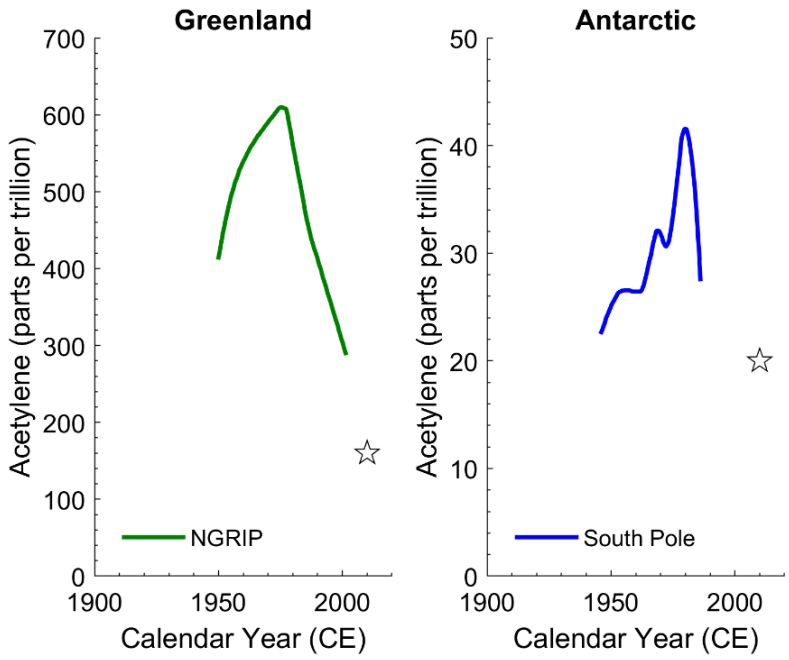

Figure 1.4: Atmospheric histories of acetylene inferred from Greenland (left) and Antarctic (right) firn measurements. Greenland history from NGRIP is from *Worton et al.* (2012) and the Antarctic history is from E. Atlas (unpublished data, personal communication).

1.2.3 Methane

Methane is emitted to the atmosphere through fossil fuel production, transport and use (including natural gas, coal and oil), biomass and biofuel burning, geologic outgassing (seepage), and biogenic sources (including wetlands, ruminant animals, terminates, agriculture and waste, and thawing permafrost) (*Etiope*, 2012; *Kirschke et al.*, 2013, *Nisbet et al.*, 2014). Roughly two-thirds of methane emissions are from human activities (Table 1.1). The main destruction of atmospheric methane occurs via oxidation with the hydroxyl radical (OH) resulting in an atmospheric lifetime of roughly 9-10 years (*Dlugokencky et al.*, 2011; *Prather et al.*, 2012; *Kirschke et al.*, 2013). Methane is also lost by reaction with Cl atoms. The magnitude of the sink term is not well constrained, but likely lies somewhere in the range of 1-5% of the total loss (*Allan et al.*, 2007; *Prather et al.*, 2012; *Wang et al.*, 2019).

Methane and ethane share common sources via fossil fuel use, biomass and biofuel burning, and geologic outgassing. Ethane does not have biogenic sources. Atmospheric ethane has been used to trace methane emissions from fossil fuel use and biomass burning during the past few decades (*Aydin et al*., 2011; *Simpson et al*., 2012; *Helmig et al*., 2016; *Hausmann et al*., 2016; *Peischl et al*., 2016, *Kort et al*., 2016, *Franco et al*., 2016). The emission factor (mass of ethane emitted per mass of methane emitted) of ethane and methane from fossil is highly variable and depends on many factors including the temperature, the pressure, the age of the fossil reservoir, and the composition of the source material (biogenic or thermogenic) (*Etiope et al*., 2008; *Etiope and Ciccioli*, 2009). This makes it challenging to quantify fossil and geologic hydrocarbon emissions by using atmospheric measurements of ethane and methane alone. The emission factors of methane and ethane from biomass and biofuel burning are better understood, but still have significant uncertainties (*Andreae and Merlet*, 2001; *Akagi et al*., 2011). Methane shares fewer sources with atmospheric acetylene: biomass and biofuel burning and fossil fuel use (mainly incomplete combustion).

Methane has been measured extensively in polar ice cores and in modern surface flasks (Figure 1.5). Over the last 2,000 years, methane levels over Antarctica ranged from 600-700 parts per billion (ppb) before increasing sharply around 1800 CE (*Etheridge et al*., 1998 (*MacFarling Meure et al*., 2006; *Mitchell et al*., 2011). Today, atmospheric methane levels are near 1850 ppb and rising (*Dlugokencky*, 2017). The increase in atmospheric methane since the preindustrial is attributed to anthropogenic activities (i.e. fossil fuel use and agriculture).

Table 1.1: Ethane[a], acetylene[b] and methane[c] sources in Tg y^{-1}

Source	Ethane	Acetylene	Methane
Fossil fuels	8-10	1.7	85-105
Biomass burning	2.4-3.4[d]	1.2-1.6[d]	32-39
Geologic	2-4[e]	--	33-75 (50-70[e)]
Wetlands (natural)	--	--	177-284
Agriculture & waste	--	--	187-224
Biofuel	2.6	3.3	10-20
Total sources	15-20	6.2-6.6	524-747

[a] *Xiao et al*. (2008)
[b] *Xiao et al*. (2007)
[c] IPCC 2013: *Ciais et al*. (2013)
[d] GFEDv4.1: *van der Werf et al.* (2017)
[e] *Etiope and Ciccioli* (2009)

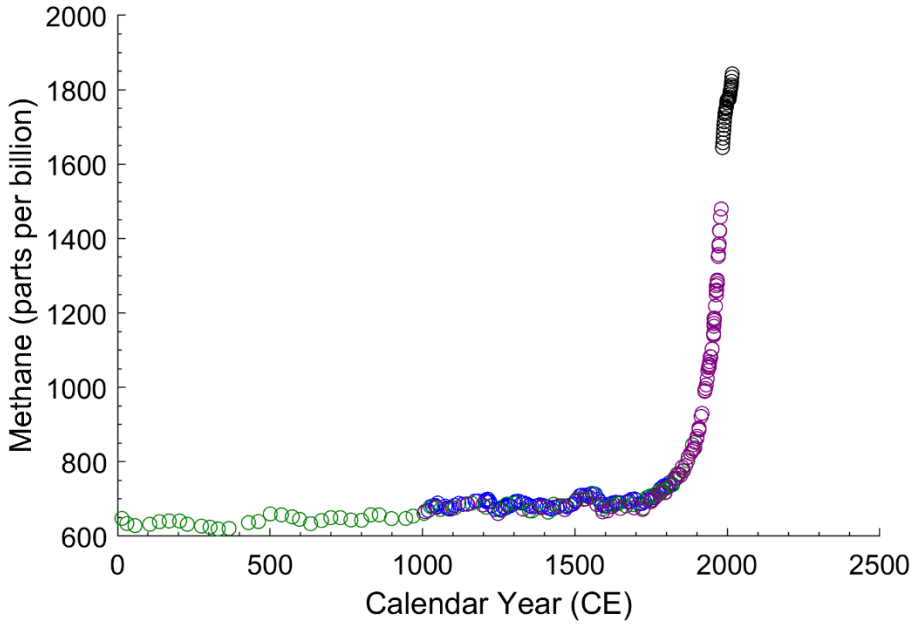

Figure 1.5: Atmospheric methane levels in Antarctic ice cores and modern surface flasks. Green: methane from the DSS ice core from Law Dome, Antarctica (*MacFarling Meure et al*., 2006), blue: methane from the WDC-05A ice core from WAIS Divide, Antarctica (*Mitchell et al*., 2011), purple: methane from the DSS ice for from Law Dome, Antarctica (*Etheridge et al*., 1998), and black: methane from modern surface flask measurements from the NOAA ESRL network (*Dlugokencky*, 2017).

1.2.4 Archive of ancient air in polar ice sheets

Ancient air is preserved in polar ice sheets. In this project, we focused on air in two forms: 1) air trapped in the perennial, unconsolidated snowpack (firn) and 2) air trapped inside bubbles locked within ice. The upper ~50-120 m of the ice sheet is the firn layer. The firn layer acts as a permeable filter through which gases from the atmosphere slowly diffuse such that the mean age of the air increases with depth in the firn column. This results in a smoothed atmospheric history of gases (Figure 1.6). Gas movement through firn is controlled by many factors, including gas diffusivity, gravitational settling, open porosity, pressure gradients, wind pumping, advection and fractionation of gases (*Battle et al*., 1996, 2011; *Schwander et al*., 1997; *Severinghaus and Battle*, 2006). Different transport mechanisms dominate in each region of the firn. In the upper-most region (~0-3 m), the convective zone, air movement is controlled mainly by convective processes (wind pumping, pressure gradients). Below this is the diffusive column, where air movement is mainly controlled by molecular diffusion, in which concentration gradients drive gas fluxes *(Craig et al*., 1988; *Battle et al*., 2011). The diffusive column is extensive and typically comprises most of the firn column. The deepest region of the firn is the lock-in zone where vertical air movement is inhibited by seasonal layers with low-permeability (*Battle et al*., 2011). The firn column ends at the firn-ice transition where the open pores close forming air bubbles that are locked within the ice matrix. The age of a gas at a depth in the firn column is not a single year, but rather a distribution of ages. This distribution can be calculated using a firn diffusion model (*Battle et al*., 2011; *Buziert et al*., 2012). Using the firn diffusion model, inversions can be completed that reconstruct atmospheric histories of gases based on firn air measurements.

Beneath the firn layer, gases are no longer in contact with the atmosphere and are instead locked inside bubbles within the ice. The depth where this occurs is called the bubble close-off depth and happens when the ice reaches a density of 800-840 kg m^{-3} (*Schwander et al*., 1997). At this depth, the air inside the ice ages at the same rate as the surrounding ice, although the air bubbles inside the ice are always younger than the ice itself. This "delta age" (age of the ice – age of the air bubbles inside the ice) is due to the time it takes for the firn to turn to ice. The depth of this firn to ice transition depends on the physical characteristics of the site, such as temperature and accumulation. Sites with high accumulation rates (and usually warmer temperatures) have a shallower firn to ice transition than sites with lower accumulation rates. For example, WAIS Divide has a firn/ice transition of ~75 m and South Pole has a firn/ice transition of ~120 m. This results in a delta age (for CH_4) at WAIS Divide of roughly 200 years and at South Pole of roughly 1000 years.

Ice cores have provided records of atmospheric CH_4 (as well as CO_2) for the last 800,000 years (Figure 1.7). Methane levels have fluctuated between 350 and 800 parts per billion (ppb) during the glacial and interglacial periods, respectively. It is important to understand how internal climate feedbacks control atmospheric methane to predict how the methane budget will change in the future. It is speculated that the large variability in methane between glacial and interglacial periods is driven mostly by wetland emissions (*Chappellaz et al*., 1990; *Brook et al*., 1996, 2000; *Loulergue et al*., 2008). The role of biomass burning emissions in this variability is not well known or constrained.

Measurements of the stable isotopes of CH_4 along with the mixing ratio of CH_4 allow for source apportioning to develop a methane budget (*Ferretti et al*., 2005; *Sowers*, 2010; *Mischler et al*., 2009; *Sapart et al.*, 2012; *Bock et al*., 2017). This analysis technique requires an

understanding of the magnitude and variability in the isotopic signature of sources through time that has proven complicated (*Sowers*, 2010). Analyzing gases such as ethane and acetylene in ice cores has the potential to reduce the uncertainty of the preindustrial CH_4 budget by providing a long-term record of biomass burning and geologic emissions through time.

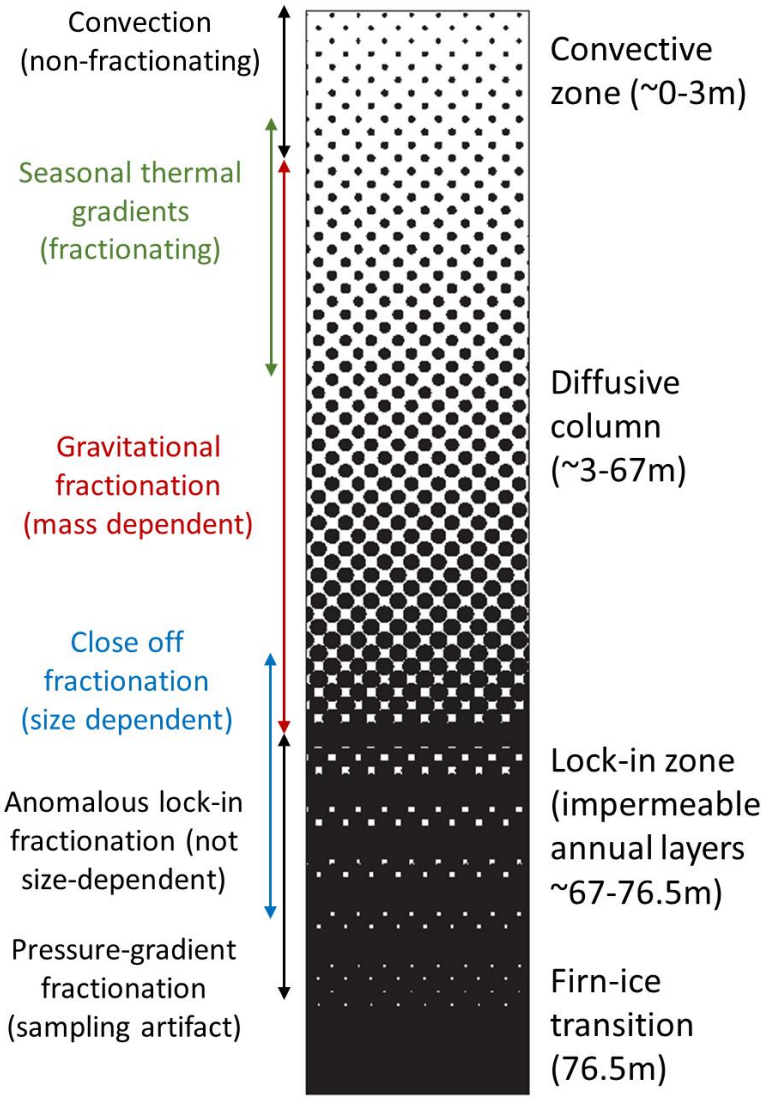

Figure 1.6: A schematic diagram of an idealized firn column from the West Antarctic Ice Sheet (WAIS) Divide (adapted from Figure 1 in *Battle et al.*, 2011).

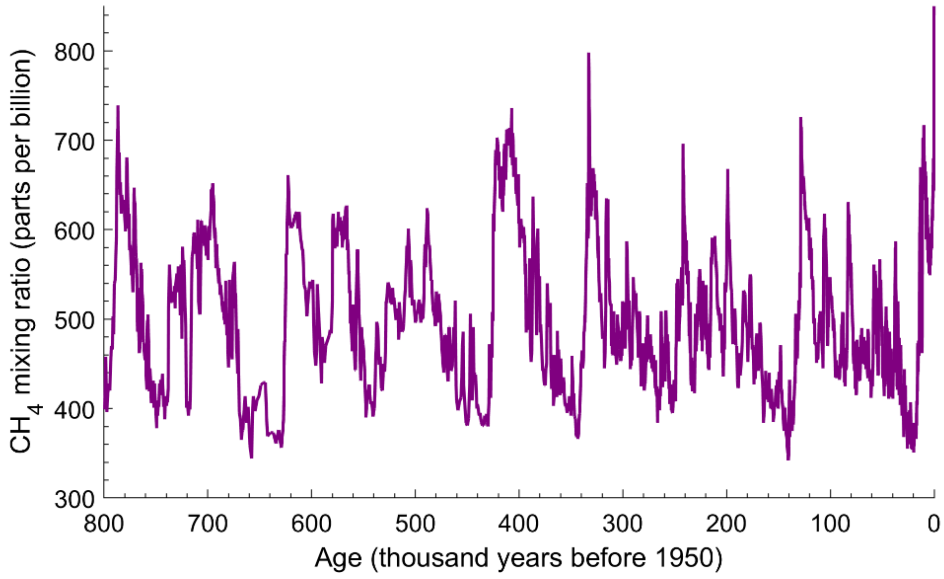

Figure 1.7: Atmospheric methane levels measured in the EPICA Dome C ice core for the last 800,000 years (*Loulergue et al*., 2008)

1.2.5 Biomass burning proxy records

Biomass burning proxy records have been developed based on fire scars from tree rings, lake sediment charcoal records, and ice core records of chemical species and isotopomers (aerosols and gases). The ice core records can be broken up into three main categories: 1) chemical species with multiple potential sources, 2) chemical species specific to biomass burning and 3) isotopic composition of trace gases (Table 1.2). All of these proxy records have inherent strengths and limitations and yield burning records covering different spatial and temporal scales (Figure 1.8). A brief discussion of each type of biomass burning proxy record is found here (*Rubino et al.*, 2015).

Fire scars on tree rings allow for the dendrochronological dating of fires for the last few centuries (*McBride*, 1983; *Holz et al*., 2012). The ability for a tree to scar during a fire is based

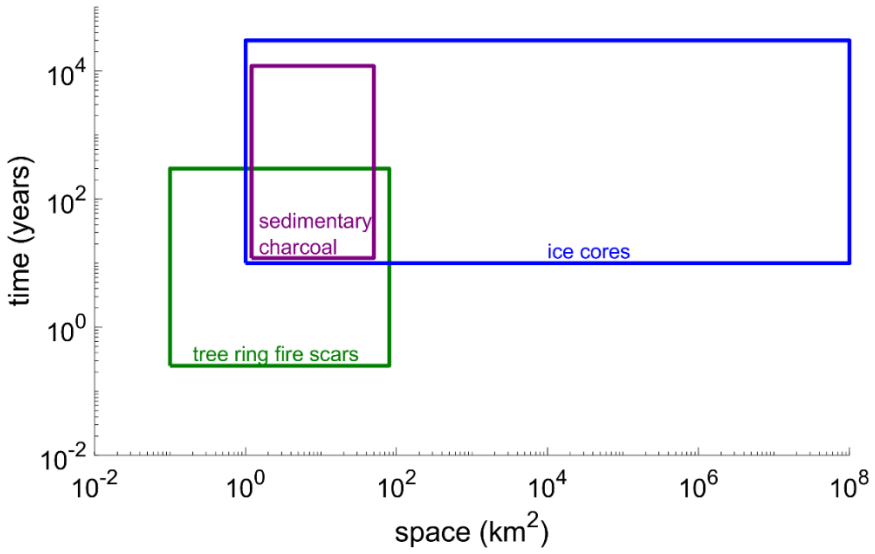

Figure 1.8: Spatial and temporal scales of biomass burning proxies (adapted from *Kehrwald et al.*, 2013)

on many factors including the tree species, bark thickness, fuel conditions and wind velocity (*McBride*, 1983). Generally, trees less than ten years old do not survive fires. Although fire scars are a useful tool, they have many limitations. They are only useful to reconstruct fire activity and cannot be used to reconstruct biomass burning emissions which is necessary to constrain the methane budget. Additionally, these records are spatially limited to forested regions and cannot provide fire activity for areas such as the savanna/grasslands, which are known to contribute significantly to the total carbon emitted from biomass burning annually (*van der Werf et al.*, 2010).

Charcoal accumulation in soils and lake sediment is the most commonly used biomass burning proxy record. The charcoal in the lake sediment reflects biomass burning within roughly ten kilometers of the sampling site. By measuring charcoal at several hundred sites, regional, hemispheric and global biomass burning records for the last ~20,000 years have been developed (*Power et al.*, 2008, 2012; *Marlon et al.*, 2008). The major finding from these records is that

there was less fire activity as compared to present day during the deglacial period from 21,000 to roughly 11,000 years before present (BP, defined as 1950 CE), greater fire activity than present day during the Holocene (10,000-6,000 years BP), and a slow decline into modern levels (4,000 years BP to present).

Marlon et al. (2008) used these charcoal records to reconstruct biomass burning variability during the last 2,000 years. The major finding from these records is that biomass burning declined from 1-1750 CE and reached a minimum during the Little Ice Age, rose sharply between 1750-1870 CE and then declined into the 1900s (Figure 1.9). *Power et al*. (2012) used a multi-regional charcoal analysis to determine if the post-1500 CE charocal decline was driven by the population collapse of the indigenous populations following European contact that resulted in less fire usage, or if it was driven by climatic conditions during the Little Ice Age that caused a decline in tropical biomass burning. They observed a decline in charcoal accumulation in all sites globally and not just in the Americas, concluding that changing global climate were the main cause of the biomass burning decline observed in the charcoal records.

There are several limitation to charcoal proxy reconstructions of fire activity, including 1) the limited spatial coverage of individual cores, 2) underrepresentation of fires from low-woody biomass regions including the grassland/shrubland/savanna biome which are responsible for a significant fraction of global carbon emissions from fires (*van der Werf et al*., 2010), 3) the qualitative nature of the charcoal signals due to site to site variations in preservation, and 3) uncertainty in sediment core dating, usually done by interpolation of a few ^{14}C dates (*Power et al*., 2008).

Aerosol-borne chemical species preserved in ice cores have been used as biomass burning proxies. *Legrand et al*. (1992) measured ammonium, formate, acetate, oxalate, and

glycolate in a Greenland ice core and suggested peaks in these species were related to biomass burning events. Other chemical species such as formaldehyde (HCHO), hydrogen peroxide (H_2O_2), potassium (K^+) and nitrate (NO_3-) have also been used as biomass burning proxies because they co-occur during peaks in ammonium (*Fuhrer et al*., 1993; *Whitlow et al.*, 1994). Interpretation of the levels of these species in ice cores is challenging because they have sources other than biomass burning. For example, ammonium also has sources from agricultural activity (animal excreta and fertilizers), lightning, soil processes, industrial processes and fossil fuels (*Bouwman et al*., 1997; *Hristov et al*., 2011). These chemical species are useful to provide insights into past biomass burning activity but need to be supported by other independent records of biomass burning.

Table 1.2: List of proxies used for reconstructing past biomass burning (adapted from *Rubino et al*., 2015)

Species with multiple sources	Species specific to biomass burning	Isotopic composition of trace gas
ammonium (NH_4^+)	levoglucosan ($C_6H_{10}O_5$)	$\delta^{13}C$-CH_4
formate (HCOO-)	dehydroabietic acid ($C_{20}H_{28}O_2$)	δD-CH_4
acetate (CH_3COO-)	vanillin ($C_8H_8O_3$)	$\delta^{18}O$-CO
glycolate ($C_2H_3O_3$-)	syringic acid ($C_9H_{10}O_5$)	$\delta^{13}C$-CO
oxalate ($C_2O_4^{2-}$)	vanillic acid ($C_8H_8O_4$)	
formaldehyde (HCHO)	galactosan ($C_6H_{12}O_6$)	
hydrogen peroxide (H_2O_2)	mannosan ($C_6H_{12}O_6$)	
potassium (K^+)		
nitrate (NO_3-)		
nitrite (NO_2-)		
electrical conductivity measurements		
black carbon		

Aerosol chemical species specific to biomass burning such as levoglucosan and vanillic acid have also been used as biomass burning proxy records (*Simoneit et al*., 1999; *Kawamura et al*., 2012; *Grieman et al*., 2017, 2018a, 2018b). These aerosols are molecular markers from

cellulose burning of high-latitude biomass. *Zennaro et al*. (2014) measured levoglucosan in a Greenland ice core and found high levels during 1500-1700 CE. Elevated levels of vanillic acid were also observed during a similar time from 1460-1660 CE in an ice core from Siberia (*Grieman et al*., 2017). However, it is known that levoglucosan degrades under high levels of hydroxyl radical and so its usefulness as a biomass burning tracer has been debated (*Hennigan et al*., 2010; *Hoffman et al*., 2010). Additionally, these compounds are deposited to the polar ice after long-distance transport in the atmosphere, so their levels may be heavily impacted by changes in transport and meteorological conditions. Variability in combustion conditions and vegetation type may also impact the emission of these compounds and ultimately impact their levels in ice cores. Although these compounds are biomass-burning specific, these records are useful only as a quantitative history of fire activity and improvements in analytical techniques for measuring these compounds are needed for a more comprehensive understanding of past fire activity.

Biomass burning emissions histories have been inferred by using measurements of CH_4, CO and their stable isotopes in ice core air bubbles (Figure 1.9) (*Ferretti et al*., 2005; *Mischler et al*., 2009; *Wang et al*., 2010; *Sapart et al*., 2012). The biomass burning source is determined by assigning isotopic end-members to the various sources and using an isotopic mass balance model to estimate source emissions through time. The CH_4 fire proxy record covers the last 2,000 years and represents a global record of biomass burning emissions due to the relatively long lifetime of methane (~9-10 years). The CO proxy record covers the last 650 years and represents only a southern hemispheric biomass burning emission record due to the short atmospheric lifetime of CO (~2 months). The ice core gas records allow for the quantitative reconstruction of biomass burning emissions that is necessary to constrain the budget of methane.

The CH_4 record indicates biomass burning emissions peaked during 800-1000 CE, declined to a minimum during 1600-1800 CE and then rose to modern levels (Figure 1.9). The roughly 40% decline in burning emissions was attributed to both climatic (cooler and wetter) and human (decline in population due to diseases) causes (*Ferretti et al*., 2005). On the contrary, the CO burning record suggests burning reached a minimum slightly earlier and for a shorter period (~100 years) before rising sharply to a maximum around 1850 CE (Figure 1.9). This peak in burning in the mid-1800s is also suggested in the sedimentary charcoal record. *van der Werf et al*. (2013) investigated this peak in burning during the mid-1800s using biogeochemical and atmospheric modeling. They concluded that it would require biomass burning levels nearly four-times modern rates to observe the levels of CO from the ice core record. This high burning rate is unlikely to have occurred in a preindustrial world with limited infrastructure (i.e. lower population and fewer machines and equipment for mass deforestation and burning). Validation of the CO record has yet to be completed.

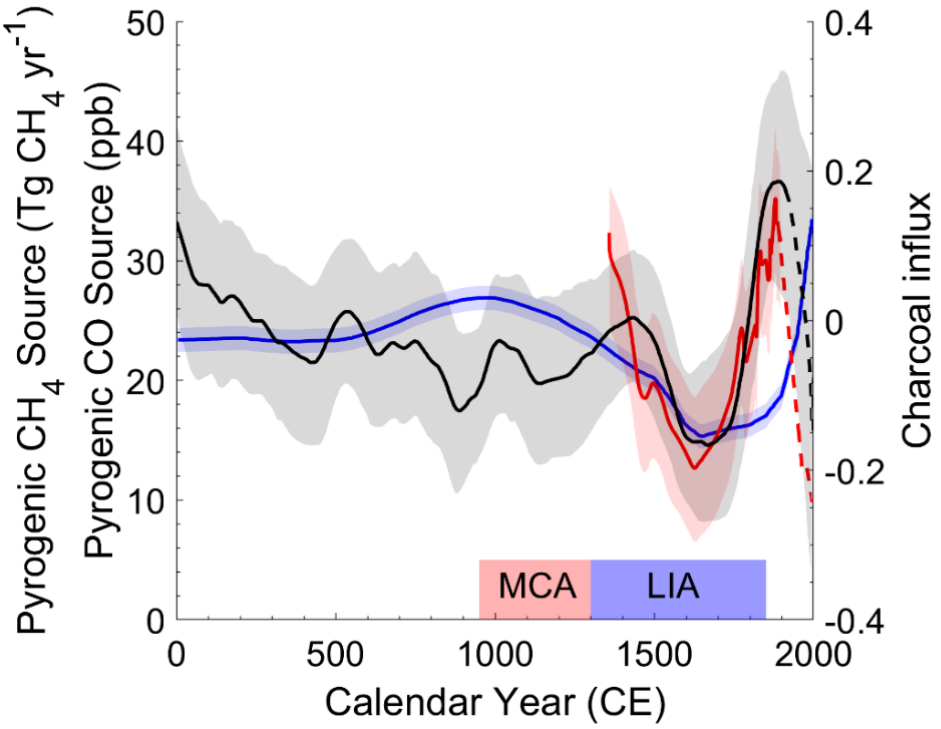

Figure 1.9: Compilation of biomass burning proxy records for the last 2,000 years adapted from *van der Werf et al*. (2013). Shaded areas highlight the timing of the Medieval Climate Anomaly (MCA) and Little Ice Age (LIA). Black: composite of sedimentary charcoal records (*Marlon et al.*, 2008), Blue: pyrogenic methane based on ice core methane and $\delta^{13}CH_4$ in an Antarctic ice core (*Ferretti et al.*, 2005), Red: Carbon monoxide, $\delta^{13}CO$ and $\delta C^{18}O$ in an Antarctic ice core (*Wang et al.*, 2010)

CHAPTER 2

Analytical methods for analysis of trace gases in ice cores

Includes excerpts from:
M. R. Nicewonger, K. R. Verhulst, M. Aydin, E. S. Saltzman, "Preindustrial atmospheric ethane levels inferred from polar ice cores: A constraint on the geologic sources of atmospheric ethane and methane," *Geophysical Research Letters*, (2016).

M. R. Nicewonger, M. Aydin, M. J. Prather, E. S. Saltzman, "Large changes in biomass burning over the last millennium inferred from paleoatmospheric ethane in polar ice cores," *Proceedings of the National Academy of Sciences*, (2018).

2.1 Overview

This chapter discusses the analytical methods used in this study to extract ice core air bubbles and analyze the air for ethane and acetylene. The chapter is organized in sections describing 1) the analysis of trace gases using gas chromatography and mass spectrometry, 2) the quantification of ethane and acetylene in air samples, 3) the wet extraction technique used to extract air from ice core samples, 4) the solubility effect during wet extraction, and 5) the ice core sites and chronologies.

2.2 Analysis of trace gases

2.2.1 Gas Chromatography/Mass Spectrometry Instrumentation

Ice core samples were analyzed using a gas chromatograph (GC - Agilent 6890) coupled with a high-resolution mass spectrometer (MS - Waters Autospec Ultima), using an electron impact ionization source (30 eV) in positive ion mode. The instrument has a dual-focusing

electro-magnetic analyzer and was operated with a mass resolution >8000 (M/ΔM at 5%). Further details of the use of this instrument for ice core analysis are given by *Aydin et al.* (2007).

2.2.2 Automatic sample preparation

Sample preparation consists of four main stages: collection, loading, refocusing, and injection. A custom, automated inlet was used to quantify, collect, and cryogenically focus the gas sample before injection into the GC/MS system (*Aydin et al*., 2007). During the loading stage, the sample flows through a trap containing glass beads which is immersed in liquid nitrogen (-196°C). The target gases (analytes) condense on the glass beads while the major components of air (N_2, O_2, Ar) flow through the trap and into a 300 cm^3 calibrated volume. The collection chamber is evacuated before each sample collection and serves to measure the size of the gas sample and provides a pressure gradient to pull the sample through the trap. The size of the gas sample is determined by measuring the pressure in the calibrated volume before and after sample collection using a capacitance manometer. Next, the calibrated volume is isolated and evacuated and the process of sample collection is repeated to collect remaining sample in the line. After sample collection is completed and loaded onto the trap, an aliquot of approximately 30 cm^3 (at STP) of isotopically labeled standard (discussed in section 2.2.3) is loaded onto the trap following the same sample collection procedure.

During the refocusing stage, the target gases and the isotope standard are transferred from the glass bead trap to a fused silica trap in a helium carrier gas stream. This trap is also immersed in liquid nitrogen. Compounds more volatile than the target gases are removed during the transfer between the first and second trap, allowing for a cleaner injection.

During the injection stage, the liquid nitrogen is removed from the second trap and the loop is heated and the gases flow into the GC column.

2.2.3 Internal and external standards

An isotope-labeled standard is added to each sample before analysis to serve as an internal reference for quantification and to monitor for changes in the mass spectrometer's response and sensitivity. The isotope standard consists of eight-isotopically labeled gases: ^{13}C-ethane ($H_3{}^{13}C–{}^{12}CH_3$), ^{13}C-propane, ^{13}C-butane, ^{13}C-carbonyl sulfide, D3-methyl chloride (CD_3Cl), D3-methyl bromide (CD_3Br), D3-acetonitrile (CD_3CN), and ^{13}C-carbon disulfide. The internal standard is diluted to ambient (ppt) levels from the primary standard (ppb-level) by using humidified N_2 in a 34L stainless steel air cylinder (*Aydin et al*., 2007). In this study, the ^{13}C-ethane peak was used to quantify the ^{12}C (unlabeled) ethane peak and the ^{12}C (unlabeled) acetylene peak.

System calibrations were performed quarterly using trace gas standards made in-house. For ethane, four primary calibration standards were used in this study (M8, M10, M11). For acetylene, two primary calibration standards were used in this study (H1 and H2). The M8, M10, and M11 gas standards were prepared from commercial-grade pure compounds (*Aydin et al.*, 2007). The H1 standard was prepared from a ppm-level commercial-grade standard which contained acetylene, ethane, and other hydrocarbons (Scott Gas, Scotty Can). The H2 standard was prepared by taking an aliquot of acetylene from the gas-stream of a high-pressure cylinder mixed with acetone. Pure ethane from commercial-grade cylinders was also added to H2. Working standards (ppt-level) were made by diluting the primary standard (ppb-level) with humidified N_2 in an electropolished stainless steel flask. Working standards were prepared when

needed and used the same day. Example calibration curves for ethane and acetylene are shown in Figure 2.1.

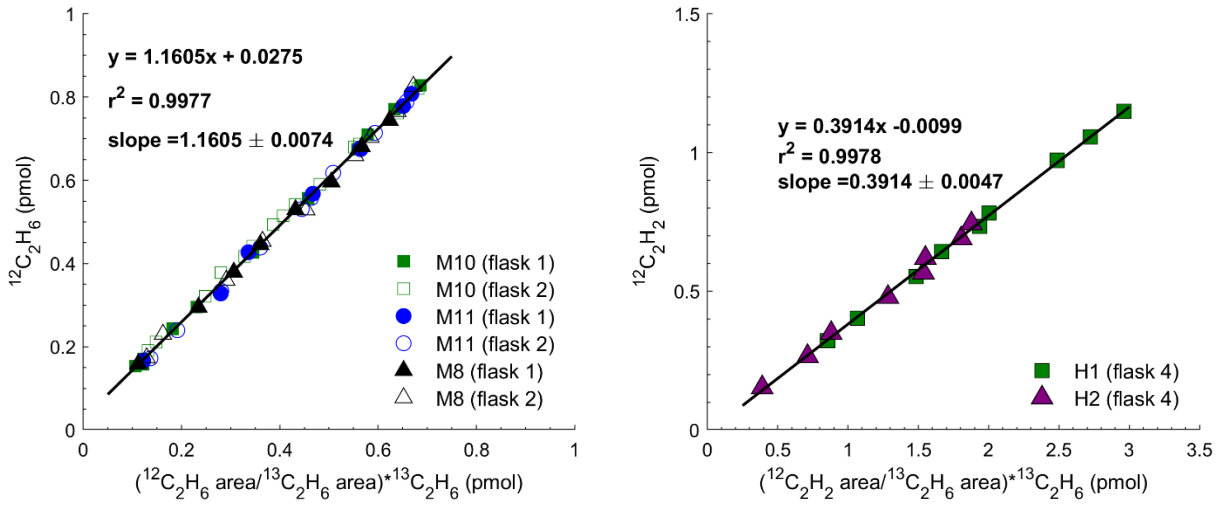

Figure 2.1: Ethane (left) and acetylene (right) calibration curves. File: CAL primary 17Oct2018

2.2.4 Gas chromatography

The gas chromatograph consists of two columns: a 5 m long DB5 pre-column (0.32 mm ID and 0.25 µm film thickness; Agilent J&W) and a 55 m long DB1 analytical column (0.32 mm ID and 0.25 µm film thickness) connected by a multi-port redirecting valve. The flow rate is 1 cm^3 min^{-1}. The chromatographic separation of gases is achieved using a temperature ramp described in Table 2.1.

Table 2.1: Temperature profile scheme for the Agilent 6890 gas chromatograph (*Aydin et al.*, 2007).

Stage	$T_{initial}$	T_{final}	Program
1	40°C	-50°C	pre-cool
2	-50°C	-50°C	isothermal for 3 min at beginning of injection
3	-50°C	-40°C	5°C/min ramp up
4	-40°C	-30°C	15°C/min ramp up
5	-30°C	150°C	30°C/min ramp up
6	150°C	150°C	isothermal for 17 min (including backflush)

2.2.5 Mass spectrometric detection

The mass spectrometer detects two peaks of ethane at masses 30.0470 amu and 31.0503 amu. Acetylene is detected at mass 26.0157 amu. The acetylene peak is fully chromatographically resolved from the ethane (C_2H_6) and ethylene peaks (C_2H_4) (Figure 2.2). Data is collected over nine time functions, measuring 23 masses at different retention times, but only two functions were pertinent to this research project, functions 1 and 3 (Table 2.2). Function 1 monitors for C_2H_2, C_2H_6, and $^{13}C_2H_6$. Function 3 monitors for CFC-12, which is used to detect modern air contamination. The total analysis time is 15 minutes. Mass calibration was performed daily by injecting approximately 0.1 µl of deuterated dodecane (d-dodecane) and 0.5 µl of acetonitrile into a reservoir upstream of the mass spectrometer source. Mass calibration was performed for the cyanide peak (CN, mass: 26.0180 amu), and then the acetonitrile was pumped out of the system after mass calibration to reduce impacting the acetylene peak during sample analysis. Different lock masses were used for each time function (Table 2.2).

Table 2.2: Masses and retention times of analytes detected by the GC/MS used in this study.

Function	Analyte	Mass (amu)	Retention Time (min)	Lock Mass
1	$^{12}C_2H_2$	26.0157	6.01	31.9898
1	$^{12}C_2H_6$	30.0470	6.15	31.9898
1	$^{13}C_2H_6$	31.0503	6.15	31.9898
3	CFC-12	84.9657	9.16	80.4100

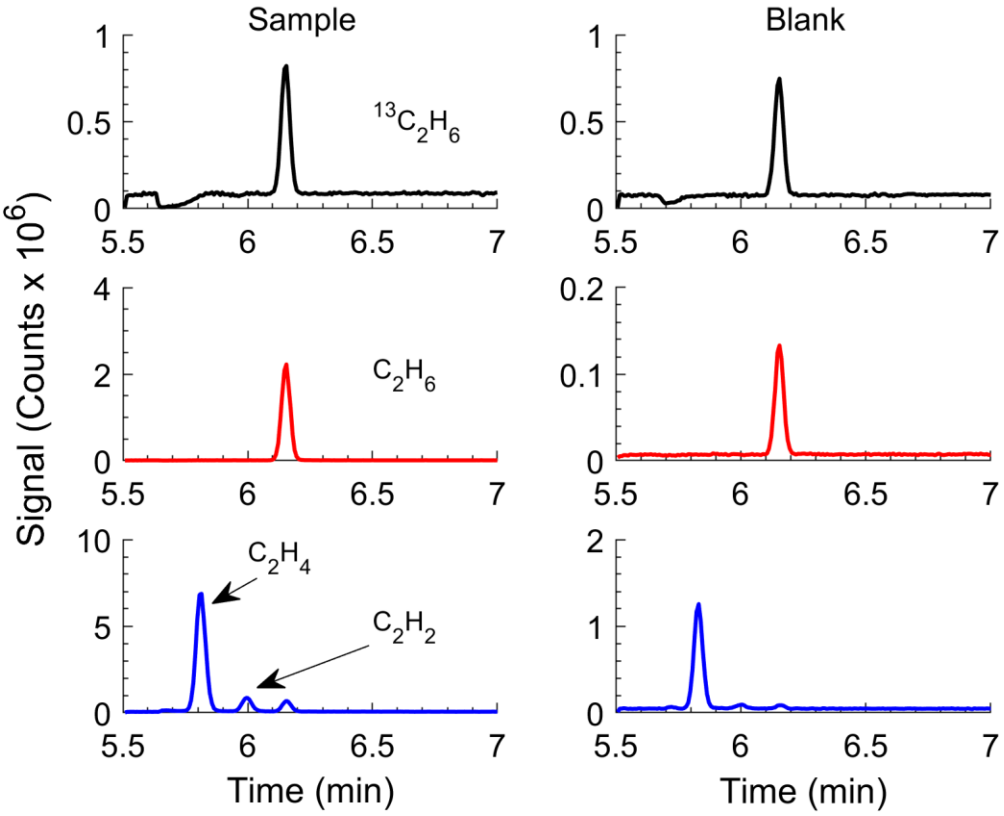

Figure 2.2: Sample chromatogram showing the $^{13}C_2H_6$ peak (top), C_2H_6 peak (middle), and C_2H_2 peak (bottom) for a Greenland sample (left) and respective post-melt analytical blank (right). Note the vertical axes scales change between sample and blank.

2.3 Ice core gas extraction method

2.3.1 Wet extraction apparatus

Trace gases were extracted from ice core samples using a wet-extraction technique which involves melting the ice core samples (*Nicewonger et al.*, 2016; 2018). A schematic diagram and photos of the wet-extraction system are is shown in Figure 2.3-2.5. Ice core samples were melted in an all-glass extraction chamber consisting of two separate pieces. The lower part of the extraction chamber is cylindrical with a rounded bottom (ID 3”). The top part of the chamber is fitted a glass shut off valve with a polytetrafluoroethylene (PTFE) o-ring (Glass Expansion

Australia). Both pieces have flat glass flanges that are sealed together using a homemade o-ring made from 0.05" OD indium wire (Indium Wire Extrusion). The glass flanges on the chamber were clamped using a Delrin (polyoxymethylene) clamp with six ¼" stainless steel bolts. The volume of the chamber is roughly 1.5 L. The extraction chamber is connected to the glass bead trap via a small glass flange sealed with a homemade indium o-ring (0.05" OD). This smaller flange is clamped using a custom-machined Derlin clamp with four (3/16") stainless steel bolts equally spaced. The glass bead trap consists of several coils (5/8" OD) of 4 mm glass beads and a reservoir to dry the air stream before collection in a ¼" OD stainless steel tube immersed in liquid helium. The trap and extraction chamber are connected to an all-glass vacuum line with an oil-free pumping system consisting of a molecular drag pump (Adixen Drytel model #1025) backed with a diaphragm pump (Pfeiffer model #MVP 070-3). An automatic switching system using pneumatic valves opens the vacuum line to the molecular drag pump (turbo) when the pressure in the line drops below 2 Torr.

The first wet extraction results in 2014 were collected using the wet-extraction system describe above, except the separate components of the vacuum line (i.e. trap, chamber) were connected using polytetrafluoroethylene (PTFE) connectors rather than the flat flanges with indium o-rings (*Nicewonger et al.*, 2016). This extraction system design is designated as "Procedure 1" in the following discussion. The extraction system in "Procedure 2", "Procedure 3", and "Procedure 4" had the flat flanges with indium o-rings (Table 2.3, Figure 2.6). Several small procedural changes occurred over the course of this research in order to reduce the level and variability of background (blank) levels in the system. Table 2.3 summarizes the differences between each of these procedures.

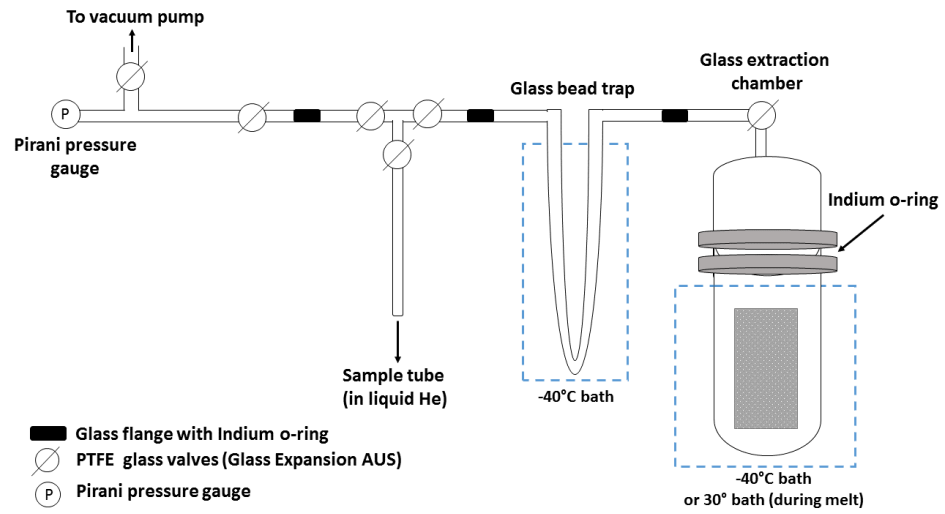

Figure 2.3: A schematic diagram of the wet extraction system used in this study.

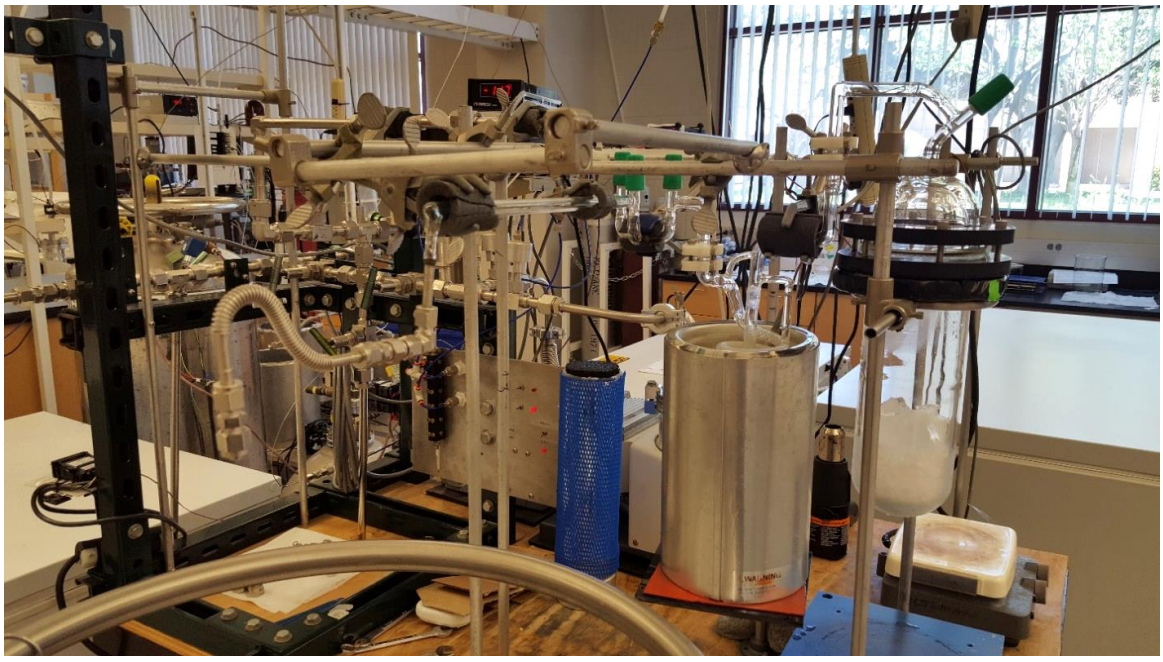

Figure 2.4: A photo of the wet-extraction line with an ice core sample in the extraction chamber. Photo by M. Nicewonger.

Figure 2.5: Photo of the extraction chamber (right) with an exploded ice core sample. The glass bead cold trap is immersed in the dry ice/ethanol bath (left). Photo by M. Nicewonger.

2.3.2 Wet extraction procedure

For all procedures, ice core samples weighing roughly 150-400 g were loaded into the two-piece glass extraction chamber. Prior to loading, the outer 3-5 mm of the sample were cleaned with a scalpel to remove surface contamination. Samples from fluid-drilled ice cores were handled and prepped in a different manner (see Section 2.3.4). After cleaning, samples were placed inside the pre-cooled extraction chamber (-40°C, dry ice/ethanol) and the chamber was sealed. Indium wire used as seals was soaked in 5% H_2SO_4 solution and rinsed with milli-Q

water prior to use to remove possible surface oxidation and contamination. The extraction chamber was then connected to the glass vacuum line. Once a leak tight seal was achieved, monitored by visual examination of the Pirani pressure gauge (< 3 mTorr), the extraction line was flushed several times with dry N_2 to remove residual lab air in the chamber and vacuum line. The sample was left pumping for roughly 45-60 minutes. The glass bead trap was immersed in a -40°C dry ice/ethanol bath for the whole duration of the wet extraction.

Table 2.3: Differences between the various wet extraction procedures.

	Procedure			
	1	2	3	4
Stir bar inside sample chamber	Yes	Yes	No	No
Thermal shock explosion with sample valve open to pump	No	No	No	Yes
Pumping time after thermal shock explosion or during analytical blank	0 min	0 min	1-2 min	5 min
Connection type between extraction line components	PTFE	indium	indium	indium
Seal on the extraction chamber	indium	indium	indium	indium

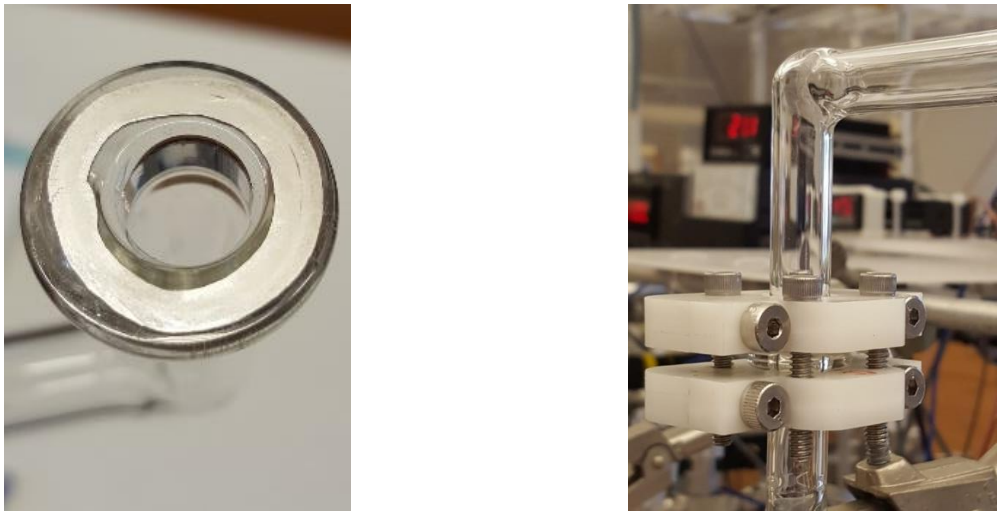

Figure 2.6: Photo of the flat glass flange connection with indium o-ring pressed flat after use (left) and the Delrin clamp (right). Photos by M. Nicewonger.

When the sample was ready to be melted, the -40°C bath surrounding the extraction chamber was replaced with a 70-80°C bath for roughly 1 minute or less to induce a thermal shock and explosion of the ice core. The bath was removed, and the chamber was left at ambient lab temperature for a preset period (0-5 minutes; Table 2.3) during which the chamber was opened to the vacuum pump. This explosion and subsequent pumping serve two purposes, 1) to increase the surface area of the ice core sample and reduce the total melting time, and 2) to flush the extraction chamber, cold trap, and vacuum line with ice core air. The chamber is then immersed in a warm bath (30°C) and isolated from the vacuum pump immediately after the ice core begins to melt. Samples analyzed during Procedure 1-3 underwent the same thermal explosion, but during the explosion, the valve on the extraction chamber was closed (Table 2.3).

When only a small piece of unmelted ice remained (<5 g), the warm bath was replaced with an ice bath (0°C) to prevent further warming during sample extraction. The valves were configured to allow the air sample to pass through the cold trap and be cryogenically pumped in the stainless still tube immersed in liquid helium (4K) for two minutes. The stainless-steel tube was then closed, removed from the extraction line, and was allowed to warm to room temperature. The collected ice core gas sample was analyzed using the GC/MS system described in Section 2.2

An analytical blank was performed after every ice core sample melt to determine the background trace gas levels in the extraction system. The ice core melt water was refrozen by replacing the ice bath with the -40°C bath while pumping to remove any dissolved gases in the melt water. Once the melt water was refrozen (roughly 30-45 minutes), the vacuum line and extraction chamber were flushed several times with N_2. Next, the -40°C bath was replaced with the warm water bath (30°C) and the ice core melt water was allowed to melt for several minutes

while being pumped on (depending on which procedure was used, see Table 2.3), similar to the post-explosion pumping step for the ice core sample. After pumping, a 20-30 cm^3 (at STP) aliquot of N_2 was isolated in the headspace above the frozen melt water by shutting the valve on the chamber. The frozen melt water was slowly melted following the same procedure for the ice core sample. The extraction and analysis of the blank was identical to the sample. Blanks for each compound are described in Section 2.4.

2.3.3 Extraction system cleaning procedure

Before loading every ice core sample, the extraction chamber was cleaned in a 1 M KOH bath, rinsed with MilliQ water, and air-dried between 60-100°C. The glass bead trap was cleaned roughly every two weeks by filling the trap with 1 M KOH and placing it in a warm bath (60°C) for 4-6 hours before being dried in an oven at 100°C. The glass bead trap was also routinely cleaned if unused for more than 2 weeks, after which blank levels of ethane and acetylene tended to increase.

2.3.4 Decontamination of ice core samples prior to analysis (dry-drilled vs. fluid drilled samples)

Ice core samples analyzed in this study were from dry-drilled and fluid-drilled cores. The fluid used for ice core drilling is typically a blend of hydrocarbons and therefore had a high potential to contaminate the hydrocarbon trace gas analysis. Dry-drilled cores were decontaminated in a one-step processes in which the outer 3-5 mm of the sample was cleaned with a scalpel. Fluid-drilled samples were decontaminated in a two-step process. First, the sample was cleaned thoroughly with a clean scalpel and/or edges were cut off using a bandsaw. For example, if a fluid-drilled sample had a rind side (the outermost side that is in contact with

the drill and drill fluid) the bandsaw would be utilized to remove roughly 3-4 mm off that rind edge. After the initial cleaning, the sample was placed into a clean lay-flat bag for temporary storage. All surfaces in contact with the ice core, such as the preparation table and scalpel blade were cleaned with MilliQ water. Second, after the initial cleaning step, fluid-drilled samples were re-cleaned following the same steps used for the dry-drilled samples. All ice core samples were handled with new polyethylene gloves.

2.4 Blank correction and determination

Analytical blanks as described in section 2.3.2 were conducted after every sample melt to quantify the background ethane and acetylene level in the extraction and analysis system. Ethane and acetylene mixing ratios in this study are reported as parts per trillion (ppt = pmol mol^{-1}). The ethane and acetylene mixing ratio (X_{cmpd}) in the ice core bubbles are calculated as follows:

$$X_{cmpd}(ppt) = \frac{m_{sample} - m_{blank}}{m_{air}} \quad (2.1)$$

where m_{sample} is the amount of ethane or acetylene measured in the sample (pmol), m_{blank} is the ethane or acetylene (pmol) in the mean post-melt blank from a series of samples and m_{air} is the dry air (mol) extracted from each ice core sample.

Due to the changes in the extraction procedure, several sets of "mean blank" were calculated to apply to different time periods of analysis. The mean blank calculation excluded blanks in which known analytical mistakes occurred and blanks which were greater than the mean + 2σ (Figure 2.7 and Figure 2.8). The mean blanks of ethane and acetylene for each procedure are outlined in Table 2.4. Procedure 4 was the longest-running procedure and several mean blanks were used over the course of analysis (Tables 2.5-2.6).

Table 2.4. Ethane and acetylene levels in the post-melt N_2 blanks (mean ± 1σ in pmol)

	Procedure 1	Procedure 2	Procedure 3	Procedure 4
Dates	7/17/2014 to 10/30/2014	10/8/2015 to 10/30/2015	11/6/2015 to 2/19/2016	2/26/2016 to 7/30/2018
Ethane	0.091 ± 0.024 (n = 40)	0.101 ± 0.034 (n = 13)	0.093 ± 0.036 (n = 20)	0.040 ± 0.015 (n = 197)
Acetylene	0.029 ± 0.012 (n = 40)	0.016 ± 0.010 (n = 13)	0.028 ± 0.012 (n = 21)	0.007 ± 0.006 (n = 213)

Table 2.5: Ethane blank during procedure 4.

Date			
Start date	End Date	Ethane blank (pmol)	n
02/26/2016	05/27/2016	0.058 ± 0.013	27
06/02/2016	10/13/2016	0.040 ± 0.007	33
10/26/2016	10/13/2017	0.048 ± 0.013	53
10/27/2017	02/16/2018	0.035 ± 0.007	32
03/07/2018	07/30/2018	0.025 ± 0.008	52
All dates		**0.040 ± 0.015**	197

Table 2.6: Acetylene blank during procedure 4.

Date			
Start date	End Date	Acetylene blank (pmol)	n
02/26/2016	04/13/2016	0.002 ± 0.003	20
04/14/2016	05/27/2016	0.021 ± 0.013	10
06/02/2016	11/02/2016	0.001 ± 0.002	42
02/14/2017	11/27/2017	0.008 ± 0.002	60
11/29/2017	05/30/2018	0.011 ± 0.004	46
06/06/2018	07/30/2018	0.006 ± 0.002	35
All dates		**0.007 ± 0.006**	213

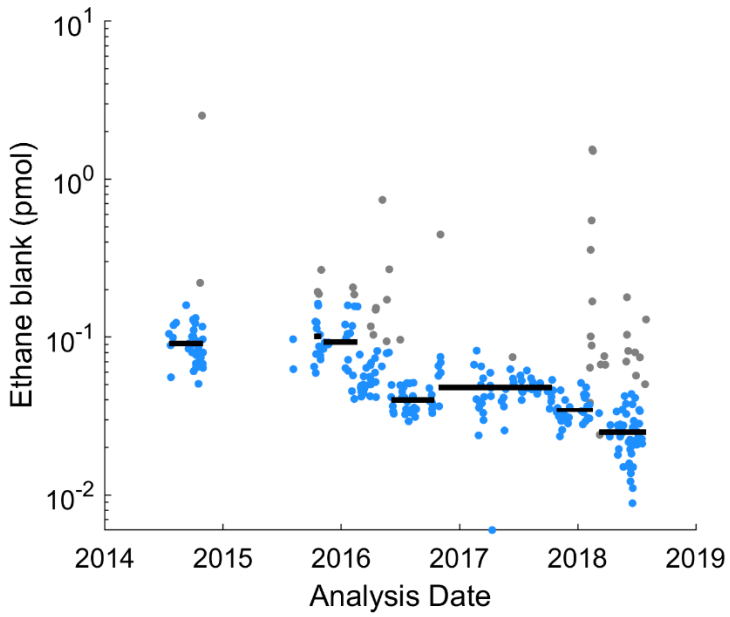

Figure 2.7: Ethane post-melt analytical blanks through time. Samples excluded from the mean blank calculations are shown in gray. Black bars indicate the mean blank used to correct samples over a certain time range as outlined in Table 2.5.

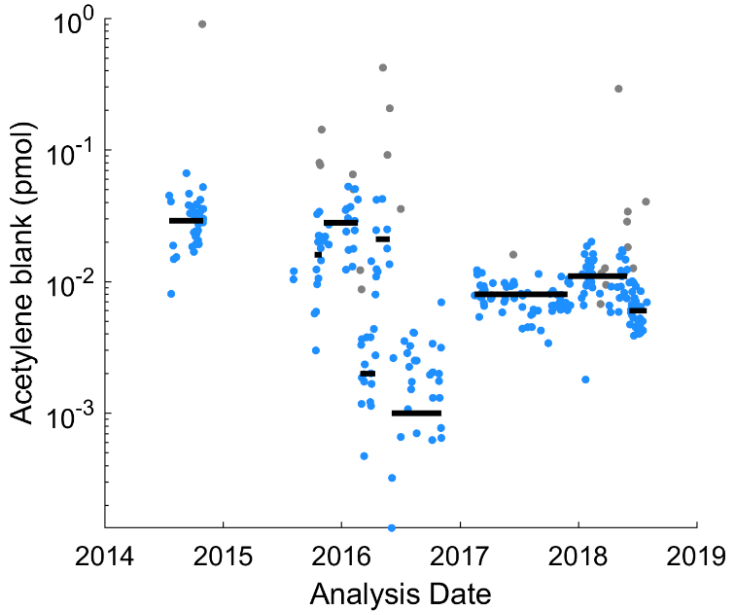

Figure 2.8: Acetylene post-melt analytical blanks through time. Samples excluded from the mean blank calculations are shown in gray. Black bars indicate the mean blank used to correct samples over a certain time range as outlined in Table 2.6.

2.5 Solubility effect during wet extraction

The fact that water is present during the extraction process means that gas solubility may have an influence on the measured mixing ratios**.** Ethane and acetylene are more soluble in water than air (Table 2.7; *Sander, 2015* and references within). The measured mixing ratios in the gas obtained via wet extraction may be biased low if a significant fraction of the ice core ethane and acetylene are left behind in the melt water. A dimensionless Henry's law solubility factor was used to examine how much ethane, acetylene, and air would be left in the ice core melt water if the extraction chamber were in equilibrium. The dimensionless Henry's Law solubility (α) for ethane and acetylene was calculated from data in Sander (2015), as follows:

$$\propto = \frac{\left(\frac{moles}{m^3}\right)_{liquid}}{\left(\frac{moles}{m^3}\right)_{gas}} \tag{2.2}$$

Using the ideal gas law:

$$\frac{n}{v} = \frac{P}{RT} \tag{2.3}$$

where P is the pressure in Pa, R is the gas constant in units of m^3 Pa K^{-1} mol^{-1} and T is the temperature in K. Gas density is therefore:

$$\frac{mol}{m^3} = \frac{1\ Pa}{8.314\ \mathrm{m^3\ Pa\ K^{-1}}\ mol^{-1} * \ 273.15K} = 4.4\ x\ 10^{-4}\ \frac{mol}{m^3} \tag{2.4}$$

Assuming a pressure of 1 Pa, the dimensionless Henry's Law constant for ethane, acetylene, and air are:

$$\alpha_{ethane} = \frac{\left(3.97\ * 10^{-5}\frac{mol}{m^3}\right)_{liquid}}{\left(4.40 * 10^{-4}\ \frac{mol}{m^3}\right)_{gas}} = 0.09 \tag{2.5}$$

$$\alpha_{acetylene} = \frac{\left(6.91 * 10^{-4} \frac{mol}{m^3}\right)_{liquid}}{\left(4.40 * 10^{-4} \frac{mol}{m^3}\right)_{gas}} = 1.57 \quad (2.6)$$

$$\alpha_{air} = \frac{\left(1.48 * 10^{-5} \frac{mol}{m^3}\right)_{liquid}}{\left(4.40 * 10^{-4} \frac{mol}{m^3}\right)_{gas}} = 0.03 \quad (2.7)$$

where the numerator in each equation is the Henry's law constant for each compound at 273.15 K (0 °C) (Table 2.7).

The dimensionless Henry's laws can be corrected for the average liquid to gas volume that is present in the extraction chamber. The extraction chamber is roughly 1.5 L and the average sample size is between 300-400 g, corresponding to melt water volume of 0.3-0.4 L. For a typical ice core sample of 300g, the volumes of gas (v_g) and water (v_l) in the extraction chamber are as follows:

$$\frac{v_g}{v_l} = \frac{0.3\ L}{(1.5 - 0.3)\ L} = 0.25 \quad (2.8)$$

If the gas and liquid phases were allowed to equilibrate, the fraction (*f*) of each gas present in the liquid phase would be calculated from the equation:

$$f = \alpha * \frac{v_g}{v_l} \quad (2.9)$$

From equation 2.9, the fraction of ethane, acetylene, and air present in the liquid phase becomes:

$$f_{ethane} = 0.09 * 0.25 = 0.023 \quad (2.10)$$

$$f_{acetylene} = 1.57 * 0.25 = 0.392 \quad (2.11)$$

$$f_{air} = 0.03 * 0.25 = 0.008 \quad (2.12)$$

The volume corrected dimensionless solubility constants mean that roughly 2.3% of the ethane, 39.2‰ of the acetylene, and 0.8% of the air from the ice core bubbles would be dissolved in the liquid if the extraction chamber were at equilibrium. This means that there would be a small solubility correction for ethane and a large solubility correction for acetylene. Such a large correction for acetylene would make the preindustrial levels reported in this study significantly higher.

A second, more empirical approach to estimating the effect of solubility was obtained by comparing results for several trace gases from wet extraction to those from the dry shredding extraction technique described by *Aydin et al*. (2007). Unfortunately, it is not possible to carry out a comparison of wet and dry extraction techniques for acetylene or ethane, because of spurious production of these gases during dry extraction. Instead, measurements of carbonyl sulfide, methyl bromide, and methyl chloride in the South Pole Ice Core (SPC14) were used (Figure 2.9). In all cases, these soluble trace gases were depleted in the wet extractions relative to the dry extractions. This effect increased with increasing gas solubility (Figure 2.10). The magnitude of the depletion, expressed as a fractional depletion (1-wet/dry) was 0.15, 0.43, and 0.52 for carbonyl sulfide, methyl chloride, and methyl bromide, respectively. These are considerably smaller than the calculated values assuming complete equilibration between gas and liquid during wet extraction (0.25, 0.67, and 0.71, respectively). The results indicate that full equilibration does not occur during wet extraction. This is presumably due to the very short gas/liquid contact time between the bubbles and the melt water as the bubbles are released from the melting ice.

Ethane is sufficiently insoluble that even assuming complete equilibrium, a solubility correction of only 0.023 would be required. This is well within experimental error of the ice core

analysis. No corrections were made to the ethane data during this study, but as the precision of ice core ethane analyses improves, it may become meaningful to correct the data for this negative bias.

Acetylene has a similar solubility at 273.15 K to carbonyl sulfide (Table 2.7), so empirically we expect that the depletion should be similar at about 0.15. Correction of the ice core data to account for this negative bias will be required but has not yet been done. For the purpose of this thesis, we chose to not correct the acetylene data for the solubility effect as further work to better characterize the solubility correction is still underway. The overall interpretations and findings (Chapter 5 and 6) drawn from the ice core acetylene record will not be impacted by this decision since the solubility correction is modest (~15%) and would be applied to all the data.

Table 2.7: Henry's law constants used for the solubility correction calculation (compilation from Sander, 2015).

Compound	**k°H @ 298.15 K**	**dln(k_H)/d(1/T)**	**k_H(T)[a] @ 273.15 K**	**Reference**
	$\left[\frac{mol}{m^3\ Pa}\right]$	[K]	$\left[\frac{mol}{m^3\ Pa}\right]$	
oxygen	1.20 x 10^{-5}	1700	1.05 x 10^{-5}	*Warneck and Williams* (2012)
nitrogen	6.40 x 10^{-6}	1600	2.02 x 10^{-5}	*Warneck and Williams* (2012)
argon	1.40 x 10^{-5}	1700	2.36 x 10^{-5}	*Warneck and Williams* (2012)
ethane	1.90 x 10^{-5}	2400	3.97 x 10^{-5}	*Sander et al*. (2011)
acetylene	4.10 x 10^{-4}	1700	6.91 x 10^{-4}	*Sander et al*. (2011)
carbonyl sulfide	2.10 x 10^{-4}	3300	5.78 x 10^{-4}	*Warneck and Williams* (2012)
methyl bromide	1.70 x 10^{-3}	3100	4.40 x 10^{-3}	*Sander et al*. (2011)
methyl chloride	1.30 x 10^{-3}	3300	3.58 x 10^{-3}	*Sander et al*. (2011)
"air"[b]	--	--	1.48 x 10^{-5}	

[a] The temperature dependent solution for the Henry's law constant is:

$k_H(T) = k°H * \exp([d(\ln(k_H))/d(1/T)] *[(1/T) - (1/T°)])$

where $d(\ln(k_H))/d(1/T)$ is the temperature dependence parameter for Henry's Law constant and k°H is the Henry's law constant for solubility of the compound in pure water at T°=298.15 K.

[b] "Air" is calculated by at 273.15 K by:

$air = 0.78*H_{nitrogen} + 0.21*H_{oxygen} + 0.01*H_{argon}$

where $H_{compound}$ is the Henry's law constant for each compound at 273.15 K.

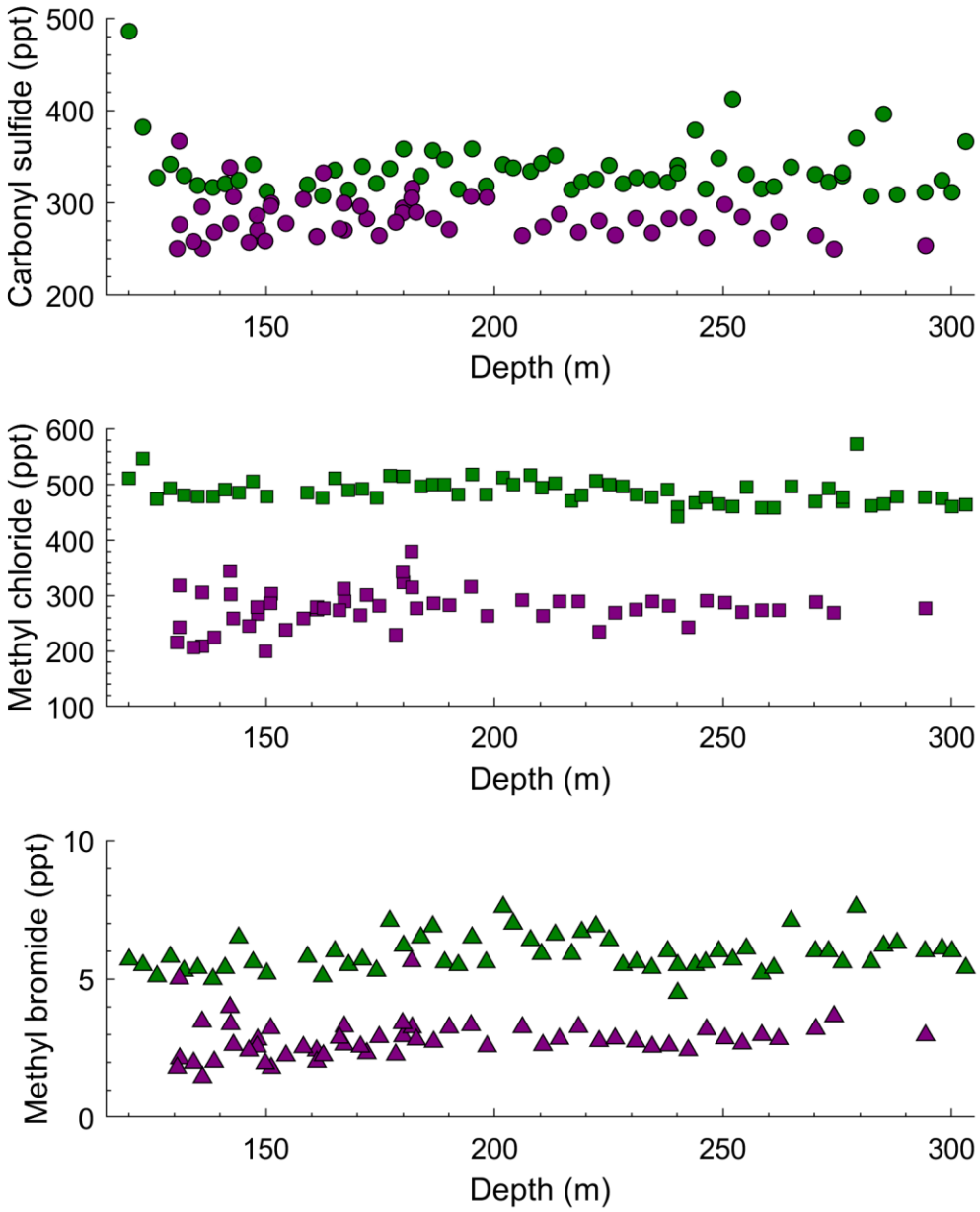

Figure 2.9: Dry-extraction (green) and wet-extraction (purple) results from the South Pole Ice Core (SPC14) for carbonyl sulfide (top, circles), methyl chloride (middle, squares) and methyl bromide (bottom, triangles). Data from dry extraction from M. Aydin (*personal communication*).

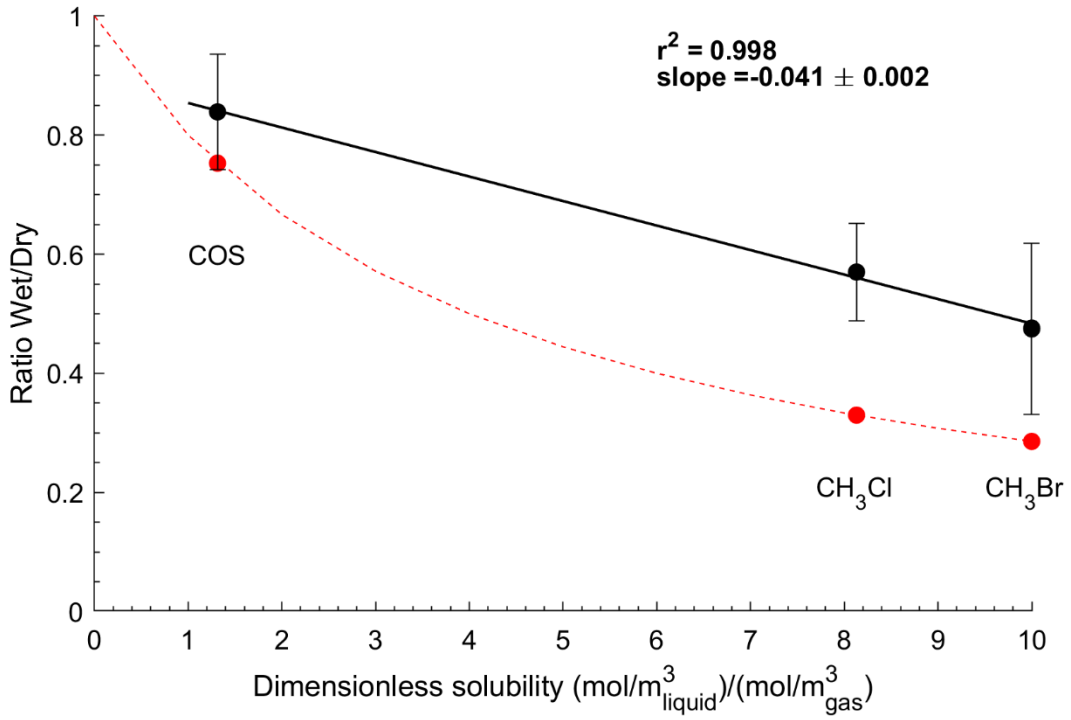

Figure 2.10: Observed (black) versus calculated equilibrium (red) solubility depletion between the wet- and dry-extraction mixing ratios measured for carbonyl sulfide (COS), methyl chloride (CH_3Cl), and methyl bromide (CH_3Br). The calculated depletions assume equilibrium (Table 2.7). The observed data are based on the measurements of South Pole ice core samples (SPC14) in Figure 2.9.

2.6 Ice core sites and chronologies

West Antarctic Ice Sheet (WAIS Divide): The WAIS Divide (WDC05A) core was dry-drilled in 2005/2006 to a depth of 298 m using a 10 cm electromechanical drill. The WDC05A site is about 1.3 km northwest of the main borehole of the main WAIS Divide deep core (WDC06A). The annual accumulation at WAIS Divide is about 22 cm y^{-1} ice equivalent and the mean annual temperature is -30°C (*Orsi et al.*, 2012).

The WDC05A samples were dated by linear interpolation from the nearest depths in the WDC05A:2 chronology based on methane measurements and subtracting a delta-age (ice age – gas age, Δage) of 208 years (*Mitchell et al.*, 2011). Air trapped in ice cores is a mixture of air from a range of years due to diffusive mixing in the firn and the chronology represents a best

estimate "mean age" (*Buizert et al.*, 2012). The smoothing function at WAIS Divide has a width at half height of roughly 20 years (*Battle et al.*, 2011). The gas age of the deepest (298.9 m) and shallowest (83.1 m) WDC05A samples analyzed in this study are 994 and 1925 CE, respectively. Uncertainty on the mean age for the WDC05A samples is roughly 1% (*Mitchell et al.*, 2011).

Samples were analyzed from the deep, fluid drilled WAIS Divide ice core (WDC06A). The drill fluid used was a mixture of Isopar-K and HCFC-141b (*Souney et al.*, 2014). The WDC06A core was drilled from 2006-2012 to a final depth of 3405 m. The WDC06A borehole is located at 79.467°S, 112.085°W. The WDC06A samples were dated by linear interpolation from the nearest depth using the WD2014 ice-age chronology and subtracting a Δage of 208 years to obtain a gas age (*Buizert et al*., 2015; *Sigl et al*., 2016). Uncertainty on the mean age for WDC06A is 0.5%. The gas age of the deepest (603.7 m) and shallowest (116.9 m) WDC06A samples used in this study are 303 BCE and 1781 CE, respectively.

South Pole Ice Core (SPC14): Samples were analyzed from the fluid-drilled South Pole Ice Core (SPC14) The drill-fluid used was Estisol 140 and Isopar-K was applied to the core in the field to help remove residual Estisol 140 prior to packaging. The SPC14 core was drilled 2.7 km from the South Pole Station during 2014-2016 to a final depth of 1751 m. The mean accumulation rate at the SPC14 site is 8 cm y^{-1} ice equivalent and the mean annual temperature is -49°C (*Casey et al.*, 2014). Samples were dated using methane ties to the WD2014 ice-age chronology ("SPC14-03" unpublished timescale; *Buizert et al.*, 2015; *Sigl et al.*, 2016). Uncertainty on the mean age is roughly ± 30 years (*C. Buizert, personal communication*). The gas age of the deepest (294.7 m) and shallowest (130.7 m) SPC14 samples used in this study are 387 BCE and 1817 CE, respectively (calculated using the "SPC14-03" timescale).

Greenland Ice Sheet Project 2 (GISP2): Samples were analyzed from the dry-drilled GISP2B ice core. The GISP2B core was dry-drilled in 1989 to a depth of ~200 meters. The annual accumulation at the GISP2 site is 24 cm y^{-1} ice equivalent and the mean annual temperature is -31°C (*Cuffey and Clow*, 1997). To date the GISP2B samples, first an ice-age scale was determined by applying a +5 year offset to the GISP2D ice-age scale (*Aydin et al.*, 2007). Ice ages at exact sample depths were calculated by linear interpolation from the nearest depths. Gas ages were calculated by subtracting Δage of 199 years from the ice age (*Meese et al.*, 1997, *Schwander et al.*, 1997). The deepest (198.9 m) and shallowest (102.0 m) GISP2B samples are dated to 1456 CE and 1862 CE, respectively. The smoothing function for the GISP2 cores is the same as WAIS Divide (width at half height approximately 20 years) because the annual mean temperature and the accumulation rate at both sites are similar (*Schwander et al.*, 1993). Uncertainty on the GISP2B gas age is 1%.

Samples from the fluid-drilled, deep GISP2D ice core were also analyzed. The drill-fluid used was n-butyl acetate. The GISP2D ice core was drilled at Summit, Greenland from 1988-1993 to a final depth of 3053 m. The accumulation rate and temperature for the GISP2D site is like that of the GISP2B site of 24 cm y^{-1} ice equivalent and -31°C (*Cuffey and Clow*, 1997). Gas ages for the GISP2D samples were calculated by linear interpolation of the GISP2D ice-age scale to the sample depths and then subtracting a Δage of 199 years (*Meese et al.*, 1997; *Schwander et al.*, 1997). The deepest (730.2 m) and shallowest (95.5 m) GISP2D samples are dated to 1206 BCE and 1892 CE, respectively. Uncertainty on the GISP2D gas age is 1%.

CHAPTER 3

Modeling methods for interpreting ice core records

Includes excerpts from:

M. R. Nicewonger, K. R. Verhulst, M. Aydin, E. S. Saltzman, "Preindustrial atmospheric ethane levels inferred from polar ice cores: A constraint on the geologic sources of atmospheric ethane and methane," *Geophysical Research Letters*, (2016).

M. R. Nicewonger, M. Aydin, M. J. Prather, E. S. Saltzman, "Large changes in biomass burning over the last millennium inferred from paleoatmospheric ethane in polar ice cores," *Proceedings of the National Academy of Sciences*, (2018).

3.1 Overview

The approach used in this thesis was to utilize and adapt models capable of simulating atmospheric ethane, acetylene, and methane levels based on specified emissions. Three models are used: 1) a steady state six-box model for ethane, 2) a three-dimensional chemistry transport model (CTM) for ethane and acetylene, and 3) a steady-state one box model for methane and methane isotopes. The models and procedures used to infer emissions are described in detail in this chapter. Application and comparison of the output of these models with the ice core observations will be described is subsequent chapters (ethane in Chapter 4, acetylene in Chapter 5, and methane in Chapter 6).

3.2 The six-box steady state model

The six-box steady state model is based on the methane BOSCAGE-8 model by *Marik* (1998). The model consists of six zonal tropospheric boxes representing 30° wide latitude bands (three in each hemisphere, Figure 3.1) (*Nicewonger et al.*, 2016). The mass of air in each box is

weighted according to the surface area represented by each box, assuming the total amount of air in the atmosphere is 1.77 x 10^{20} moles. We presumed that 80% of the air was contained in the troposphere (defined as 1000-200 hPa) resulting in 1.42 x 10^{20} moles of air. The mass of air in the topical boxes (boxes 3 and 4) are each scaled up by 5%, while the mass of air in the remaining boxes are scaled down by 5% to represent the higher (shallower) height of the troposphere in the tropical (polar) regions. Exchange between the adjacent boxes occurs via transport parameters (k) calibrated to the observed distribution of SF_6 (Table 3.1). The transport parameters are weighted based on the mass of air exiting each box such that each term represents the turnover rate (in units of y^{-1}) between boxes. For example, the transport parameter k_{12} represents the transport rate of air between box 1 to box 2, while k_{21} represents the transport rate between box 2 to box 1, etc. The calculation for this example is as follows:

$$k_{12} = \frac{f\ (1,2)\ *\ m_{trop}}{m_{box1}} \tag{3.1}$$

$$k_{21} = \frac{f\ (1,2)\ *\ m_{trop}}{m_{box2}} \tag{3.2}$$

where f is the flow rate coefficient (unit of y^{-1}) between the two boxes of interest (in this example boxes 1 and 2), m_{trop} is the moles of air in the troposphere and $m_{box1,\ 2}$ is the moles of air in the respective box. The resulting transport rate constants for each transport term are shown in Table 3.1. Average k_{OH} (y^{-1}) is calculated for each box using the temperature and OH distribution fields from *Spivakosky et al*. (2000) and are shown in Table 3.2.

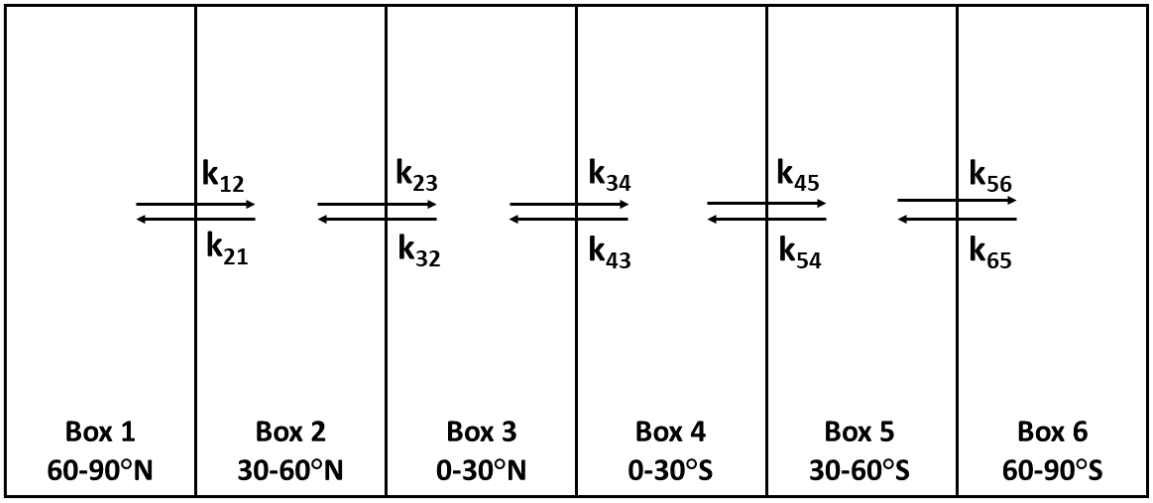

Figure 3.1: Schematic diagram depicting the six-box steady-state model and the transport parameters (y^{-1}) for each box (*Nicewonger et al.*, 2016).

Table 3.1: Transport and flow rate coefficients used in the six-box steady state model (*Nicewonger et al.*, 2016).

Parameter	Transport rate coefficent (y^{-1})	Flow rate coefficient (*f*, fraction of global air mass y^{-1})
k_{12}	3.73	0.25
k_{21}	1.37	0.25
k_{23}	4.92	0.90
k_{32}	3.60	0.90
k_{34}	2.40	0.60
k_{43}	2.40	0.60
k_{45}	3.60	0.90
k_{54}	4.92	0.90
k_{56}	3.28	0.60
k_{65}	8.96	0.60

Table 3.2: Average k_{OH} (y^{-1}) for each box in the steady state model.

	Box 1	**Box 2**	**Box 3**	**Box 4**	**Box 5**	**Box 6**
kOH	1.46	4.18	8.75	8.87	3.49	1.04

In the model, fossil fuel, biofuel and biomass burning sources were geographically distributed following the CMIP5 emission inventory for ethane (*Lamarque et al.*, 2010; *Nicewonger et al.*, 2016). To achieve reasonable agreement (± 5%) with the observed modern

levels of atmospheric ethane over Greenland, Antarctica, and the tropics during the 2000-2010 CE period (*Simpson et al*., 2006; *Aydin et al.*, 2011; *Simpson et al.*, 2012; *Blake*, 2013; *Helmig et al.*, 2014), the emissions were shifted between boxes and the final geographic distribution is described in Table 3.3. Fossil fuel, biofuel, and biomass burning emissions were adjusted to create an emission inventory with 93%, 80%, and 53% of emissions in the northern hemisphere, respectively (*Xiao et al*., 2008). Geologic ethane emissions were geographically distributed with 85% of emissions in the northern hemisphere based on seepage data and locations from *Etiope and Ciccioli* (2009).

The six-box model calculates a steady state mass balance equation for each box. An example of the mass balance equation for box 3 is shown below:

$$\frac{\mathrm{d}}{dt}(\text{box 3}) = k_{23} + k_{43} - k_{OH}(\text{box 3}) - k_{32} - k_{34}) + E_3 \quad (3.3)$$

where k represents the transport of ethane between boxes (with positive terms describing transport into the box and negative terms describing transport out of the box), k_{OH} represents ethane loss in box 3 due to OH oxidation and E (Tg y^{-1}) is the emissions into box 3. k_{OH} is different between boxes (Table 3.2). This system of six linear equations for the mass balance of each box is generated and assuming steady state (d/dt = 0), we invert the 6x6 matrix to solve for any combuition of emissions. MATLAB code for the six-box model is found in Appendix A.

Table 3.3: Latitudinal distribution of ethane sources in the six-box model for all simulations. The value given is the fraction of the source in each box (in Tg).

	Box Source/Total					
Source	**60–90°N**	**30-60°N**	**0–30°N**	**0–30°S**	**30–60°S**	**60–90°S**
Fossil fuel	0.05	0.58	0.30	0.05	0.02	0
Geologic	0.04	0.48	0.33	0.11	0.04	0
Biofuel	0.03	0.39	0.38	0.15	0.05	0
Biomass burning	0.03	0.09	0.46	0.35	0.07	0

3.2.1 Six-box steady state model: preindustrial simulation

The six-box model was used to simulate preindustrial atmospheric ethane levels over a range of biomass burning and geologic emission ranges (*Nicewonger et al*., 2016). Geologic and biomass burning sources were allowed to vary from 1-5 Tg y^{-1} at 0.01 Tg y^{-1} increments. Ethane mixing ratios in the polar regions (60-90°) were calculated for all permutations of geologic and biomass burning emissions. The permutations resulted in 501 x 501 possible combinations of geologic and biomass burning emissions and the corresponding ethane mixing ratios over the polar regions. Fossil fuel emissions were assumed to be zero. Biofuel emissions were held constant at 0.5 Tg y^{-1} according to *van Aardenne et al.* (2001).

The modeled ethane mixing ratios were compared with the ice core observations from Greenland and Antarctica. Model scenarios of geologic and biomass burning emissions that yielded ethane levels in the 60-90°N and 60-90°S boxes that fell within ±2 standard errors of the preindustrial mean from the ice core data were considered viable (*Nicewonger et al*., 2016). This resulted in a range of both biomass burning and geologic ethane emissions which we judged as successful reconstructions of the ice core ethane levels.

3.2.2 Six-box steady state model: modern simulation

A similar approach was taken to simulate modern atmospheric levels of ethane during two time periods: 1980 CE when ethane levels peaked and during the 2000-2010 CE period. In these simulations, fossil fuel and biomass burning emissions were varied from 0-20 Tg y^{-1} at 0.05 Tg increments. Geologic emissions were fixed at a “low-end” and “high-end” value. This range was determined as the plausible range in the geologic ethane source strength based on the preindustrial simulation and the ice core ethane observations.

For the 1980 CE simulation, biofuel emissions were held at 1.5 Tg y^{-1} based on historical emissions from the EDGAR-HYDE inventory (*van Aardenne et al.,* 2001). This resulted in 401 x 401 possible scenarios of fossil fuel and biomass burning emissions for the "low-end" geologic scenario and the same number for the "high-end" geologic scenario. Ethane mixing ratios in the polar regions (60-90°) were calculated for all permutations of fossil fuel and biomass burning emissions for the two geologic scenarios. Emission scenarios were considered viable if they yielded ethane levels in the 60-90°N and 60-90°S boxes that agreed within ± 5% of the atmospheric ethane level around 1980 CE as inferred from Greenland and Antarctica firn air measurements (*Aydin et al.,* 2011; *Nicewonger et al.*, 2016)

For the 2000-2010 CE simulation, biofuel emissions were held at 2.0 Tg y^{-1} based on the EDGAR-HYDE inventory (*van Aardenne et al.*, 2001). Again, this simulation resulted in 401 x 401 possible scenarios of fossil fuel and biomass burning emissions for the "low-end" geologic scenario and the same number for the "high-end" geologic scenario. Ethane mixing ratios in the each of the six boxes were calculated for all permutations of fossil fuel and biomass burning emissions for the two geologic scenarios. Modern atmospheric observations of ethane over Greenland, Antarctica, and the tropics (30°N-30°S) were used to constrain successful model emission scenarios. To constrain ethane in the tropics, the average ethane level was computed for the northern tropics (0–30°N) and southern tropics (0–30°S) boxes and the results were compared to the modern average ethane level measured in flasks during 2000–20010 C.E. (*Simpson et al.*, 2006; *Blake,* 2013). An example of the results from the six-box model is shown in Figure 3.2.

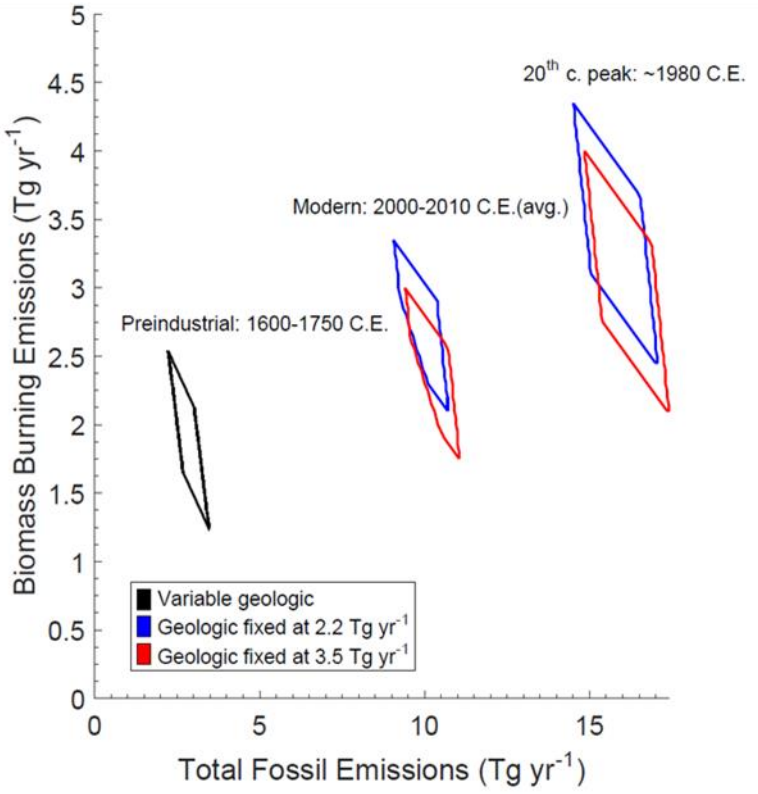

Figure 3.2: Results from the six-box model for the preindustrial and modern simulation (*Nicewonger et al.*, 2016). The preindustrial simulation constrained the range of geologic emissions that were used in the two modern simulations (2000-2010 CE and 1980 CE). Viable scenarios are enclosed by the colored contours.

3.4 Chemistry transport model

The UCI-Chemistry Transport Model (UCI-CTM) is a three-dimensional tropospheric CTM and for this work it is run in a configuration with roughly 2.8° x 2.8° horizontal resolution and 57 vertical layers (*Prather and Hsu*, 2010; *Holmes et al.*, 2013). Transport in the UCI-CTM is driven by reanalysis-forecast meteorological fields from the European Center for Medium-Range Weather Forecasting (ECMWF). The major tropospheric chemistry reactions are described by *Holmes et al.* (2013). Fossil fuel emissions of ethane and acetylene were based on the RCP year 2000 inventories from *Lamarque et al.* (2010) but scaled up to best estimates of the current emissions (*Xiao et al.*, 2007, 2008). Biomass burning emissions of dry matter were based on the Global Fire Emissions Database version 3.1 (GFED3.1; *van der Werf et al.*, 2010).

Emission factors from *Akagi et al.* (2011) were used to calculate biomass burning emissions of ethane and acetylene from dry matter emissions (Table 3.4). The modeled methane lifetime due to troposopheric OH oxidation is 8.96 years, which is 25% lower than the OH methane lifetime of 11.2 years dervived from CH_3CCl_3 observations from (*Prather et al*., 2012). To account for the high levels of OH in the UCI-CTM, the lifetimes of ethane and acetylene were increased by 25% by correspondingly reducing their reaction rate coefficients with OH. The OH loss of is calculated using $k_{OH+C2H6}(T) = 6.53 \times 10^{-12} \exp(-1070/T)$ cm^3 $molecules^{-1}$ s^{-1} (scaled by 0.75 from *Sander et al.*, 2006). The OH loss of acetylene is calculated by: $k_o(T) = 4.125 \times 10^{-30}$ cm^3 $molecules^{-1}$ s^{-1} and $k_\infty(T) = 6.225 \times 10^{-13} (T/300)^2$ cm^3 $molecules^{-1}$ s^{-1}, where k_o is the low-pressure limit and k_∞ is the high-pressure limit (scaled by 0.75 from *Burkholder et al.*, 2015). For the CTM simulations, all results were obtained from the final year (2007) of three-year simulations (years 2005-2007).

Table 3.4: Emission factors used in the UCI-CTM simulations to calculate emissions of ethane and acetylene from dry matter emissions. Based on the GFED 3.1 database (*van der Werf et al.*, 2010; *Akagi et al.*, 2011).

Biome	Ethane EF (g kg^{-1})	Acetylene EF (g kg^{-1})
Agriculture	1.24	0.27
Deforestation	0.88	0.44
Forest	0.67	0.27
Peat	0.88	0.06
Savanna	0.39	0.24
Woodland	0.64	0.26

3.4.1 CTM perturbations and sensitivity calculations

Tracer experiments were designed to estimate the response (sensitivity) of ethane and acetylene levels over Greenland and Antarctica to small changes in emissions from various spatial/temporal geographic patterns of major ethane and acetylene sources. This approach is slightly different from the "perturbation" approach used in *Nicewonger et al*. (2018) to calculate

sensitivities. Details on this approach can be found in *Nicewonger et al*. (2018) and in Appendix D. To calculate the sensitivity factors, ethane-like and acetylene-like tracer species are emitted at known emissions (Tg y^{-1}) from each of our specific source regions (there are no background emissions from other sources). The tracer species reacts in the model with the same OH kinetics and stratospheric loss as either ethane or acetylene, but it does not alter the background chemistry and OH levels. Simulations were carried out in which emissions of ethane and acetylene tracer were added to various geographical regions and the resulting mixing ratios over Greenland and Antarctica were calculated. The sensitivities for Greenland and Antarctic abundance levels versus regional emission levels is calculated as:

$$\text{Sensitivity} = \frac{\text{ppt}}{\text{Tg y}^{-1}} \tag{3.4}$$

Ethane and acetylene abundance levels (in ppt) were calculated by integrating the column average of the compound up to model layer 19 (roughly 500 hPa) and by integrating the area-weighted average of air to the same model layer over the horizontal polar regions (60-90°N for Greenland and 60-90°S for Antarctica).

Sensitivities were computed for ethane and acetylene levels over Greenland and Antarctica for global emissions from biomass burning, biofuels, fossil fuels and geologic emissions. Sensitivities were also calculated for biomass burning from different geographic emissions. An example of the geographic distribution of ethane emissions from biomass burning used in the CTM and the resulting annual mean surface ethane mixing ratios (integrated to 500 mb) are shown in Figure 3.3. Table 3.5 shows the resulting model sensitivities for ethane and acetylene for various source/geographic regions. Table 3.6 describes each tracer simulation.

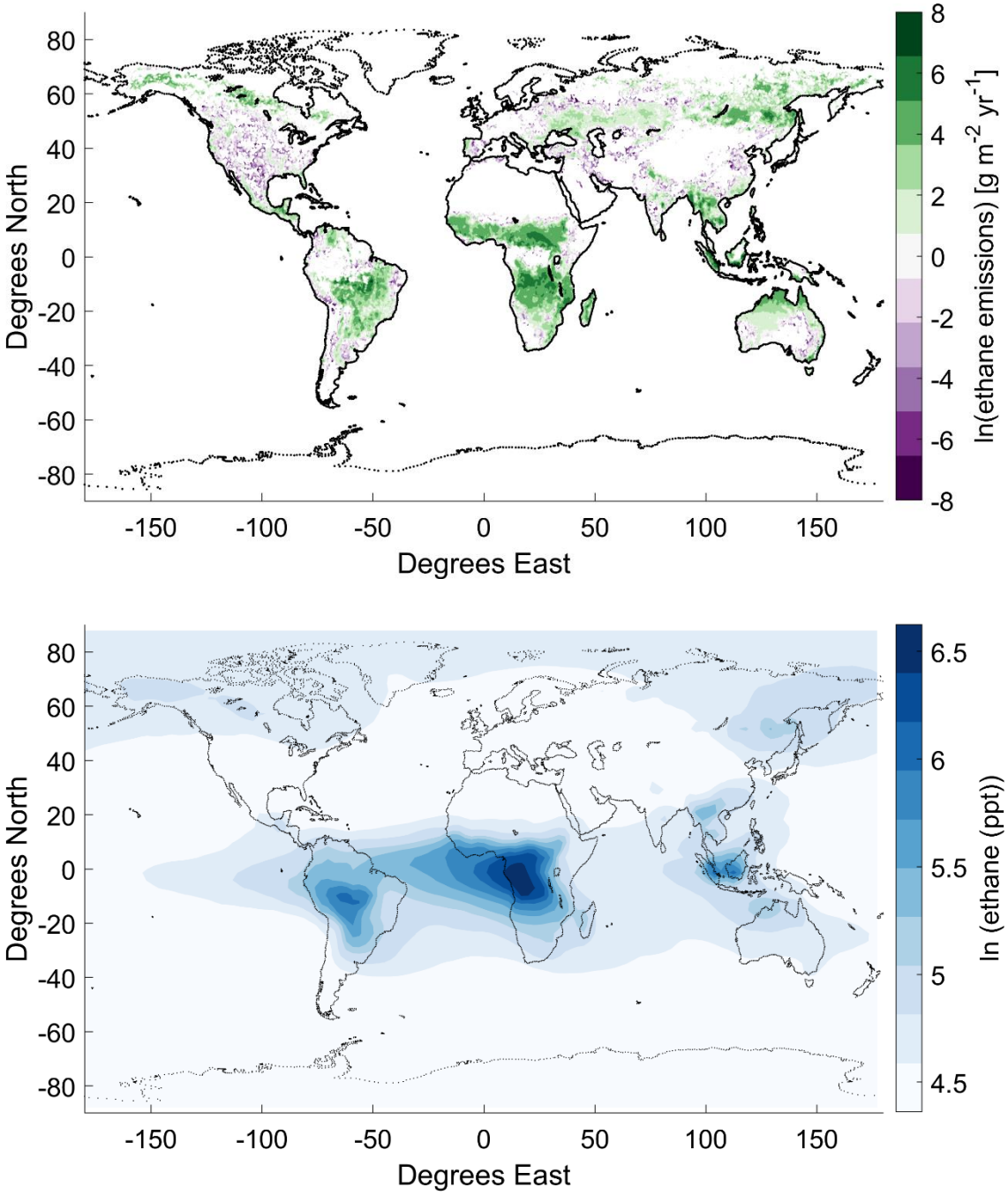

Figure 3.3: UCI-CTM global biomass burning emissions and resulting annual mean ethane mixing ratios in the tracer simulation. **Top**: Biomass burning emissions of ethane in the CTM (GFED3.1, *van der Werf et al*., 2010). Note the scale is in natural log (emissions) to show the range in emission magnitude. **Bottom**: Resulting mixing ratio of ethane across the globe from the global biomass burning tracer simulation. Note the scale is in natural log (ethane) to show the range in global ethane mixing ratios from this tracer simulation.

Table 3.5: UCI-CTM sensitivities for ethane and acetylene for Greenland (GRN) and Antarctica (ANT) from different tracer simulations.

		Fraction of total emissions (%)		Modeled sensitivities (ppt/Tg y^{-1}) *Ethane*		*Acetylene*	
Source	**Geographic region**	**Ethane**	**Acetylene**	**GRN**	**ANT**	**GRN**	**ANT**
Fossil fuel	Globe	100	100	73.9	14.2	35.3	2.8
Biofuel	Globe	100	100	79.1	16.7	37.7	3.1
Geologic	Globe	100	--	88.0	20.3	--	--
Biomass burning							
	Non-boreal	89.7	91.0	21.5	31.8	3.8	6.8
	Boreal	10.3	9.0	214.3	4.4	106.8	0.0
	Southern Hemisphere Africa	24.1	25.9	12.8	33.1	0.5	6.7
	Southern Hemisphere America	15.8	16.9	10.1	60.7	0.5	18.9
	Australia	4.9	6.1	11.5	50.0	0.6	12.1
	Tropics	86.1	88.1	18.5	31.7	2.6	6.4
	Globe	100	100	41.4	29.0	13.1	6.2

Table 3.6: Different emission sesntivity calculations with the of UCI-CTM.

Perturbation	Description
Fossil fuel	Fossil fuel emissions from the RCP 60-year 2000 inventory (*Lamarque et al*., 2000)
Biofuel	Biofuel source of ethane and acetylene with a geographic distribution based on *Yevich and Logan* (2003).
Geologic	Geologic source of ethane with a geographic distribution based on *Etiope and Ciccioli* (2009).
Biomass burning: non-boreal	Biomass burning emissions from 50°N to 90°S (all longitudes)
Biomass burning: boreal – all	Biomass burning emissions from 50°N to 90°N (all longitudes)
Biomass burning: Southern Hemisphere Africa	Biomass burning emissions in the southern hemisphere portion of Africa bound by 0-35°S and 13-60°E (includes Madagascar and small islands)
Biomass burning: Southern Hemisphere America	Biomass burning emissions in southern hemisphere America bound by 0-60°S and 35-81°W
Biomass burning: Australia	Biomass burning emissions in Australia bound by 9-55°S and 111-168°E
Biomass burning: Tropics	Biomass burning emissions from 30°N to 30°S (all longitudes)
Biomass burning: Globe	Global biomass burning emissions using GFED3 climatology from 1997-2009 (*van der Werf et al.*, 2010) (all latitudes and longitudes)

3.4.2 Simulating atmospheric levels with CTM sensitivities

The CTM sensitivities calculated from the 10 emission patterns (Table 3.6) were used to simulate atmospheric ethane and acetylene levels over a range of biomass burning and geologic (ethane only) emission scenenarios over the 1000 to 2000 CE period. The sources could vary over a set range resulting in multiple emission scenarios. Atmospheric levels of ethane and acetylene were calculated for each scenario summing over the various types of emissions multiplied by the sensitivity of that emission type.

The modeled Greenland and Antarctica ethane and acetylene levels were compared to the ice core observations. Emission scenarios were evaluated for defined time periods by using the following functions, with ethane as an example:

$$\Delta_{ethane,grn} = \frac{|m_{grn} - \bar{o}_{grn}|}{\bar{o}_{grn}} \quad (3.5)$$

$$\Delta_{ethane,ant} = \frac{|m_{ant} - \bar{o}_{ant}|}{\bar{o}_{ant}} \quad (3.6)$$

where m stands for the modeled ethane level and o for the observed mean level of ethane from the ice core record from Greenland (grn) and Antarctica (ant). A modeled emission scenario was considered viable if $\Delta_{ethane,grn}$ and $\Delta_{ethane,ant}$ were both <0.1. A modeled emission scenario was rejected if either $\Delta_{ethane,grn}$ or $\Delta_{ethane,ant}$, were >0.1. Details of the application of the CTM sensitives and interpretation of the ethane and acetylene ice core records are found in subsequent chapters.

3.5 One-box steady-state methane model

The atmospheric lifetime of methane is long relative to the time scale for tropospheric transport, and north-south gradients are small relative to the change in abundance since the preindustrial. Thus, a one box, steady-state atmospheric box model was used to infer methane emissions during the preindustrial era. The methane box model includes sources of methane from biogenic (wetlands, agriculture), biomass and biofuel burning, and geologic outgassing. Two versions of the model were used.

Version 1 used in *Nicewonger et al*. (2018) assigns the $^{13}C/^{12}C$ ratios for each methane source after *Schwietzke et al*. (2016) (Table 3.7). The rate constants for each methane loss pathway (OH, soil, stratosphere) were based on previous estimates and isotope fractionation

factors (*Mischler et al.*, 2009, Table 3.8). The atmospheric lifetime of methane to OH in the model is set to 9.5 years based on the three-dimensional global OH and temperature distributions from *Spivakovksy et al.* (2000). The model solves the mass balance equations for CH_4, $^{12}CH_4$ and $^{13}CH_4$ as follows:

$$CH_4 = \frac{\sum sources}{k_{total}} = \frac{geologic + microbial + biomass + biofuel}{(k_{OH} + k_{soil} + k_{strat})} \tag{3.7}$$

$$^{12}CH_4 = \frac{\sum {}^{12}CH_4 \text{ sources}}{(k_{OH} + k_{soil} + k_{strat})} \tag{3.8}$$

$$^{13}CH_4 = \frac{\sum {}^{13}CH_4 \; sources}{(\alpha_{OH} * k_{OH} + \alpha_{soil} * k_{OH} + \alpha_{strat} * k_{strat})} \tag{3.9}$$

$$\delta^{13}\mathrm{CH_4} = \left(\left(\frac{(^{13}\mathrm{CH_4}/^{12}\mathrm{CH_4})_{\mathrm{sample}}}{(^{13}\mathrm{CH_4}/^{12}\mathrm{CH_4})_{\mathrm{std}}} \right) - 1 \right) * 1000 \tag{3.10}$$

where sources are in Tg $y^{-1.}$ The loss constants (k) are calculated by multiplying by their respective relative contributions to the total loss term ($1/k_{total}$) as follows:

$$k_{total} = \frac{\frac{1}{9.5 \; years}}{0.88} \tag{3.11}$$

where 9.5 years is the assigned methane lifetime due to OH oxidation and 0.88 is the relative contribution of the OH oxidation to the total methane sink (*Mischler et al*., 2009). The stratospheric and soil sink relative contribution are 7% and 5%, respectively (*Mischler et al*., 2009). Isotope fractionation factors were assigned to each sink based on *Mischler et al.* (2009)

(Table 3.8). The $^{13}C/^{12}C$ standard used is 0.0112372 (*Craig*, 1957). MATLAB script for Version 1 of the one-box methane model is found in Appendix A.

In version 2 of the model, the end-member $^{13}C/^{12}C$ for biomass burning, biofuel burning and biogenics were adjusted by 1.8‰ to account for the depletion in the source material $\delta^{13}CO_2$ which has occurred since industrialization (*Rubino et al.*, 2013, Table 3.7). This correction provides a better estimate of the $^{13}C/^{12}C$ of methane sources during the preindustrial period. Version 2 includes an additional methane loss to Cl. The Cl sink is estimated at 5% of the total methane loss (*Allan et al*., 2007; *Prather et al.*, 2012). The lifetime of methane with respect to OH, soil, stratosphere and Cl is 11.2 y, 200 y, 120 y, and 200 y, respectively (*Curry*, 2007; *Prather et al*., 2012). The isotope fractionation factors for each sink were assigned from *Lassey et al.* (2007). The OH, soil, stratosphere, and Cl fractionation factors are 0.995, 0.980, 0.970, and 0.940, respectively (Table 3.8). The model solves the mass balances equations for CH_4, $^{12}CH_4$ and $^{13}CH_4$ as in Version 1. MATLAB script for Version 2 of the one-box methane model is found in Appendix A.

3.5.1 Simulating atmospheric methane levels

The one-box model was used to calculate the atmospheric methane mixing ratio and $\delta^{13}CH_4$ for various emission scenarios. Emissions of methane from biomass burning, microbial, and geologic sources were varied over a set range. The resulting methane mixing ratio and $\delta^{13}CH_4$ from each emission scenario were compared to ice core records of $^{12}CH_4$ and $\delta^{13}CH_4$ (Table 3.9).

Emission scenarios were evaluated for defined time periods by using the following functions:

$$\Delta_{CH_4} = \frac{\left|m_{[CH_4]} - \bar{o}_{[CH_4]}\right|}{\bar{o}_{[CH_4]}} \tag{3.12}$$

$$\Delta_{\delta 13 CH_4} = \frac{\left|m_{\delta^{13}CH_4} - \bar{o}_{\delta^{13}CH_4}\right|}{\left|\delta^{13}CH_{4_{max}} - \delta^{13}CH_{4_{min}}\right|} \tag{3.13}$$

where m stands for the modeled methane value and o for the observed mean methane value from the ice core record. A modeled emission scenario was considered viable if Δ_{CH4} and $\Delta_{\delta 13CH4}$ were both <0.1. A modeled emission scenario was rejected if either Δ_{CH4} or $\Delta_{\delta 13CH4}$ were >0.1. The denominator in the second part of the calculation is the absolute value of the observed range in the $\delta^{13}CH_4$ ice core record over the 2,000-year period of interest in this study, roughly 3‰. Details of the application of this model are discussed in Chapter 6.

Table 3.7: Methane isotopic source end-member signatures used in the two versions of the box model.

Source	**$\delta^{13}C$ (‰)**	
	Version 1	**Version 2**
Microbial (wetlands, agriculture)	-62.3	-60.5
Geologic/Fossil	-43.0	-43.0
Biomass burning	-22.3	-20.5
Biofuel burning	-22.3	-20.5

Table 3.8: Kinetic isotope effect (α) for the methane losses used in the one-box model. Version 1 data is from *Mischler et al.* (2009) and version 2 data is from *Lassey et al*. (2007).

Loss	**$\alpha = k(^{13}CH_4)/_k(^{12}CH_4)$**	
	Version 1	**Version 2**
Troposphere (OH)	0.9961	0.9950
Stratosphere	0.9847	0.9800
Soils	0.9824	0.9700
Chlorine (Cl)	--	0.9400

Table 3.9: Ice core methane mixing ratios and $\delta^{13}CH_4$ used in the box model. Methane mixing ratios are from *MacFaurling Muere et al.* (2006), *Mitchell et al.* (2011), and *Sowers* (2010). Ice core $\delta^{13}CH_4$ measurements are from *Ferretti et al.* (2005), *Mischler et al.* (2009), and *Bock et al.* (2017).

	Mean $[CH_4]$ (ppb)	Mean $\delta^{13}CH_4$ (‰)
Medieval Period (MP)	682.5	-47.49
Little Ice Age (LIA)	700.6	-48.91

CHAPTER 4

Polar ice core records of ethane

Includes excerpts from:

M. R. Nicewonger, K. R. Verhulst, M. Aydin, E. S. Saltzman, "Preindustrial atmospheric ethane levels inferred from polar ice cores: A constraint on the geologic sources of atmospheric ethane and methane," *Geophysical Research Letters*, (2016)

M. R. Nicewonger, M. Aydin, M. J. Prather, E. S. Saltzman, "Large changes in biomass burning over the last millennium inferred from paleoatmospheric ethane in polar ice cores," *Proceedings of the National Academy of Sciences*, (2018).

4.1 Overview

In this chapter, ethane measurements in air extracted from ice cores from Greenland and Antarctica are presented. The ice core samples analyzed span the last ~3,000 years. This is the first millennial-scale record of ethane in ice cores and the first attempt to use ice core ethane to constrain preindustrial biomass burning emissions. The chapter is organized by first describing the ethane results from two different analytical methods (as described in Chapter 2) and comparing the similarities and differences between the two ethane datasets. Then, preindustrial budgets for ethane are inferred using atmospheric models (Chapter 3) with the ice core ethane records collected using the improved analytical procedure (procedure 4).

4.2 Results and discussion

4.2.1 Procedure 1 results

Ethane results from WAIS-Divide (WDC05A) and Summit (GISP2B) using wet-extraction procedure 1 (see Chapter 2 for description) are shown in Figure 4.1. The WDC05A measurements were conducted as three separate sets with 11 samples measured in 2011, 7

samples measured in 2012, and 15 samples measured in 2014 (*Nicewonger et al.*, 2016; *Verhulst*, 2014). The measurements were blank corrected using the average of all applicable post-melt N_2 blanks from the measurement year, excluding 2σ outliers (Table 4.1). For the WDC05A samples analyzed in 2014, the blanks were roughly 50% of ethane measured in an average WDC05A sample. Blanks for GISP2B samples were similar and comprise roughly 20% of the ethane in an average GISP2B sample. The blank variability is the largest source of measurement uncertainty. The overall uncertainty for an individual ice core measurement is calculated by propagating the variance in the calibrations and blanks and average ±7% and ±17% (1σ) for GISP2B and WDC05A samples analyzed using procedure 1, respectively.

Table 4.1. Ethane levels in the post melt N_2 blanks from procedure 1 (mean + 2σ).

Year	Core	1st N_2 blank pmol C_2H_6	2nd N_2 blank pmol C_2H_6	3rd N_2 blank pmol C_2H_6
2011	WDC05A	0.16 ± 0.05	0.16 ± 0.05	0.13 ± 0.07
2012	WDC05A	0.12 ± 0.07		
2014	WDC05A	0.09 ± 0.03	0.10 ± 0.14	
2014	GISP2B	0.09 ± 0.05	0.11 ± 0.07	

The Greenland GISP2B samples cover the period from 1456-1862 CE at a resolution of 20–30 years (Figure 4.1). Ethane levels from 1450-1750 CE range from 356-520 ppt with a mean of 409 ± 49 ppt (±1σ, n=17). There are slightly higher ethane levels in younger samples, with the measurements from 1750-1862 CE averaging 528 ± 37 ppt (n=8). The increase in ethane levels in the GISP2B samples after 1750 CE may be the beginning of the increasing ethane trend in the northern hemisphere. Many of the shallow GISP2B samples have low but measurable levels of CFC-12 (1 ppt ≤ CFC-12 ≤ 10 ppt, Figure 4.1) which makes it challenging to determine if the rise in the Greenland ethane level after 1750 CE is an atmospheric signal or an artifact caused by

modern air contamination. The ethane rise in the northern hemisphere during the 1700's has since been verified with measurements in CFC-free ice core air (see section 4.2.2).

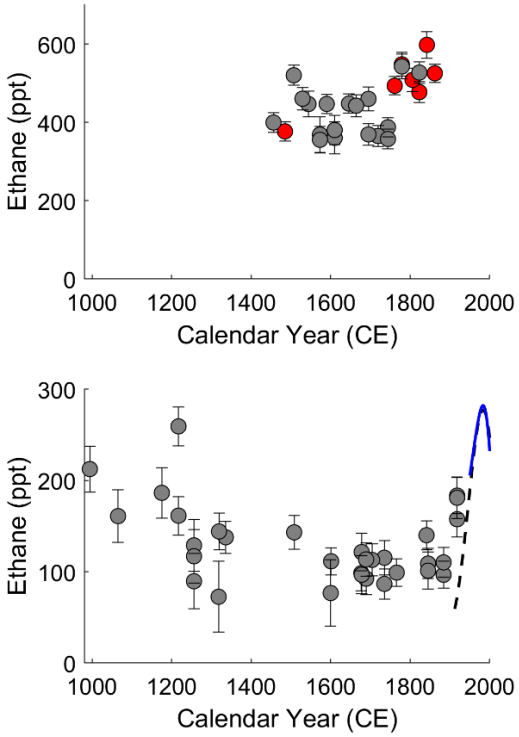

Figure 4.1: Atmospheric ethane from (top) Summit, Greenland (GISP2B) and (bottom) WAIS Divide, Antarctica (WDC05A) ice core samples using wet-extraction procedure 1. Reconstructions of atmospheric ethane levels over Antarctica from firn air measurements from WAIS Divide (blue line) and South Pole (black dashed line) are also shown (*Aydin et al*., 2011). Samples with CFC-12 levels > 1ppt are shown by the red circles. Ethane errors presented as 1σ.

The WDC05A samples from Antarctica cover the time period from 994-1918 CE at an average resolution of 30 years (Figure 4.1). The ethane measurements from 1450-1750 CE range from 77-143 ppt with a mean of 106 ± 19 ppt (n=11). Over the 900-year measurement period, ethane is highest around 1000 CE at nearly 200 ppt and steadily declines over the next few hundred years. The WDC05A measurements after 1750 CE are slightly higher at 131 ± 35 ppt (n = 9) because of three elevated replicates from 1918 CE (>150 ppt). The mean of the two sets of replicates from 1845 C.E. and 1884 CE is 112 ppt (n=5) and is not significantly different from

the 1450–1750 CE mean. Overall, eight out of ten replicate measurements from WDC05A agree within analytical uncertainties. The two exceptions are samples older than 1400 CE that were analyzed in 2011 and 2012 when the blank uncertainties were larger (Table 4.1).

4.2.2 Procedure 4 results

Ethane measurements in the GISP2D, GISP2B, WDC05A, WDC06A and SPC14 cores conducted using the improved wet-extraction procedure (procedure 4) are shown in Figure 4.2 and Figure 4.3. The Greenland ethane measurements are from the fluid-drilled GISP2D core and the shallow, dry-drilled GISP2B core. The GISP2D samples range from 95.6 m to 730.4 m depth, corresponding to gas ages of 1892 CE and 1206 BCE, respectively. The GISP2B samples range from 87.6 m to 194.1 m depth, corresponding to gas ages of 1918 CE and 1477 CE, respectively. There is good agreement between ethane levels in samples of contemporaneous age from the GISP2B and GISP2D ice cores, indicating ethane can be successfully measured in ice cores without interference and contamination from hydrocarbon-based drill fluids.

The Antarctic ethane measurements are from the shallow, dry-drilled WDC05A core and the deep, fluid-drilled WDC06A and SPC14 cores. The WDC05A samples ranged from 83.2 m to 298 m depth, corresponding to gas ages of 1926 CE and 994 CE, respectively. The WDC06A samples ranged from 116.9 m to 603.7 m depth, corresponding to gas ages of 1781 CE and 303 BCE, respectively. The SPC14 samples ranged from 130.7 m to 294.4 m depth, corresponding to gas ages of 1817 CE and 387 BCE, respectively. There is good agreement between ethane levels from the three Antarctic ice cores in samples from contemporaneous age during the 1000-1900 CE period. Prior to 1000 CE, samples of concurrent age from different sites have higher scatter which may be due to experimental issues. For example, around 1000 CE, ethane levels range

from 80 to 147 ppt (WDC06A [gas age 1007 CE] = 93 ppt, WDC05A [gas age 994 CE] = 80 ppt, and SPC14 [gas age 988 CE] = 147 ppt).

Procedure 4 samples with elevated levels of CFC-12 (>1 ppt), known experimental issues, or exceptionally high ethane levels were excluded from analysis and interpretation. Twenty-four samples from the GISP2D core, 10 samples from the WDC05A core, 3 samples from the SPC14 core, and 2 samples from the WDC06A core were excluded. These data are shown in Figure 4.2 and are listed in Appendix B.

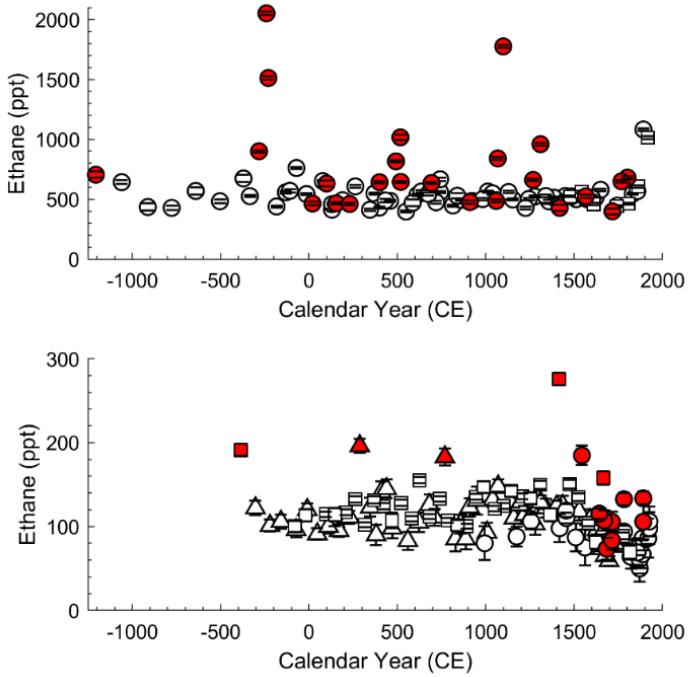

Figure 4.2: Ethane ice core data from procedure 4 excluded from analysis and interpretation (red). Data is found in Appendix B. Top: Greenland ethane from GISP2B (squares) and GISP2D (circles). Bottom: Antarctic ethane from WDC05A (circles), WDC06A (triangles), and SPC14 (squares).

The Greenland ethane record exhibits some variability over the roughly 3,000-year period (Figure 4.3). The average ethane level over Greenland for the whole record is 520 ± 70 ppt (excluding the shallowest samples with gas ages of 1892 and 1918 CE). The Greenland record

exhibits more scatter prior to 1000 CE with ethane levels ranging from 398 to 761 ppt. The mean ethane level (523 ± 86 ppt) prior to 1000 CE is not significantly different from the mean ethane level of the whole record. There is good consistency with the ethane measurements after 1000 CE. The mean Greenland ethane level during 983-1512 CE is 515 ± 34 ppt. The Greenland ethane level declines slightly after 1500 CE. Greenland ethane levels are 489 ± 49 ppt from 1600-1807 CE. After roughly 1807 CE, ethane levels begin to quickly rise, likely due to anthropogenic ethane emissions.

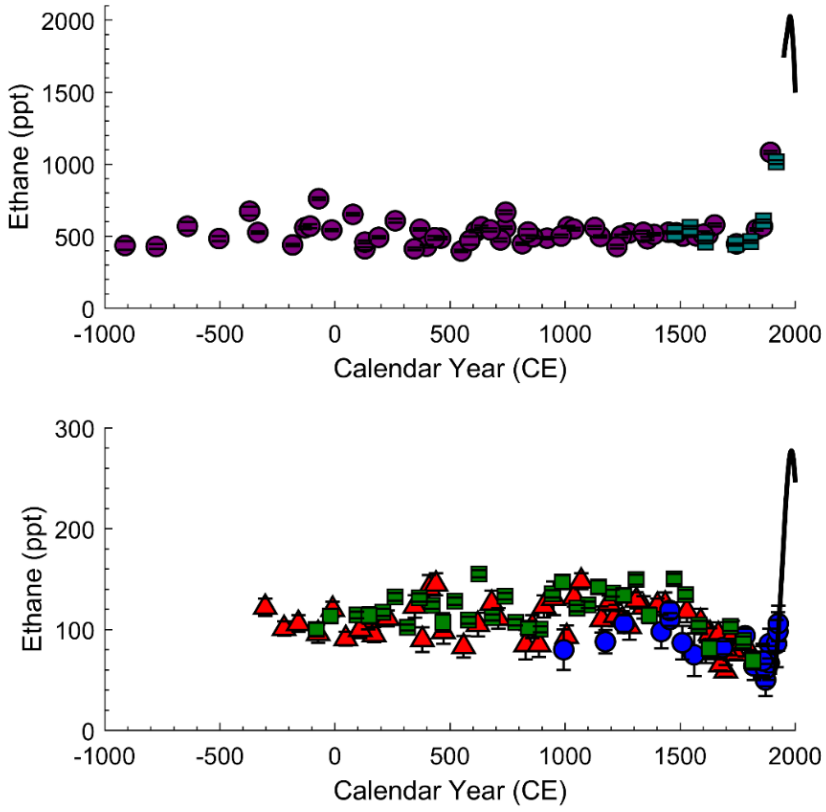

Figure 4.3: Atmospheric ethane from Greenland (top) and Antarctica (bottom) ice cores using wet-extraction procedure 4. Measurements from Greenland are from the GISP2D (purple circles) and GISP2B (teal squares) ice cores. Measurements from Antarctica are from the WDC05A (blue circles), WDC06A (red triangles) and SPC14 (green squares) ice cores. Atmospheric ethane levels over Summit, Greenland and South Pole, Antarctica reconstructed from firn air measurements (black lines) are also shown (*Aydin et al*., 2011). Ethane errors presented as 1σ.

The Antarctic record displays significant variability over the 2,300-year time period (Figure 4.3). The mean ethane level for the whole record is 106 ± 23 ppt, which is roughly 50% of the mean annual ethane level observed over Antarctica today (~210 ppt). Ethane levels are relatively high from 303 BCE-1474 CE with a mean level of 116 ± 18 ppt. After 1500 CE, ethane levels in all three cores drop by about 30% reaching a minimum from 1611-1887 CE of 79 ± 14 ppt. After the late-1800s, ethane levels over Antarctica begin to slowly rise, which likely indicates the early onset of anthropogenic ethane emissions to Antarctica. The late 19th century rise in ethane levels over Antarctica is delayed by several decades from what is observed over Greenland.

4.2.3 Comparison of procedure 1 and 4 ethane results

The ethane results from using analytical procedure 1 (section 4.2.1) and procedure 4 (section 4.2.2) are shown together in Figure 4.4. Overall, Greenland ethane levels from procedure 1 are generally lower than those from procedure 4, although there are time periods where contemporaneous samples agree well, such as after 1850 CE. From 1400-1750 CE, the mean ethane level from procedure 1 and procedure 4 are statistically different ($p = 4.4x10^{-6}$). Nearly all procedure 1 Antarctic ethane data are higher than that from procedure 4. From 980-1920 CE, the mean Antarctic ethane level from procedure 1 and procedure 4 are statistically different ($p = 6.2x10^{-5}$).

Although the two datasets collected with different procedures are statistically different, the trends observed in both the Greenland and Antarctic data are similar (Figure 4.5 and Figure 4.6). Both datasets indicate ethane levels over Greenland were declining from 1400-1750 CE, but the decline in procedure 1 ethane levels is not statistically significant (slope = -0.16 ± 0.19 [±1 SE] with an r^2 <0.01). When the post-1750 CE data is included, both datasets show increasing

Greenland ethane levels into the modern era with slopes of 0.31 ± 0.11 and 0.39 ± 0.23 for procedure 1 and procedure 4, respectively. The positive trend is driven by the increasing ethane levels after 1750 CE, which is likely caused by early anthropogenic ethane emissions in the northern hemisphere. Although the mean ethane levels between the two datasets are not statistically similar, the overall increasing trend observed over Greenland from 1400-1900 CE is the same between the two procedures.

The Antarctic datasets both show statistically significant declines in ethane levels from 1000 to late-1800 CE with slopes of -0.09 ± 0.02 and -0.07 ± 0.01 for procedure 1 and procedure 4, respectively (Figure 4.6). Interestingly, although the mean ethane levels are statistically different between the two data sets, the overall decreasing trend is similar. This indicates that although procedure 1 ethane data was elevated, likely due to high analytical blanks, the analysis

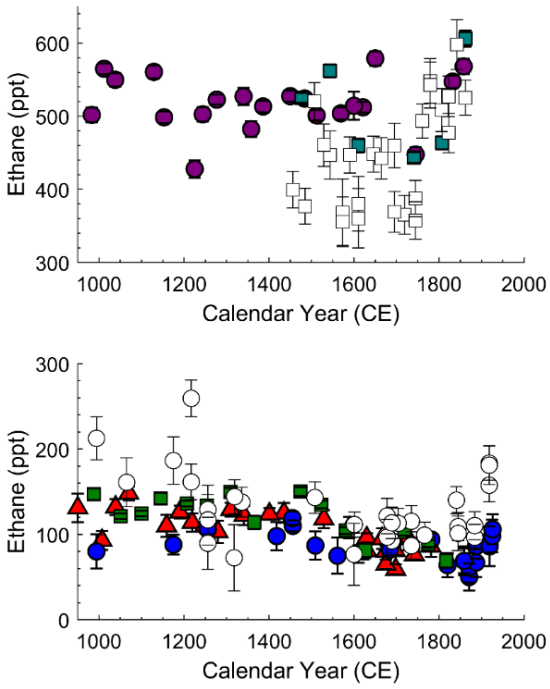

Figure 4.4: Ethane measured in Greenland (top) and Antarctic (bottom) samples using analytical procedure 1 (white markers) and procedure 4 (colored markers).

technique was still capturing an atmospheric signal. Both datasets also suggest increasing Antarctic ethane levels at the turn of the 20th century (white circles in Fig. 4.6), which likely marks the timing of anthropogenic ethane emissions impacting Antarctic ethane levels.

Analysis and interpretation of the ice core ethane records is completed only on the procedure 4 data set because of 1) increased analytical blanks in procedure 1 vs. procedure 4 (Chapter 2) and 2) the statistical evidence which shows the two datasets are different.

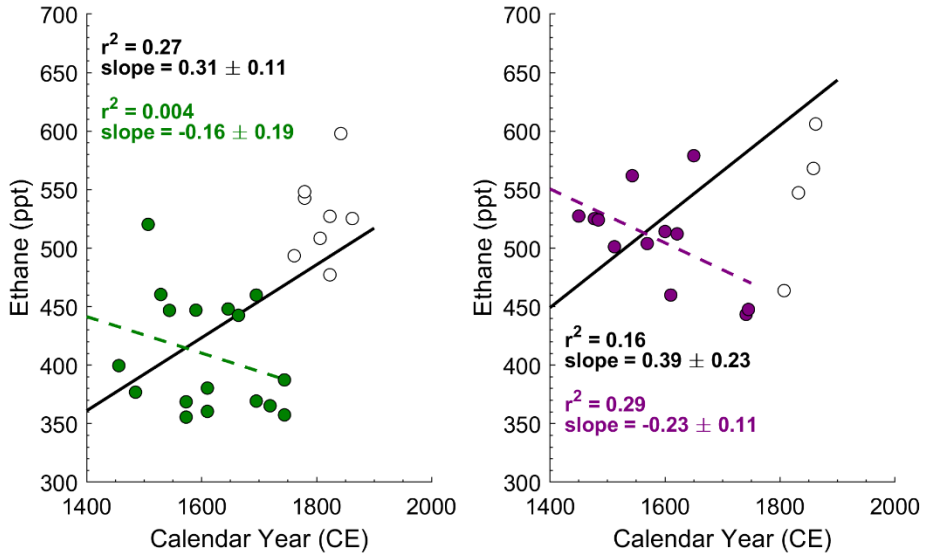

Figure 4.5: Trends in the Greenland ethane data. Greenland ethane levels (in ppt) from procedure 1 (left) and procedure 4 (right). For procedure 1, the green data points indicate the data that was used for the linear regression from 1400-1750 CE. The resulting regression line (dashed line), slope, and r^2 are also shown in green. The black line indicates the linear regression performed on the entire data set from 1400-1900 CE. For procedure 4, the purple data points indicate the data that was used for the linear regression from 1400-1750 CE. The resulting regression line (dashed line), slope, and r^2 are shown in purple. The black line indicates the linear regression performed on the whole data set from 1400-1900 CE. The uncertainty on the slopes is 1 SE.

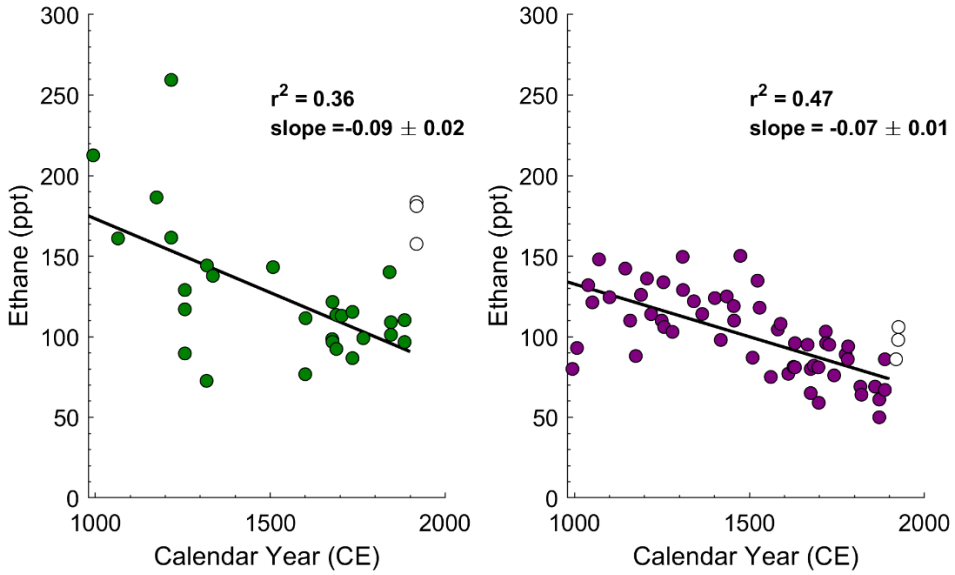

Figure 4.6: Trends in the Antarctic ethane data. Antarctic ethane levels from procedure 1 (left) and procedure 4 (right). The linear regression is performed on the filled data points. The uncertainty on the slope is 1 SE.

4.3 Implications for the preindustrial ethane budget

Large changes are observed in the ice core ethane levels, particularly over Antarctica during the last 1,000 years. Using the UCI-CTM sensitivities (Table 3.5) for biomass burning, biofuel burning, and geologic ethane sources, various emission scenarios can be explored that reconstruct the ice core ethane data. The ice core data were divided into two time periods: 1) the Medieval Period (MP) from 1000-1500 CE and 2) the Little Ice Age (LIA) from 1600-1800 CE. A grid-search method was used to explore a range of emissions scenarios and identify those compatible with the ice core results. In all scenarios, biofuel emissions of ethane were fixed at 0.5 Tg y^{-1} based on *van Aardenne et al.* (2000). Mixing ratios were calculated by summing the sources of each gas multiplied by their respective sensitivities. Viable emission scenarios were determined using equations 3.5 and 3.6 as described in Chapter 3.

4.3.1 Ethane budget with no Cl sink

For the first set of emission scenarios, it was assumed that there was no Cl sink in the ethane budget and the only sink of ethane was due to OH oxidation. Scenarios of global biomass burning (GFED3.1) and geologic emissions that could reproduce the Greenland and Antarctica ice core ethane levels during the two time periods were explored. In this 2-D approach, there are no emissions scenarios which can reproduce the ice core data during both the MP and LIA. This suggests that biomass burning emissions during the last 1,000 years did not change in sync globally, but rather varied independently in different geographic regions.

To allow for more freedom, we explored emissions scenarios that permitted the non-boreal biomass burning emissions (50°N to 90°S) and boreal biomass burning emissions (>50°N) to vary independently through time. The non-boreal region accounts for roughly 80% of ethane biomass burning emissions, with most of these emissions occurring in the tropical zone (30°N-30°S). This approach is suitable because the Greenland and Antarctic ethane levels have different sensitivities to biomass burning emissions in the two regions. For example, the Greenland ethane sensitivity to boreal fire emissions 214 ppt/Tg y^{-1} while the Antarctic ethane sensitivity to boreal fire emissions is roughly 4 ppt/Tg y^{-1}. Boreal, non-boreal, and geologic ethane emissions could vary from 0 to 3 Tg y^{-1}, 0 to 5 Tg y^{-1}, and 0 to 7 Tg y^{-1}, respectively. The valid emission scenarios for the MP and LIA are shown in Figure 4.7 in contours of goodness of fit. The goodness of fit is calculated as:

$$Goodness\ of\ fit_{ethane} = \sqrt{\left(\frac{|m_{grn} - o_{grn}|}{o_{grn}}\right)^2 + \left(\frac{|m_{ant} - o_{ant}|}{o_{ant}}\right)^2} \quad (4.2)$$

where m stands for the modeled value and o for the observed mean value from the ice core records. The goodness of fit was calculated for the MP and LIA separately. The goodness of fit ranges from 0 to 0.14, with 0 corresponding to a perfect fit to the mean of the ice core records.

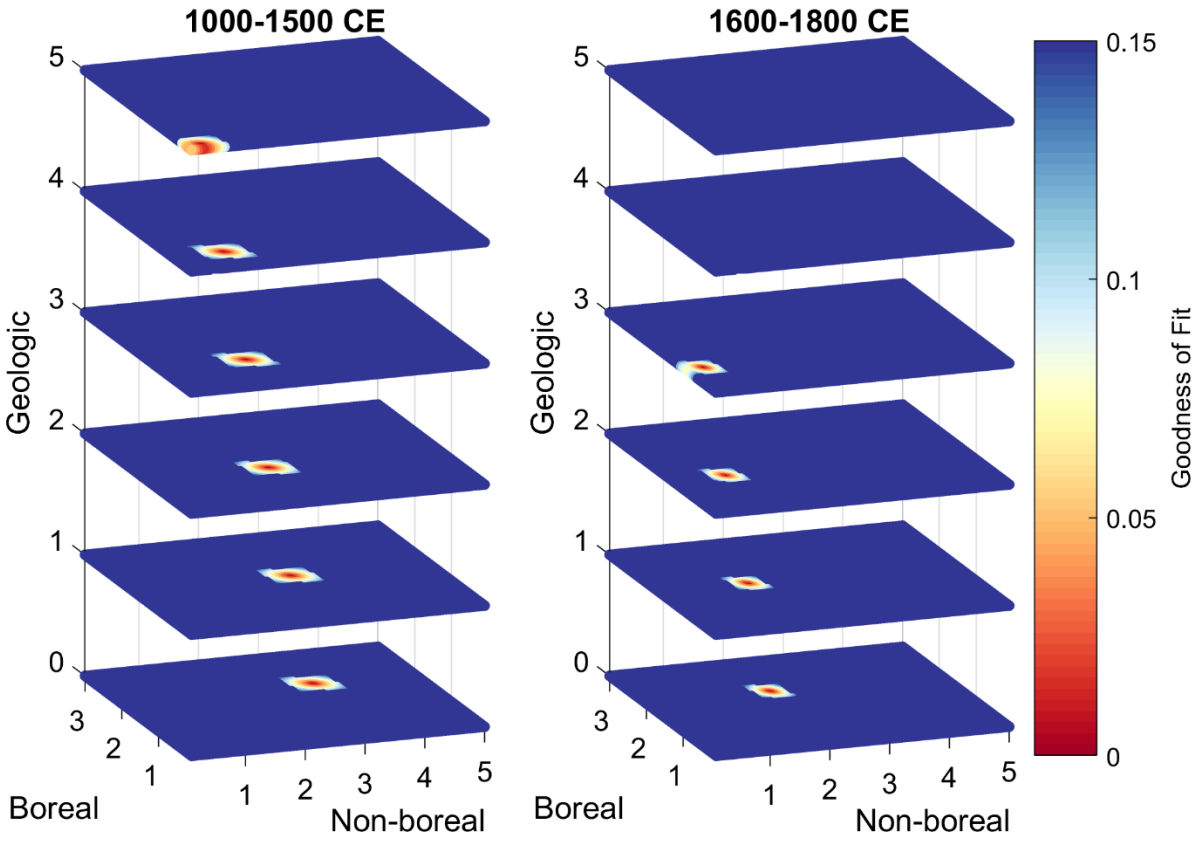

Figure 4.7: Modeled ethane boreal and non-boreal biomass burning and geologic emission scenarios for the Medieval Period (1000-1500 CE, left) and Little Ice Age (1600-1800 CE, right). Contours are of goodness of fit with a value of 0 corresponding to a perfect fit to the mean of the ice core records. Emissions are in Tg ethane y^{-1}.

There are valid emission scenarios during the MP of non-boreal and boreal biomass burning ranging over the 0-5 Tg y^{-1} geologic range. However, during the LIA, valid emission scenarios are not obtained for geologic emissions greater than 3 Tg y^{-1}. The magnitude of geologic hydrocarbon emissions is heavily debated (*Etiope and Ciccioli,* 2009*; Petrenko et al.*, 2017). Estimates of geologic ethane emissions in the contemporary atmosphere range from 2-4

Tg y^{-1} (*Etiope and Ciccioli*, 2009). *Petrenko et al*. (2017) used ice core $\Delta^{14}C$ measurements of methane in ice cores to estimate the radiocarbon depleted source of methane (i.e. fossil or geologic source) in the preindustrial atmosphere and found that this component is small and closer to zero than the contemporary estimates. From this analysis, and more recent analysis of ice cores covering the last few hundred-year time period (*M. Dyonisius., personal communication*), the geologic hydrocarbon source of methane, and ultimately ethane, has been quantified at minimal values (near zero). For the purpose of interpreting the ice core ethane records, we assume geologic ethane emissions are low, but constant through time and range from 0 to 2 Tg y^{-1}.

For geologic ethane emissions of 0 Tg y^{-1}, boreal and non-boreal ethane emissions during the MP of 3.2 ± 0.2 Tg y^{-1} and 1.9 ± 0.1 Tg y^{-1}, respectively, are required to reconstruct the ice core levels during that time (Figure 4.8). The MP total burning ethane budget is 5.1 ± 0.2 Tg y^{-1} which is a nearly a factor of 1.5 greater than modern ethane biomass burning emissions estimate from the Global Fire Emissions Database 4 (GFED4.1) inventory (3.4 Tg y^{-1}; *van der Werf et al.*, 2017; globalfiredata.org). During the LIA, non-boreal ethane emissions decline to 2.1 ± 0.2 Tg y^{-1}, while boreal emissions stay nearly constant at 1.9 ± 0.1 Tg y^{-1} (Figure 4.8 and Table 4.3). The LIA total burning ethane budget is 3.9 ± 0.2 Tg y^{-1}. The ice core data indicates that with zero geologic emissions, biomass burning emissions are required to decline by 23% with most of the decline occurring in the non-boreal region (tropics). During both the MP and LIA, this scenario requires preindustrial biomass burning ethane emissions greater than the modern-day estimate from GFED4.1.

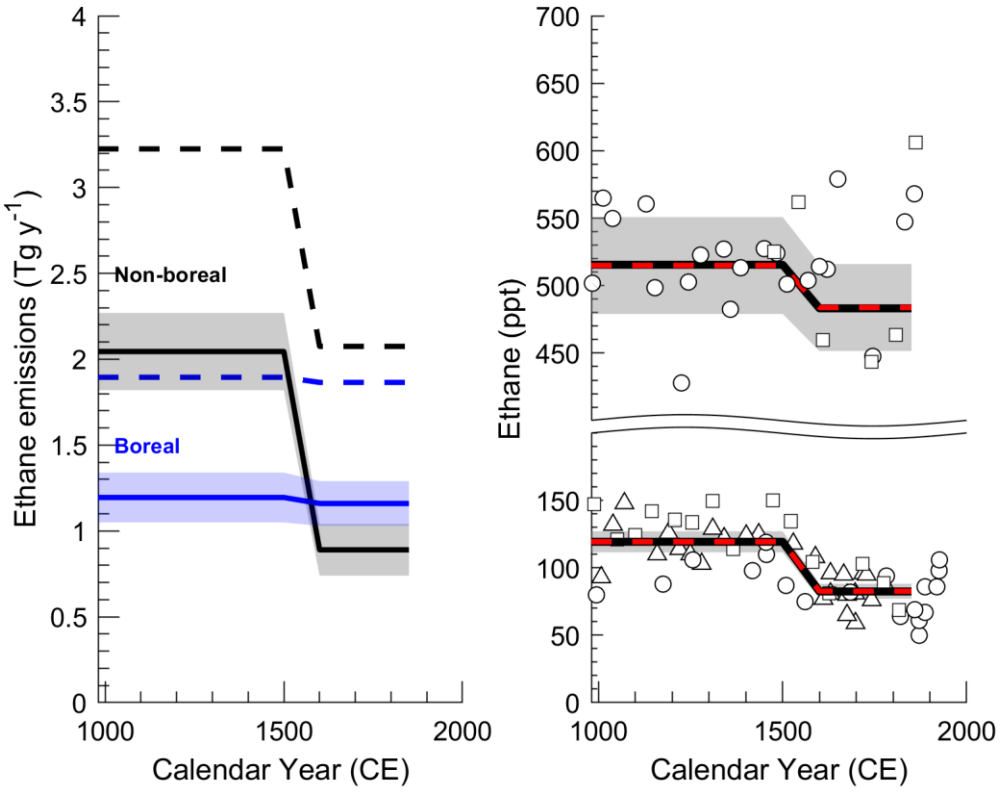

Figure 4.8: Biomass burning scenarios for ethane (left) for geologic ethane emissions fixed at 0 Tg y^{-1} (dashed lines) and 2 Tg y^{-1} (solid lines) and the resulting ethane mixing ratios over Greenland and Antarctica (right). Boreal emissions (blue) and non-boreal emissions (black) could vary independently through time. The solid or dashed lines represented the mean and the shaded area is the ±1σ uncertainty.

Assuming geologic emissions are higher at 2 Tg y^{-1}, boreal and non-boreal ethane emissions during the MP of 2.0 ± 0.2 Tg y^{-1} and 1.2 ± 0.1 Tg y^{-1}, respectively, are required to reconstruct the ice core levels during that time (Figure 4.9). The MP total burning ethane budget is 3.2 ± 0.2 Tg y^{-1}. During the LIA, non-boreal emissions decline by 56% to 0.9 ± 0.2 Tg y^{-1}. Similarly to the zero-geologic case, boreal ethane emissions stay nearly constant between the two time periods with LIA emissions of 1.2 ± 0.1 Tg y^{-1} (Table 4.3). The LIA total burning ethane budget is 2.1 ± 0.2 Tg y^{-1}. The ice core data indicates that with 2 Tg y^{-1} geologic emissions, biomass burning emissions are required to decline by 37% with most of the decline occurring in the non-boreal region (tropics). During the MP, ethane biomass burning emissions are

comparable to the modern-day ethane biomass burning estimate from GFED4.1, while LIA ethane biomass burning emissions are roughly 60% of the modern-day estimate.

These simulations suggest that 1) biomass burning ethane emissions during the MP were higher than, or comparable to modern biomass burning ethane emissions, 2) biomass burning ethane emissions during the LIA were comparable to, or less than modern biomass burning ethane emissions, and 3) biomass burning ethane emissions in the non-boreal region declined from the MP to LIA. The implications of these biomass burning scenarios on global fire and how the trends in the ethane biomass burning records compares with those inferred from ice core acetylene and methane is discussed in Chapter 6.

4.3.2 Ethane budget with Cl sink

The Cl sink for ethane has been largely ignored in previous budget analyses for ethane (ex: *Xiao et al.*, 2007; *Tzompa-Sosa et al*., 2017). However, it is possible that the ethane Cl sink is significant (~20% of total sink; *Wang et al*., 2019). If so, including the Cl sink would significantly change not only the modern ethane budget, but also the inferred biomass burning histories presented in Section 4.3.1. Here we attempt to make a conservative estimate of the magnitude of the Cl ethane sink based on previous analysis of the Cl sink for methane. Then, we use this estimated Cl ethane sink strength to re-evaluate the preindustrial ethane budget based on the ice core data.

Allan et al. (2007) suggested that the methane Cl sink was roughly 5% of the total methane sink loss based on the stable isotope measurements of methane ($\delta^{13}C$) and the differing kinetic isotope effect that occurs between the OH sink and the Cl sink. Recently, *Wang et al*. (2019) developed a comprehensive simulation of global tropospheric Cl using a GEOS-Chem 3D model of oxidant-aerosol-halogen atmospheric chemistry. In this model, the Cl atoms contribute

to 1% of the global oxidation of methane and 20% of the global oxidation of ethane (*Wang et al., 2019*). Using this information, along with the relative reaction coefficients between ethane and methane with Cl, we estimated a conservative magnitude for the Cl ethane sink as described below.

The reaction rate (k_{ethane}) for ethane with Cl at 298 K is 5.69×10^{-11} cm^3 $molecules^{-1}$ s^{-1} (*Burkholder et al.*, 2015). The reaction rate ($k_{methane}$) for methane with Cl at 298 K is 1.00×10^{-13} cm^3 $molecules^{-1}$ s^{-1} (*Burkholder et al.*, 2015). The ratio of $k_{ethane}/k_{methane}$ is roughly 586. Assuming that the methane + Cl sink strength is about 5% of the total methane loss, the resulting methane lifetime due to Cl loss is about 200 years (*Prather et al.*, 2012). Using this lifetime, and the $k_{ethane}/k_{methane}$ ratio, we calculated the impact on the ethane sink as follows:

$$k_{total} = k_{OH} + k_{Cl} \tag{4.3}$$

where k_{OH} is the inverse lifetime of ethane due to OH oxidation (which we assumed is 2.5 months or roughly 0.21 years [k_{OH} = 1/0.21 years]), k_{Cl} is the inverse lifetime of ethane due to Cl oxidation which we calculated by:

$$k_{Cl} = \frac{1}{\left(\frac{200\ years}{k_{ethane}/k_{methane}}\right)} = \frac{1}{\left(\frac{200\ years}{586}\right)} = 2.84\ years^{-1} \tag{4.4}$$

where 200 years is the methane lifetime due to Cl oxidation, and $k_{ethane}/k_{methane}$ is the relative ratio between the reaction rates of ethane and methane to Cl. k_{total} becomes:

$$k_{total} = k_{OH} + k_{Cl} = \frac{1}{0.21\ years} + \frac{1}{2.84\ years} = 7.64\ years^{-1} \tag{4.5}$$

The addition of a Cl ethane sink proportional to a 5% Cl methane sink results in a change in k_{total} of roughly 60% from 4.80 $years^{-1}$ to 7.64 $years^{-1}$ for ethane.

Sensitivities were calculated from the UCI-CTM over a range of lifetimes for ethane (Appendix C). With the relationship between ethane lifetime (or inverse lifetime, k_{total}) and sensitivity known, new sensitivities could be computed for a lifetime that includes a 60% Cl sink for ethane. This approach assumes that the Cl field is identical to the OH field in the UCI-CTM which may not be realistic but is a decent approximation of the impact of an additional sink on the ethane budget (*Wang et al.*, 2019). The sensitivities for ethane with a 60% Cl sink are shown in Table 4.2. Using these sensitivities, the preindustrial ethane budget was re-analyzed following the same grid search approach as described in Section 4.3.1. The full solution space over a range of boreal and non-boreal biomass burning and geologic emissions is shown in Figure 4.9.

For geologic ethane emissions of 0 Tg y^{-1} and a 60% Cl sink, boreal and non-boreal ethane emissions during the MP of 5.8 ± 0.4 Tg y^{-1} and 2.5 ± 0.2 Tg y^{-1}, respectively, are required to reconstruct the ice core levels during that time (Figure 4.10). The MP total burning ethane budget is 8.3 ± 0.4 Tg y^{-1} which is a nearly a factor of 2.5 greater than modern ethane biomass burning emissions estimate from the GFED4.1 inventory (3.4 Tg y^{-1}; *van der Werf et al.*, 2017). During the LIA, non-boreal ethane emissions decline to 3.9 ± 0.3 Tg y^{-1}, while boreal emissions stay nearly constant at 2.4 ± 0.2 Tg y^{-1} (Table 4.4). The LIA total burning ethane

Table 4.2 UCI-CTM sensitivities for ethane assuming a 60% Cl sink strength.

Source	k ($month^{-1}$)	Lifetime (months)	Greenland sensitivity (ppt/Tg y^{-1})	Antarctica sensitivity (ppt/Tg y^{-1})
Non-boreal biomass burning	0.71	1.41	12.63	19.24
Boreal biomass burning	0.64	1.56	166.63	1.05
Geologic	0.65	1.54	66.96	11.98
Biofuel	0.66	1.52	58.67	9.07

budget is 6.4 ± 0.4 Tg y^{-1}. The ice core data indicates that with zero geologic emissions, biomass burning emissions are required to decline by 23% with most of the decline occurring in the non-boreal region (tropics). This emission scenario requires preindustrial biomass burning ethane emissions during the MP that are a factor of 2.5 and emissions during the LIA that are a factor of 1.9 greater than the modern-day ethane biomass burning emission from the GFED4.1 inventory. This emission scenario suggests that modern biomass burning ethane emissions are significantly lower than anytime during the last 1,000 years.

Assuming geologic emissions are higher at 2 Tg y^{-1} and a 60% Cl sink, boreal and non-boreal ethane emissions during the MP of 4.6 ± 0.4 Tg y^{-1} and 1.8 ± 0.2 Tg y^{-1}, respectively, are required to reconstruct the ice core levels during that time (Figure 4.10). The MP total burning ethane budget is 6.4 ± 0.4 Tg y^{-1}. During the LIA, non-boreal emissions decline by 41% to 2.7 ± 0.3 Tg y^{-1}. Similarly, to the zero-geologic case, boreal ethane emissions stay nearly constant between the MP and LIA with LIA emissions of 1.7 ± 0.2 Tg y^{-1} (Table 4.4). The LIA total burning ethane budget is 4.4 ± 0.4 Tg y^{-1}. During the MP, ethane biomass burning emissions are required to be nearly double the modern-day ethane biomass burning estimate from GFED4.1. LIA ethane biomass burning emissions are roughly 30% greater than the modern-day ethane biomass burning estimate.

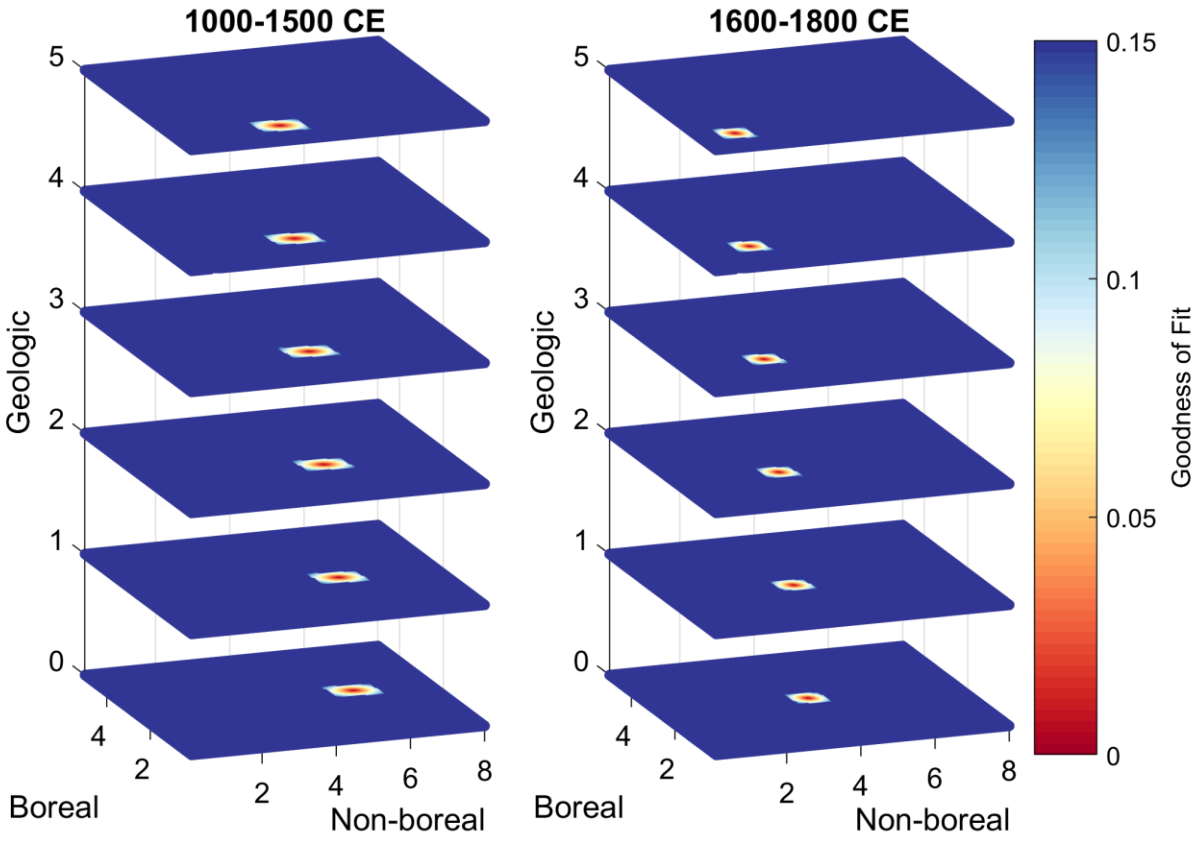

Figure 4.9: Modeled ethane boreal and non-boreal biomass burning and geologic emission scenarios for the Medieval Period (1000-1500 CE, left) and Little Ice Age (1600-1800 CE, right) assuming a 60% Cl sink. Contours are of goodness of fit with a value of 0 corresponding to a perfect fit to the mean of the ice core records. Emissions are in Tg ethane y^{-1}.

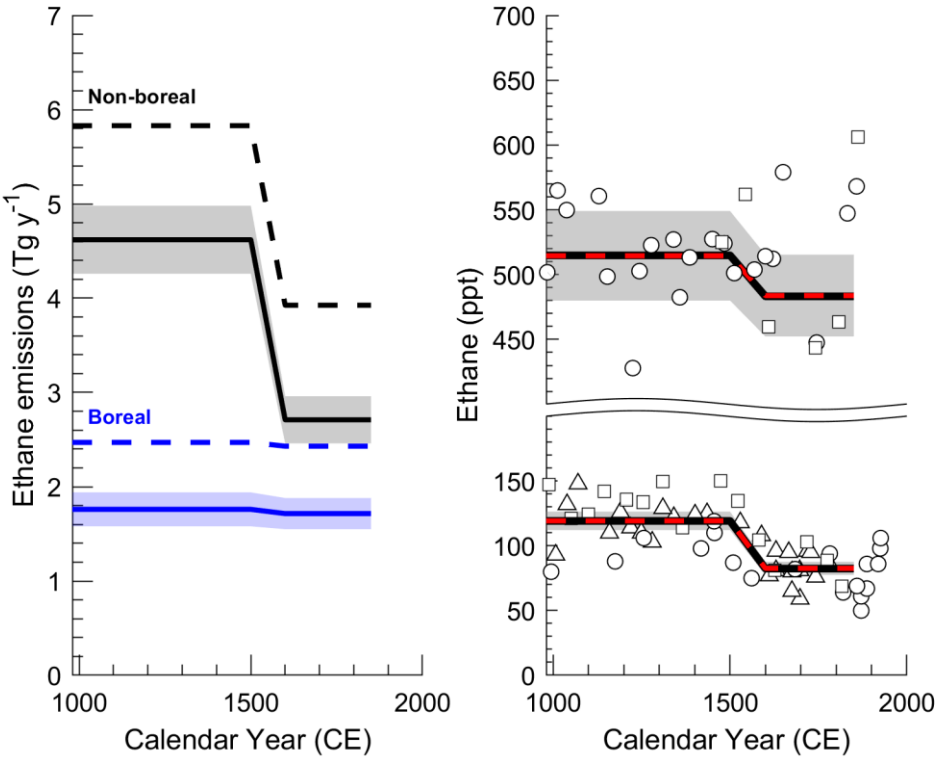

Figure 4.10: Biomass burning scenarios for ethane (left) for geologic ethane emissions fixed at 0 Tg y^{-1} (dashed lines) and 2 Tg y^{-1} (solid lines) assuming a 60% Cl ethane sink and the resulting ethane mixing ratios over Greenland and Antarctica (right). Boreal emissions (blue) and non-boreal emissions (black) could vary independently through time. The solid or dashed lines represented the mean and the shaded area is the ±1σ uncertainty.

Table 4.3: Preindustrial ethane budget with no Cl sink. Emissions are in Tg ethane y^{-1}.

	Medieval Period		Little Ice Age	
Geologic	Non-boreal	Boreal	Non-boreal	Boreal
0	3.22 ± 0.22	1.90 ± 0.14	2.07 ± 0.15	1.87 ± 0.14
2	2.04 ± 0.22	1.19 ± 0.14	0.89 ± 0.15	1.16 ± 0.13

Table 4.4: Preindustrial ethane budget with a 60% Cl sink. Emissions are in Tg ethane y^{-1}.

	Medieval Period		Little Ice Age	
Geologic	Non-boreal	Boreal	Non-boreal	Boreal
0	5.83 ± 0.36	2.47 ± 0.18	3.92 ± 0.25	2.43 ± 0.17
2	4.62 ± 0.36	1.76 ± 0.18	2.71 ± 0.25	1.71 ± 0.17

CHAPTER 5

Polar ice core records of acetylene

5.1 Overview

In this chapter, acetylene measurements in air extracted from ice cores from Greenland and Antarctica are presented. The ice core samples analyzed span the last ~3,000 years. This is the first millennial-scale record of acetylene in ice cores and the first attempt to use ice core acetylene to constrain preindustrial biomass burning emissions. The chapter is organized by first describing the acetylene results from two different analytical methods (as described in Chapter 2) and comparing the similarities and differences between the two acetylene datasets. Then, preindustrial budgets for acetylene are inferred using atmospheric models (Chapter 3) with the ice core acetylene records collected using the improved analytical procedure (procedure 4).

5.2 Results and discussion

5.2.1 Procedure 1 results

Acetylene results from WAIS Divide, Antarctica (WDC05A) and Summit, Greenland (GISP2B) using wet-extraction procedure 1 are shown in Figure 5.1. The WDC05A measurements were conducted in 2014. The measurements were blank corrected using the average blank of all applicable post-melt N_2 blanks, excluding 2σ outliers (Table 5.1). For the WDC05A samples, the blanks were roughly 37% of acetylene measured in an average WDC05A sample. Blanks for GISP2B samples were similar and comprise roughly 17% of the acetylene in an average GISP2B sample.

The Greenland GISP2B samples from procedure 1 cover the period from 1456-1862 CE, at a resolution of 20-30 years (Figure 5.1). Nine samples had CFC-12 levels > 1 ppt which is an

indication of modern air contamination, either through poor sample quality or leaks during analysis. Excluding these samples, the average acetylene level over the length of the GISP2B record is 92 ± 12 ppt (±1σ). The average acetylene level from 1450-1750 CE is 91 ± 11 ppt. After 1750 CE, acetylene levels increase slightly to a mean of 106 ± 10 ppt, but 6 out of the 8 samples during this time period have elevated levels of CFC-12. This makes it challenging to deduce if the rise is an atmospheric signal or an artifact from modern air contamination. All six samples which were analyzed as duplicates agree within analytical uncertainties.

The Antarctic WDC05A samples from procedure 1 cover the time period from 1336-1918 CE with an average resolution of roughly 45 years (Figure 5.1). The mean acetylene level over the whole record is 24 ± 17 ppt (excluding two samples with acetylene >100 ppt). All three samples which were analyzed as duplicates agree within analytical uncertainties. There is no obvious trend to the WDC05A acetylene record due to the high scatter and low resolution of the data.

Table 5.1: Acetylene levels in the post melt N_2 blanks from procedure 1(mean + 2σ).

Year	Core	1st N_2 blank pmol C_2H_2	2nd N_2 blank pmol C_2H_2
2014	WDC-05A	0.023 ± 0.008	0.022 ± 0.006
2014	GISP2B	0.023 ± 0.008	0.019 ± 0.008

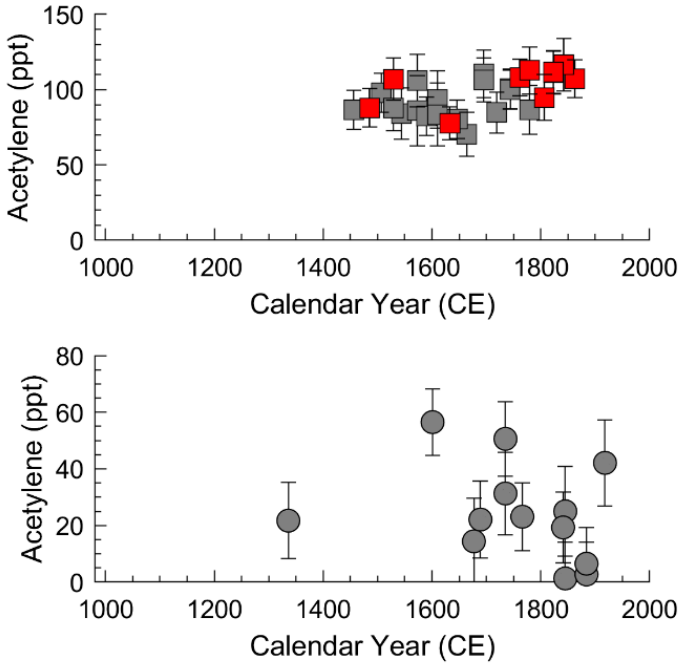

Figure 5.1: Ice core acetylene analyzed with procedure 1 from Summit, Greenland (GISP2B, top) and WAIS Divide, Antarctica (WDC05A, bottom). Samples with CFC-12 > 1 ppt are colored red. Error bars denote 1σ uncertainties. Data are found in Appendix B.

5.2.2 Procedure 4 results

Acetylene measurements in the GISP2D, GISP2B, WDC05A, WDC06A and SPC14 cores conducted using an improved wet-extraction procedure (procedure 4) are shown in Figure 5.2 and Figure 5.3. The Greenland acetylene measurements with procedure 4 are from the fluid-drilled GISP2B core and the shallow, dry-drilled GISP2B core. The GISP2D samples analyzed with procedure 4 range in depth from 95.6 m to 730.6 m, corresponding to gas ages of 1892 CE and 1206 BCE, respectively. The GISP2B samples range from 87.6 m to 194.1 m corresponding to gas ages of 1918 CE and 1477 CE. There is good agreement between acetylene levels in samples of contemporaneous age from the GISP2B and GISP2D ice cores, indicating acetylene can be successfully measured in ice cores without interference and contamination from hydrocarbon-based drill fluids. The Antarctic acetylene measurements are from the shallow, dry-

drilled WDC05A core and the deep, fluid-drilled WDC06A and SPC14 cores. The WDC05A samples range in depth from 83 to 298 m, corresponding to gas ages of 1926 CE and 994 CE, respectively. The WDC06A samples range from 117 m to 604 m, corresponding to gas ages of 1781 CE and 303 BCE, respectively. The SPC14 samples range from 140 m to 294 m, corresponding to gas ages of 1817 CE and 387 BCE, respectively. There is good agreement between acetylene levels in the samples from contemporaneous age during the whole 2,300-year record.

Procedure 4 samples which had high levels of CFC-12 (>1 ppt), known experimental issues, or exceptionally high acetylene levels were excluded from analysis. Eight samples from the GISP2D core and 11 samples from the WDC05A were excluded. These data are shown in Figure 5.2 and are listed in Appendix B.

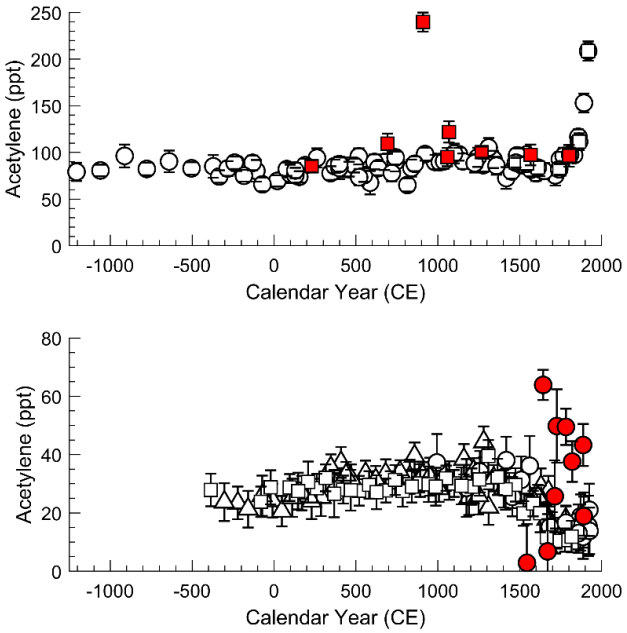

Figure 5.2: Acetylene ice core data from procedure 4 excluded from analysis (red). Data is listed in Appendix B. *Top*: Greenland acetylene from GISP2B (squares) and GISP2D (circles). *Bottom*: Antarctic acetylene from WDC05A (circles), WDC06A (triangles), and SPC14 (squares).

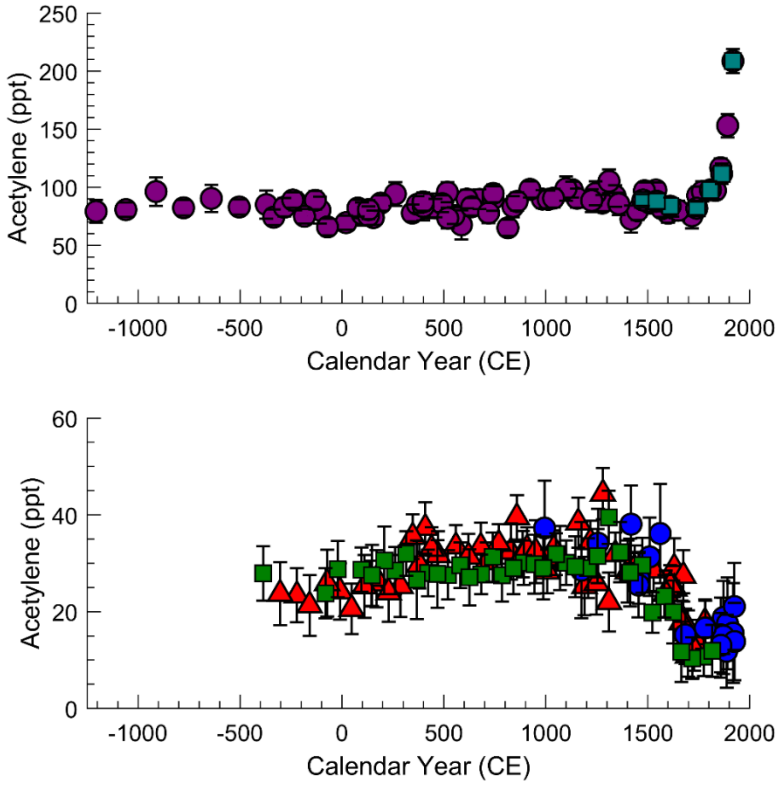

Figure 5.3: Ice core acetylene from procedure 4. Greenland (top) measurements are from GISP2B (teal squares) and GISP2D (purple circles). Antarctica (bottom) measurements are from WDC05A (blue circles), WDC06A (red triangles), and SPC14 (green squares). Error bars represent the ±1σ uncertainty.

The Greenland acetylene record exhibits little variability over the 3,000-year period (Figue 5.3 and Figure 5.4). The average acetylene level over the whole period is 86 ± 10 ppt (excluding the two shallowest samples with gas ages of 1892 CE and 1918 CE). Between ~1000-1500 CE, acetylene levels are slightly higher at 91 ± 7 ppt. Acetylene levels decline slightly to a mean of 80 ± 6 ppt during the 1600-1745 CE period, although there are few samples during this time (n=6). Greenland acetylene levels begin to rise after the mid-1700s, likely due to anthropogenic emissions. The maximum acetylene occurs at a gas age of 1918 CE at 209 ± 10 ppt. Overall, the Greenland record exhibits a slight increasing trend during the last 3,000 years (Figure 5.4).

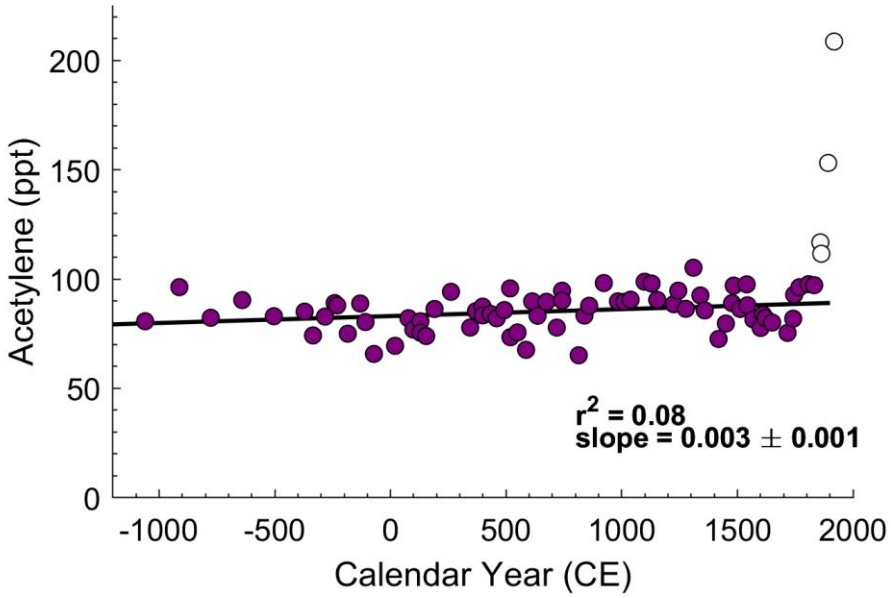

Figure 5.4: Greenland ice core acetylene record from procedure 4 with trendline up to 1832 CE. White markers indicate samples excluded from trendline analysis.

The Antarctic acetylene record displays significant variability over the 2,300-year period (Figure 5.2 and Figure 5.5). The mean acetylene level over the full record is 26 ± 7 ppt. From 387 BCE – 1509 CE, the mean acetylene level is 30 ± 4 ppt. This is roughly 50% higher than the modern-day mean Antarctic acetylene level of 18-20 ppt. A slight increasing trend ($r^2 = 0.18$) is apparent in the data during the 387 BCE – 1509 CE period with a slope of 0.004 ± 0.001. After 1500 CE, Antarctic acetylene levels decline quickly and reach a minimum during the 1600-1800 CE period at 16 ± 6 ppt. This results in a decline of acetylene levels of nearly 50%. This decline is statistically significant (slope = -0.029 ± 0.008 [± 1 SE] with an $r^2 = 0.30$). The 1600-1800 CE mean acetylene level in the ice cores is comparable to the modern-day level over Antarctica. Contrary to the Greenland acetylene record, the Antarctic record suggests atmospheric acetylene declined during the last few hundred years.

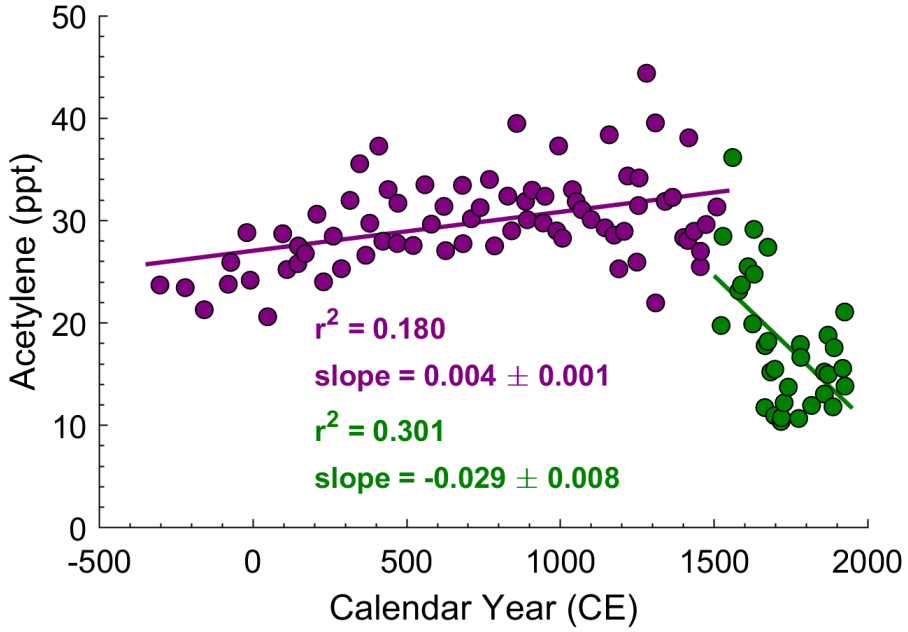

Figure 5.5: Antarctic acetylene from procedure 4 with trends highlighted. An increasing trend is apparent in the data from 303 BCE to 1509 CE (purple) and a decreasing trend is apparent after 1529 CE (green). Uncertainties on the slopes are ± 1 SE.

5.2.3 Comparison of procedure 1 and 4 acetylene results

The acetylene results from analytical procedure 1 and procedure 4 are shown together in Figure 5.6. Overall, the Greenland acetylene levels from procedure 1 and procedure 4 agree relatively well. From 1400-1750 CE, the mean acetylene level from procedure 1 and procedure 4 are not statistically different ($p = 0.17$). For Antarctica, nearly all procedure 1 acetylene data are higher than that from procedure 4. From 1550-1925 CE, the mean acetylene level from procedure 1 and procedure 4 are statistically different ($p = 0.04$).

The trends observed in the Greenland ice core acetylene records from the two datasets show different trends (Figure 5.7). Between 1400-1750 CE, procedure 1 acetylene indicates a slight increasing trend, while procedure 4 acetylene shows a slight decreasing trend. Neither of these trends are statistically significant. When the post-1750 CE data is included, both data sets show increasing acetylene levels into the modern era with slopes of 0.05 ± 0.02 and 0.13 ± 0.04

for procedure 1 and procedure 4, respectively. The positive trend is driven by the high acetylene levels after 1750 CE which is apparent in both datasets.

The Antarctic acetylene data from procedure 1 is poorer quality than that from procedure 4 which makes interpreting any trends in the data challenging. Antarctic acetylene from procedure 1 suggests a slight declining trend between 1300-1900 CE, although the slope is not statistically significant from zero (-0.03 ± 0.03, Figure 5.8). On the contrary, the procedure 4 Antarctic acetylene record displays as strong decline between 1300-1900 CE ($r^2 = 0.32$).

Analysis and interpretation of the ice core acetylene records is completed only on the procedure 4 data set because of 1) increased analytical blanks in procedure 1 vs. procedure 4 (Chapter 2) and 2) the statistical evidence which shows the two datasets are different, especially for the Antarctica data.

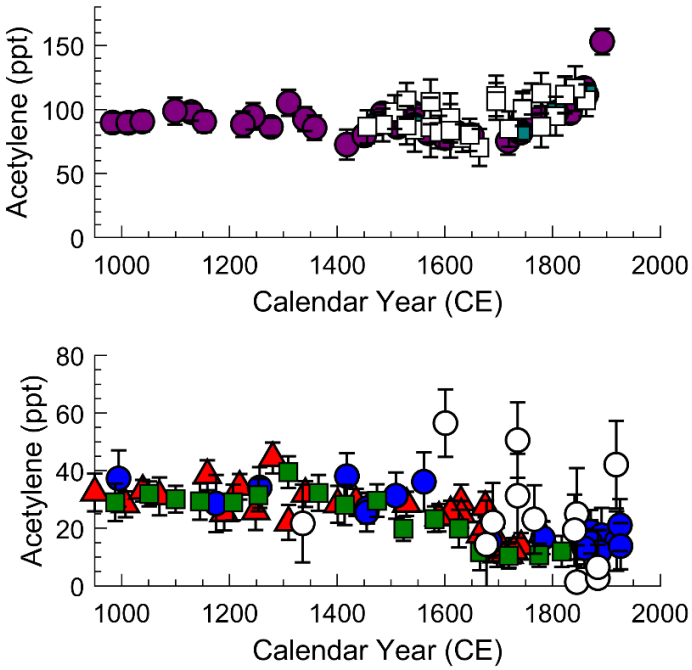

Figure 5.6: Acetylene measured in Greenland (top) and Antarctic (bottom) samples using analytical procedure 1 (white markers) and procedure 4 (colored markers).

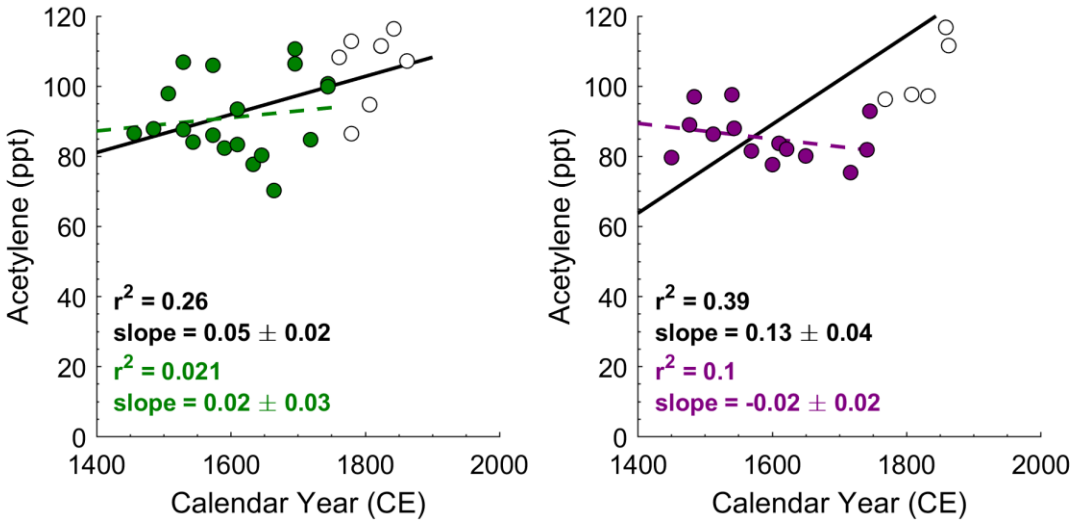

Figure 5.7: Trends in Greenland acetylene data. Greenland acetylene (in ppt) from procedure 1 (left) and procedure 4 (right). For procedure 1, the green data points indicate the data which was used for the linear regression from 1400-1750 CE. The resulting regression line (dashed line), slope, and r^2 are also shown in green. The black line indicates the linear regression performed on the whole data set from 1400-1900 CE. For procedure 4, the purple data points indicate the data which was used for the linear regression from 1400-1750 CE. The resulting regression line (dashed line), slope, and r^2 are shown in purple. The black line indicates the linear regression performed on the whole data set from 1400-1900 CE. The uncertainty on the slopes is 1 SE.

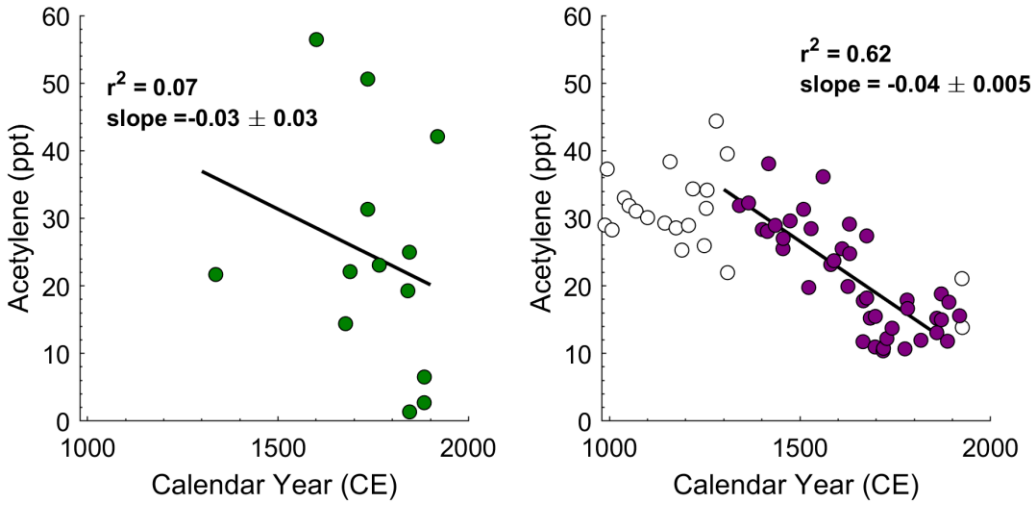

Figure 5.8: Trends in Antarctic acetylene data. Antarctic acetylene (in ppt) from procedure 1 (left) and procedure 4 (right). The linear regression is performed on the filled data points. The uncertainty on the slope is 1 SE.

5.3 Implications for the preindustrial acetylene budget

Large changes are observed in the ice core acetylene levels, particularly over Antarctica, during the last 1,000 years. Using the UCI-CTM sensitivities (Table 3.5) for biomass burning and biofuel burning acetylene sources, various emission scenarios can be explored which reconstruct the ice core acetylene data. The ice core data were divided into two time periods: 1) the Medieval Period (MP) from 1000-1500 CE and 2) the Little Ice Age (LIA) from 1600-1800 CE. A grid-search method was used to explore a range of emissions scenarios and identify those compatible with the ice core results. In all scenarios, biofuel emissions of acetylene were fixed at 0.5 Tg y^{-1} based on *van Aardenne et al*. (2000). Mixing ratios were calculated by summing the sources of each gas multiplied by their respective sensitivities. Viable emission scenarios were determined by using equations 3.5 and 3.6 as described in Chapter 3.

For the first scenario, we explored a scenario in which global biomass burning emissions could vary through time. This assumes the geographic footprint of biomass burning emissions does not change through time and is identical to the Global Fire Emissions Database version 3.1 distribution (GFED3.1; *van der Werf et al.,* 2010). With this approach, global biomass burning acetylene emissions of 5.1 ± 0.2 Tg y^{-1} are required to obtain reasonable agreement (±10%) with the mean levels observed in the Greenland and Antarctic ice core records during the MP (Figure 5.9). With this magnitude of emissions, Greenland acetylene mixing ratios during the MP fall towards the lower bounds of agreement, while Antarctica acetylene mixing ratios fall towards the upper bounds of agreement. Forcing all global biomass burning acetylene emissions to change in sync cannot reproduce the ice core levels observed in both Greenland and Antarctica during the LIA. Rather, it is possible to reproduce the Antarctic acetylene levels during the LIA if global

biomass burning acetylene emissions decline by 52% to 2.4 ± 0.2 Tg y^{-1}. With this decline in all global biomass burning acetylene emissions, LIA Greenland acetylene levels are roughly 35 ppt lower than what is observed in the ice core records.

A second emission scenario was explored which allowed biomass burning emissions in different geographic locations to vary independently through time. Boreal (>50°N) biomass burning emissions and non-boreal (50°N to 90°S) biomass burning emissions were separated and could change independently between the two time periods. This approach is suitable because the Greenland and Antarctic acetylene levels have largely different sensitivities to biomass burning emissions in the two regions. For example, the Greenland acetylene sensitivity to boreal fire emissions is 107 ppt/Tg y^{-1} while the Antarctic ethane sensitivity to boreal fire emissions is roughly 0.05 ppt/Tg $y^{-1.}$ Boreal acetylene emissions account for roughly 10% of global acetylene biomass burning emissions today based on the GFED4.1 distribution and non-boreal emissions account for the remaining 90% with most of these emissions occurring in the tropical region (*van der Werf et al.*, 2017). Boreal and non-boreal emissions were varied between 0-5 Tg y^{-1} and the resulting mixing ratios over Greenland and Antarctica were calculated by summing over the sources multiplied by their respective sensitivities. Emission scenarios of boreal and non-boreal emissions which reproduced the ice core levels during the two periods are shown in Figure 5.9.

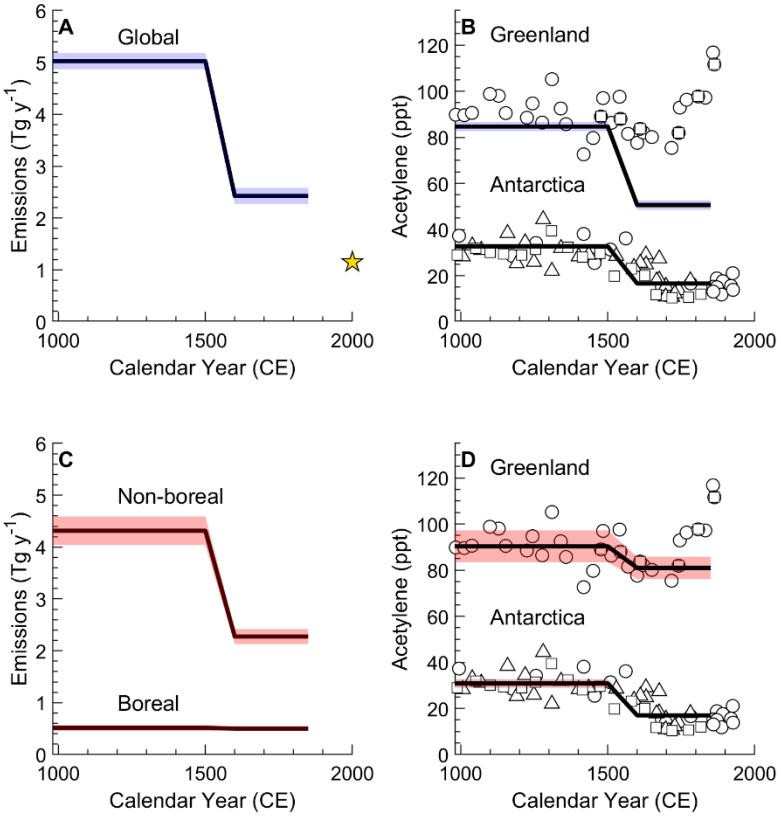

Figure 5.9: Biomass burning acetylene emission scenarios for the global biomass burning footprint (top panels) and when separating emissions into the non-boreal and boreal zones (bottom panels). A) Global biomass burning emissions which reconstruct the Greenland and Antarctic data during the MP and only the Antarctic data during the LIA. B) Resulting Greenland and Antarctic acetylene mixing ratios from the emissions in Panel A. C) Biomass burning emissions allowing the non-boreal and boreal emissions to vary independently through time. D) Resulting Greenland and Antarctic acetylene mixing ratios from the emissions in Panel C. Shaded areas are the 1σ uncertainty on the mean emission value.

In this scenario, non-boreal and boreal biomass burning emissions during the MP of 4.3 ± 0.3 Tg y^{-1} and 0.5 ± 0.1 Tg y^{-1} are required to reproduce the ice core acetylene levels. The MP total burning budget is 4.8 ± 0.3 Tg y^{-1} which is roughly four times the modern biomass burning emissions of acetylene estimated in the GFED4.1 inventory (1.2 Tg y^{-1}; *van der Werf et al.*, 2017). Non-boreal acetylene emissions decline to 2.3 ± 0.2 Tg y^{-1} and boreal acetylene emissions increase slightly to 0.6 ± 0.1 Tg y^{-1} during the LIA (Table 5.2). The LIA total burning acetylene budget is 2.8 ± 0.2 Tg y^{-1} which is roughly 2.5 times the modern biomass burning acetylene

budget from GFED4.1 (*van der Werf et al.*, 2017). The decline in burning emissions from the MP to LIA is about 42%, with all the decline occurring the non-boreal zone.

Table 5.2: Preindustrial biomass burning acetylene emissions from the boreal and non-boreal scenario. Emissions are in Tg acetylene y^{-1}.

	Medieval Period (1000-1500 CE)	Little Ice Age (1600-1800 CE)
Boreal	0.52 ± 0.05	0.55 ± 0.04
Non-boreal	4.32 ± 0.27	2.28 ± 0.15

A third emission scenario was explored to see if varying burning in regions in closest proximity to Antarctica with high acetylene sensitivities could lower the overall emissions required to explain the ice core data. In this scenario, we allowed South American emissions to vary independently from boreal emissions and the remaining "rest of the world" emissions. To calculate the "rest of the world" region's Greenland and Antarctic acetylene sensitivity, the following equation was used:

$$S_{all} * F_{all} = S_{SA} * F_{SA} + S_B * F_B + S_{ROW} * F_{ROW} \quad (5.2)$$

where S stands for the acetylene sensitivity for Greenland and Antarctica from the different source regions and F is the fraction of global biomass burning emissions in that region. The source regions used are the global biomass burning footprint (all), South America (SA), boreal (B), and rest of the world (ROW). The fractions (F) used and the resulting sensitivities are shown in Table 5.3.

Table 5.3: Biomass burning regions, their relative fractions of total global biomass burning, and their Greenland and Antarctic acetylene sensitivities used for the South American emission scenario.

Region	Fraction (F, % of total global burning acetylene emissions)	Greenland sensitivity (ppt acetylene/Tg y^{-1})	Antarctic sensitivity (ppt acetylene/Tg y^{-1})
South America	0.16	0.63	18.85
Boreal	0.09	106.84	0.05
Global	1	13.08	6.17
Rest of the world	0.74	4.54	4.02

For the South American emission scenario, boreal emissions ranged from 0 to 1 Tg y^{-1}, South American emissions ranged from 0 to 3 Tg y^{-1}, and the rest of the world emissions ranged from 0 to 5 Tg y^{-1}. The emissions scenarios which reproduced the Greenland and Antarctic ice core acetylene levels during the two times periods are shown in Figure 5.10 as a goodness of fit. The goodness of fit is calculated as:

$$Goodness\ of\ fit_{acetylene} = \sqrt{\left(\frac{|m_{grn} - o_{grn}|}{o_{grn}}\right)^2 + \left(\frac{|m_{ant} - o_{ant}|}{o_{ant}}\right)^2} \quad (5.2)$$

where m stands for the modeled value and o for the observed mean value from the ice core records. The goodness of fit was calculated for the MP and LIA separately. The goodness of fit ranges from 0 to 0.14, with 0 corresponding to a perfect fit to the mean of the ice core records.

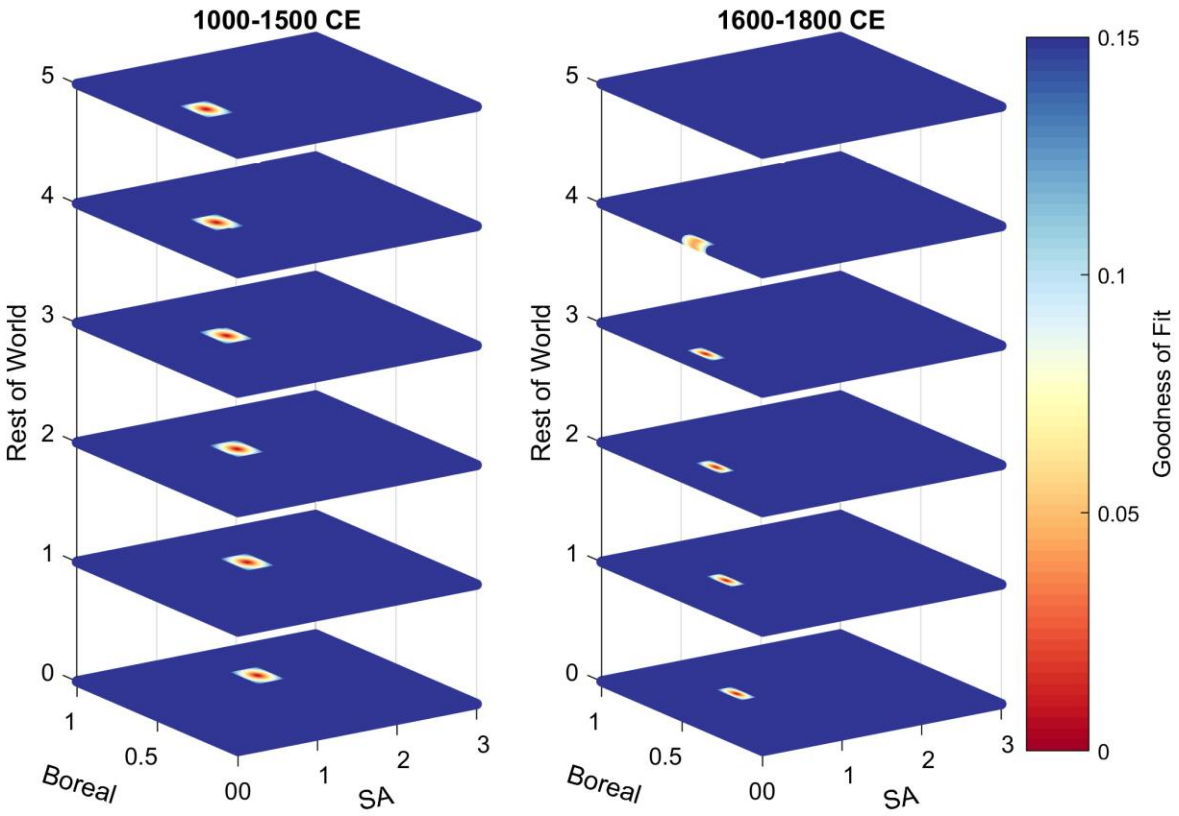

Figure 5.10: Modeled acetylene boreal, rest of world and South American emission scenarios for the Medieval Period (1000-1500 CE, left) and Little Ice Age (1600-1800 CE, right). Contours are of goodness of fit with a value of 0 corresponding to a perfect fit to the mean of the ice core records. Emissions are in Tg acetylene y^{-1}.

For "rest of world" acetylene emissions of 0 Tg y^{-1}, 1.57 ± 0.10 Tg y^{-1} emissions from the South American region and 0.67 ± 0.05 Tg y^{-1} emissions from the boreal zone are necessary to reproduce the mean ice core level during the MP (Table 5.4). The South American region accounts for roughly 17% of the global acetylene biomass burning emissions today, or about 0.20 Tg y^{-1}. This scenario requires South American emissions during the MP to be nearly eight-times larger than what is estimated for this region today. Boreal emissions today are about 9% of the global acetylene biomass burning emissions, or about 0.12 Tg y^{-1}. This scenario requires biomass burning boreal emissions to be about six-times larger than what is estimated for this

region today. The total MP budget is 2.24 Tg y^{-1} which is roughly double the modern GFED4.1 estimate for global acetylene biomass burning emissions (*van der Werf et al.,* 2017). During the LIA, the South American acetylene emissions decline by roughly 48% to 0.82 ± 0.05 Tg y^{-1} and boreal emissions decline by 15% to 0.57 ± 0.04 Tg y^{-1}. This scenario requires South American acetylene emissions which are a factor of four larger than modern and boreal acetylene emissions which are a factor of five larger than modern are required to yield levels in agreement with the ice core data during the LIA. The LIA budget is 1.39 Tg y^{-1} which is comparable to the modern-day global acetylene biomass burning emission estimate of 1.14 Tg y^{-1} (*van der Werf et al.,* 2017). This scenario assumes the "rest of the world" emissions to be 0 Tg y^{-1}, which is not a realistic assumption given that the "rest of the world" is 74% of total global acetylene biomass burning emissions with most of these emissions occurring the in tropical region.

If the "rest of the world" acetylene emissions are held at 1 Tg y^{-1}, which is similar to the modern distribution of acetylene emissions from the GFED4.1 inventory, then South American acetylene emissions of 1.35 ± 0.10 Tg y^{-1} and boreal acetylene emissions of 0.62 ± 0.05 Tg y^{-1} are required during the MP (*van der Werf et al.,* 2017). This scenario requires South American emissions to be nearly 7-times larger than today and boreal emissions to be about 5-times larger than today. The total MP biomass burning budget is 2.97 Tg y^{-1} versus the modern-day global biomass burning acetylene budget of 1.14 Tg y^{-1} (*van der Werf et al.,* 2017). During the LIA, South American emissions decline by 55% to 0.60 ± 0.05 Tg y^{-1} and boreal emissions decline by 15% to 0.53 ± 0.04 Tg y^{-1}. During the LIA, the South American emissions are a factor of 3 greater than the modern estimate for this region and the boreal emissions are a factor of 4.5 greater than the modern estimate for this region. The total LIA biomass burning budget is 2.13 Tg y^{-1}.

The South American scenario requires: 1) total biomass burning emissions to be less than that from the non-boreal/boreal scenario, 2) most of the change in emissions between the MP and LIA to be driven by a decline in the South American region and 3) emissions in the South American region and boreal region to be several times greater than modern emissions in these regions.

In summary, all the biomass burning scenarios require preindustrial acetylene emissions to be significantly higher than the modern-day estimate from GFED4.1. All the scenarios require acetylene emissions in a region (i.e. non-boreal or South America) to decline by roughly 50% from the MP to LIA in order to reconstruct the decline observed in the ice core acetylene records during this time.

Table 5.4: Preindustrial acetylene budget for the South American simulation. Emissions are in Tg acetylene y^{-1}.

Rest of World	**Mean South America**		**Mean Boreal**	
	1000-1500 CE	1600-1800 CE	1000-1500 CE	1600-1800 CE
0	1.57 ± 0.10	0.82 ± 0.05	0.67 ± 0.05	0.57 ± 0.04
1	1.35 ± 0.10	0.60 ± 0.05	0.62 ± 0.05	0.53 ± 0.04
2	1.15 ± 0.10	0.39 ± 0.05	0.58 ± 0.05	0.49 ± 0.04
3	0.93 ± 0.10	0.18 ± 0.05	0.54 ± 0.05	0.44 ± 0.04
4	0.72 ± 0.10	0.03 ± 0.02	0.50 ± 0.05	0.40 ± 0.04
5	0.51 ± 0.10	no solutions	0.46 ± 0.05	no solutions

CHAPTER 6

Comparison of biomass burning histories from ethane, acetylene, and methane

6.1 Overview

In this chapter, the ethane and acetylene biomass burning emission histories inferred from the ice core records are compared with that from methane. Similarities and differences between the biomass burning histories from each gas are discussed. To determine if these gases record a single fire history, the biomass burning histories from each compound are then converted into a global fire (dry matter burned) history by applying emission factors to each record. The similarities and differences between the inferred dry matter burned histories from these gases are discussed. In summary, it has proved challenging to reconstruct a single fire history over the last 1,000 years from the three gas records. There are some major discrepancies between the dry matter burning histories inferred from the three gases and no scenario explored provides a consistent history of dry matter burned. Factors which may explain the observed discrepancies are discussed in Chapter 7.

6.2 Preindustrial methane biomass burning histories

Measurements of methane and its stable isotopes in ice cores have been used to develop biomass burning emission histories over the last few thousand years (*Ferretti et al*., 2005; *Mischler et al*., 2009; *Sowers*, 2010; *Sapart et al*., 2012; *Bock et al*., 2017). We used the steady-state one box model of methane described in Chapter 2 along with ice core methane concentrations and $\delta^{13}CH_4$ data to develop methane biomass burning emission scenarios using

different assumptions about the Cl sink strength and geologic source strength. The ice core data were broken up into two time periods similarly to the methods for ethane and acetylene: the Medieval Period (MP: 1000-1500 CE) and the Little Ice Age (LIA: 1600-1800). Emission scenarios of biomass burning, microbial, and geologic methane emissions which yield both methane mixing ratios and $\delta^{13}CH_4$ within 10% of the ice core mean values were considered viable (see equations 3.12 and 3.13). Because of the long atmospheric lifetime of methane (as compared to ethane and acetylene), the boreal and non-boreal biomass burning emissions are not able to be distinguished for methane. Instead total global biomass burning emissions are inferred. The results are described below.

The resulting emission scenarios of biomass burning, microbial and geologic emissions which reproduce the ice core methane and $\delta^{13}CH_4$ data for the two time periods assuming the Cl sink for methane is 5% of the total sink are shown in Figure 6.1 and Table 6.1. For geologic methane emissions at 0 Tg y^{-1}, biomass burning emissions of 21.6 ± 1.8 Tg y^{-1} and microbial emissions of 180.8 ± 10.1 Tg y^{-1} are required. Biomass burning emissions decline by 31% to 14.8 ± 1.5 Tg y^{-1} and microbial emissions increase by 7% to 192.9 ± 11.7 Tg y^{-1} during the LIA. The same overall trend in the biomass burning and microbial emissions is observed between the MP to LIA if geologic methane emissions are higher, but the overall magnitudes shift. For example, if geologic emissions are 20 Tg y^{-1}, the decline in biomass burning methane emissions between the MP and LIA increases to 53%. This is because the initial biomass burning methane emissions during the MP are lower with this scenario of geologic emissions. Regardless of the geologic source strength, the biomass burning methane decline is approximately 7 Tg y^{-1} and the increase in microbial emissions is rouhgly 11 Tg y^{-1}.

The magnitude of the Cl methane sink is debated but is likely between 0-5% of the total methane loss (*Allan et al.*, 2007; *Prather et al.*, 2012). To provide flexibility in the preindustrial emission scenarios, we also explored what the impact on the methane budget would be if the Cl sink term were zero. The results are shown in Figure 6.2 and Table 6.1. For geologic methane emissions at 0 Tg y^{-1}, biomass burning emissions of 32.6 ± 2.5 Tg y^{-1} and microbial emissions of 161.2 ± 10.0 Tg y^{-1} are required. Biomass burning emissions decline by 20% to 26.1 ± 2.0 Tg y^{-1} and microbial emissions increase by 7% to 171.9 ± 9.6 Tg y^{-1} decline into the LIA. The same overall trends in the biomass burning and microbial emissions are observed between the MP to LIA regardless of the geologic source strength, but the magnitudes of the decline or increase in emissions change. For example, if geologic emissions are 20 Tg y^{-1}, then the decline in biomass burning emissions between the MP and LIA is 26%.

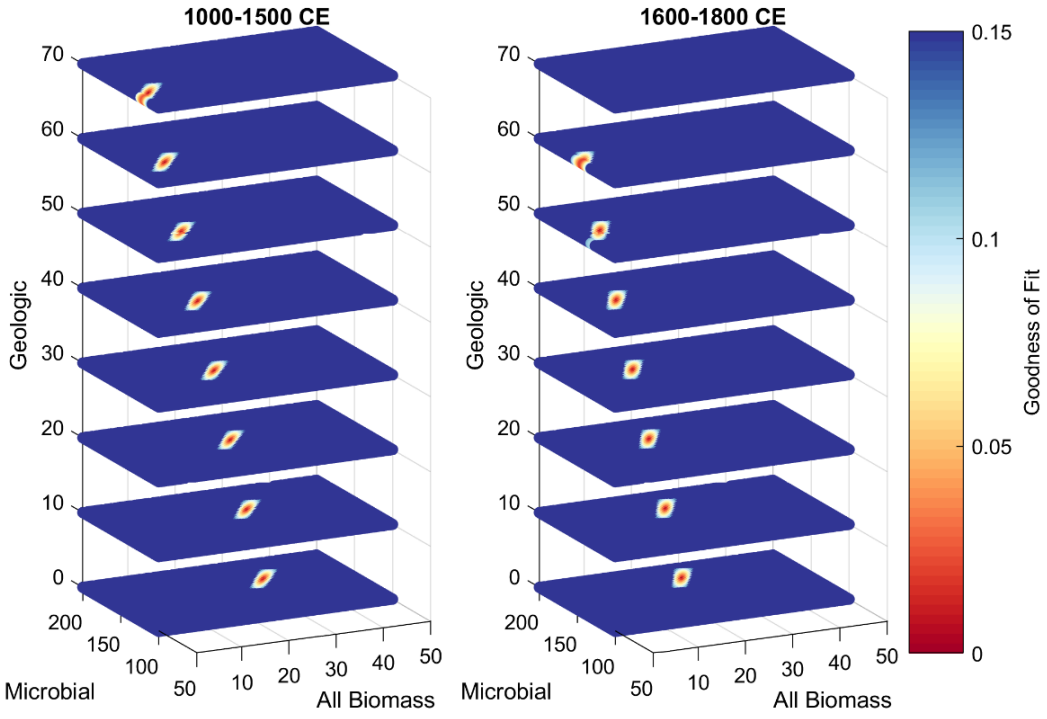

Figure 6.1: Modeled methane emission scenarios assuming a 5% Cl sink for the MP (left) and LIA (right). Contours are of goodness of fit with a value of 0 corresponding to a perfect fit to the mean of the ice core records. Emissions are in Tg methane y^{-1}.

Overall, there are two main differences between the preindustrial methane budgets with a 0% and 5% Cl sink. First, the 0% Cl sink methane budget allows for more geologic methane emissions (60+ Tg y^{-1} versus 50 Tg y^{-1}). Second, biomass burning emissions in the 0% Cl sink case must be greater than the 5% Cl sink case at the same geologic source strength (ex: 32.6 Tg y^{-1} versus 21.6 Tg y^{-1}). This is due to the strong kinetic isotope effect of the Cl sink which leads to an enrichment of the heavier isotope (^{13}C) in the atmosphere and requires more emissions from lighter (more ^{12}C) sources such as biomass burning (*Lassey et al*., 2007).

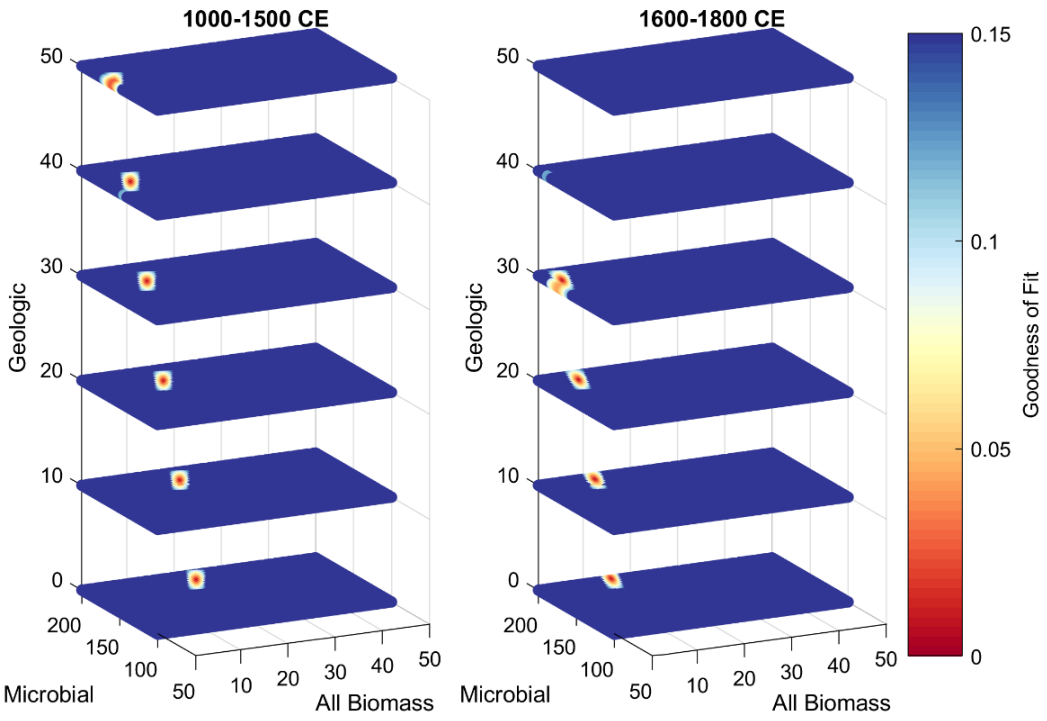

Figure 6.2: Modeled methane emission scenarios assuming a 0% Cl sink for the MP (left) and LIA (right). Contours are of goodness of fit with a value of 0 corresponding to a perfect fit to the mean of the ice core records. Emissions are in Tg methane y^{-1}.

6.3 Impact of atmospheric oxidative changes on the preindustrial budgets

All three of the ice core gas records (ethane, acetylene, and methane) indicate large changes have occurred in their atmospheric budgets over the last 1,000 years. We assume these

changes were driven by emissions rather than by changes in their lifetimes caused by variability in the oxidative capacity of the atmosphere. This assumption is based on recent work from an Atmospheric Chemistry and Climate Model Intercomparison Project (ACCMIP) which compared 17 chemistry/climate models and showed a multi-model mean change in the atmospheric methane lifetime from preindustrial (1850 CE) to modern (2000 CE) of $\tau_{modern}/\tau_{1850}$ = 2.0 ± 8.8% (*Naik et al*., 2013). The models were split between positive and negative changes in methane lifetime. In other words, the current chemistry/climate models disagree on the magnitude and sign of the change, but there is strong consensus that the change in methane lifetime from the preindustrial to modern was less than ± 10%. This change is influenced by several competing factors: 1) increased CH_4, which has the net effect of suppressing OH, 2) increased CO and NOx, which increase tropospheric ozone, the primary source of OH, 3) loss of stratospheric ozone resulting in increased ultraviolet radiation, and 4) increased global temperature, which increases water vapor (and OH production) but also increases rate constants, including that for reaction of OH with ethane. *Naik et al*. (2013) suggest that, of these four factors, the differences in CO and NOx variability/chemistry appear to contribute most to the OH variance between model simulations from preindustrial to modern.

The ice core ethane, acetylene, and methane records show significant variability over the 1000-1900 CE time period. Atmospheric impacts of industrialization start to become apparent after 1850 CE, with the bulk of the changes occurring during the 20th century. Prior to 1850 CE, atmospheric methane was relatively stable in the 650-800 ppb range and global temperature variations were about 0.5°C, less than half of the >1°C rise that followed (*PAGES 2k Consortium*, 2013). Preindustrial changes in NOx were likely also small based on the < 20% variability in Greenland ice core nitrate prior to 1850 CE, as compared to the near doubling since

1850 CE *(Fischer et al.,* 1998). Ice core data suggests that preindustrial CO variability was comparable to or less than the CO change during industrialization (*Wang et al.*, 2010; *Hann et al*., 1998). Based on the ice core CO stable isotope measurements, *Wang et al*. (2010) suggest that most of the preindustrial CO variability was driven by changes in emissions rather than OH. There is no evidence to suggest that OH variability in the preindustrial atmosphere was larger than the 10% upper limit suggested for the preindustrial to modern change. Therefore, we assume that ice core ethane, acetylene, and methane variability is primarily driven by changes in emissions rather than atmospheric reactivity.

6.4 Biomass burning histories from ethane, acetylene and methane

Four biomass burning emission scenarios have been inferred for ethane and methane based on assumptions of the magnitude of the Cl sink and geologic emissions (Table 6.1 and Table 6.2). For simplicity, they are identified as:

1) **noGEO-noCl**: emission scenario with zero geologic emissions and zero Cl sink

2) **noGEO-highCl:** emission scenario with zero geologic emissions and a high Cl sink (5% for methane and 60% for ethane)

3) **lowGEO-noCl**: emission scenario with low geologic emissions (2 Tg y^{-1} for ethane and 20 Tg y^{-1} for methane) and a zero Cl sink

4) **lowGEO-highCl**: emission scenario with low geologic emissions and a high Cl sink

The biomass burning emission histories from ethane and methane from each of these scenarios are compared with the non-boreal vs. boreal biomass burning scenario for acetylene. The acetylene atmospheric budget is not complicated by a Cl sink or geologic sources. Therefore, for

every scenario (1-4) discussed, the inferred acetylene biomass burning emission history is identical.

There are similarities in the biomass burning emissions of ethane, acetylene, and methane over the last 1,000 years. All three gas records show a large decline in biomass burning emissions from the MP to the LIA. However, the magnitude of the decline differs between the gases. For acetylene, the decline in biomass burning emissions from the MP to LIA is 43% with all the decline being driven by a decrease in non-boreal (tropical) emissions. For ethane and methane, the magnitude of the decline depends on what is assumed for the Cl sink strength and geologic emissions (Tables 6.1 and 6.2). With the noGEO-noCl scenario, the decline in biomass burning ethane from the MP to LIA is 23% and for methane is 20%. With the noGEO-highCl scenario, the decline in biomass burning ethane is 23% and for methane is 31%. With the lowGEO-noCl scenario, the decline is 37% for ethane and 26% for methane. Finally, with the lowGEO-highCl scenario, the decline in biomass burning ethane is 31% and for methane is 53%. Interestingly, the scenarios for ethane and methane which yield a similar percent decline that is observed in the acetylene scenario are not the same scenario (scenario 3 for ethane and scenario 4 for methane).

Comparing the preindustrial biomass burning emission histories with their modern-day biomass burning estimates requires the introduction of emission factors. Emission factors are defined as the amount of a compound released per amount of a dry fuel (matter) consumed/burned and are expressed in units of g kg^{-1} (*Andreae and Merlet*, 2001). Satellite-based climatological estimates of dry matter burned are available from the Global Fire Emissions Database (GFED4.1, globalfiredata.org, *van der Werf et al.*, 2017). Emission factors for ethane, acetylene, and methane from different fuel types are used to covert the dry matter burned

estimates from the GFED4.1 inventory into an estimate of the modern-day biomass burning emissions of each of these gases (*Akagi et al.*, 2011, *Andreae and Merlet*, 2001 and updates via personal communication). These emission factors are based on compilations of field measurements and laboratory experiments. Globally-weighted emission factors for each gas were calculated by multiplying the Global Fire Emissions Database version 4.1 (GFED4.1) 1997-2017 dry matter burned (kg y^{-1}) climatological estimate with the biome-specific emission factor for each gas (Table 6.3). The modern biomass burning emissions for ethane, acetylene, and methane from this approach are 2.5 ± 0.5 Tg y^{-1}, 1.4 ± 0.2 Tg y^{-1}, and 16.1 ± 0.7 Tg y^{-1}, respectively.

There are some distinct differences in the trends in biomass burning emissions between the LIA and modern (satellite-era) between the three gases (Figure 6.3). In all four scenarios, the acetylene emission history is identical and as such, the trends between LIA and modern for acetylene are only discussed for the first scenario but are true for all scenarios.

1) **noGEO-noCl**: In this scenario, all three gases suggest LIA burning rates were greater than modern. The methane record suggests that biomass burning emissions declined substantially from the LIA to modern. LIA methane burning emissions are about 60% higher than the modern methane biomass burning rate. The acetylene record also indicates LIA rates greater than modern, with LIA burning rates nearly two-times the best-estimate for modern biomass burning acetylene emissions. The ethane LIA burning emissions are roughly 60% higher than the modern ethane biomass burning rate.

2) **noGEO-highCl**: In this scenario, the methane record indicates that biomass burning emissions during the LIA were comparable to or slightly less than modern day biomass burning methane emissions (roughly 10%). The ethane record suggests LIA biomass burning rates were roughly 2.5-times higher than the modern ethane burning rate.

Table 6.1: Modeled methane emissions for the scenarios of geologic emissions and Cl sink strength. All emissions are in Tg methane y^{-1}. The reported percent changes are calculated as (MP−LIA)/MP.

			Methane emissions					
			MP		LIA			
Scenario	Geologic	Cl sink	Biomass burning	Microbial	Biomass burning	Microbial	Change in burning (%)	Change in microbial (%)
1	zero	zero	32.6 ± 2.5	161.2 ± 10.0	26.1 ± 2.0	171.9 ± 9.6	-20	7
2	zero	high	21.6 ± 1.8	180.8 ± 10.1	14.8 ± 1.5	192.9 ± 11.7	-31	7
3	low	zero	23.5 ± 2.5	149.2 ± 9.5	17.5 ± 2.3	160.0 ± 10.2	-26	7
4	low	high	13.1 ± 1.9	182.1 ± 11.1	6.1 ± 1.5	182.1 ± 11.1	-53	7

Table 6.2: Modeled ethane emissions for the scenarios of geologic emissions and Cl sink strength. All emissions are in Tg ethane y^{-1}. The reported percent changes are calculated as (MP−LIA)/MP.

			Ethane emissions				
			MP		LIA		
Scenario	Geologic	Cl sink	Non-boreal	Boreal	Non-boreal	Boreal	Change in total burning (%)
1	zero	zero	3.22 ± 0.22	1.90 ± 0.14	2.07 ± 0.15	1.87 ± 0.14	-23
2	zero	high	5.83 ± 0.36	2.47 ± 0.18	3.92 ± 0.25	2.43 ± 0.17	-23
3	low	zero	2.04 ± 0.22	1.19 ± 0.14	0.89 ± 0.15	1.16 ± 0.13	-37
4	low	high	4.62 ± 0.36	1.76 ± 0.18	2.71 ± 0.25	1.71 ± 0.17	-31

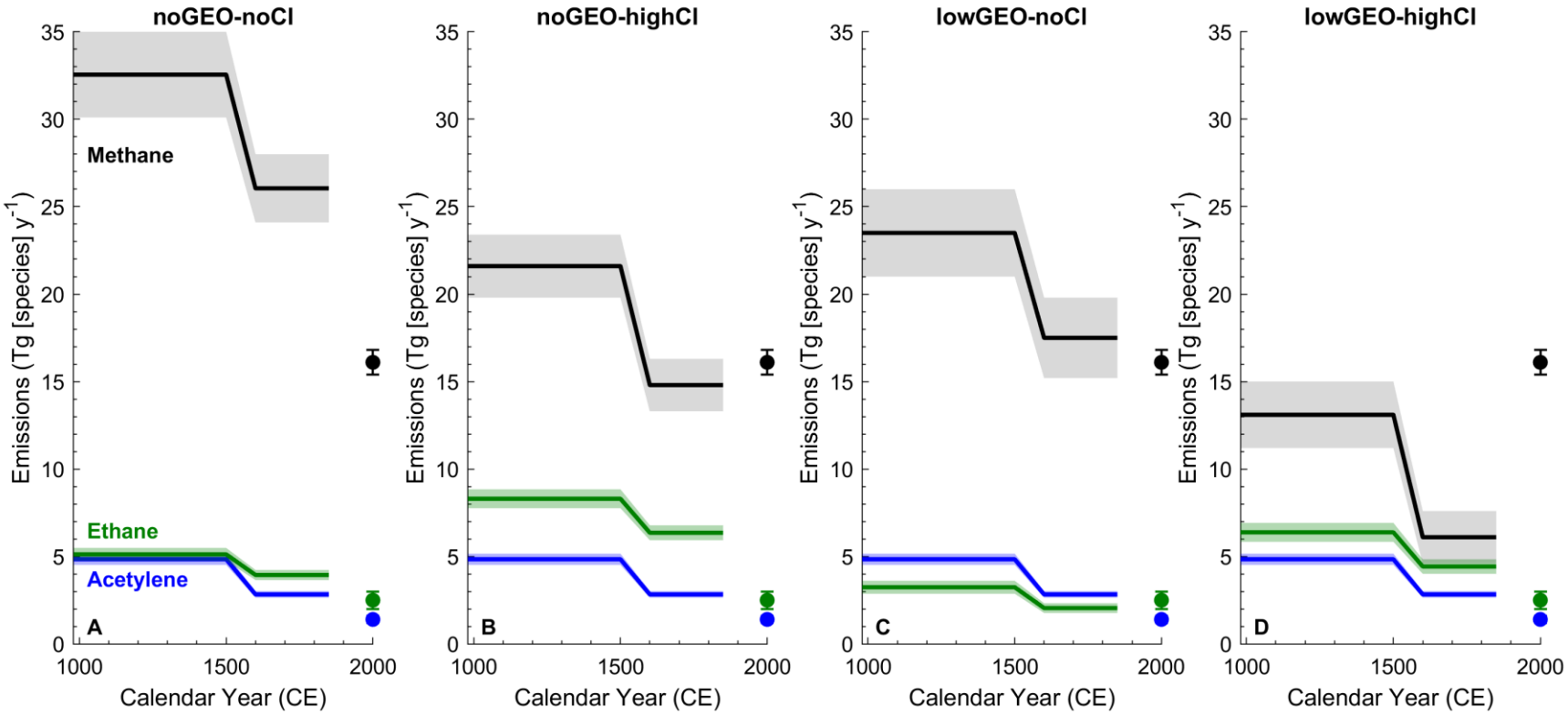

Figure 6.3: Biomass burning emission scenarios for the ethane (green), acetylene (blue), and methane (black). Scenarios 1 to 4 are the same as described in Table 6.1 and Table 6.2. Acetylene emission history is identical in all four scenarios. Shaded regions reflect the ±1σ uncertainty on the mean value (solid line). Solid dots are the 1997-2017 average biomass burning emission estimate for each gas calculated by multiplying the GFED4 dry matter emissions (*Giglio et al.*, 2013; *van der Werf et al.*, 2017; globalfiredata.org) by the emission factors in Tables 6.3-6.5.

3) **lowGEO-noCl**: In this scenario, LIA methane burning rates are slightly greater than or comparable to modern day. The mean LIA methane burning rate is roughly 10% greater than modern, but given the uncertainties on the LIA emissions rate, the modern and LIA values are statistically similar. The LIA ethane burning emissions are about 20% less than modern day but are comparable to the modern ethane burning estimate given the uncertainties on the modern and LIA estimates.

4) **lowGEO-highCl**: Methane LIA burning rates in this scenario are roughly 65% lower than the modern methane biomass burning emission estimate. Ethane LIA burning rates are 70% higher than the modern ethane biomass burning rate.

There are similarities between the MP and modern biomass burning rates for ethane, acetylene and methane amongst the four scenarios. Two out of the four scenarios indicate MP biomass burning emissions for all three gases exceeded their modern rates. The remaining two scenarios indicate MP biomass burning emissions for two of the gases exceed their modern rates. In all scenarios, MP biomass burning emissions of acetylene are much higher than the modern acetylene biomass burning emissions estimate. The magnitude of the differences between MP burning emissions and modern emissions vary between the scenarios and those differences are described below.

1) **noGEO-noCl**: Methane MP burning emissions are slightly more than two-times modern methane burning rates. Ethane MP burning emissions are about 1.5-times modern ethane biomass burning emissions. Acetylene MP burning emissions are identical in all four scenarios with a rate roughly four-times the modern estimate. All three gases indicate MP biomass burning emissions were significantly higher than modern day.

2) **noGEO-highCl**: The MP methane burning rate is roughly 40% greater than the modern methane emission burning estimate. Ethane MP burning emissions are roughly 2.5-times higher than modern ethane burning emissions. Acetylene MP burning emissions are identical to the first scenario at roughly four-times modern rates. All three gas records suggest MP burning emission greater than modern rates.

3) **lowGEO-noCl:** The methane MP burning emission rate is about 1.5-times modern methane burning emissions in this scenario. Acetylene MP emissions are four-times modern rates. On the contrary, the ethane MP burning emissions are comparable to the modern ethane burning emission estimate. All three gases suggest MP burning rates were comparable to or higher than modern rates.

4) **lowGEO-highCl**: In this scenario, the MP methane burning emissions are less than the modern estimate. The mean MP rate is about 15% less than the modern estimate. The ethane MP emission rate is roughly 2.5-times greater than modern. This is the only scenario in which methane MP burning emissions are less than modern.

6.4 Is there a single preindustrial fire history?

Ideally, the three independent trace gas biomass burning histories inferred from the ice core records should record a single fire history. To determine if this is true, the emission histories from the three gases were converted to a common factor, dry matter burned. For ethane and acetylene conversion to dry matter burned was accomplished by multiplying the biome-specific emissions (boreal and non-boreal) by weighted emission factors (g species/ kg dry matter burned) (see Tables 6.4 and 6.5). The emission histories from methane were converted to dry matter by multiplying the emission histories by a globally-weightedemission factor since boreal

Table 6.3: Dry matter burned emissions for different biomes from the GFED4 database (1997-2017 climatology, *Giglio et al.*, 2013; *van der Werf et al.*, 2017) and biome-specific emission factors used for each compound to calculate a globally-weighted average emission factor and uncertainty. Emission factors are from the updated *Andreae and Merlet* (2001) compilation (*A. Andreae personal communication*)

	DM (kg/yr)	% of total	Ethane EF (g/kg)	Ethane EF unc[1] (g/kg)	Acetylene EF (g/kg)	Acetylene EF unc (g/kg)	Methane EF (g/kg)	Methane EF unc (g/kg)
Agriculture	2.62×10^{11}	11	0.70	0.15	0.31	0.08	5.70	1.45
Boreal	3.79×10^{11}	9	0.98	0.11	0.30	0.04	5.50	0.56
Deforestation	5.86×10^{11}	13	0.94	0.11	0.43	0.24	6.30	0.52
Peat	9.85×10^{10}	2	1.85	0.18	0.11	0.03	9.30	0.67
Savanna	2.92×10^{12}	67	0.40	0.06	0.32	0.05	2.50	0.14
Temperate	1.02×10^{11}	2	0.71	0.13	0.32	0.02	5.80	1.01
Total	**4.34×10^{12}**	100						
Globally-weighted EF			***0.58***	***0.12***	***0.33***	***0.05***	***3.70***	***0.16***

[1] Uncertainties (unc) are standard errors: SE = σ/√number of studies

and non-boreal emissions are not delineated for methane (Table 6.3). The results for each scenario are shown in Figure 6.4 and Table 6.6

As expected, the inferred dry matter histories from ethane, acetylene, and methane all show a large decline from the MP to the LIA. The magnitude of the decline for ethane and methane are different between each scenario and are described below.

1) **noGEO-noCl:** The dry matter decline inferred from methane between the MP to LIA is 20%. The decline from the MP to LIA inferred from ethane is 27%. For acetylene, the decline is 40% and is identical in all scenarios.

2) **noGEO-highCl:** The dry matter decline between the MP and LIA from methane is 31% and from ethane is 26%.

3) **lowGEO-noCl:** The dry matter decline between the MP and LIA from methane is 25% and from ethane is 43%.

4) **lowGEO-highCl**: The dry matter decline between the MP and LIA from methane is 53% and from ethane is 34%.

The inferred dry matter burned histories from the three gases suggest large changes to the dry matter burned amounts from the LIA to the modern. The modern dry matter burned is about 4.3 Pg C y^{-1} (GFED4.1, *Giglio et al.*, 2013; *van der Werf et al.*, 2017). The similarities and differences between the LIA and modern dry matter burned rates inferred from the three gases are described below for each scenario.

1) **noGEO-noCl**: In this scenario, all three gases suggest dry matter burned rates were greater than modern during the LIA. For methane, the dry matter burned during the LIA is roughly 65%

higher than modern. For ethane, the dry matter burned is about 35% greater than modern during the LIA. The inferred dry matter burned from acetylene during the LIA is nearly a factor of 2 greater than the modern rate.

2) **noGEO-highCl**: In this scenario, ethane and acetylene suggest dry matter burnined rates were greater than modern rates during the LIA. The ethane and acetylene dry matter burned rates during the LIA are similar within uncertainties. Methane suggests dry matter burned during the LIA was comparable to or slightly less than modern. Ethane dry matter burned during the LIA is roughly a factor of 2.3 larger than the modern dry matter burned estimate.

3) **lowGEO-noCl:** Methane dry matter burned during the LIA is comparable to or slightly greater than the modern-day dry matter burned estimate. Ethane LIA dry matter burned is roughly 35% lower than the modern rate.

4) **lowGEO-highCl**: Ethane and acetylene dry matter burned during the LIA issignificantly higher than modern dry matter burned in this scenario. Methane dry matter burned during the LIA is much lower than the modern estimate. The LIA ethane dry matter burned is roughly 60% higher than the modern rate. The LIA methane dray matter burned is about one-third of the modern dry matter burned rate.

There are many similarities between the relative dry matter burned rates during the MP amongst the four scenarios. In three of the four scenarios, all three inferred dry matter histories suggest MP dry matter burned rates were higher than, or comparable to the modern-day rate from GFED4.1. In the final scenario, two of the three inferred dry matter histories indicate that MP dry matter burned rates were significantly higher than modern rates. However, the magnitude of

change in dry matter burned rates from the MP to modern between the three gases vary within in the same scenarios. The similarities and differences are highlighted below.

1) **noGEO-noCl**: In this scenario, dry matter burned rates during the MP inferred from ethane and methane are similar within their uncertainties, but that of acetylene is nearly a factor of two greater. The ethane and methane dry matter burned rates during the MP are roughly double the modern dry matter burned rate. Acetylene MP dry matter burned is a factor of 3.5 greater than the modern dry matter burned rate. All three gases suggest MP dry matter burned is greater than modern.

2) **noGEO-highCl**: In this scenario, dry matter burned rates during the MP inferred from ethane and acetylene agree within their uncertainties, but that of methane is nearly a factor of 2.5 less. Ethane dry matter during the MP is about three times the modern dry matter burned rate. The methane MP dry matter burned is roughly 40% greater than the modern rate. All three gases suggest MP dry matter burned is greater than the modern rate.

3) **lowGEO-noCl**: Ethane and methane MP dry matter burned rates agree within uncertainties. The methane MP dry matter rate is about 25% greater than the ethane MP dry matter rate and roughly 45% greater than the modern dry matter burned estimate. The ethane MP dry matter burned is slightly greater than, but comparable within uncertainties to the modern-day dry matter burned rate. All three gas records indicate MP dry matter burned is higher than or comparable to the modern rate.

4) **lowGEO-highCl**: The ethane and acetylene MP dry matter burned rates are greater than the modern rate while the methane dry matter burned during the MP is slightly less than, but comparable within uncertainties to the modern dry matter burned estimate. The ethane dry matter

burned rate during the MP is more than a factor of two greater than modern. The methane MP dry matter burned is about 20% lower than the modern estimate, but within the uncertainties is comparable to the modern dry matter burned rate.

6.5 Conclusions

Overall, the dry matter burned histories inferred from the three gases indicate biomass burning emissions declined substantially from the MP to the LIA. Almost all scenarios explored suggest MP dry matter burned rates were greater than, or at least comparable to modern dry matter burned. However, there are some major discrepancies between the dry matter burned histories inferred from the three gases, and none of the scenarios explored (1-4) provides a consistent history of dry matter burned for the last 1,000 years. Factors which may explain the discrepancies observed between the three gas records are explored in Chapter 7.

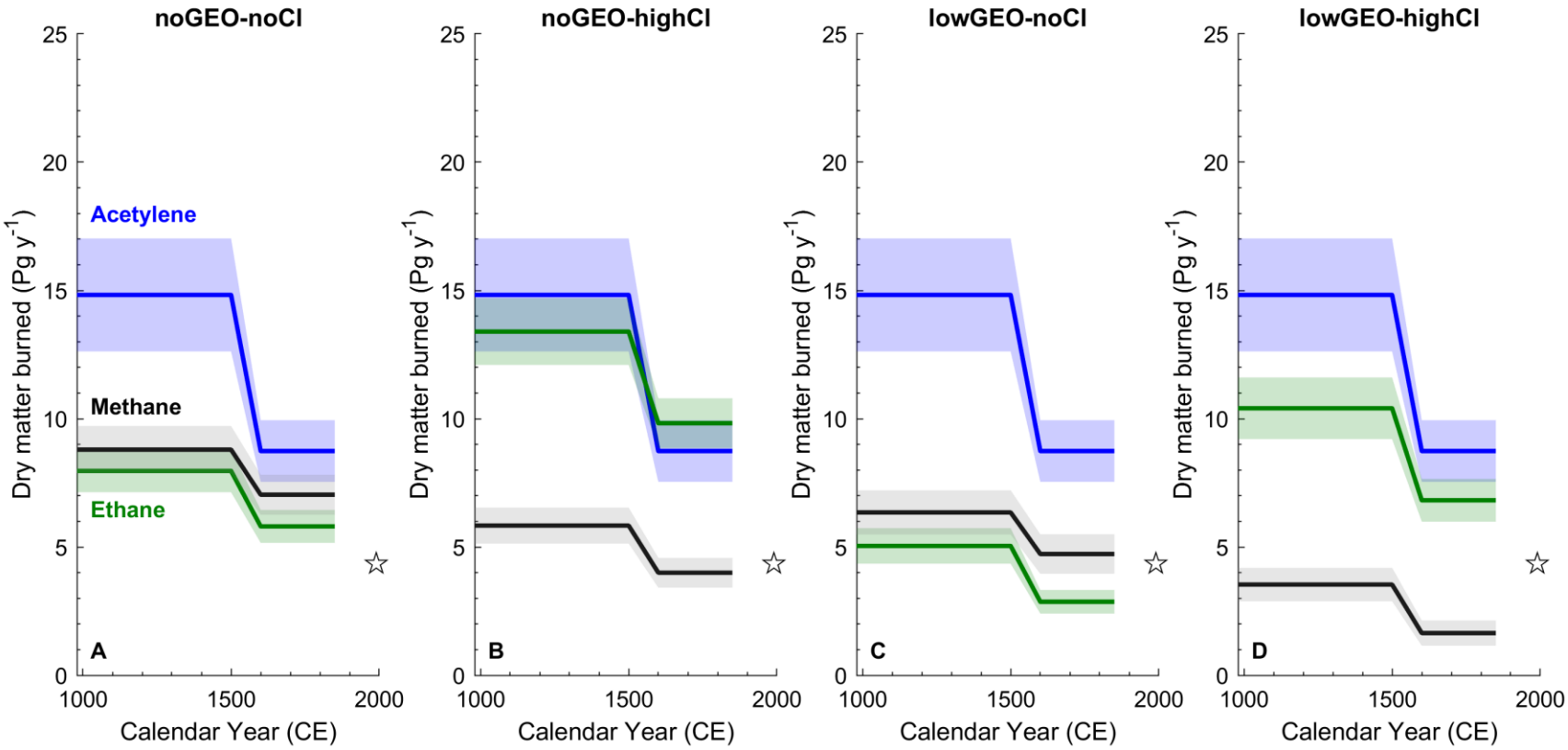

Figure 6.4: Dry matter burned (Pg C y^{-1}) inferred from acetylene (blue), ethane (green), and methane (black) ice core data after applying weighted emission factors (Tables 6.3-6.5) to the emission histories of each gas from each scenario. Shaded areas reflect the ±1σ uncertainty by propagating the errors on the emissions and emission factors. The black star is the GFED4 1997-2017 climatology dry matter burned estimate (4.3 Pg C y^{-1}, *Giglio et al.*, 2013; *van der Werf et al.*, 2017; globalfiredata.org)

Table 6.4: Boreal (>50°N) dry matter emissions (kg y^{-1}) from the GFED4 inventory and the resulting regionally-weighted emission factors (g kg^{-1}) and their uncertainties (unc.) for ethane and acetylene

Biome	DM (kg y^{-1})	% of total	Ethane EF (g kg^{-1})	Ethane EF unc. (g kg^{-1})	Acetylene EF (g kg^{-1})	Acetylene EF unc. (g kg^{-1})
Agriculture	5.11×10^{10}	11	0.15	0.31	0.08	5.70
Boreal	3.55×10^{11}	80	0.11	0.30	0.04	5.50
Deforestation	0	0	0.11	0.43	0.24	6.30
Peat	1.43×10^{10}	3	0.18	0.11	0.03	9.30
Savanna	1.52×10^{10}	3	0.06	0.32	0.05	2.50
Temperate	1.04×10^{10}	2	0.13	0.32	0.02	5.80
Total	**4.46×10^{11}**	100	**0.95**	**0.09**	**0.30**	**0.03**

Table 6.5: Non-boreal (50°N-90°S) dry matter emissions (kg y^{-1}) from the GFED4 inventory and the resulting regionally-weighted emission factors (g kg^{-1}) and their uncertainties (unc.) for ethane and acetylene

Biome	DM (kg y^{-1})	% of total	Ethane EF (g kg^{-1})	Ethane EF unc (g kg^{-1})	Acetylene EF (g kg^{-1})	Acetylene EF unc (g kg^{-1})
Agriculture	2.10×10^{10}	5	0.15	0.31	0.08	5.70
Boreal	2.41×10^{10}	1	0.11	0.30	0.04	5.50
Deforestation	5.86×10^{11}	15	0.11	0.43	0.24	6.30
Peat	8.42×10^{10}	2	0.18	0.11	0.03	9.30
Savanna	2.90×10^{12}	74	0.06	0.32	0.05	2.50
Temperate	9.18×10^{10}	2	0.13	0.32	0.02	5.80
Total	**3.90×10^{12}**	100	**0.54**	**0.05**	**0.33**	**0.05**

Table 6.6: Dry matter burned (Pg C y^{-1}) inferred from the three ice core gas records.

	Acetylene		*Ethane*		*Methane*	
Scenario	**MP**	**LIA**	**MP**	**LIA**	**MP**	**LIA**
noGEO-noCl	14.82 ± 2.20	8.74 ± 1.20	7.97 ± 0.83	5.81 ± 0.64	8.80 ± 0.98	7.04 ± 0.78
noGEO-highCl	14.82 ± 2.20	8.74 ± 1.20	13.40 ± 1.30	9.83 ± 0.97	5.84 ± 0.70	4.00 ± 0.58
lowGEO-noCl	14.82 ± 2.20	8.74 ± 1.20	5.04 ± 0.69	2.87 ± 0.46	6.35 ± 0.86	4.73 ± 0.77
lowGEO-highCl	14.82 ± 2.20	8.74 ± 1.20	10.41 ± 1.20	6.82 ± 0.83	3.54 ± 0.65	1.65 ± 0.49

CHAPTER 7

Conclusions

7.1 Overview

This thesis advanced our understanding of paleo-fire emissions and their variability through time by using ice core ethane and acetylene as new biomass burning emission proxies. Understanding and quantifying the climatic controls and feedback on fire emissions is important for constraining fire models and future projections of climate change (*Hantson et al*., 2016). In addition, quantifying preindustrial fire emissions will provide new insights and constraints on the variability observed in the ice core methane record. The goals of this thesis were to 1) develop an analytical technique to measure ethane and acetylene in polar ice cores with low and stable analytical background levels, 2) use the ice core results to interpret preindustrial biomass burning emissions using atmospheric models, and 3) develop a global fire history that can be used to better understand the contribution of fire to the preindustrial methane budget. Goals 1 and 2 were accomplished (*Nicewonger et al.*, 2016; 2018). Goal 3 has proven to be more challenging because there are significant differences between the fire histories inferred from ethane, acetylene, and methane ice core measurements.

The goal of this chapter is to briefly summarize the main findings of this project and to explore various hypotheses to account for the observed differences between the fire histories inferred from ice core ethane, acetylene, and methane. Implications for modeling past and future fire and areas of future research are also discussed.

7.2 Biomass burning trends

This study showed consistency in the temporal trends in the ethane, acetylene, and methane biomass burning emission histories. The Antarctic data show that both ethane and acetylene were elevated during the warm Medieval Period (1000-1500 CE) and declined concurrently with the onset of the cooler Little Ice Age (1600-1800 CE). Using a chemical transport model, biomass burning emissions were inferred from the ice core ethane and acetylene data. The inferred trends in the ice core ethane and acetylene biomass burning emissions are consistent with prior interpretations of ice core $\delta^{13}CH_4$ data (*Ferretti et al*., 2005; *Mischler et al.*, 2009).

Ethane and acetylene in Greenland ice exhibit little change between the MP and LIA. The different trends between the Greenland and Antarctic acetylene and ethane levels provides a new constraint on the location of the biomass burning changes. The decline in biomass burning emissions from the Medieval Period to Little Ice Age was mainly in the non-boreal (tropical) biome and indicates the Little Ice Age influenced climate conditions globally and was not a regional phenomenon restricted to the extratropical Northern Hemisphere (*Mann et al*., 2009). The driver of the decline in biomass burning emissions into the Little Ice Age may be due to climate changes, the catastrophic decline in indigenous populations who used fires caused by European exploration in the Americas, or potentially a combination of both (*Ferretti et al*., 2005; *Koch et al.*, 2019). Unfortunately, the ice core ethane and acetylene records are unable to provide additional constraints on the drivers of the biomass burning decline during this time period.

7.3 Do the ethane, acetylene, and methane records indicate a single fire history?

The main finding of this thesis work is that the ethane, acetylene, and methane ice core records do not easily reconstruct a single fire history during the last 1,000 years. Although the temporal trends are similar, there are differences in the magnitude of dry matter burned inferred from the three gas records. These differences may be caused by assumptions made in the interpretations of biomass burning emissions for each gas and the subsequent translation into dry matter burned. Here the uncertainties are discussed and a few hypotheses which may resolve the differences between the three records are explored.

Atmospheric transport in this study was assumed to be identical to modern and constant through time. If atmospheric transport was significantly different in the preindustrial than in the modern, the sensitivities used to generate emission histories for ethane and acetylene would be impacted. Climate proxies from South America suggest that during the last 1,000 years, notable shifts occurred in the location of the Intertropical Convergence Zone (ITCZ). It is hypothesized that the ITCZ shifted southward during the Little Ice Age (*Haug et al*., 2001; *Sachs et al*., 2009) which led to an enhanced South American summer monsoon (*Vuille et al*., 2012). Speleothem $\delta^{18}O$ from multiple locations in South America all record a strengthening of the South American monsoon intensity during the Little Ice Age (*Vuille et al.*, 2012). In general, an increased South American monsoon would lead to wetter conditions which would not be suitable for biomass burning. A decline in biomass burning during the Little Ice Age agrees with the biomass burning emission histories inferred from ethane, acetylene, and methane. Changes in the location of the ITCZ and the intensity of the South American summer monsoon are not accounted for in our chemistry transport model simulations. Therefore, the sensitivities used to calculate ethane and acetylene biomass burning emission histories do not account for changes in transport which may

result from variability in the ITCZ location. One could envision that shifting the ITCZ north or south would impact not only the location of fires, but how efficiently ethane and acetylene are transported to the polar regions. As such, the emission histories inferred from ethane and acetylene in this study would be impacted. Because methane has a much longer lifetime than ethane or acetylene, changes in transport on this scale would not impact methane levels at the poles. Future work should determine how the location of the ITCZ and the variability in other circulation patterns such as the South American monsoon would impact the levels of ethane and acetylene over Antarctica and Greenland and ultimately the inferred biomass burning emission histories presented here.

This study also assumed that geographic distribution of ecosystems (biomes) was identical to the modern and did not change through time. This is important because the emission factors applied to the biomass burning histories from each gas are dependent on the type of biomass burned. If the distribution of ecosystems in the preindustrial were significantly different from today, then the inferred biomass burning histories from this study would not be valid. Pollen records in Meso- and South America during the last 2,000 years show the succession from forests to savanna likely driven by human activities (*Flantua et al*., 2016). Additional changes in vegetation in these regions are observed in the pollen records after the catastrophic depopulation which occurred in these regions following European contact in the mid to late 14th century (*Koch et al.*, 2019 and references within). Similar pollen studies in New Zealand also show shifts in vegetation due to human activities (*Elliot et al.*, 1998). An individual pollen analysis is regional at best. An extensive synthesis would be required to generate a comprehensive hemispheric or global record of vegetation shifts from pollen records. We did not account for shifts in vegetation patterns or the impact these shifts would have on the inferred biomass burning scenarios for the

three gases. Future work should attempt to address how shifting vegetation patterns would impact the inferred ethane and acetylene biomass burning histories.

The magnitude and geographic distribution of biofuel emissions is uncertain. The biofuel distribution used to reconstruct the biomass burning histories was based on the modern-day distribution of biofuel use and may not reflect the location of biofuel use in the preindustrial world (*Yevich and Logan*, 2003). A recent analysis by *Koch et al*. (2019) illustrated that the biofuel source, both magnitude and location, may have changed during the last 600 years due to large population declines in the 14^{th} to 15^{th} centuries. The work presented in this thesis did not allow the magnitude or the location of biofuel emissions to vary through time. If biofuel emissions were centered more in the tropics, as suggested by the interpretations of *Koch et al.* (2019), then the impact of these emissions on the ethane and acetylene levels over Antarctica would be underestimated in this study. Higher biofuel emissions would require the total biomass burning emissions to be lower, especially for acetylene which is highly sensitive to emissions in South America. Future work should investigate the impact of the location and variability of biofuel emissions on the inferred biomass burning histories from ethane and acetylene.

This study assumed the methane source isotopic end-members were constant through time. There is evidence to suggest this may not be true over the last 2,000 years based on vegetation shifts recorded in pollen records (*Flauntua et al.*, 2016 and references within). The methane isotope end-members from biomass burning emissions are heavily dependent on the type of vegetation which is burned, in particular C_3 versus C_4 plants. The $\delta^{13}C$ of C_3 vegetation is roughly -25‰ and the $\delta^{13}C$ of C_4 vegetation is about -12‰ (*Farquhar et al*., 1989; *Quay et al*., 1999; *Ferretti et al.*, 2005).

If large changes in the C_3/C_4 ratio occurred during the last 1,000 years, the impact on the $\delta^{13}CH_4$ budget was not captured with our analysis because the isotopic end-members were held constant through time. The potential impact of the $\delta^{13}C$ end-members on the methane budget was explored by varying the $\delta^{13}C$ value for the biogenic and biomass burning methane sources across the range of their best-estimates. To increase biomass burning methane emissions, both the biogenic and biomass burning $\delta^{13}C$ signatures must become heavier (more negative). If biomass burning $\delta^{13}CH_4$ is -25‰ and biogenic $\delta^{13}CH_4$ is -65‰, the inferred dry matter burned from methane is nearly doubled, thus reducing the difference observed between the ethane and acetylene records (Figure 7.1). With this scenario, the Little Ice Age dry matter burned history from methane agrees with that from ethane and acetylene. The methane dry matter burned is still about 30% lower than that inferred from ethane and acetylene during the Medieval Period.

Changing the methane isotopic end-members does not fully reconcile the differences between the ethane, acetylene, and methane dry matter burned histories. It is plausible that the methane isotope end-members are dynamic and change through time, particularly due to ecosystem shifts and changes in the C_3/C_4 ratio. The complicated nature of the methane isotope budget makes interpreting paleo-biomass burning emissions challenging. We are unable to fully address all the complexities of the methane budget in this study. Future work should focus on better quantifying the methane source isotopic end-members, their potential variability through time, and the impact this would have on the biomass burning component of the methane budget.

The magnitude and location of geologic emissions of acetylene is a factor which was not fully explored in this thesis. There is theoretical evidence to suggest that geologic emissions of acetylene occur through the partial combustion of methane in geologic plumes. There is little data to quantify the magnitude of the acetylene emissions from this source (*Gunther and*

Musgrave, 1971; *G. Etiope*, personal communication). A geologic source of acetylene would reduce some of the biomass burning emissions required to reproduce the ice core levels. Future would should attempt to quantify the magnitude of this potential acetylene source and the impact it would have on the inferred biomass burning histories presented in this thesis.

In summary, there are several factors which we are unable to fully constrain, and this may have led to some of the differences observed in the inferred dry matter histories from ethane, acetylene, and methane. Because of these complexities and uncertainties, we cannot completely rule out that the ethane, acetylene, and methane emission histories are incompatible with a single fire history. Future work should focus on reconciling the ice core ethane, acetylene, and methane biomass burning records by investigating the hypotheses outlined above.

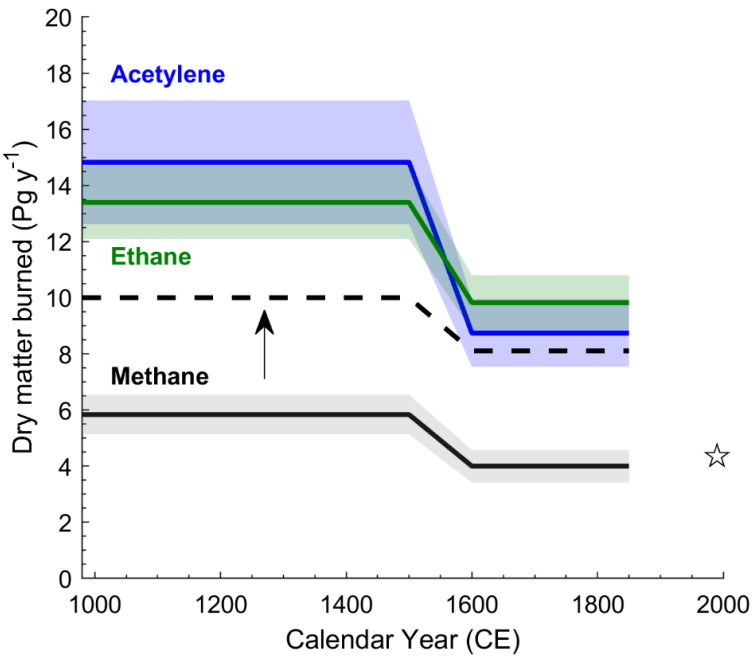

Figure 7.1: Inferred dry matter burned from scenario 2 (solid lines, Chapter 6) and dry matter burned from methane (black dashed) that results from changing the $\delta^{13}C$ end-members of biogenic and biomass burning methane sources. $\delta^{13}CH_4$ for biomass burning methane is -25‰ and for biogenic methane is -65‰ (*Farquhar et al.*, 1989; *Quay et al.*, 1999; *Ferretti et al.*, 2005).

7.4 Modeling past and future fire

There is debate about whether fire emissions today are greater than or less than the preindustrial period. Paleo-evidence from charcoal records and ice core gas measurements of CO suggest preindustrial fire occurrence or emissions may have exceeded modern rates (*Marlon et al*., 2008; *Wang et al*., 2010). On first order, it is thought that humans have increased fire activity and emissions through ignitions and deforestation practices (*Bowman et al.*, 2009; *Aragão and Shimabukuro*, 2010). This logic is applied to most global fire models which scale fire emissions positively with human population density (*Hantson et al.*, 2016). However, recent modeling work and analysis of satellite-derived global burned area shows a negative correlation between burned area and human population density (*Bistinas et al*., 2014; *Knorr et al*., 2014; *van der Werf et al*., 2017). *Andela et al*. (2018) proposed this negative relationship is due to land use change. *Arora and Melton* (2018) suggest an overall decline in global burned area of 25-30% since 1850 CE. Therefore, challenges lie in projecting future fire emissions and the impact on climate. Questions which need to be addressed include: 1) What is the relationship between humans and fires? and 2) What is the relationship between climate and fires?

Preindustrial burning rates for ethane, acetylene, and methane were most likely greater than modern day based on the research in this thesis project. The acetylene biomass burning emissions during the Medieval Period were nearly four-times modern day emissions. Analysis by *van der Werf et al*. (2013) argued that burning rates of this magnitude during the preindustrial would be challenging to obtain and would require drastic shifts in fire regimes and dynamics which are considered infeasible. If the modern fire budget is underestimated, then the magnitude of the actual differences between the preindustrial and current biomass burning rates may not be

as severe. In this case, the viability of two or three-times modern burning rates during the preindustrial comes into question.

Most modern biomass burning rates are estimated via satellite-based instrumentation of fire activity and these measurement techniques have inherent uncertainties and caveats which need to be considered when comparing preindustrial versus modern data (*Giglio et al*., 2003; 2013; 2018). First, there is a limit to the minimum size of fire which can be detected remotely (*Giglio et al*., 2013). Many agriculture and cropland fires are smaller than this size (*McCarty et al.*, 2009). Second, cloud coverage limits the detection of both active fires and fire scars. Therefore, burned areas are likely underestimated in regions with persistent cloud cover. *Giglio et al.* (2018) used a new global burned area mapping algorithm and determined that global burned area in the Global Fire Emissions Database version 4.1 (which was used in this thesis) may be underestimated by about 26%. Future work should explore the implications and feasibility of the preindustrial biomass burning rates observed in this study.

7.5 Future work

This thesis advanced the carbon cycle and fire modeling field by providing a new approach to study the long-term history of fire emissions through the analysis of ice core ethane and acetylene. Extending the ice core ethane and acetylene records further back in time will provide information about the relationship between climate and fire. This will provide a new dataset that can be used to validate and constrain coupled vegetation/climate/fire models. These models are necessarily to project how fire emissions and the carbon cycle will be impacted in the future.

BIBLIOGRAPHY

Akagi, S. K., Yokelson, R. J., Wiedinmyer, C., Alvarado, M. J., Reid, J. S., Karl, T., et al. (2011). Emission factors for open and domestic biomass burning for use in atmospheric models. *Atmospheric Chemistry and Physics*, *11*(9), 4039–4072. https://doi.org/10.5194/acp-11-4039-2011

Allan, W., Struthers, H., & Lowe, D. C. (2007). Methane carbon isotope effects caused by atomic chlorine in the marine boundary layer: Global model results compared with Southern Hemisphere measurements. *Journal of Geophysical Research*, *112*(D04306), 1–10. https://doi.org/10.1029/2006JD007369

Andela, N., Morton, D. C., Giglio, L., Chen, Y., Werf, G. R. Van Der, Kasibhatla, P. S., et al. (2017). A human-driven decline in global burned area. *Science*, *356*(6345), 1356–1362. https://doi.org/10.1126/science.aal4108

Anderson, R. C. (1958). Acetylene as an intermediate in combustion of petroleum hydrocarbons. *Advances in Chemistry*, *20*, 49–57. https://doi.org/10.1021/ba-1958-0020.ch005

Andreae, M. O., & Merlet, P. (2001). Emission of trace gases and aerosols from biomass burning. *Global Biogeochemical Cycles*, *15*(4), 955–966. https://doi.org/10.1029/2000GB001382

Aragão, L. E. O. C., & Shimabukuro, Y. E. (2010). The incidence of fire in Amazonian forests with implications for REDD. *Science*, *328*(5983), 1275–1279. https://doi.org/10.1126/science.1186925

Archibald, S., Roy, D. P., van Wilgen, B. W., & Scholes, R. J. (2009). What limits fire? An examination of drivers of burnt area in Southern Africa. *Global Change Biology*, *15*(3), 613–630. https://doi.org/10.1111/j.1365-2486.2008.01754.x

Arora, V. K., & Melton, J. R. (2018). Reduction in global area burned and wildfire emissions since 1930s enhances carbon uptake by land. *Nature Communications*, *9*(1326). https://doi.org/10.1038/s41467-018-03838-0

Aydin, M., Williams, M. B., & Saltzman, E. S. (2007). Feasibility of reconstructing paleoatmospheric records of selected alkanes, methyl halides, and sulfur gases from Greenland ice cores. *Journal of Geophysical Research*, *112*(D7), D07312. https://doi.org/10.1029/2006JD008027

Aydin, M., Verhulst, K. R., Saltzman, E. S., Battle, M. O., Montzka, S. A., Blake, D. R., et al. (2011). Recent decreases in fossil-fuel emissions of ethane and methane derived from firn air. *Nature*, *476*(7359), 198–201. https://doi.org/10.1038/nature10352

Battle, M. O., Severinghaus, J. P., Sofen, E. D., Plotkin, D., Orsi, A. J., Aydin, M., et al. (2011). Controls on the movement and composition of firn air at the West Antarctic Ice Sheet

Divide. *Atmospheric Chemistry and Physics*, *11*(21), 11007–11021. https://doi.org/10.5194/acp-11-11007-2011

Battle, M., Bender, M., Sowers, T., Tans, P. P., Butler, J. H., Elkins, J. W., et al. (1996). Atmospheric gas concentrations in firn air at the South pole. *Nature*, *383*, 231–235. https://doi.org/10.1038/383231a0

Beck, J., Bock, M., Schmitt, J., Seth, B., Blunier, T., & Fischer, H. (2018). Bipolar carbon and hydrogen isotope constraints on the Holocene methane budget. *Biogeosciences*, *15*(23), 7155–7175. https://doi.org/10.5194/bg-15-7155-2018

Bistinas, I., Harrison, S. P., Prentice, I. C., & Pereira, J. M. C. (2014). Causal relationships versus emergent patterns in the global controls of fire frequency. *Biogeosciences*, *11*, 5087–5101. https://doi.org/10.5194/bg-11-5087-2014

Blake, D. (2013). Methane, nonmethane hydrocarbons, alkyl nitrates, and chlorinated carbon compounds including 3 chlorofluorocarbons (CFC-11, CFC-12, and CFC-113) in whole-air samples. Carbon dioxide information analysis center, Oak Ridge National Laboratory, U.S. Department of Energy, Oak Ridge Tenn., U.S.A.

Blake, N. J., Blake, D. R., Simpson, I. J., Lopez, J. P., Johnston, N. A. C., Swanson, A. L., et al. (2001). Large-scale latitudinal and vertical distributions of NMHCs and selected halocarbons in the troposphere over the Pacific Ocean during the March-April 1999 PEM-Tropics B. *Journal of Geophysical Research*, *106*(D23), 32627–32644. https://doi.org/10.1029/2000JD900773

Bock, M., Schmitt, J., Beck, J., Seth, B., Chappellaz, J., & Fischer, H. (2017). Glacial/interglacial wetland, biomass burning, and geologic methane emissions constrained by dual stable isotopic CH_4 ice core records. *Proceedings of the National Academy of Sciences*, *114*(29), 5778–5786. https://doi.org/10.1073/pnas.1613883114

Bouwman, A. F., Lee, D. S., Asman, W. A. H., Dentener, F. J., Hoek, K. W. Van Der, & Olivier, J. G. J. (1997). A global high-resolution emission inventory for ammonia. *Global Biogeochemical Cycles*, *11*(4), 561–587. https://doi.org/10.1029/97GB02266

Bowman, D. M. J. S., Balch, J. K., Artaxo, P., Bond, W. J., Carlson, J. M., Cochrane, M. A., et al. (2009). Fire in the earth system. *Science*, *324*(5926), 481–484. https://doi.org/10.1126/science.1163886

Bowman, D. M. J. S., Balch, J., Artaxo, P., Bond, W. J., Cochrane, M. A., D'Antonio, C. M., et al. (2011). The human dimension of fire regimes on Earth. *Journal of Biogeography*, *38*(12), 2223–2236. https://doi.org/10.1111/j.1365-2699.2011.02595.x

Brook, E. J., Harder, S., Severinghaus, J., Steig, E. J., & Sucher, C. M. (2000). On the origin and timing of rapid changes in atmospheric methane during the last glacial period. *Global Biogeochemical Cycles*, *14*(2), 559–572. https://doi.org/10.1029/1999GB001182

Brook, E. J., Sowers, T., & Orchardo, J. (1996). Rapid variations in atmospheric methane concentration during the past 110,000 years. *Science*, *273*(5278), 1087–1091. https://doi.org/10.1126/science.273.5278.1087

Buizert, C., Cuffey, K. M., Severinghaus, J. P., Baggenstos, D., Fudge, T. J., Steig, E. J., et al. (2015). The WAIS Divide deep ice core WD2014 chronology − Part 1: Methane synchronization (68-31 ka BP) and the gas age-ice age difference. *Climate of the Past*, *11*(2), 153–173. https://doi.org/10.5194/cp-11-153-2015

Buizert, C., Martinerie, P., Petrenko, V. V, Severinghaus, J. P., Trudinger, C. M., Witrant, E., et al. (2012). Gas transport in firn: multiple-tracer characterisation and model intercomparison for NEEM, Northern Greenland. *Atmospheric Chemistry and Physics*, *12*(9), 4259–4277. https://doi.org/10.5194/acp-12-4259-2012

Burkholder, J. B., Sander S. P., Abbatt J., Barker, J. R., Huie, R. E., Kolb, C. E., et al. (2015) "Chemical Kinetics and Photochemical Data for Use in Atmospheric Studies, Evaluation No. 18," JPL Publication 15-10, Jet Propulsion Laboratory, Pasadena http://jpldataeval.jpl.nasa.gov.

Casey, K. A., Fudge, T. J., Neumann, T. A., Steig, E. J., Cavitte, M. G. P., & Blankenship, D. D. (2014). The 1500m South Pole ice core: recovering a 40 ka environmental record. *Annals of Glaciology*, *55*(68), 137–146. https://doi.org/10.3189/2014AoG68A016

Chappellaz, J., Barnola, J. M., Raynaud, D., Korotkevich, Y. S., & Lorius, C. (1990). Ice-core record of atmospheric methane over the past 160,000 years. *Nature*, *345*, 127–131. https://doi.org/10.1038/383231a0

Ciais, P., Sabine, C., Bala G., Bopp L., Brovkin, V., Canadell, J., et al. (2013). Carbon and Other Biogeochemical Cycles in *Climate Change 2013: The Physical Science Basis. Contribution of Working Group I to the Fifth Assessment Report of the Intergovernmental Panel on Climate Change* [Stocker, T.F., D. Qin, G.-K. Plattner, M. Tignor, S.K. Allen, J. Boschung, A. Nauels, Y. Xia, V. Bex and P.M. Midgley (eds.)]. Cambridge University Press, Cambridge, United Kingdom and New York, NY, USA.

Clarkson, T. S., Martin, R. J., & Rudolph, J. (1997). Ethane and propane in the southern marine troposphere. *Atmospheric Environment*, *31*(22), 3763–3771. https://doi.org/10.1016/S1352-2310(97)00220-3

Collatz, G. J., Berry, J. A., & Clark, J. S. (1998). Effects of climate and atmospheric CO_2 partial pressure on the global distribution of C_4 grasses: present, past, and future. *Oecologia*, *114*, 441–454. https://doi.org/10.1007/s004420050

Craig, H. (1957). Isotopic standards for carbon and oxygen and correction factors for mass-spectrometric analysis of carbon dioxide. *Geochimica et Cosmochimica Acta*, *12*(1–2), 133–149. https://doi.org/10.1016/0016-7037(57)90024-8

Craig, H., Y. Horibe, and T. Sowers (1988), Gravitational separation of gases and isotopes in polar ice caps, *Science*, *242*(4886), 1675–1678, doi:10.1126/science.242.4886.1675

Crutzen, P. J., & Andreae, M. O. (1990). Biomass burning in the tropics: impact on atmospheric chemistry and biogeochemical cycles. *Science*, *250*(4988), 1669–1678. https://doi.org/10.1126/science.250.4988.1669

Cuffey, K. M., & Clow, G. D. (1997). Temperature, accumulation, and ice sheet elevation in central Greenland through the last deglacial transition. *Journal of Geophysical Research*, *102*(C12), 26383–26396. https://doi.org/10.1029/96JC03981

Curry, C. L. (2007). Modeling the soil consumption of atmospheric methane at the global scale. *Global Biogeochemical Cycles*, *21*(GB4012), 1–15. https://doi.org/10.1029/2006GB002818

Dalsøren, S. B., Myhre, G., Hodnebrog, Ø., Myhre, C. L., Stohl, A., Pisso, I., et al. (2018). Discrepancy between simulated and observed ethane and propane levels explained by underestimated fossil emissions. *Nature Geoscience*, *11*(3), 178–184. https://doi.org/10.1038/s41561-018-0073-0

Dlugokencky, E. J. (2017) Atmospheric methane dry air mole fractions from the NOAA ESRL carbon cycle cooperative global air sampling network, 1983-2016. Version 2017-07-28. Available at ftp://aftp.cmdl.noaa.gov/products/trends/ch4/ch4_annmean_gl.txt. Accessed April 24, 2018.

Dlugokencky, E. J., Nisbet, E. G., Fisher, R., & Lowry, D. (2011). Global atmospheric methane: budget, changes and dangers. *Philosophical Transactions of the Royal Society A: Mathematical, Physical and Engineering Sciences*, *369*(1943), 2058–2072. https://doi.org/10.1098/rsta.2010.0341

Elliot, M. B., Flenley, J. R., & Sutton, D. G. (1998). A late Holocene pollen record of deforestation and environmental change from the Lake Tauanui catchment, Northland, New Zealand. *Journal of Paleolimnology*, *19*, 23–32. https://doi.org/10.1023/A:100792102

Etheridge, D. M., Pearman, G. I., & de Silva, F. (1988). Atmospheric trace-gas variations as revealed by air trapped in an ice core from Law Dome, Antarctica. *Annals of Glaciology*, *10*. https://doi.org/10.3189/S0260305500004110

Etheridge, D. M., Steele, L. P., Francey, R. J., & Langenfelds, R. L. (1998). Atmospheric methane between 1000 A.D. and present: evidence of anthropogenic emissions and climatic variability. *Journal of Geophysical Research*, *103*(D13), 15979–15993. https://doi.org/10.1029/98JD00923

Etiope, G. (2012). Climate science: methane uncovered. *Nature Geoscience*, *5*, 373–374. https://doi.org/10.1038/ngeo1483

Etiope, G., & Ciccioli, P. (2009). Earth's degassing: a missing ethane and propane source. *Science*, *323*(5319), 478. https://doi.org/10.1126/science.1165904

Etiope, G., Lassey, K. R., Klusman, R. W., & Boschi, E. (2008). Reappraisal of the fossil methane budget and related emission from geologic sources. *Geophysical Research Letters*, *35*(9), L09307. https://doi.org/10.1029/2008GL033623

Farquhar, G. D., Ehleringer, J. R., & Hubick, K. T. (1989). Carbon isotope discrimination and photosynthesis. *Annual Review of Plant Physiology and Plant Molecular Biology*, *40*, 503–537. https://doi.org/10.1146/annurev.pp.40.060189.002443

Ferretti, D. F., Miller, J. B., White, J. W. C., Etheridge, D. M., Lassey, K. R., Lowe, D. C., et al. (2005). Unexpected changes to the global methane budget over the past 2000 years. *Science*, *309*(5741), 1714–1717. https://doi.org/10.1126/science.1115193

Fischer, H., Wagenbach, D., & Kipfstuhl, J. (1998). Sulfate and nitrate firn concentrations on the Greenland ice sheet 2. Temporal anthropogenic deposition changes. *Journal of Geophysical Research*, *103*(D17), 935–942. https://doi.org/doi:10.1029/98JD01886

Flantua, S. G. A., Hooghiemstra, H., Vuille, M., Behling, H., Carson, J. F., Gosling, W. D., et al. (2016). Climate variability and human impact in South America during the last 2000 years: synthesis and perspectives from pollen records. *Climate of the Past*, *12*, 483–523. https://doi.org/10.5194/cp-12-483-2016

Franco, B., Mahieu, E., Emmons, L. K., Tzompa-Sosa, Z. A., Fischer, E. V, Sudo, K., et al. (2016). Evaluating ethane and methane emissions associated with the development of oil and natural gas extraction in North America. *Environmental Research Letters*, *11*(4). https://doi.org/10.1088/1748-9326/11/4/044010

Fuhrer, K., Neftel, A., Anklin, M., & Maggi, V. (1993). Continuous measurements of hydrogen peroxide, formaldehyde, calcium and ammonium concentrations along the new grip ice core from summit, Central Greenland. *Atmospheric Environment*, *27*(12), 1873–1880. https://doi.org/10.1016/0960-1686(93)90292-7

Giglio, L., Boschetti, L., Roy, D. P., Humber, M. L., & Justice, C. O. (2018). Remote Sensing of Environment The Collection 6 MODIS burned area mapping algorithm and product. *Remote Sensing of Environment*, *217*(July), 72–85. https://doi.org/10.1016/j.rse.2018.08.005

Giglio, L., Descloitres, J., Justice, C. O., & Kaufman, Y. J. (2003). An enhanced contextual fire detection algorithm for MODIS. *Remote Sensing of Environment*, *87*(2–3), 273–282. https://doi.org/10.1016/S0034-4257(03)00184-6

Giglio, L., Randerson, J. T., & van der Werf, G. R. (2013). Analysis of daily, monthly, and annual burned area using the fourth-generation global fire emissions database (GFED4). *Journal of Geophysical Research: Biogeosciences*, *118*(1), 317–328. https://doi.org/10.1002/jgrg.20042

Grieman, M. M., Aydin, M., Isaksson, E., Schwikowski, M., & Saltzman, E. S. (2018a). Aromatic acids in an Arctic ice core from Svalbard: a proxy record of biomass burning. *Climate of the Past*, *14*, 637–6512. https://doi.org/10.5194/cp-2016-126

Grieman, M. M., Aydin, M., Fritzsche, D., McConnell, J. R., Opel, T., Sigl, M., & Saltzman, E. S. (2017). Aromatic acids in a Eurasian Arctic ice core: a 2600-year proxy record of biomass burning. *Climate of the Past*, 395–410. https://doi.org/10.5194/cp-13-395-2017

Grieman, M. M., Aydin, M., McConnell, J. R., & Saltzman, E. S. (2018b). Burning-derived vanillic acid in an Arctic ice core from Tunu, northeastern Greenland. *Climate of the Past*, *14*, 1625–1637. https://doi.org/10.5194/cp-14-1625-2018

Gunter, B. D., & Musgrave, B. C. (1971). New evidence on the origin of methane in hydrothermal gases. *Geochimica et Cosmochimica Acta*, *35*, 113–118. https://doi.org/10.1016/0016-7037(71)90109-8

Hann, D., & Raynaud, D. (1998). Ice core record of CO variations during the last two millennia: atmospheric implications and chemical interactions within the Greenland ice. *Tellus, Series B: Chemical and Physical Meteorology*, *50*(3), 253–262. https://doi.org/10.3402/tellusb.v50i3.16101

Hantson, S., Arneth, A., Harrison, S. P., Kelley, D. I., Prentice, I. C., Rabin, S. S., et al. (2016). The status and challenge of global fire modelling. *Biogeosciences*, *13*, 3359–3375. https://doi.org/10.5194/bg-13-3359-2016

Haug, G. H., Hughen, K. A., Sigman, D. M., Peterson, L. C., & Ro, U. (2001). Southward migration of the intertropical convergence zone through the Holocene. *Science*, *293*(5533), 1304–1309. https://doi.org/10.1126/science.1059725

Hausmann, P., Sussmann, R., & Smale, D. (2016). Contribution of oil and natural gas production to renewed increase in atmospheric methane (2007-2014): Top-down estimate from ethane and methane column observations. *Atmospheric Chemistry and Physics*, *16*(5), 3227–3244. https://doi.org/10.5194/acp-16-3227-2016

Helmig, D. (2017). Atmospheric hydrocarbons as tracers for climate change, air transport, and oxidation chemistry in the Arctic, GEOSummit, Greenland, 2008-2017. Arctic Data Center. doi:10.18739/A2RS0X.

Helmig, D., Petrenko, V., Martinerie, P., Witrant, E., Röckmann, T., Zuiderweg, A., et al. (2014). Reconstruction of Northern Hemisphere 1950-2010 atmospheric non-methane hydrocarbons. *Atmospheric Chemistry and Physics*, *14*(3), 1463–1483. https://doi.org/10.5194/acp-14-1463-2014

Helmig, D., Bottenheim, J., Galbally, I. E., Lewis, A., Milton, M. J. T., Penkett, S., et al. (2009). Volatile organic compounds in the global atmosphere. *Eos, Transactions, American Geophysical Union*, *90*(52), 513–514. https://doi.org/10.1029/2009EO520001

Helmig, D., Rossabi, S., Hueber, J., Tans, P., Montzka, S. A., Masarie, K., et al. (2016). Reversal of global atmospheric ethane and propane trends largely due to US oil and natural gas production. *Nature Geoscience*, *9*(7), 490–495. https://doi.org/10.1038/ngeo2721

Hennigan, C. J., Sullivan, A. P., Collett Jr., J. L., & Robinson, A. L. (2010). Levoglucosan stability in biomass burning particles exposed to hydroxyl radicals. *Geophysical Research Letters*, *37*(L09806), 2–5. https://doi.org/10.1029/2010GL043088

Hoffmann, D., Tilgner, A., Iinuma, Y., & Herrmann, H. (2010). Atmospheric sability of levoglucosan: a detailed laboratory and modeling study. *Environmental Science and Technology*, *44*(2), 694–699. https://doi.org/10.1021/es902476f

Holmes, C. D., Prather, M. J., Søvde, O. A., & Myhre, G. (2013). Future methane, hydroxyl, and their uncertainties: key climate and emission parameters for future predictions. *Atmospheric Chemistry and Physics*, *13*(1), 285–302. https://doi.org/10.5194/acp-13-285-2013

Holz, A., Haberle, S., Veblen, T. T., De Pol-Holz, R., & Southon, J. (2012). Fire history in western Patagonia from paired tree-ring fire-scar and charcoal records. *Climate of the Past*, *8*, 451–466. https://doi.org/10.5194/cp-8-451-2012

Hristov, A. N., Hanigan, M., Cole, A., Todd, R., McAllister, T. A., Ndegwa, P. M., & Rotz, A. (2011). Review: Ammonia emissions from dairy farms and beef feedlots. *Canadian Journal of Animal Science*, *91*(1). https://doi.org/10.4141/CJAS10034

Kanakidou, M., Bonsang, B., Le Roulley, J. C., Lambert, G., Martin, D., & Sennequier, G. (1988). Marine source of atmospheric acetylene. *Nature*, *333*, 51–52. https://doi.org/10.1038/333051a0

Kaspers, K. A., van de Wal, R. S. W., de Gouw, J. A., Hofstede, C. M., van den Broeke, M. R., van der Veen, C., et al. (2004). Analyses of firn gas samples from Dronning Maud Land, Antarctica: Study of nonmethane hydrocarbons and methyl chloride. *Journal of Geophysical Research*, *109*(D2), D02307. https://doi.org/10.1029/2003JD003950

Kawamura, K., Izawa, Y., Mochida, M., & Shiraiwa, T. (2012). Ice core records of biomass burning tracers (levoglucosan and dehydroabietic, vanillic and *p*-hydroxybenzoic acids) and total organic carbon for past 300 years in the Kamchatka Peninsula, Northeast Asia. *Geochimica et Cosmochimica Acta*, *99*, 317–329. https://doi.org/10.1016/j.gca.2012.08.006

Kehrwald, N. M., Whitlock, C., Barbante, C., Brovkin, V., Daniau, A. L., Kaplan, J. O., et al. (2013). Fire research: linking past, present, and future data. *Eos, Transactions, American Geophysical Union*, *94*(46), 421–422. https://doi.org/10.1002/2013EO460001

Kirschke, S., Bousquet, P., Ciais, P., Saunois, M., Canadell, J. G., Dlugokencky, E. J., et al. (2013). Three decades of global methane sources and sinks. *Nature Geoscience*, *6*(10), 813–823. https://doi.org/10.1038/ngeo1955

Knipping, E. M., & Dabdub, D. (2003). Impact of chlorine emissions from sea-salt aerosol on coastal urban ozone. *Environmental Science and Technology*, *37*(2), 275–284. https://doi.org/10.1021/es025793z

Knorr, W., Kaminski, T., Arneth, A., & Weber, U. (2014). Impact of human population density on fire frequency at the global scale. *Biogeosciences*, *11*, 1085–1102. https://doi.org/10.5194/bg-11-1085-2014

Koch, A., Brierley, C., Maslin, M. M., & Lewis, S. L. (2019). Earth system impacts of the European arrival and Great Dying in the Americas after 1492. *Quaternary Science Reviews*, *207*, 13–36. https://doi.org/10.1016/j.quascirev.2018.12.004

Kort, E. A., Smith, M. L., Murray, L. T., Gvakharia, A., Brandt, A. R., Peischl, J., et al. (2016). Fugitive emissions from the Bakken shale illustrate role of shale production in global ethane shift. *Geophysical Research Letters*, *43*(9), 4617–4623. https://doi.org/10.1002/2016GL068703

Lamarque, J. F., Bond, T. C., Eyring, V., Granier, C., Heil, A., Klimont, Z., et al. (2010). Historical (1850-2000) gridded anthropogenic and biomass burning emissions of reactive gases and aerosols: methodology and application. *Atmospheric Chemistry and Physics*, *10*(15), 7017–7039. https://doi.org/10.5194/acp-10-7017-2010

Lassey, K. R., Etheridge, D. M., Lowe, D. C., Smith, A. M., & Ferretti, D. F. (2007). Centennial evolution of the atmospheric methane budget: what do the carbon isotopes tell us? *Atmospheric Chemistry and Physics*, *7*(8), 2119–2139. https://doi.org/10.5194/acp-7-2119-2007

Lawler, M. J., Finley, B. D., Keene, W. C., Pszenny, A. A. P., Read, K. A., von Glasow, R., & Saltzman, E. S. (2009). Pollution-enhanced reactive chlorine chemistry in the eastern tropical Atlantic boundary layer. *Geophysical Research Letters*, *36*(8), 3–7. https://doi.org/10.1029/2008GL036666

Legrand, M., De Angelis, M., Staffelbach, T., Neftel, A., & Stauffer, B. (1992). Large perturbations of ammonium and organic acids content in the Summit-Greenland ice core. Fingerprint from forest fires? *Geophysical Rese*, *19*(5), 473–475. https://doi.org/10.1029/91GL03121

Liu, Y., Zhang, Q., & Wang, T. (2017). Detailed chemistry modeling of partial combustion of natural gas for coproducing acetylene and syngas. *Combustion Science and Technology*, *189*(5), 908–922. https://doi.org/10.1080/00102202.2016.1256879

Loulergue, L., Schilt, A., Spahni, R., Masson-Delmotte, V., Blunier, T., Lemieux, B., et al. (2008). Orbital and millennial-scale features of atmospheric CH_4 over the past 800,000 years. *Nature*, *453*, 383–386. https://doi.org/10.1038/nature06950

MacFarling Meure, C., Etheridge, D., Trudinger, C., Steele, P., Langenfelds, R., van Ommen, T., et al. (2006). Law Dome CO2, CH_4 and N_2O ice core records extended to 2000 years BP. *Geophysical Research Letters*, *33*(14), L14810. https://doi.org/10.1029/2006GL026152

Mann, M. E., Zhang, Z., Rutherford, S., Bradley, R. S., Hughes, M. K., Shindell, D., et al. (2009). Global signatures and dynamical origins of the Little Ice Age and Medieval Climate Anomaly. *Science*, *326*, 1256–1261. https://doi.org/10.1126/science.1177303

Marik, T. (1998), Atmospheric $\delta^{13}C$ and δD measurements to balance the global methane budget, PhD thesis, Ruprecht-Karls-University, Heidelberg, Germany.

Marlon, J. R., Bartlein, P. J., Carcaillet, C., Gavin, D. G., Harrison, S. P., Higuera, P. E., et al. (2008). Climate and human influences on global biomass burning over the past two millennia. *Nature Geoscience*, *2*(4), 307–307. https://doi.org/10.1038/ngeo468

McBride, J. R. (1983). Analysis of tree rings and fire scars to establish fire history. *Tree-Ring Bulletin*, *43*.

McCarty, J. L., Korontzi, S., Justice, C. O., & Loboda, T. (2009). The spatial and temporal distribution of crop residue burning in the contiguous United States. *Science of the Total Environment*, *407*(21), 5701–5712. https://doi.org/10.1016/j.scitotenv.2009.07.009

Meese, D. A., Gow, A. J., Alley, R. B., Zielinski, G. A., Grootes, P. M., Ram, M., et al. (1997). The Greenland Ice Sheet Project 2 depth-age scale: methods and results. *Journal of Geophysical Research*, *102*(C12), 26,411-26,423. https://doi.org/10.1029/97JC00269

Mischler, J. A., Sowers, T. A., Alley, R. B., Battle, M., McConnell, J. R., Mitchell, L., et al. (2009). Carbon and hydrogen isotopic composition of methane over the last 1000 years. *Global Biogeochemical Cycles*, *23*(GB4024). https://doi.org/10.1029/2009GB003460

Mitchell, L. E., Brook, E. J., Sowers, T., McConnell, J. R., & Taylor, K. (2011). Multidecadal variability of atmospheric methane, 1000-1800 C.E. *Journal of Geophysical Research*, *116*(G02007). https://doi.org/10.1029/2010JG001441

Naik, V., Voulgarakis, A., Fiore, A. M., Horowitz, L. W., Lamarque, J. F., Lin, M., et al. (2013). Preindustrial to present-day changes in tropospheric hydroxyl radical and methane lifetime from the Atmospheric Chemistry and Climate Model Intercomparison Project (ACCMIP). *Atmospheric Chemistry and Physics*, *13*(10), 5277–5298. https://doi.org/10.5194/acp-13-5277-2013

Nicewonger, M. R., Aydin, M., Prather, M. J., & Saltzman, E. S. (2018). Large changes in biomass burning over the last millennium inferred from paleoatmospheric ethane in polar ice cores. *Proceedings of the National Academy of Sciences*, *115*(49), 12413–12418. https://doi.org/10.1073/pnas.1807172115

Nicewonger, M. R., Verhulst, K. R., Aydin, M., & Saltzman, E. S. (2016). Preindustrial atmospheric ethane levels inferred from polar ice cores: a constraint on the geologic sources of atmospheric ethane and methane. *Geophysical Research Letters*, *43*(1), 1–8. https://doi.org/10.1002/2015GL066854.Received

Nisbet, E. G., Dlugokencky, E. J., & Bousquet, P. (2014). Methane on the rise - again. *Science*, *343*, 493–496. https://doi.org/10.1126/science.1247828

Orsi, A. J., Cornuelle, B. D., & Severinghaus, J. P. (2012). Little Ice Age cold interval in West Antarctica: evidence from borehole temperature at the West Antarctic Ice Sheet (WAIS) Divide. *Geophysical Research Letters*, *39*(9), 1–7. https://doi.org/10.1029/2012GL051260

PAGES 2k Consortium (2013). Continental-scale temperature variability during the past two millennia. *Nature Geoscience*, *6*, 339–346. https://doi.org/10.1038/NGEO1797

Peischl, J., Karion, A., Sweeney, C., Kort, E. A., Smith, M. L., Brandt, A. R., et al. (2016). Quantifying atmospheric methane emissions from oil and natural gas production in the Bakken shale region of North Dakota. *Journal of Geophysical Research; Atmospheres*, *119*, 6101–6111. https://doi.org/10.1002/2015JD024631

Petrenko, V. V., Smith, A. M., Schaefer, H., Riedel, K., Brook, E., Baggenstos, D., et al. (2017). Minimal geological methane emissions during the Younger Dryas–Preboreal abrupt warming event. *Nature*, *548*(7668), 443–446. https://doi.org/10.1038/nature23316

Plass-Dülmer, C., Koppmann, R., Ratte, M., & Rudolph, J. (1995). Light nonmethane hydrocarbons in seawater. *Global Biogeochemical Cycles*, *9*(1), 79–100. https://doi.org/10.1029/94GB02416

Poisson, N., Kanakidou, M., & Crutzen, P. J. (2000). Impact of non-methane hydrocarbons on tropospheric chemistry and the oxidizing power of the global troposphere: 3-dimensional modelling results. *Journal of Atmospheric Chemistry*, *36*(2), 157–230. https://doi.org/10.1023/A:1006300616544

Power, M. J., Mayle, F. E., Bartlein, P. J., Marlon, J. R., Anderson, R. S., Behling, H., et al. (2012). Climatic control of the biomass-burning decline in the Americas after AD 1500. *The Holocene*, *23*(1). https://doi.org/10.1177/0959683612450196

Power, M. J., Marlon, J., Ortiz, N., Bartlein, P. J., Harrison, S. P., Mayle, F. E., et al. (2008). Changes in fire regimes since the last glacial maximum: An assessment based on a global synthesis and analysis of charcoal data. *Climate Dynamics*, *30*(7–8), 887–907. https://doi.org/10.1007/s00382-007-0334-x

Pozzer, A., Pollmann, J., Taraborrelli, D., Jöckel, P., Helmig, D., Tans, P., et al. (2010). Observed and simulated global distribution and budget of atmospheric C2-C5 alkanes. *Atmospheric Chemistry and Physics*, *10*(9), 4403–4422. https://doi.org/10.5194/acp-10-4403-2010

Prather, M. J., Holmes, C. D., & Hsu, J. (2012). Reactive greenhouse gas scenarios: systematic exploration of uncertainties and the role of atmospheric chemistry. *Geophysical Research Letters*, *39*(9), 6–10. https://doi.org/10.1029/2012GL051440

Prather, M. J., & Hsu, J. (2010). Coupling of nitrous oxide and methane by global atmospheric chemistry. *Science*, *330*(6006), 952–955. https://doi.org/10.1126/science.1196285

Quay, P., Stutsman, J., Wilbur, D., Snover, A., Dlugokencky, E., & Brown, T. (1999). The isotopic composition of atmospheric methane. *Global Biogeochemical Cycles*, *13*(2), 445–461. https://doi.org/10.1029/1998GB900006

Rubino, M., Etheridge, D. M., Trudinger, C. M., Allison, C. E., Battle, M. O., Langenfelds, R. L., et al. (2013). A revised 1000 year atmospheric $\delta^{13}C$-CO_2 record from Law Dome and South Pole, Antarctica. *Journal of Geophysical Research Atmospheres*, *118*, 8482–8499. https://doi.org/10.1002/jgrd.50668

Rubino, M., D'Onofrio, A., Seki, O., & Bendle, J. A. (2015). Ice-core records of biomass burning. *The Anthropocene Review*, *3*(2), 140–162. https://doi.org/10.1177/2053019615605117

Rudolph, J. (1995). The tropospheric distribution and budget of ethane. *Journal of Geophysical Research*, *100*(D6), 11369–11381. https://doi.org/10.1029/95JD00693

Rudolph, J., & Ehhalt, D. H. (1981). Measurements of C2-C5 hydrocarbons over the North Atlantic. *Journal of Geophysical Research*, *86*(1), 959–964. https://doi.org/10.1029/JC086iC12p11959

Sachs, J. P., Sachse, D., Smittenberg, R. H., Zhang, Z., Battisti, D. S., & Golubic, S. (2009). Southward movement of the Pacific intertropical convergence zone AD 1400-1850. *Nature Geoscience*, *2*(7), 519–525. https://doi.org/10.1038/ngeo554

Sander, R. (2015). Compilation of Henry's law constants (version 4.0) for water as solvent. *Atmospheric Chemistry and Physics*, *15*, 4399–4981. https://doi.org/10.5194/acp-15-4399-2015.

Sander, S.P., Abbatt, J. P. D., Barker, J. R., Burkholder, J. B., Golden, D. M., Kolb, C. E., et al. (2011) "Chemical Kinetics and Photochemical Data for Use in Atmospheric Studies, Evaluation No. 17," JPL Publication 10-6, Jet Propulsion Laboratory, Pasadena http://jpldataeval.jpl.nasa.gov.

Sander, S.P., Ravishankara, A. R., Golden, D. M., Kolb, C. E., Kurylo, M. J., Molina, M. J., et al. (2006) "Chemical Kinetics and Photochemical Data for Use in Atmospheric Studies, Evaluation No. 15," JPL Publication 06-2, Jet Propulsion Laboratory, Pasadena http://jpldataeval.jpl.nasa.gov.

Sapart, C. J., Monteil, G., Prokopiou, M., van de Wal, R. S. W., Kaplan, J. O., Sperlich, P., et al. (2012). Natural and anthropogenic variations in methane sources during the past two millennia. *Nature*, *490*(7418), 85–88. https://doi.org/10.1038/nature11461

Schwander, J., Barnola, J.-M., Andrie, C., Leuenberger, M., Ludin, A., Raynaud, D., & Stauffer, B. (1993). The age of the air in the firn and the ice at Summit, Greenland. *Journal of Geophysical Research*, *98*(D2), 2831–2838. https://doi.org/10.1029/92JD02383

Schwander, J., Sowers, T., Barnola, J.-M., Blunier, T., Fuchs, A., & Malaize, B. (1997). Age scale of the air in the summit ice: Implication for glacial-interglacial temperature change. *Journal of Geophysical Research*, *102*(D16), 19483–19493. https://doi.org/10.1029/97JD01309

Schwietzke, S., Sherwood, O. A., Bruhwiler, L. M. P., Miller, J. B., Etiope, G., Dlugokencky, E. J., et al. (2016). Upward revision of global fossil fuel methane emissions based on isotope database. *Nature*, *538*(7623), 88–91. https://doi.org/10.1038/nature19797

Severinghaus, J. P., & Battle, M. O. (2006). Fractionation of gases in polar ice during bubble close-off: New constraints from firn air Ne, Kr and Xe observations. *Earth and Planetary Science Letters*, *244*, 474–500. https://doi.org/10.1016/j.epsl.2006.01.032

Sigl, M., Fudge, T. J., Winstrup, M., Cole-Dai, J., Ferris, D., McConnell, J. R., et al. (2016). The WAIS Divide deep ice core WD2014 chronology − Part 2: Annual-layer counting (0-31 ka BP). *Climate of the Past*, *12*(3), 769–786. https://doi.org/10.5194/cp-12-769-2016

Singh, H. B., & Zimmerman, P. B. (1992), Atmospheric distributions and sources of nonmethane hydrocarbons, in *Gaseous Pollutants: Characterization and Cycling*, edited by J.O. Niragu, pp. 177- 225, John Wiley, New York

Simoneit, B. R. T., Schauer, J. J., Nolte, C. G., Oros, D. R., Elias, V. O., Fraser, M. P., et al. (1999). Levoglucosan, a tracer for cellulose in biomass burning and atmospheric particles. *Atmospheric Environment*, *33*, 173–182. https://doi.org/doi.org/10.1016/S1352-2310(98)00145-9

Simpson, I. J., Andersen, M. P. S., Meinardi, S., Bruhwiler, L., Blake, N. J., Helmig, D., et al. (2012). Long-term decline of global atmospheric ethane concentrations and implications for methane. *Nature*, *488*(7412), 490–494. https://doi.org/10.1038/nature11342

Simpson, I. J., Rowland, F. S., Meinardi, S., & Blake, D. R. (2006). Influence of biomass burning during recent fluctuations in the slow growth of global tropospheric methane. *Geophysical Research Letters*, *33*, L22208. https://doi.org/10.1029/2006GL027330

Solomon, S., D. Qin, M. Manning, Z. Chen, M. Marquis, K. Averyt, M. Tignor, and H. Miller (2007), The physical science basis, *Contribution of working group I to the fourth assessment report of the intergovernmental panel on climate change*, pp. 235-337.

Souney, J. M., Twickler, M. S., Hargreaves, G. M., Bencivengo, B. M., Kippenhan, M. J., Johnson, J. A., et al. (2014). Core handling and processing for the WAIS Divide ice-core project. *Annals of Glaciology*, *55*(68), 15–26. https://doi.org/10.3189/2014AoG68A008

Sowers, T. (2010). Atmospheric methane isotope records covering the Holocene period. *Quaternary Science Reviews*, *29*(1–2), 213–221. https://doi.org/10.1016/j.quascirev.2009.05.023

Spivakovsky, C. M., Logan, J. A., Montzka, S. A., Balkanski, Y. J., Jones, D. B. A., Horowitz, L. W., et al. (2000). Three-dimensional climatological distribution of tropospheric OH: Update and evaluation. *Journal of Geophysical Research*, *105*(D7), 8931–8980. https://doi.org/10.1029/1999JD901006

Stein, O., & Rudolph, J. (2007). Modeling and interpretation of stable carbon isotope ratios of ethane in global chemical transport models. *Journal of Geophysical Research*, *112*, D14308. https://doi.org/10.1029/2006JD008062

Tzompa-Sosa, Z. A., Mahieu, E., Franco, B., Keller, C. A., Turner, A. J., Helmig, D., et al. (2017). Revisiting global fossil fuel and biofuel emissions of ethane. *Journal of Geophysical Research: Atmospheres*, *122*(4), 2493–2512. https://doi.org/10.1002/2016JD025767

van Aardenne, J. A., Dentener, F. J., Olivier, J. G. J., Klein Goldewijk, C. G. M., & Lelieveld, J. (2001). A 1x1 resolution data set of historical anthropogenic trace gas emissions for the period 1890-1990. *Global Biogeochemical Cycles*, *15*(4), 909–928. https://doi.org/10.1029/2000GB001265

van der Werf, G. R., Peters, W., van Leeuwen, T. T., & Giglio, L. (2013). What could have caused pre-industrial biomass burning emissions to exceed current rates? *Climate of the Past*, *9*(1), 289–306. https://doi.org/10.5194/cp-9-289-2013

van der Werf, G. R., Randerson, J. T., Giglio, L., Collatz, G. J., Mu, M., Kasibhatla, P. S., et al. (2010). Global fire emissions and the contribution of deforestation, savanna, forest, agricultural, and peat fires (1997-2009). *Atmospheric Chemistry and Physics*, *10*(23), 11707–11735. https://doi.org/10.5194/acp-10-11707-2010

van der Werf, G. R., Randerson, J. T., Giglio, L., van Leeuwen, T. T., Chen, Y., Rogers, B. M., et al. (2017). Global fire emissions estimates during 1997-2016. *Earth System Science Data*, *9*, 697–720. https://doi.org/10.5194/essd-9-697-2017

van Marle, M. J. E., Kloster, S., Magi, B. I., Marlon, J. R., Daniau, A. L., Field, R. D., et al. (2017). Historic global biomass burning emissions for CMIP6 (BB4CMIP) based on merging satellite observations with proxies and fire models (1750-2015). *Geoscientific Model Development*, *10*(9), 3329–3357. https://doi.org/10.5194/gmd-10-3329-2017

Verhulst, K. R. (2014). Atmospheric histories of ethane and carbon monoxide from polar firn air and ice cores. PhD thesis, University of California, Irvine.

Vuille, M., Burns, S. J., Taylor, B. L., Cruz, F. W., Bird, B. W., Abbott, M. B., et al. (2012). of the Past A review of the South American monsoon history as recorded in stable isotopic proxies over the past two millennia. *Climate of the Past*, *8*, 1309–1321. https://doi.org/10.5194/cp-8-1309-2012

Wang, Z., Chappellaz, J., Park, K., & Mak, J. E. (2010). Large variations in Southern Hemisphere biomass burning during the last 650 years. *Science*, *330*(6011), 1663–6. https://doi.org/10.1126/science.1197257

Wang, X., Jacob, D. J., Eastham, S. D., Sulprizio, M. P., Zhu, L., Chen, Q., et al. (2019). The role of chlorine in global tropospheric chemistry. *Atmospheric Chemistry and Physics*, *19*, 3981–4003. https://doi.org/10.5194/acp-19-3981-2019

Warneck, P. and Williams, J. (2012) The Atmospheric Chemist's Companion: Numerical Data for Use in the Atmospheric Sciences, Springer Verlag.

Watt, L. J. (1951). The production of acetylene from methane by partial oxidation. Master's thesis, The University of British Columbia.

Whitby, R. A., & Altwicker, E. R. (1978). Acetylene in the atmosphere: sources, representative ambient concentrations and ratios to other hydrocarbons. *Atmospheric Environment*, *12*(6–7), 1289–1296. https://doi.org/10.1016/0004-6981(78)90067-7

Whitlow, S., Mayewski, P., Dibb, J., Holdsworth, G., & Twickler, M. (1994). An ice-core-based record of biomass burning in the Arctic and Subarctic, 1750-1980. *Tellus*, *46B*, 234–242. https://doi.org/10.1034/j.1600-0889.1994.t01-2-00006.x

Worton, D. R., Sturges, W. T., Reeves, C. E., Newland, M. J., Penkett, S. A., Atlas, E., et al. (2012). Evidence from firn air for recent decreases in non-methane hydrocarbons and a 20th century increase in nitrogen oxides in the northern hemisphere. *Atmospheric Environment*, *54*, 592–602. https://doi.org/10.1016/j.atmosenv.2012.02.084

Xiao, Y., Jacob, D. J., & Turquety, S. (2007). Atmospheric acetylene and its relationship with CO as an indicator of air mass age. *Journal of Geophysical Research*, *112*(D12), D12305. https://doi.org/10.1029/2006JD008268

Xiao, Y., Logan, J. A., Jacob, D. J., Hudman, R. C., Yantosca, R., & Blake, D. R. (2008). Global budget of ethane and regional constraints on U.S. sources. *Journal of Geophysical Research*, *113*, D21306. https://doi.org/10.1029/2007JD009415

Yevich, R., & Logan, J. A. (2003). An assessment of biofuel use and burning of agricultural waste in the developing world. *Global Biogeochemical Cycles*, *17*(4). https://doi.org/10.1029/2002GB001952

Zennaro, P., Kehrwald, N., Mcconnell, J. R., Schüpbach, S., Maselli, O. J., Marlon, J., et al. (2014). Fire in ice: two millennia of boreal forest fire history from the Greenland NEEM ice core. *Climate of the Past, 10,* 1905–1924. https://doi.org/10.5194/cp-10-1905-2014

APPENDIX A

MATLAB codes

Six-box steady-state ethane model

```
%%%%%%%%%%%%%%%%%%%%%%%%%%%%%%%%%%%%%%%%%%%%%%%%%%%%%%%%%%%%%%%%%%%%%%%%%%%%%%%
This box model calculates the geologic and biomass burning emissions that
%are necessary to observe the ice core ethane data (Nicewonger et al.
%2016). The model varies emissions by every 0.01 Tg and then determines the
%high northern latitude (HNL) and high sothern latitude (HSL) ethane mixing
%ratios. If these mixing ratios fall within the 2*std error range (+/-) of
%the ice core mean value for 1600-1750 CE, the model returns a true
statement.
%All other conditions return a false. The model then creates a contour plot
of all
%the true statments, i.e. the range of emissions of geologic and biomass
%burning that satisfy the ice core data from Greenland and Antarctica
%
%C2H6 box model --> steady state
%6 boxes (every 30 degrees)
%loss --> reaction with OH & transport
%%%%%%%%%%%%%%%%%%%%%%%%%%%%%%%%%%%%%%%%%%%%%%%%%%%%%%%%%%%%%%%%%%%%%%%%%%%%%%%
clear all
close all


dlat_box = 30; %width of each latitude box in model
lat_top = [90:-dlat_box:-60]';
lat_bot = [60:-dlat_box:-90]';

%function which uses Spivakovsky et al. 2010 3D climatological OH &
%temperature fields combined with JPL reaction rates for ethane to
%calculate k_OH for each box
[k_OH] = calc_koh_ethane(lat_top, lat_bot);

%constants
SA = 4*pi*(6378100^2); %total surface area of earth
mol_atmo = 1.77*10^20; %moles of "air" in the atmosphere (air = 29g/mol)
mol_trop = 0.8*mol_atmo; %moles of "air" in the troposphere (up to 200 hPa,
80%)
m_trop = 4.11*10^21; % mass of troposphere in grams (80% of mass)

A1 = 2*pi*(6378100^2)*(sind(90)-sind(60)); %surface area in latitude bands
A2 = 2*pi*(6378100^2)*(sind(60)-sind(30));
A3 = 2*pi*(6378100^2)*(sind(30)-sind(0));
areas = [A1/SA, A2/SA, A3/SA, A3/SA, A2/SA, A1/SA]; %ratio of SA in each lat
band
mass = m_trop*areas; % mass of air in each "box" [g]
scaler = [0.95, 0.95, 1.05, 1.05, 0.95, 0.95]; %mass in each box scaled based
on trop. height (shallow in poles)
```

```
mass = mass.*scaler;


%EBAMM model refers to "mass" in # of moles
mass_box = mol_trop*[A1/SA, A2/SA, A3/SA, A3/SA, A2/SA, A1/SA]'; %mass of
each box in moles
C2H6_g_mol = 30.07; % C2H6 grams/mol

%transport coefficents between boxes
%F0_1 is box1 (reversed from the EBAMM model where Box1 is the HSL)
Fo = [0.25, 0.9, 0.6, 0.9, 0.6];

k12 = (Fo(1)*mol_trop)/mass_box(1);
k21 = (Fo(1)*mol_trop)/mass_box(2);

k23 = (Fo(2)*mol_trop)/mass_box(2);
k32 = (Fo(2)*mol_trop)/mass_box(3);

k34 = (Fo(3)*mol_trop)/mass_box(3);
k43 = (Fo(3)*mol_trop)/mass_box(4);

k45 = (Fo(4)*mol_trop)/mass_box(4);
k54 = (Fo(4)*mol_trop)/mass_box(5);

k56 = (Fo(5)*mol_trop)/mass_box(5);
k65 = (Fo(5)*mol_trop)/mass_box(6);

%Inversion matrix for steady state - solves for mass of gas in each box
A = [(k_OH(1) + k12), -k21, 0, 0, 0, 0;

    -k12, (k_OH(2) + k21 +k23), -k32, 0, 0, 0;

    0, -k23, (k_OH(3) + k32 + k34), -k43, 0, 0;

    0, 0, -k34, (k_OH(4) + k43 + k45), -k54, 0;

    0, 0, 0, -k45, (k_OH(5) + k54 + k56), -k65;

    0, 0, 0, 0, -k56, (k_OH(6) + k65)];


%estimate of the global lifetime
glob_lftm = ((1./k_OH).*365);
glob_lftm = sum(glob_lftm.*areas);

%geographic distributions updated: 06/17/2015
burn =      1e12*[0.03, 0.09, 0.46, 0.35, 0.07, 0]';
anthro =    0e12*[0.05, 0.58, 0.30, 0.05, 0.02, 0]';
biofuel =   0.5e12*[0.03, 0.39, 0.38, 0.15, 0.05, 0]'; %Xiao et al 2008 has
80% biofuel in NH
geo =       1e12*[0.04, 0.48, 0.33, 0.11, 0.04, 0]';

%creates emisison grids
```

```
B=[0:.01:5];

burnnew = zeros(length(B),6);
geonew = zeros(length(B),6);
biofuelnew = zeros(length(B),6);
anthronew = zeros(length(B),6);

for i=1:length(B)
    burnnew(i,:) = B(i)*burn;   %Ferretti [2005] level
    geonew(i,:) = B(i)*geo;
end
burngrid = zeros(length(B),length(B),6);
geogrid = zeros(length(B),length(B),6);
sourcegrid = zeros(length(B),length(B),6);
M = zeros(length(B),length(B),6);

for j=1:6
 [burngrid(:,:,j),geogrid(:,:,j)] = meshgrid(burnnew(:,j),geonew(:,j));
   sourcegrid(:,:,j) = burngrid(:,:,j)+geogrid(:,:,j)+anthro(j)+biofuel(j);
%anthro & biofuel are constants (0 and 0.5 Tg/yr, respectively)
end

for x = 1:length(B)
    for y = 1:length(B)
        M(x,y,:) = A\squeeze(sourcegrid(x,y,:));
    end
end

%calulation of box mixing ratios for modern (M) and pre-industiral (M2)
out_ppt = zeros(length(B), length(B),6);
for i=1:6
    out_ppt(:,:,i) = 1e12.*(M(:,:,i)./C2H6_g_mol)./mass_box(i)';
end

% % % %%%%%%%%%%PUBLSIHED GISP mean%%%%%%%%%%%%%%%%
G = 396.8;
G_std = 27.6;

% % % %%%%%%%PUBLISHED WDC mean%%%%%%%%%%%%%%%%%
W = 102.6;
W_std = 9.2;

%creating empty arrays for true scenarios
scenario = zeros(length(out_ppt),length(out_ppt),6);
scenario_true = zeros(length(out_ppt),length(out_ppt));


for i = 1:length(out_ppt)
    for j=1:length(out_ppt)
% %conditional statement for HNL
if (out_ppt(i, j, 1) >= G-2*G_std) && (out_ppt(i,j,1) <= G+2*G_std)
   scenario(i,j,1) = 1;  %two sigma
end
% conditional statement for HSL
if (out_ppt(i, j, 6) >= W-2*W_std) && (out_ppt(i,j,6) <= W+2*W_std)
```

```
   scenario(i,j,6) = 1; %two sigma
end
% if HNL & HSL are within ice core range = 1
if (scenario(i,j,1) ==1) && (scenario(i,j,6) == 1);
    scenario_true(i,j) = 1;
end
   end
end

%%Plotting the valid emisison scenario as a contour (everything inside the
%%contour is a emission scenario which can reproduce the mean ice core
%%levels

f1 = figure(1); set(gcf,'clipping','off','color','w');
v = [0,1];
contour(B,B,scenario_true, v)
colormap([rgb('Beige'); rgb('Navy'); rgb('SeaGreen'); rgb('Maroon')]);
xlabel('Biomass Burning Emissions (Tg/yr)', 'Fontsize', 14);
set(gca, 'Fontsize', 14)
ylabel('Geologic Emissions (Tg/yr)', 'Fontsize', 14);
title('Preindustrial Simulations', 'Fontsize', 14);
```

Methane box model: version 1

```
function [CH4_Mtot, CH4_delC, CH4_delD] = methaneModel1Box_mrn(S, L_OH,
iso_flag)
%%%%%%%%%%%%%%%%%%%%%%%%%%%%%%%%%%%%%%%%%%%%%%%%%%%%%%%%%%%%%%%%%%%%
%INPUTS:
%S = methane source structure
%L_OH = methane lifetime (yrs)
%iso_flag = 'old' or 'new' for end-members
%OUTPUTS:
%CH4_Mtot = mass of methane
%CH4_delC = 13C signature of methane (in per mil)
%CH4_delD = deuterium signature of methane
%%%%%%%%%%%%%%%%%%%%%%%%%%%%%%%%%%%%%%%%%%%%%%%%%%%%%%%%%%%%%%%%%%%%
% This methane model (VERSION 1) solves for the mass of methane and the delC
and delD signature of methane.

global S13C S12C SD L

% %source histories in Tg/yr CH4
% S.year =  [ 1700 1800 1900 1920 1940 1960 1980 2000 ];
% S.ag =    [ 10 10 15 30 60 60 80 50 ];
% S.geo =   [ 10 10 19 30 60 115 125 100 ];
% S.micro = [ 220 220 220 220 240 275 275 275 ];
% S.bb =    [ 18 18 20 25 25 25 25 25 ];
S.totalTg = S.ag + S.geo + S.micro + S.bb + S.ff + S.bio;
S.totalTMol = S.totalTg/16; %approximate

%13C source isotope ratios
if strcmp('new', iso_flag)
    Rstd13C = 0.0112372; %Craig, 1957
    SdelC.ag = -62.3/1000; %uncertainty is %-60/1000;
    SdelC.geo = -43/1000;
    SdelC.micro = -62.3/1000;
    SdelC.bb = -22.3/1000; %Shwietzke et al 2017
    SdelC.bio = -22.3/1000; %Shwietzke et al 2017
    SdelC.ff = -43/1000; %Shwietzke et al 2017
else
    Rstd13C = 0.0112372; %Craig, 1957
    SdelC.ag = -60/1000;
    SdelC.geo = -40/1000;
    SdelC.micro =  -60/1000;
    SdelC.bb = -20/1000;
    SdelC.bio = -20/1000;
    SdelC.ff = -40/1000;
end

S13Cratio.ag = (SdelC.ag + 1) * Rstd13C;
S13Cratio.geo =  (SdelC.geo + 1) * Rstd13C;
S13Cratio.micro = (SdelC.micro + 1) * Rstd13C;
S13Cratio.bb = (SdelC.bb + 1) * Rstd13C;
S13Cratio.ff = (SdelC.ff +1) * Rstd13C;
S13Cratio.bio = (SdelC.bio +1) * Rstd13C;
```

```
%check on source del 13C
sourceDel13C_1 = 1e3*(SdelC.ag*S.ag + SdelC.geo*S.geo + SdelC.micro*S.micro +
SdelC.bb*S.bb + SdelC.bio*S.bio + SdelC.ff*S.ff)./16./S.totalTMol(1);
%compute isotope sources by solving simultaneous equations:
%   17*TMol13C + 16*TMol12 = TgTotal
%   TMol12C*R = TMol13C
S13C.agTMol = S.ag./(17+(16/S13Cratio.ag));
S13C.geoTMol = S.geo./(17+(16/S13Cratio.geo));
S13C.microTMol = S.micro./(17+(16/S13Cratio.micro));
S13C.bbTMol = S.bb./(17+(16/S13Cratio.bb));
S13C.ffTMol = S.ff./(17+(16/S13Cratio.ff));
S13C.bioTMol = S.bio./(17+(16/S13Cratio.bio));

S12C.agTMol = S.ag./((17*S13Cratio.ag+16));
S12C.geoTMol = S.geo./((17*S13Cratio.geo+16));
S12C.microTMol = S.micro./((17*S13Cratio.micro+16));
S12C.bbTMol = S.bb./((17*S13Cratio.bb+16));
S12C.ffTMol = S.ff./((17*S13Cratio.ff+16));
S12C.bioTMol = S.bio./((17*S13Cratio.bio+16));

S13C.totalTMol = S13C.agTMol + S13C.geoTMol + S13C.microTMol + S13C.bbTMol +
S13C.ffTMol + S13C.bioTMol;
S12C.totalTMol = S12C.agTMol + S12C.geoTMol + S12C.microTMol + S12C.bbTMol +
S12C.ffTMol + S12C.bioTMol;
%recheck source del 13C
%S12C.totalTMol = S.totalTMol - S13C.totalTMol;
sourceDel13C_2 = (((S13C.totalTMol./S12C.totalTMol)/Rstd13C)-1)*1000;

%13C source histories in Tg/yr 13CH4
S13C.ag = S13C.agTMol .* 17;
S13C.geo = S13C.geoTMol * 17;
S13C.micro = S13C.microTMol * 17;
S13C.bb = S13C.bbTMol * 17;
S13C.ff = S13C.ffTMol * 17;
S13C.bio = S13C.bioTMol * 17;
S13C.totalTg = S13C.ag + S13C.geo + S13C.micro + S13C.bb + S13C.ff +
S13C.bio;

%12C source histories in Tg/yr 12CH4
S12C.ag = S12C.agTMol .* 16;
S12C.geo = S12C.geoTMol .* 16;
S12C.micro = S12C.microTMol  .* 16;
S12C.bb = S12C.bbTMol  .* 16;
S12C.ff = S12C.ffTMol  .* 16;
S12C.bio = S12C.bioTMol  .* 16;
S12C.totalTg = S12C.ag + S12C.geo + S12C.micro + S12C.bb + S12C.ff +
S12C.bio;


%D source isotope ratios - ******CHECK THIS BEFORE USING
RstdD = 155.76 * 1E-6;  %D/H ratio in V-SMOW Gonfantini, 1978 should be
increased by 0.2 per mil
SdelD.ag = -330/1000;
SdelD.geo = -175/1000;
SdelD.micro = -322/1000;
SdelD.bb = -169/1000;
```

```
SdelD.ff = -175/1000;
SdelD.bio = -169/1000;

SDratio.ag = (SdelD.ag + 1) * RstdD;
SDratio.geo = (SdelD.geo + 1) * RstdD;
SDratio.micro = (SdelD.micro + 1) * RstdD;
SDratio.bb = (SdelD.bb + 1) * RstdD;
SDratio.ff = (SdelD.ff + 1) * RstdD;
SDratio.bio = (SdelD.bio + 1) * RstdD;

%D source histories in Tg/yr D CH4
SD.ag = S12C.ag * SDratio.ag * (18/16);
SD.geo = S12C.geo * SDratio.geo * (18/16);
SD.micro = S12C.micro * SDratio.micro * (18/16);
SD.bb = S12C.bb * SDratio.bb * (18/16);
SD.ff = S12C.ff * SDratio.ff * (18/16);
SD.bio = S12C.bio * SDratio.bio * (18/16);

SD.totalTg = SD.ag + SD.geo + SD.micro + SD.bb + SD.ff + SD.bio;
SD.totalTMol = SD.totalTg/18;


L.k.total = (1/L_OH)/.88; %present day methane total lifetime
L.k.OH = 0.88 * L.k.total;
L.k.soil = 0.07 * L.k.total;
L.k.strat = 0.05 * L.k.total;
L.k.Cl = 0 * L.k.total; %zero Cl oxidation

L.C13alpha.OH = 0.9961;
L.C13alpha.soil = 0.9847;
L.C13alpha.strat = 0.9824;
L.C13alpha.Cl = 1/1.0621; %Tyler et al. GRL 2000 at 298
L.k13C.OH = L.k.OH * L.C13alpha.OH;
L.k13C.soil = L.k.soil * L.C13alpha.soil;
L.k13C.strat = L.k.strat * L.C13alpha.strat;
L.k13C.Cl = L.k.Cl * L.C13alpha.Cl;

L.Dalpha.OH = 0.7729;
L.Dalpha.soil = 0.7005;
L.Dalpha.strat = 0.8764;
L.Dalpha.Cl = 1/1.474; %Tyler et al. GRL 2000 at 298
L.kD.OH = L.k.OH * L.Dalpha.OH;
L.kD.soil = L.k.soil * L.Dalpha.soil;
L.kD.strat = L.k.strat * L.Dalpha.strat;
L.kD.Cl = L.k.Cl * L.Dalpha.Cl;

%initial conditions in atmosphere - assume steady state
massAtm = (5E18)/1e12; %Tg
molAtm = 5E18*1E3/30; %g/30 = moles of air
InitAtm13Cdel = -49/1000;
InitAtm13Cratio = (InitAtm13Cdel + 1) * Rstd13C;

InitAtmTMol(1) = S.totalTMol(1) ./ L.k.total; %0.7*1E-6 * molAtm/1E12;
InitAtmTMol(2) = S12C.totalTMol(1) ./ L.k.total; %InitAtmTMol(1)/(1 +
InitAtm13Cratio);
```

```
InitAtmTMol(3) = S13C.totalTMol(1) ./ (L.k13C.OH + L.k13C.soil +
L.k13C.strat); %InitAtmTMol(1)/(1 + (1/InitAtm13Cratio));
InitAtmTMol(4) = SD.totalTMol(1) ./ (L.kD.OH + L.kD.soil + L.kD.strat);
%check initial atm isotope ratio
InitAtm13Cdel = (((InitAtmTMol(3)./InitAtmTMol(2))./Rstd13C)-1)*1000;

CH4_Mtot = InitAtmTMol(1);
CH4_delC = InitAtm13Cdel;
CH4_delD = InitAtmTMol(4);
```

Methane box model: version 2

```
function [CH4_Mtot, CH4_delC, CH4_delD] = methaneModel1Box_mrn(S, L_OH,
iso_flag)
%%%%%%%%%%%%%%%%%%%%%%%%%%%%%%%%%%%%%%%%%%%%%%%%%%%%%%%%%%%%%%%%%%%%
%INPUTS:
%S = methane source structure
%L_OH = methane lifetime (yrs)
%iso_flag = 'old' or 'new' for end-members
%OUTPUTS:
%CH4_Mtot = mass of methane
%CH4_delC = 13C signature of methane (in per mil)
%CH4_delD = deuterium signature of methane
%%%%%%%%%%%%%%%%%%%%%%%%%%%%%%%%%%%%%%%%%%%%%%%%%%%%%%%%%%%%%%%%%%%%
%VERSION 2 of the methane model; updated calculation of methane lifetimes

global S13C S12C SD L

% %source histories in Tg/yr CH4
% S.year =  [ 1700 1800 1900 1920 1940 1960 1980 2000 ];
% S.ag =    [ 10 10 15 30 60 60 80 50 ];
% S.geo =   [ 10 10 19 30 60 115 125 100 ];
% S.micro = [ 220 220 220 220 240 275 275 275 ];
% S.bb =    [ 18 18 20 25 25 25 25 25 ];
S.totalTg = S.geo + S.micro + S.bb + S.ff + S.bio;
S.totalTMol = S.totalTg/16; %approximate

%13C source isotope ratios
if strcmp('new', iso_flag)
    Rstd13C = 0.0112372; %Craig, 1957
    SdelC.geo = -43/1000; Shwietzke et al 2017
    SdelC.micro =  -62.3/1000; Shwietzke et al 2017
    SdelC.bb = -22.3/1000; Shwietzke et al 2017
    SdelC.bio = -22.3/1000; %Shwietzke et al 2017
    SdelC.ff = -43/1000; %Shwietzke et al 2017
else
    Rstd13C = 0.0112372; %Craig, 1957
    SdelC.geo = -43/1000;
    SdelC.micro = -60.5/1000; %adjusting for 1.8 per mil change in 13CO2 from
      1800s to modern
    SdelC.bb =  -20.5/1000; %adjusting for 1.8 per mil change in 13CO2 from
      1800s to modern
    SdelC.bio = -20.5/1000;
    SdelC.ff = -43/1000;
end

S13Cratio.geo =  (SdelC.geo + 1) * Rstd13C;
S13Cratio.micro = (SdelC.micro + 1) * Rstd13C;
S13Cratio.bb = (SdelC.bb + 1) * Rstd13C;
S13Cratio.ff = (SdelC.ff +1) * Rstd13C;
S13Cratio.bio = (SdelC.bio +1) * Rstd13C;

%check on source del 13C
```

```
sourceDel13C_1 = 1e3*(SdelC.geo*S.geo + SdelC.micro*S.micro + SdelC.bb*S.bb +
SdelC.bio*S.bio + SdelC.ff*S.ff)./16./S.totalTMol(1);
%compute isotope sources by solving simultaneous equations:
%   17*TMol13C + 16*TMol12 = TgTotal
%   TMol12C*R = TMol13C
S13C.geoTMol = S.geo./(17+(16/S13Cratio.geo));
S13C.microTMol = S.micro./(17+(16/S13Cratio.micro));
S13C.bbTMol = S.bb./(17+(16/S13Cratio.bb));
S13C.ffTMol = S.ff./(17+(16/S13Cratio.ff));
S13C.bioTMol = S.bio./(17+(16/S13Cratio.bio));

S12C.geoTMol = S.geo./((17*S13Cratio.geo+16));
S12C.microTMol = S.micro./((17*S13Cratio.micro+16));
S12C.bbTMol = S.bb./((17*S13Cratio.bb+16));
S12C.ffTMol = S.ff./((17*S13Cratio.ff+16));
S12C.bioTMol = S.bio./((17*S13Cratio.bio+16));

S13C.totalTMol = S13C.geoTMol + S13C.microTMol + S13C.bbTMol + S13C.ffTMol +
S13C.bioTMol;
S12C.totalTMol = S12C.geoTMol + S12C.microTMol + S12C.bbTMol + S12C.ffTMol +
S12C.bioTMol;
%recheck source del 13C
%S12C.totalTMol = S.totalTMol - S13C.totalTMol;
sourceDel13C_2 = (((S13C.totalTMol./S12C.totalTMol)/Rstd13C)-1)*1000;

%13C source histories in Tg/yr 13CH4
S13C.geo = S13C.geoTMol * 17;
S13C.micro = S13C.microTMol * 17;
S13C.bb = S13C.bbTMol * 17;
S13C.ff = S13C.ffTMol * 17;
S13C.bio = S13C.bioTMol * 17;
S13C.totalTg = S13C.geo + S13C.micro + S13C.bb + S13C.ff + S13C.bio;

%12C source histories in Tg/yr 12CH4
S12C.geo = S12C.geoTMol .* 16;
S12C.micro = S12C.microTMol  .* 16;
S12C.bb = S12C.bbTMol  .* 16;
S12C.ff = S12C.ffTMol  .* 16;
S12C.bio = S12C.bioTMol  .* 16;
S12C.totalTg = S12C.geo + S12C.micro + S12C.bb + S12C.ff + S12C.bio;

%D source isotope ratios - ******CHECK THIS BEFORE USING
RstdD = 155.76 * 1E-6;  %D/H ratio in V-SMOW Gonfantini, 1978 should be
increased by 0.2 per mil
SdelD.geo = -175/1000;
SdelD.micro = -322/1000;
SdelD.bb = -169/1000;
SdelD.ff = -175/1000;
SdelD.bio = -169/1000;

SDratio.geo = (SdelD.geo + 1) * RstdD;
SDratio.micro = (SdelD.micro + 1) * RstdD;
SDratio.bb = (SdelD.bb + 1) * RstdD;
SDratio.ff = (SdelD.ff + 1) * RstdD;
SDratio.bio = (SdelD.bio + 1) * RstdD;
```

```
%D source histories in Tg/yr D CH4
SD.geo = S12C.geo * SDratio.geo * (18/16);
SD.micro = S12C.micro * SDratio.micro * (18/16);
SD.bb = S12C.bb * SDratio.bb * (18/16);
SD.ff = S12C.ff * SDratio.ff * (18/16);
SD.bio = S12C.bio * SDratio.bio * (18/16);

SD.totalTg = SD.geo + SD.micro + SD.bb + SD.ff + SD.bio;
SD.totalTMol = SD.totalTg/18;

%sinks
L.k.OH = (1/L_OH);
L.k.soil = (1/200); %(1/200); %TAR value see Curry, 2008 paper see Prather et
al 2012 paper||0.07 * L.k.total;
L.k.strat = (1/120); %Prather et al., 2012 || 0.05 * L.k.total;
L.k.Cl = (1/200); %(1/200); %Prather et al., 2012
L.k.total = L.k.OH + L.k.soil + L.k.strat + L.k.Cl; %present day methane
total lifetime - Eric had (1/7.6)

L.C13alpha.OH = 0.995; %[Lassey et al., 2007] %0.9961;
L.C13alpha.soil = 0.98; %[Lassey et al., 2007] %0.9847;
L.C13alpha.strat = 0.9970; %[Lassey et al., 2007] %0.9824;
L.C13alpha.Cl = 0.94; %[Lassey et al., 2007 using Allen et al., 2004,2007]
%1/1.0621; %Tyler et al. GRL 2000 at 298
L.k13C.OH = L.k.OH * L.C13alpha.OH;
L.k13C.soil = L.k.soil * L.C13alpha.soil;
L.k13C.strat = L.k.strat * L.C13alpha.strat;
L.k13C.Cl = L.k.Cl * L.C13alpha.Cl;

L.Dalpha.OH = 0.7729;
L.Dalpha.soil = 0.7005;
L.Dalpha.strat = 0.8764;
L.Dalpha.Cl = 1/1.474; %Tyler et al. GRL 2000 at 298
L.kD.OH = L.k.OH * L.Dalpha.OH;
L.kD.soil = L.k.soil * L.Dalpha.soil;
L.kD.strat = L.k.strat * L.Dalpha.strat;
L.kD.Cl = L.k.Cl * L.Dalpha.Cl;

%initial conditions in atmosphere - assume steady state
massAtm = (5E18)/1e12; %Tg
molAtm = 5E18*1E3/30; %g/30 = moles of air
InitAtm13Cdel = -49/1000;
InitAtm13Cratio = (InitAtm13Cdel + 1) * Rstd13C;

InitAtmTMol(1) = S.totalTMol(1) ./ L.k.total; %0.7*1E-6 * molAtm/1E12;
InitAtmTMol(2) = S12C.totalTMol(1) ./ L.k.total; %InitAtmTMol(1)/(1 +
InitAtm13Cratio);
InitAtmTMol(3) = S13C.totalTMol(1) ./ (L.k13C.OH + L.k13C.soil + L.k13C.strat
+ L.k13C.Cl); %InitAtmTMol(1)/(1 + (1/InitAtm13Cratio));
InitAtmTMol(4) = SD.totalTMol(1) ./ (L.kD.OH + L.kD.soil + L.kD.strat +
L.kD.Cl);
%check initial atm isotope ratio
InitAtm13Cdel = (((InitAtmTMol(3)./InitAtmTMol(2))./Rstd13C)-1)*1000;
```

```
CH4_Mtot = InitAtmTMol(1);
CH4_delC = InitAtm13Cdel;
CH4_delD = InitAtmTMol(4);
```

Methane grid search code

```
%%%%%%%%%%%%%%%%%%%%%%%%%%%%%%%%%%%%%%%%%%%%%%%%%%%%%%%%%%%%%%%%%%%%%%%%%%%%
%%% This script calculates the methane mixing ratio (ppb) and the 13CH4 and
%%% delD-CH4 over a range of emissions using the methane box model function
%(methaneModel1Box). Emission scenarios are compared to the ice core data and
%those which are consistent with the ice core data are considered "valid".
%The valid emission scenarios are calculated and plotted as "goodness of
%fit"
%%%%%%%%%%%%%%%%%%%%%%%%%%%%%%%%%%%%%%%%%%%%%%%%%%%%%%%%%%%%%%%%%%%%%%%%%%%%
clear all
close all

global L

%set up range for each emission type
E_CH4.geo = [0:10:70];
E_CH4.micro = [100:1:250];
E_CH4.bb = [0:1:50];
E_CH4.bio = 6;
E_CH4.ff = 0;

L_OH = 11.2; %Prather et al., 2012 methane chemical lifetime %Voulgarakis et
al 2013 ACCMIP Multimodel mean
iso_flag = 'old';

CH4_Mtot = zeros(length(E_CH4.micro), length(E_CH4.bb), length(E_CH4.geo));
CH4_delC = zeros(length(E_CH4.micro), length(E_CH4.bb), length(E_CH4.geo));
CH4_delD = zeros(length(E_CH4.micro), length(E_CH4.bb), length(E_CH4.geo));

E_temp.bio = E_CH4.bio(1);
E_temp.ff = E_CH4.ff(1);

for i = 1:length(E_CH4.micro)
  E_temp.micro = E_CH4.micro(i);
 for j = 1:length(E_CH4.bb)
    E_temp.bb = E_CH4.bb(j);
    for k = 1:length(E_CH4.geo)
      E_temp.geo = E_CH4.geo(k);
  [CH4_Mtot(i,j,k), CH4_delC(i,j,k), CH4_delD(i,j,k)] =
methaneModel1Box_montecarlo_noCl_2019_0213(E_temp, L_OH, iso_flag);
    end
 end
end
CH4_ppb = (CH4_Mtot*10^12/(1.77*10^20))*1e9;

%%
scenario_MCA_chi = zeros(length(E_CH4.micro), length(E_CH4.bb),
length(E_CH4.geo));
scenario_MCA_true = zeros(length(E_CH4.micro), length(E_CH4.bb),
length(E_CH4.geo));
scenario_LIA_chi = zeros(length(E_CH4.micro), length(E_CH4.bb),
length(E_CH4.geo));
```

```
scenario_LIA_true = zeros(length(E_CH4.micro), length(E_CH4.bb));

% geo = 1;

%ice core mean values
CH4_ppb_MCA = 682.5;
CH4_ppb_LIA = 700.6;
CH4_delC_MCA = -47.49;
CH4_delC_LIA = -48.91;

for i = 1:length(E_CH4.micro)
    for j=1:length(E_CH4.bb)
        for k=1:length(E_CH4.geo)

            chi1(i,j,k) = abs(CH4_ppb(i,j,k) - CH4_ppb_MCA)./CH4_ppb_MCA;
            chi2(i,j,k) = (abs(CH4_delC(i,j,k) - CH4_delC_MCA)./3);

            chi10(i,j,k) = abs(CH4_ppb(i,j,k) - CH4_ppb_LIA)./CH4_ppb_LIA;
            chi20(i,j,k) = abs((CH4_delC(i,j,k) - CH4_delC_LIA))./3;
%
        end
    end
end

chi_MCA_true = NaN(length(E_CH4.micro), length(E_CH4.bb), length(E_CH4.geo));
chi_LIA_true = NaN(length(E_CH4.micro), length(E_CH4.bb), length(E_CH4.geo));
for i = 1:length(E_CH4.micro)
    for j=1:length(E_CH4.bb)
        for k=1:length(E_CH4.geo)
    if (chi1(i,j,k) <= 0.10) && (chi2(i,j,k) <=0.10)
        chi_MCA_true(i,j,k) = 1;
    end
        if chi10(i,j,k) <= 0.10 && chi20(i,j,k) <=0.10
            chi_LIA_true(i,j,k) = 1;
        end
     end
        end
end

%goodness of fit calculation
chi_MCA_rms= sqrt(chi1.^2 + chi2.^2);
chi_MCA_rms = chi_MCA_rms.*chi_MCA_true;

chi_LIA_rms= sqrt(chi10.^2 + chi20.^2);
chi_LIA_rms = chi_LIA_rms.*chi_LIA_true;

[vx, vy] = meshgrid(E_CH4.bb,E_CH4.micro);

%calculates the mean & std of the "true" scenarios at each geologic
valid_MCA = zeros(2,2,8);
for i = 1:length(E_CH4.geo)
    temp = chi_MCA_true(:,:,i);
    temp2 = temp(:);
    vrows = find(temp2==1);
    vburn =vx(vrows);
```

```
    vmicrobe = vy(vrows);
    valid_MCA(1,1,i) = mean(vburn);
    valid_MCA(2,1,i) = std(vburn);
    valid_MCA(1,2,i) = mean(vmicrobe);
    valid_MCA(2,2,i) = std(vmicrobe);
end

valid_LIA = zeros(2,2,8);
for i = 1:length(E_CH4.geo)
    temp = chi_LIA_true(:,:,i);
    temp2 = temp(:);
    vrows = find(temp2==1);
    vburn =vx(vrows);
    vmicrobe = vy(vrows);
    valid_LIA(1,1,i) = mean(vburn);
    valid_LIA(2,1,i) = std(vburn);
    valid_LIA(1,2,i) = mean(vmicrobe);
    valid_LIA(2,2,i) = std(vmicrobe);
end

%plotting the "pizza" slices
brewermap('RdYlBu')
data=chi_MCA_rms;
data2=chi_LIA_rms;

f3 = figure('position', [0, 0, 700,500]);
set(gcf,'clipping','on','color','w');
[x,y,z]=meshgrid(E_CH4.bb,E_CH4.micro,E_CH4.geo);
s1 = subplot(1,2,1);
data(isnan(data))=10; %replacing NaNs with 10 for plotting
scatter3(x(:),y(:),z(:),30,data(:),'filled');
%view(40,35)
hold on
title('1000-1500 CE');
xlabel({'All Biomass'}, 'Rotation', 0);
ylabel({'Microbial'}, 'Rotation', 0);
zlabel('Geologic');
%xlabel('xx');
caxis([0 0.15]);
% colorbar('eastoutside');
colormap(brewermap);
view(-26,8);
% c.Label.String = 'Chi-squared';
hold off
pos = get(gca, 'Position'); %[left bottom width height]
pos(1) = 0.10;
pos(2) = 0.10;
pos(3) = 0.32;
pos(4) = 0.80;
set(gca, 'Position', pos, 'Fontsize', 10, 'box', 'off', 'XColor', 'k',
'YColor', 'k', 'ZColor', 'k')
axis([0.5 50 50 200 0 70]);

s2 = subplot(1,2,2);
data2(isnan(data2))=10; %replacing NaNs with 10 for plotting
scatter3(x(:),y(:),z(:),30,data2(:),'filled');
```

```
title('1600-1800 CE');
xlabel({'All Biomass'}, 'Rotation', 0);
ylabel({'Microbial'}, 'Rotation', 0);
zlabel('Geologic');
%xlabel('xx');
caxis([0 0.15]);
colormap(brewermap);
view(-26,8);
% c.Label.String = 'Chi-squared';
hold off
pos = get(gca, 'Position'); %[left bottom width height]
pos(1) = 0.52;
pos(2) = 0.10;
pos(3) = 0.32;
pos(4) = 0.80;
set(gca, 'Position', pos, 'Fontsize', 10, 'box', 'off', 'XColor', 'k',
'YColor', 'k', 'ZColor', 'k');
h=colorbar('EastOutside');
axis([0.5 50 50 200 0 70]);
set(h, 'Position', [.86 .10 .05 .80], 'FontSize', 10);
h.Label.String = 'Goodness of Fit';
h.Label.FontSize = 10;
h.Color = 'k';
```

Ethane grid search MATLAB code

```
%%%%%%%%%%%%%%%%%%%%%%%%%%%%%%%%%%%%%%%%%%%%%%%%%%%%%%%%%%%%%%%%%%%%%%%%%%%%
%%%% This script calculates ethane mixing ratio over Greenland and
%%%% Antarctica for various emission scenarios by multiplying the emissions
%%%% (in Tg yr-1) by their respective UCI-CTM sensitivity (in ppt/Tg yr-1).
%%%% Emission scenarios which yield ethane levels over Greenland and
%%%% Antarctica which are within 10% of the mean ice core levels are
%%%% considered valid. The mean and std dev. of the valid scenarios over a
%%%% range of geologic emissions are calculated and plotted as a "pizza"
%%%% slice plot.
%%%%%%%%%%%%%%%%%%%%%%%%%%%%%%%%%%%%%%%%%%%%%%%%%%%%%%%%%%%%%%%%%%%%%%%%%%%%

close all
clear all

%set range for each emission type
geo = [0:1:7];
burn = [0:0.05:5];
boreal = [0:0.05:3];
bio = 0.5;

%%
for i = 1:length(boreal)
 for j = 1:length(burn)
     for k = 1:length(geo)
ethane_grn(i,j,k) = 87.95.*geo(k) + 21.50.*burn(j)+ 79.10*bio +
214.29*boreal(i);
ethane_ant(i,j,k) = 20.33.*geo(k) + 31.81.*burn(j)+ 16.86*bio +
4.44*boreal(i);
    end
 end
end

%%%%%%%%%% MEAN VALUES UPDATED AND VERIFIED 1.30.2019 %%%%%%%%%%%%%%%%%%%%%%
ant_ts1 = 119.3;
ant_ts2 = 82.6;
grn_ts1 = 514.8;
grn_ts2 = 483.8;

for i = 1:length(boreal)
    for j=1:length(burn)
        for k=1:length(geo)

            chi_ant_MCA(i,j,k) = abs((ethane_ant(i,j,k) - ant_ts1))./ant_ts1;
            chi_grn_MCA(i,j,k) = abs((ethane_grn(i,j,k) - grn_ts1))./grn_ts1;
            chi_ant_LIA(i,j,k) = abs((ethane_ant(i,j,k) - ant_ts2))./ant_ts2;
            chi_grn_LIA(i,j,k) = abs((ethane_grn(i,j,k) - grn_ts2))./grn_ts2;
    end
end
end

chi_MCA_true = NaN(length(boreal), length(burn), length(geo));
chi_LIA_true = NaN(length(boreal), length(burn), length(geo));
```

```
for i = 1:length(boreal)
   for  j = 1:length(burn)
       for k = 1:length(geo)
    if chi_ant_MCA(i,j,k) <= 0.10 && chi_grn_MCA(i,j,k) <=0.10
        chi_MCA_true(i,j,k) = 1;
    end
        if chi_ant_LIA(i,j,k) <= 0.10 && chi_grn_LIA(i,j,k) <=0.10
            chi_LIA_true(i,j,k) = 1;
        end
        end
    end
end

chi_MCA_rms= sqrt(chi_ant_MCA.^2 + chi_grn_MCA.^2);
chi_MCA_rms = chi_MCA_rms.*chi_MCA_true;

chi_LIA_rms= sqrt(chi_ant_LIA.^2 + chi_grn_LIA.^2);
chi_LIA_rms = chi_LIA_rms.*chi_LIA_true;

chi_MCA_true(isnan(chi_MCA_true))=0;
chi_LIA_true(isnan(chi_LIA_true))=0;

%%
[vx, vy] = meshgrid(burn,boreal);

valid_MCA = zeros(2,2,length(geo));
for i = 1:length(geo)
    temp = chi_MCA_true(:,:,i);
    temp2 = temp(:);
    vrows = find(temp2==1);
    vburn =vx(vrows);
    vboreal = vy(vrows);
    valid_MCA(1,1,i) = mean(vburn);
    valid_MCA(2,1,i) = std(vburn);
    valid_MCA(1,2,i) = mean(vboreal);
    valid_MCA(2,2,i) = std(vboreal);
end

valid_LIA = zeros(2,2,length(geo));
for i = 1:length(geo)
    temp = chi_LIA_true(:,:,i);
    temp2 = temp(:);
    vrows = find(temp2==1);
    vburn =vx(vrows);
    vboreal = vy(vrows);
    valid_LIA(1,1,i) = mean(vburn);
    valid_LIA(2,1,i) = std(vburn);
    valid_LIA(1,2,i) = mean(vboreal);
    valid_LIA(2,2,i) = std(vboreal);
end



%%
```

```
brewermap('RdYlBu')
[x,y,z]=meshgrid(burn,boreal,geo);
f2 = figure('position', [0, 0, 700,500]);
set(gcf,'clipping','on','color','w');
subplot(1,2,1);
colormap(brewermap);
chi_MCA_rms_temp=chi_MCA_rms;
chi_MCA_rms_temp(isnan(chi_MCA_rms_temp))=999;
scatter3(x(:),y(:),z(:),20,chi_MCA_rms_temp(:),'filled');
caxis([0 0.15]);
view(-20,8)
hold off
xlabel({'Non-boreal'}, 'Rotation',0);
ylabel({'Boreal'}, 'Rotation', 0);
zlabel('Geologic');
title('1000-1500 CE');
pos = get(gca, 'Position'); %[left bottom width height]
pos(1) = 0.10;
pos(2) = 0.10;
pos(3) = 0.32;
pos(4) = 0.80;
set(gca, 'Position', pos, 'Fontsize', 12, 'box', 'off', 'XColor', 'k',
'YColor', 'k', 'ZColor', 'k')
axis([0.1 5 0.1 3 0 5]);

subplot(1,2,2);
colormap(brewermap);
chi_LIA_rms_temp=chi_LIA_rms;
chi_LIA_rms_temp(isnan(chi_LIA_rms_temp))=999;
scatter3(x(:),y(:),z(:),20,chi_LIA_rms_temp(:),'filled');
caxis([0 0.15]);
view(-20,8)
hold off
xlabel({'Non-boreal'}, 'Rotation', 0);
ylabel({'Boreal'}, 'Rotation', 0);
zlabel('Geologic');
title('1600-1800 CE');
pos = get(gca, 'Position'); %[left bottom width height]
pos(1) = 0.52;
pos(2) = 0.10;
pos(3) = 0.32;
pos(4) = 0.80;
set(gca, 'Position', pos, 'Fontsize', 12, 'box', 'off', 'XColor', 'k',
'YColor', 'k', 'ZColor', 'k');
h=colorbar('EastOutside');
axis([0.1 5 0.1 3 0 5]);
set(h, 'Position', [.86 .10 .05 .80]);
h.Label.String = 'Goodness of Fit';
% h.Label.FontSize = 12;
h.Color = 'k';
```

Acetylene grid search MATLAB code

```
%%%%%%%%%%%%%%%%%%%%%%%%%%%%%%%%%%%%%%%%%%%%%%%%%%%%%%%%%%%%%%%%%%%%%%%%%%%%%%%%
%%%%%%%%% Acetylene grid search for boreal vs. non-boreal emissions%%%%%%%
%%%%%%%%%%%%%%%%%%%%%%%%%%%%%%%%%%%%%%%%%%%%%%%%%%%%%%%%%%%%%%%%%%%%%%%%%%%%%%%%

close all
clear all

%set up range of emissions
burn = [0:0.05:5]; %nonboreal
bor = [0:0.05:5]; %boreal
bio = 0.5;

chi_ts1_true = NaN(length(burn), length(bor));
chi_ts2_true = NaN(length(burn), length(bor));

%%%%%%%%%%%%%%%% BOREAL VS NONBOREAL%%%%%%%%%%%%%55
%%%%%%%%%%% UPDATED WITH NEW BOREAL, NONBOREAL SENSITIVITIES UCI-CTM
1/28/2019
for i = 1:length(burn)
     for j = 1:length(bor)
acet_grn(i,j) = 106.8.*bor(j) + 3.8.*burn(i)+ 37.7*bio;
acet_ant(i,j) = 0.05.*bor(j) + 6.8.*burn(i)+ 3.1*bio;
    end
end

%%%%%%%%%%%%UPDATED WITH NEW MEANS 11/20/18 %%%%%%%%%%%%%%%%%%%%%%%%%%%%%5
ant_ts1 = 31.2;
ant_ts2 = 16.9;
grn_ts1 = 90.3;
grn_ts2 = 80.1;

for i = 1:length(burn)
    for j=1:length(bor)

        chi_ant_ts1(i,j) =  abs((acet_ant(i,j) - ant_ts1))./ant_ts1;
        chi_grn_ts1(i,j) = abs((acet_grn(i,j) - grn_ts1))./grn_ts1;

        chi_ant_ts2(i,j) = abs((acet_ant(i,j) - ant_ts2))./ant_ts2;
        chi_grn_ts2(i,j) = abs((acet_grn(i,j) - grn_ts2))./grn_ts2;
    end
end

for i = 1:length(burn)
   for  j = 1:length(bor)
    if chi_ant_ts1(i,j) <= 0.10 && chi_grn_ts1(i,j) <=0.10
        chi_ts1_true(i,j) = 1;
    end
        if chi_ant_ts2(i,j) <= 0.10 && chi_grn_ts2(i,j) <=0.10
            chi_ts2_true(i,j) = 1;
        end
        end
end
```

```
chi_ts1_true(isnan(chi_ts1_true))=0;
chi_ts2_true(isnan(chi_ts2_true))=0;

[vx, vy] = meshgrid(burn,bor);

valid_ts1 = zeros(2,2);
    temp = chi_ts1_true(:,:);
    temp2 = temp(:);
    vrows = find(temp2==1);
    vburn =vx(vrows);
    vrest = vy(vrows);
    valid_ts1(1,1) = mean(vburn);
    valid_ts1(2,1) = std(vburn);
    valid_ts1(1,2) = mean(vrest);
    valid_ts1(2,2) = std(vrest);

valid_ts2 = zeros(2,2);
    temp = chi_ts2_true(:,:);
    temp2 = temp(:);
    vrows = find(temp2==1);
    vburn =vx(vrows);
    vrest = vy(vrows);
    valid_ts2(1,1) = mean(vburn);
    valid_ts2(2,1) = std(vburn);
    valid_ts2(1,2) = mean(vrest);
    valid_ts2(2,2) = std(vrest);
```

APPENDIX B

Ice core data

Table A.1: Ethane wet extraction results (in ppt) measured in the WDC05A, WDC06A, SPC14, GISP2B, and GISP2D ice cores. These data are not corrected for solubility depletion. All data were analyzed with procedure 4.

Ice core	Top depth (m)	Bottom depth (m)	Gas Age (CE)	Ethane (ppt)	Ethane error (ppt, 1σ)	CFC-12 (ppt)
SPC14	130.60	130.80	1823	69.0	8.4	0.1
SPC14	134.10	134.30	1776	89.0	4.0	0.1
SPC14	138.60	138.80	1726	103.2	4.5	0.0
SPC14	146.30	146.50	1640	81.3	8.9	0.0
SPC14	149.80	149.90	1584	104.5	4.0	0.0
SPC14	154.30	154.50	1512	134.8	4.4	0.0
SPC14	158.10	158.30	1458	150.2	5.2	0.0
SPC14	166.10	166.30	1350	114.1	7.8	0.1
SPC14	170.60	170.80	1287	149.6	5.0	0.0
SPC14	174.80	175.00	1227	133.8	6.9	0.1
SPC14	178.30	178.50	1178	136.1	3.5	0.0
SPC14	182.80	183.00	1119	142.3	6.6	0.0
SPC14	186.60	186.80	1077	124.5	3.4	0.0
SPC14	190.00	190.20	1037	121.3	3.2	0.0
SPC14	194.77	194.97	974	147.1	6.8	0.0
SPC14	198.30	198.50	926	135.5	3.6	0.0
SPC14	202.30	202.50	872	100.4	3.1	0.1
SPC14	206.10	206.30	823	101.4	6.7	0.0
SPC14	210.50	210.70	764	107.2	3.0	0.0
SPC14	214.10	214.30	713	133.0	3.1	0.0
SPC14	218.30	218.50	645	112.0	3.0	0.1
SPC14	222.80	223.00	581	155.3	3.5	0.0
SPC14	226.30	226.50	544	109.3	3.3	0.0
SPC14	230.80	231.00	491	128.1	3.7	0.0
SPC14	234.50	234.70	445	107.0	9.2	0.0
SPC14	238.10	238.30	398	124.2	3.5	0.1
SPC14	242.30	242.50	345	131.6	4.2	0.0
SPC14	246.30	246.50	294	102.1	3.1	0.0
SPC14	250.30	250.50	243	132.4	3.7	0.1
SPC14	254.10	254.30	193	117.1	3.6	0.0
SPC14	258.50	258.70	135	114.1	8.1	0.0
SPC14	262.10	262.30	87	114.5	3.3	0.0

SPC14	270.30	270.50	-23	113.4	7.2	0.0
SPC14	274.30	274.50	-90	100.2	6.6	0.0
WDC06A	116.80	117.00	1781	86.0	12.6	0.0
WDC06A	126.15	126.30	1742	75.7	5.5	0.1
WDC06A	129.20	129.40	1728	95.2	13.5	0.0
WDC06A	131.24	131.39	1719	95.9	5.4	0.1
WDC06A	136.00	136.15	1698	59.0	5.7	0.0
WDC06A	136.15	136.30	1697	81.3	5.2	0.1
WDC06A	141.24	141.39	1675	80.0	6.3	0.0
WDC06A	141.24	141.39	1675	65.2	5.6	0.0
WDC06A	143.20	143.40	1666	94.6	12.1	0.0
WDC06A	145.24	145.39	145	106.4	5.7	0.4
WDC06A	151.24	151.39	1630	96.0	5.5	0.0
WDC06A	151.39	151.54	1630	81.1	7.1	0.1
WDC06A	156.10	156.30	1611	77.1	10.2	0.0
WDC06A	160.80	161.00	1589	108.4	12.5	0.1
WDC06A	174.40	174.60	1529	117.7	10.5	1.0
WDC06A	196.20	196.30	1435	124.6	11.7	0.0
WDC06A	204.20	204.30	1401	123.7	6.7	0.0
WDC06A	218.00	218.20	1341	122.3	11.1	0.0
WDC06A	225.20	225.40	1310	128.5	8.0	0.0
WDC06A	232.00	232.20	1280	102.5	13.1	0.0
WDC06A	239.80	240.00	1249	109.5	8.4	0.0
WDC06A	246.80	247.00	1219	114.1	10.8	0.0
WDC06A	253.80	254.00	1190	126.2	7.5	0.0
WDC06A	261.30	261.50	1159	109.5	12.9	0.0
WDC06A	283.20	283.40	1070	148.4	8.1	0.0
WDC06A	290.40	290.50	1039	131.6	9.4	0.0
WDC06A	297.80	298.00	1007	93.3	11.2	0.0
WDC06A	304.00	304.20	908	123.5	10.9	0.0
WDC06A	311.20	311.40	950	130.8	16.6	0.0
WDC06A	326.80	327.00	887	84.7	12.0	0.0
WDC06A	333.80	334.00	858	102.9	11.3	0.0
WDC06A	340.80	341.00	829	84.7	14.6	0.0
WDC06A	369.20	369.40	710	110.6	10.2	-1.1
WDC06A	376.00	376.20	681	126.2	12.4	0.0
WDC06A	390.10	390.30	621	105.1	11.7	0.0
WDC06A	404.70	404.80	559	82.7	10.7	0.0
WDC06A	424.50	424.60	471	97.6	12.2	0.1
WDC06A	431.40	431.60	439	145.0	11.0	0.0
WDC06A	438.80	439.00	409	140.8	13.0	0.0

WDC06A	445.40	445.50	380	89.5	12.2	0.0
WDC06A	452.80	453.00	347	123.4	11.2	0.0
WDC06A	480.10	480.30	229	110.7	7.9	0.1
WDC06A	493.40	493.50	170	94.6	7.5	0.1
WDC06A	507.40	507.60	110	99.7	8.5	0.0
WDC06A	521.70	521.90	47	91.0	6.8	0.1
WDC06A	534.40	534.60	-10	119.5	7.5	0.0
WDC06A	549.80	550.00	-73	95.9	9.0	-0.1
WDC06A	570.10	570.30	-159	106.0	8.4	0.0
WDC06A	584.80	584.90	-221	101.1	7.2	0.1
WDC06A	603.60	603.80	-303	121.8	8.6	0.0
WDC05A	83.13	83.28	1926	105.8	17.7	0.1
WDC05A	83.28	83.43	1925	97.8	19.2	0.5
WDC05A	84.79	84.88	1919	85.6	23.3	0.3
WDC05A	91.78	91.93	1887	85.7	14.7	0.2
WDC05A	91.93	92.08	1887	67.3	16.9	0.3
WDC05A	95.53	95.68	1871	50.2	16.0	0.1
WDC05A	95.53	95.68	1871	61.4	17.2	0.1
WDC05A	98.72	98.87	1859	68.9	16.8	0.1
WDC05A	98.72	98.87	1859	69.3	14.6	0.0
WDC05A	107.89	108.04	1820	63.8	14.2	0.1
WDC05A	116.45	116.60	1782	94.2	6.8	0.1
WDC05A	139.43	139.58	1684	81.9	6.5	0.0
WDC05A	167.54	167.69	1561	75.1	21.1	0.1
WDC05A	179.24	179.36	1509	87.2	16.7	0.0
WDC05A	190.86	191.01	1456	110.4	6.4	0.0
WDC05A	191.01	191.16	1455	118.5	7.9	0.0
WDC05A	199.56	199.71	1418	97.9	16.5	0.1
WDC05A	236.16	236.34	1256	106.3	8.4	0.1
WDC05A	255.85	255.99	1175	87.7	11.6	0.0
WDC05A	297.90	298.06	994	79.8	20.1	0.1
GISP2D	95.50	95.60	1892	1082.5	10.6	0.1
GISP2D	104.10	104.20	1858	568.1	10.5	0.0
GISP2D	111.00	111.20	1832	547.3	8.7	0.1
GISP2D	132.00	132.10	1745	447.6	9.9	0.0
GISP2D	154.30	154.40	1650	579.0	9.9	0.0
GISP2D	161.10	161.20	1621	512.2	7.4	0.1
GISP2D	166.10	166.20	1600	514.2	19.2	0.2
GISP2D	173.70	173.80	1569	503.9	8.4	0.1
GISP2D	187.00	187.20	1512	501.2	7.3	0.0
GISP2D	193.60	193.70	1484	524.1	8.2	0.0

GISP2D	201.10	201.20	1450	527.4	7.8	0.0
GISP2D	214.90	215.00	1386	513.3	8.0	0.0
GISP2D	220.90	221.00	1358	482.5	10.9	0.0
GISP2D	225.28	225.39	1340	527.1	11.8	0.0
GISP2D	239.90	240.00	1277	522.7	6.9	0.0
GISP2D	247.40	247.60	1244	502.7	10.0	0.0
GISP2D	251.80	251.90	1225	427.9	11.9	0.1
GISP2D	268.50	268.60	1153	498.5	8.1	0.0
GISP2D	274.26	274.37	1129	560.6	9.1	0.1
GISP2D	294.90	295.00	1038	549.8	9.2	0.0
GISP2D	301.20	301.30	1012	564.9	7.6	0.1
GISP2D	307.79	307.90	983	501.8	10.0	0.0
GISP2D	321.80	321.90	922	486.6	8.0	0.1
GISP2D	335.90	336.00	859	495.4	9.6	0.1
GISP2D	340.60	340.70	839	529.3	21.4	0.1
GISP2D	345.50	345.70	814	448.5	8.1	0.0
GISP2D	360.00	360.10	742	667.1	13.3	-0.1
GISP2D	360.10	360.20	742	559.2	8.9	0.0
GISP2D	364.80	364.90	719	475.1	10.5	0.1
GISP2D	373.80	373.90	675	544.1	10.9	0.3
GISP2D	381.90	382.00	636	565.2	8.9	1.0
GISP2D	386.80	386.90	613	535.5	9.2	0.0
GISP2D	392.20	392.30	586	470.2	28.9	0.2
GISP2D	399.80	399.90	549	397.8	8.2	0.0
GISP2D	417.80	418.00	459	487.1	9.2	0.0
GISP2D	423.00	423.10	433	489.6	13.2	0.0
GISP2D	429.90	430.00	398	430.8	9.1	0.0
GISP2D	434.90	435.00	370	549.0	8.4	0.0
GISP2D	439.89	440.00	345	412.9	9.3	0.0
GISP2D	456.94	457.05	262	607.6	13.0	0.5
GISP2D	472.00	472.10	190	492.2	8.8	0.0
GISP2D	484.00	484.10	130	413.3	9.9	0.0
GISP2D	484.10	484.20	130	459.3	9.9	0.1
GISP2D	494.20	494.30	78	651.8	9.0	0.0
GISP2D	511.80	511.90	-14	543.2	7.8	0.0
GISP2D	523.20	523.30	-71	760.8	9.1	0.0
GISP2D	530.50	530.60	-108	570.6	14.5	0.2
GISP2D	534.90	535.00	-131	558.8	9.6	-0.1
GISP2D	545.50	545.60	-184	440.1	7.7	0.0
GISP2D	574.20	574.30	-335	526.1	8.2	0.0
GISP2D	580.90	581.00	-371	673.8	30.9	0.1

GISP2D	605.46	605.57	-504	483.7	17.0	0.0
GISP2D	630.25	630.35	-641	569.5	29.3	0.1
GISP2D	655.69	655.80	-777	428.5	17.3	0.0
GISP2D	680.44	680.55	-912	435.8	30.4	0.1
GISP2D	705.69	705.79	-1060	643.0	16.9	0.0
GISP2B	87.55	87.67	1918	1014.9	13.7	33.1
GISP2B	102.00	102.11	1862	606.1	11.0	0.0
GISP2B	116.01	116.13	1807	463.7	9.1	0.0
GISP2B	131.85	132.00	1741	443.4	7.3	0.0
GISP2B	162.74	162.86	1610	459.9	9.4	0.9
GISP2B	178.58	178.73	1543	561.9	8.8	0.1
GISP2B	194.00	194.16	1477	525.2	6.9	0.0

Table A.2: Wet extraction ethane results from procedure 4 excluded from analysis and interpretation.

Ice core	Top depth (m)	Bottom depth (m)	Gas Age (CE)	Ethane (ppt)	Ethane error (ppt, 1σ)	CFC-12 (ppt)
GISP2D	118.50	118.60	1802	681.2	11.6	38.2
GISP2D	126.80	127.00	1768	649.8	8.8	0.0
GISP2D	138.90	139.00	1717	399.1	24.8	-0.1
GISP2D	174.37	174.48	1566	524.3	14.0	2.9
GISP2D	208.00	208.20	1418	428.1	26.9	0.3
GISP2D	232.40	232.50	1310	960.1	12.2	0.1
GISP2D	241.64	241.75	1268	661.7	8.7	0.2
GISP2D	280.90	281.00	1099	1775.7	13.2	0.1
GISP2D	287.90	288.00	1068	840.8	11.4	-0.1
GISP2D	290.00	290.10	1059	485.9	12.3	2.7
GISP2D	324.40	324.51	910	476.8	13.2	7.2
GISP2D	369.90	370.00	693	636.0	9.5	0.1
GISP2D	406.00	406.10	519	645.0	8.0	-1.4
GISP2D	406.30	406.40	517	1017.0	21.1	-0.3
GISP2D	411.10	411.20	492	816.8	8.8	0.1
GISP2D	429.80	429.90	399	642.5	10.9	0.0
GISP2D	463.90	464.00	230	460.9	8.2	17.6
GISP2D	479.50	479.60	154	466.1	7.5	0.3
GISP2D	489.89	490.00	99	631.4	25.5	0.1
GISP2D	505.30	505.40	20	464.5	14.6	0.0
GISP2D	554.30	554.40	-230	1512.4	13.7	0.0
GISP2D	556.50	556.60	-241	2051.8	12.7	0.0
GISP2D	564.50	564.60	-283	900.6	10.1	0.0
GISP2D	730.30	730.40	-1206	705.2	25.7	0.2
SPC14	142.80	143.00	1665	157.8	8.2	0.0
SPC14	162.48	162.68	1414	275.8	7.6	0.1
SPC14	294.30	294.50	-387	191.4	7.1	0.0
WDC06A	354.80	355.00	769	182.9	10.1	0.0
WDC06A	466.70	466.90	287	196.0	8.4	-0.1
WDC05A	90.97	91.09	1891	133.6	8.1	34.9
WDC05A	91.09	91.21	1891	105.7	20.8	0.0
WDC05A	116.45	116.60	1782	132.5	7.5	0.6
WDC05A	129.44	129.59	1714	105.5	11.9	0.1
WDC05A	129.80	129.91	1726	351.2	10.5	0.1
WDC05A	131.90	132.05	1670	107.0	12.1	0.1
WDC05A	131.90	132.05	1544	184.8	11.6	0.0
WDC05A	139.43	139.57	1684	73.5	13.0	0.0

WDC05A	142.92	143.07	1714	83.4	11.3	0.1
WDC05A	171.38	171.58	1643	115.4	6.3	0.1

Table A.3: Acetylene wet extraction results (in ppt) measured in the WDC05A, WDC06A, SPC14, GISP2B, and GISP2D ice cores. These data are not corrected for solubility depletion. All data were analyzed with procedure 4.

Ice core	Top depth (m)	Bottom depth (m)	Gas Age (CE)	Acetylene (ppt)	Acetylene error (ppt, 1σ)	CFC-12 (ppt)
SPC14	130.60	130.80	1823	11.9	5.4	0.1
SPC14	134.10	134.30	1776	10.7	4.0	0.1
SPC14	138.60	138.80	1726	10.4	4.3	0.0
SPC14	142.80	143.00	1685	11.7	6.2	0.0
SPC14	146.30	146.50	1640	19.9	6.5	0.0
SPC14	149.80	149.90	1584	23.2	4.4	0.0
SPC14	154.30	154.50	1512	19.8	4.2	0.0
SPC14	158.10	158.30	1458	29.6	5.7	0.0
SPC14	162.48	162.68	1399	28.1	7.0	0.1
SPC14	166.10	166.30	1350	32.3	6.2	0.1
SPC14	170.60	170.80	1287	39.5	5.5	0.0
SPC14	174.80	175.00	1227	31.5	5.6	0.1
SPC14	178.30	178.50	1178	29.0	6.2	0.0
SPC14	182.80	183.00	1119	29.3	6.3	0.0
SPC14	186.60	186.80	1077	30.1	4.6	0.0
SPC14	190.00	190.20	1037	31.9	4.3	0.0
SPC14	194.77	194.97	974	29.0	6.5	0.0
SPC14	198.30	198.50	926	29.8	6.1	0.0
SPC14	202.30	202.50	872	30.1	4.6	0.1
SPC14	206.10	206.30	823	29.0	5.4	0.0
SPC14	210.50	210.70	764	27.5	5.4	0.0
SPC14	214.10	214.30	713	31.3	5.1	0.0
SPC14	218.30	218.50	645	27.7	4.1	0.1
SPC14	222.80	223.00	581	27.1	5.8	0.0
SPC14	226.30	226.50	544	29.6	4.7	0.0
SPC14	230.80	231.00	491	27.6	5.1	0.0
SPC14	234.50	234.70	445	27.8	7.0	0.0
SPC14	238.10	238.30	398	28.0	4.8	0.1
SPC14	242.30	242.50	345	26.6	8.1	0.0
SPC14	246.30	246.50	294	32.0	4.6	0.0
SPC14	250.30	250.50	243	28.5	4.9	0.1
SPC14	254.10	254.30	193	30.6	7.0	0.0
SPC14	258.50	258.70	135	27.5	6.3	0.0
SPC14	262.10	262.30	87	28.7	4.6	0.0
SPC14	270.30	270.50	-23	28.8	5.8	0.0
SPC14	274.30	274.50	-90	23.8	5.2	0.0

SPC14	294.30	294.50	-391	27.9	5.6	0.0
WDC06A	116.80	117.00	1781	17.9	4.6	0.0
WDC06A	126.15	126.30	1742	13.7	4.6	0.1
WDC06A	129.20	129.40	1728	12.2	4.4	0.0
WDC06A	131.24	131.39	1719	10.7	4.4	0.1
WDC06A	136.00	136.15	1698	15.5	4.8	0.0
WDC06A	136.15	136.30	1697	10.9	4.3	0.1
WDC06A	141.24	141.39	1675	27.4	5.3	0.0
WDC06A	141.24	141.39	1675	18.2	5.6	0.0
WDC06A	143.20	143.40	1666	17.8	4.5	0.0
WDC06A	145.24	145.39	145	25.8	4.7	0.4
WDC06A	151.24	151.39	1630	24.8	4.6	0.0
WDC06A	151.39	151.54	1630	29.1	6.1	0.1
WDC06A	156.10	156.30	1611	25.5	4.1	0.0
WDC06A	160.80	161.00	1589	23.7	4.8	0.1
WDC06A	174.40	174.60	1529	28.5	4.2	1.0
WDC06A	196.20	196.30	1435	29.0	4.7	0.0
WDC06A	204.20	204.30	1401	28.3	6.4	0.0
WDC06A	218.00	218.20	1341	31.9	4.5	0.0
WDC06A	225.20	225.40	1310	22.0	6.1	0.0
WDC06A	232.00	232.20	1280	44.4	5.3	0.0
WDC06A	239.80	240.00	1249	25.9	6.5	0.0
WDC06A	246.80	247.00	1219	34.4	4.4	0.0
WDC06A	253.80	254.00	1190	25.3	6.0	0.0
WDC06A	261.30	261.50	1159	38.4	5.2	0.0
WDC06A	283.20	283.40	1070	31.1	6.6	0.0
WDC06A	290.40	290.50	1039	33.0	3.8	0.0
WDC06A	297.80	298.00	1007	28.3	4.5	0.0
WDC06A	304.00	304.20	908	33.0	4.4	0.0
WDC06A	311.20	311.40	950	32.4	6.5	0.0
WDC06A	326.80	327.00	887	31.9	4.8	0.0
WDC06A	333.80	334.00	858	39.5	4.6	0.0
WDC06A	340.80	341.00	829	32.4	5.8	0.0
WDC06A	354.80	355.00	769	34.0	4.1	0.0
WDC06A	369.20	369.40	710	30.2	4.1	-1.1
WDC06A	376.00	376.20	681	33.4	5.0	0.0
WDC06A	390.10	390.30	621	31.4	4.7	0.0
WDC06A	404.70	404.80	559	33.5	4.4	0.0
WDC06A	424.50	424.60	471	31.7	4.9	0.1
WDC06A	431.40	431.60	439	33.0	4.5	0.0
WDC06A	438.80	439.00	409	37.3	5.3	0.0

WDC06A	445.40	445.50	380	29.7	4.9	0.0
WDC06A	452.80	453.00	347	35.5	4.6	0.0
WDC06A	466.70	466.90	287	25.3	6.4	-0.1
WDC06A	480.10	480.30	229	24.0	6.1	0.1
WDC06A	493.40	493.50	170	26.8	5.9	0.1
WDC06A	507.40	507.60	110	25.2	6.5	0.0
WDC06A	521.70	521.90	47	20.6	5.2	0.1
WDC06A	534.40	534.60	-10	24.2	5.8	0.0
WDC06A	549.80	550.00	-73	25.9	6.9	-0.1
WDC06A	570.10	570.30	-159	21.3	6.3	0.0
WDC06A	584.80	584.90	-221	23.4	5.6	0.1
WDC06A	603.60	603.80	-303	23.7	6.5	0.0
WDC05A	83.13	83.28	1926	13.8	8.0	0.1
WDC05A	83.28	83.43	1925	21.1	9.0	0.5
WDC05A	84.79	84.88	1919	15.6	10.3	0.3
WDC05A	91.09	91.21	1891	17.6	9.5	0.0
WDC05A	91.93	92.08	1887	11.8	7.5	0.3
WDC05A	95.53	95.68	1871	18.8	7.6	0.1
WDC05A	95.53	95.68	1871	15.0	7.9	0.1
WDC05A	98.72	98.87	1859	15.2	7.7	0.1
WDC05A	98.72	98.87	1859	13.1	6.7	0.0
WDC05A	116.45	116.60	1782	16.6	5.6	0.1
WDC05A	139.43	139.58	1684	15.2	5.4	0.0
WDC05A	167.54	167.69	1561	36.2	10.2	0.1
WDC05A	179.24	179.36	1509	31.3	8.1	0.0
WDC05A	190.86	191.01	1456	27.0	5.3	0.0
WDC05A	191.01	191.16	1455	25.5	6.6	0.0
WDC05A	199.56	199.71	1418	38.1	8.1	0.1
WDC05A	236.16	236.34	1256	34.2	7.1	0.1
WDC05A	255.85	255.99	1175	28.6	9.9	0.0
WDC05A	297.90	298.06	994	37.3	9.8	0.1
GISP2D	730.30	730.40	-1206	79.2	9.9	0.2
GISP2D	705.69	705.79	-1060	80.7	6.2	0.0
GISP2D	680.44	680.55	-912	96.3	12.2	0.1
GISP2D	655.69	655.80	-777	82.3	6.8	0.0
GISP2D	630.25	630.35	-641	90.4	11.6	0.1
GISP2D	605.46	605.57	-504	83.0	6.6	0.0
GISP2D	580.90	581.00	-371	85.1	12.1	0.1
GISP2D	574.20	574.30	-335	74.2	6.7	0.0
GISP2D	564.50	564.60	-283	82.8	7.8	0.0
GISP2D	556.50	556.60	-241	89.0	6.6	0.0

GISP2D	554.30	554.40	-230	87.9	7.8	0.0
GISP2D	545.50	545.60	-184	75.0	6.3	0.0
GISP2D	534.90	535.00	-131	88.8	7.8	-0.1
GISP2D	530.50	530.60	-108	80.3	11.6	0.2
GISP2D	523.20	523.30	-71	65.8	7.1	0.0
GISP2D	505.30	505.40	20	69.5	6.2	0.0
GISP2D	494.20	494.30	78	82.1	7.2	0.0
GISP2D	489.89	490.00	99	76.9	9.9	0.1
GISP2D	484.10	484.20	130	80.7	8.1	0.1
GISP2D	484.00	484.10	130	75.5	8.1	0.0
GISP2D	479.50	479.60	154	73.9	6.1	0.3
GISP2D	472.00	472.10	190	86.3	6.7	0.0
GISP2D	456.94	457.05	262	94.2	10.2	0.5
GISP2D	439.89	440.00	345	77.8	7.3	0.0
GISP2D	434.90	435.00	370	85.3	7.2	0.0
GISP2D	429.90	430.00	398	87.4	7.6	0.0
GISP2D	429.80	429.90	399	83.4	12.2	0.0
GISP2D	423.00	423.10	433	84.0	10.6	0.0
GISP2D	417.80	418.00	459	82.1	8.0	0.0
GISP2D	411.10	411.20	492	85.8	7.2	0.1
GISP2D	406.30	406.40	517	95.7	8.7	-0.3
GISP2D	406.00	406.10	519	73.4	8.8	-1.4
GISP2D	399.80	399.90	549	75.6	7.1	0.0
GISP2D	392.20	392.30	586	67.6	12.6	0.2
GISP2D	386.80	386.90	613	89.8	8.0	0.0
GISP2D	381.90	382.00	636	83.2	7.6	1.0
GISP2D	373.80	373.90	675	89.6	8.5	0.3
GISP2D	364.80	364.90	719	77.8	8.6	0.1
GISP2D	360.10	360.20	742	94.7	7.7	0.0
GISP2D	360.00	360.10	742	90.2	10.5	-0.1
GISP2D	345.50	345.70	814	65.1	7.0	0.0
GISP2D	340.60	340.70	839	83.3	9.2	0.1
GISP2D	335.90	336.00	859	87.8	7.9	0.1
GISP2D	321.80	321.90	922	98.2	7.0	0.1
GISP2D	307.79	307.90	983	89.8	7.7	0.0
GISP2D	301.20	301.30	1012	89.6	7.6	0.1
GISP2D	294.90	295.00	1038	90.6	8.0	0.0
GISP2D	280.90	281.00	1099	98.8	10.6	0.1
GISP2D	274.26	274.37	1129	98.0	6.8	0.1
GISP2D	268.50	268.60	1153	90.5	8.3	0.0
GISP2D	251.80	251.90	1225	88.5	9.9	0.1

GISP2D	247.40	247.60	1244	94.7	10.3	0.0
GISP2D	239.90	240.00	1277	86.4	6.9	0.0
GISP2D	232.40	232.50	1310	105.2	10.2	0.1
GISP2D	225.28	225.39	1340	92.5	9.3	0.0
GISP2D	220.90	221.00	1358	85.7	9.5	0.0
GISP2D	208.00	208.20	1418	72.6	11.7	0.3
GISP2D	201.10	201.20	1450	79.7	7.9	0.0
GISP2D	193.60	193.70	1484	97.0	7.2	0.0
GISP2D	187.00	187.20	1512	86.3	7.4	0.0
GISP2D	180.60	180.70	1540	97.6	6.5	0.3
GISP2D	173.70	173.80	1569	81.5	7.2	0.1
GISP2D	166.10	166.20	1600	77.6	8.2	0.2
GISP2D	161.10	161.20	1621	82.1	7.5	0.1
GISP2D	154.30	154.40	1650	80.1	8.5	0.0
GISP2D	138.90	139.00	1717	75.4	10.8	-0.1
GISP2D	132.00	132.10	1745	92.9	7.7	0.0
GISP2D	126.80	127.00	1768	96.3	8.8	0.0
GISP2D	111.00	111.20	1832	97.2	7.5	0.1
GISP2D	104.10	104.20	1858	116.8	8.0	0.0
GISP2D	95.50	95.60	1892	153.1	10.1	0.1
GISP2B	87.55	87.67	1918	211.4	10.4	33.1
GISP2B	102.00	102.11	1862	111.0	8.8	0.0
GISP2B	116.01	116.13	1807	99.7	7.5	0.0
GISP2B	131.85	132.00	1741	74.5	5.4	0.0
GISP2B	162.74	162.86	1610	95.8	8.3	0.9
GISP2B	178.58	178.73	1543	86.0	6.7	0.1
GISP2B	194.00	194.16	1477	84.6	4.9	0.0

Table A.4: Wet extraction acetylene results from procedure 4 excluded from analysis and interpretation.

Ice core	Top depth (m)	Bottom depth (m)	Gas Age (CE)	Acetylene (ppt)	Acetylene error (ppt, 1σ)	CFC-12 (ppt)
GISP2D	118.50	118.60	1802	96.3	11.7	38.2
GISP2D	174.37	174.48	1566	97.3	11.3	2.9
GISP2D	241.64	241.75	1268	100.3	6.1	0.2
GISP2D	287.90	288.00	1068	122.0	11.4	-0.1
GISP2D	290.00	290.10	1059	95.0	9.8	2.7
GISP2D	324.40	324.51	910	239.7	10.1	7.2
GISP2D	369.90	370.00	693	109.4	10.8	0.1
GISP2D	463.90	464.00	230	85.1	6.7	17.6
WDC05A	90.97	91.09	1891	18.9	6.7	34.9
WDC05A	91.775	91.925	1887	43.3	7.2	0.2
WDC05A	107.89	108.04	1820	37.6	7.0	0.1
WDC05A	116.45	116.6	1782	49.5	6.2	0.6
WDC05A	129.44	129.59	1714	25.7	12.3	0.1
WDC05A	129.8	129.91	1726	49.8	12.6	0.1
WDC05A	131.9	132.05	1670	6.8	12.8	0.1
WDC05A	131.9	132.05	1544	2.9	13.2	0.0
WDC05A	139.425	139.572	1684	97.4	12.8	0.0
WDC05A	142.915	143.065	1714	108.1	11.3	0.1
WDC05A	171.375	171.575	1643	63.9	5.2	0.1

APPENDIX C

UCI-CTM lifetime versus sensitivity simulations

Table A.5: Ethane UCI-CTM sensitivities for the global GFED3 biomass burning footprint (*van der Werf.*, 2010)

			Sensitivity [ppt/Tg y^{-1}]	
k [cm^3 $molecule^{-1}$ s^{-1}]	Lifetime [months]	k_{eff} [$months^{-1}$]	Greenland	Antarctica
6.090 x 10^{-12}	2.44	0.41	43.93	31.44
6.525 x 10^{-12}	2.29	0.44	41.38	28.98
6.960 x 10^{-12}	2.16	0.46	39.13	26.83
7.308 x 10^{-12}	2.06	0.49	37.50	25.30
8.700 x 10^{-12}	1.75	0.57	32.18	20.41
1.740 x 10^{-11}	0.90	1.11	17.28	8.25

Table A.6: Ethane UCI-CTM sensitivities for the tropical biomass burning footprint (30°N- 30°S).

			Sensitivity [ppt/Tg y^{-1}]	
k [cm^3 $molecule^{-1}$ s^{-1}]	Lifetime [months]	k_{eff} [$months^{-1}$]	Greenland	Antarctica
6.090 x 10^{-12}	2.41	0.41	20.32	34.38
6.525 x 10^{-12}	2.26	0.44	18.50	31.72
6.960 x 10^{-12}	2.13	0.47	16.903	29.38
7.308 x 10^{-12}	2.03	0.49	15.82	27.70
8.700 x 10^{-12}	1.73	0.58	12.33	22.36
1.740 x 10^{-11}	0.89	1.13	4.19	8.96

Table A.7: Ethane UCI-CTM sensitivities for the boreal biomass burning footprint (>50°N).

			Sensitivity [ppt/Tg y^{-1}]	
k [cm^3 $molecule^{-1}$ s^{-1}]	Lifetime [months]	k_{eff} [$months^{-1}$]	Greenland	Antarctica
6.090 x 10^{-12}	2.65	0.38	222.21	5.29
6.525 x 10^{-12}	2.49	0.40	214.29	4.44
6.960 x 10^{-12}	2.35	0.43	207.00	3.75
7.308 x 10^{-12}	2.24	0.45	201.55	3.29
8.700 x 10^{-12}	1.91	0.52	182.65	2.02
1.740 x 10^{-11}	1.00	1.00	117.22	0.20

Table A.8: Ethane UCI-CTM sensitivities for the non-boreal biomass burning footprint (50°N-90°S).

k [cm^3 $molecule^{-1}$ s^{-1}]	Lifetime [months]	k_{eff} [$months^{-1}$]	Sensitivity [ppt/Tg y^{-1}] Greenland	Antarctica
6.090 x 10^{-12}	2.42	0.41	23.42	34.44
6.525 x 10^{-12}	2.27	0.44	21.50	31.81
6.960 x 10^{-12}	2.13	0.47	19.82	29.49
7.308 x 10^{-12}	2.04	0.49	18.63	27.83
8.700 x 10^{-12}	1.73	0.58	14.88	22.52
1.740 x 10^{-11}	0.89	1.13	5.79	9.18

Table A.9: Ethane UCI-CTM sensitivities for the Australian biomass burning footprint.

k [cm^3 $molecule^{-1}$ s^{-1}]	Lifetime [months]	k_{eff} [$months^{-1}$]	Sensitivity [ppt/Tg y^{-1}] Greenland	Antarctica
6.090 x 10^{-12}	2.49	0.40	12.93	53.46
6.525 x 10^{-12}	2.34	0.43	11.49	50.01
6.960 x 10^{-12}	2.20	0.45	10.27	46.95
7.308 x 10^{-12}	2.10	0.48	9.41	44.73
8.700 x 10^{-12}	1.78	0.56	6.82	37.51
1.740 x 10^{-11}	0.91	1.10	1.43	17.60

Table A.10: Ethane UCI-CTM sensitivities for the southern hemisphere Africa biomass burning footprint.

k [cm^3 $molecule^{-1}$ s^{-1}]	Lifetime [months]	k_{eff} [$months^{-1}$]	Sensitivity [ppt/Tg y^{-1}] Greenland	Antarctica
6.090 x 10^{-12}	2.32	0.43	14.44	35.84
6.525 x 10^{-12}	2.16	0.46	12.79	33.05
6.960 x 10^{-12}	2.03	0.49	11.38	30.61
7.308 x 10^{-12}	1.93	0.52	10.39	28.86
8.700 x 10^{-12}	1.62	0.62	7.36	23.29
1.740 x 10^{-11}	0.78	1.28	1.28	9.26

Table A.11: Ethane UCI-CTM sensitivities for the southern hemisphere South America biomass burning footprint.

k [cm^3 $molecule^{-1}$ s^{-1}]	Lifetime [months]	k_{eff} [$months^{-1}$]	Sensitivity [ppt/Tg y^{-1}] Greenland	Antarctica
6.090 x 10^{-12}	2.64	0.38	11.38	64.42
6.525 x 10^{-12}	2.49	0.40	10.14	60.69
6.960 x 10^{-12}	2.35	0.43	9.09	57.35
7.308 x 10^{-12}	2.26	0.44	8.35	54.93
8.700 x 10^{-12}	1.94	0.51	6.08	46.95
1.740 x 10^{-11}	1.07	0.93	1.33	24.06

Table A.12: Ethane UCI-CTM sensitivities for the Southern Hemisphere biomass burning footprint.

k [cm^3 $molecule^{-1}$ s^{-1}]	Lifetime [months]	k_{eff} [$months^{-1}$]	Sensitivity [ppt/Tg y^{-1}] Greenland	Antarctica
6.090 x 10^{-12}	2.45	0.41	15.50	43.76
6.525 x 10^{-12}	2.30	0.44	12.96	40.71
6.960 x 10^{-12}	2.16	0.46	11.64	38.02
7.308 x 10^{-12}	2.07	0.48	10.71	36.09
8.700 x 10^{-12}	1.76	0.57	7.84	29.85
1.740 x 10^{-11}	0.91	1.10	1.71	13.38

Table A.13: Ethane UCI-CTM sensitivities for the Southern Hemisphere to 5°N biomass burning footprint. (5°N to 90°S)

k [cm^3 $molecule^{-1}$ s^{-1}]	Lifetime [months]	k_{eff} [$months^{-1}$]	Sensitivity [ppt/Tg y^{-1}] Greenland	Antarctica
6.090 x 10^{-12}	2.45	0.41	15.14	41.79
6.525 x 10^{-12}	2.30	0.44	13.57	38.82
6.960 x 10^{-12}	2.16	0.46	12.22	36.19
7.308 x 10^{-12}	2.07	0.48	11.27	34.31
8.700 x 10^{-12}	1.79	0.57	8.34	28.23
1.740 x 10^{-11}	0.91	1.10	2.01	12.34

Table A.14: Ethane UCI-CTM sensitivities for the fossil fuel footprint (*Lamarque et al.*, 2010).

k [cm^3 $molecule^{-1}$ s^{-1}]	Lifetime [months]	k_{eff} [$months^{-1}$]	Sensitivity [ppt/Tg y^{-1}]	
			Greenland	Antarctica
6.090×10^{-12}	2.51	0.40	77.61	15.66
6.525×10^{-12}	2.36	0.42	73.91	14.16
6.960×10^{-12}	2.23	0.45	70.59	12.86
7.308×10^{-12}	2.14	0.47	68.18	11.96
8.700×10^{-12}	1.89	0.55	60.18	9.18
1.740×10^{-11}	0.99	1.01	36.47	3.15

Table A.15: Ethane UCI-CTM sensitivities for the biofuel footprint. (*Yevich and Logan*, 2003).

k [cm^3 $molecule^{-1}$ s^{-1}]	Lifetime [months]	k_{eff} [$months^{-1}$]	Sensitivity [ppt/Tg y^{-1}]	
			Greenland	Antarctica
6.090×10^{-12}	2.57	0.39	82.79	18.49
6.525×10^{-12}	2.42	0.41	79.10	16.86
6.960×10^{-12}	2.29	0.44	75.79	15.46
7.308×10^{-12}	2.19	0.46	73.38	14.47
8.700×10^{-12}	1.88	0.53	65.37	11.39
1.740×10^{-11}	1.02	0.98	41.24	4.36

Table A.16: Ethane UCI-CTM sensitivities for the geologic footprint. (*Etiope and Ciccioli*, 2009).

k [cm^3 $molecule^{-1}$ s^{-1}]	Lifetime [months]	k_{eff} [$months^{-1}$]	Sensitivity [ppt/Tg y^{-1}]	
			Greenland	Antarctica
6.090×10^{-12}	2.61	0.38	91.63	22.04
6.525×10^{-12}	2.46	0.41	87.95	20.33
6.960×10^{-12}	2.33	0.43	84.66	18.85
7.308×10^{-12}	2.23	0.45	82.26	17.80
8.700×10^{-12}	1.93	0.52	74.28	14.54
1.740×10^{-11}	1.07	0.93	49.97	6.82

Table A.17: Acetylene UCI-CTM sensitivities for the global GFED3 biomass burning footprint (*van der Werf.*, 2010*)*

k_0 [cm^3 $molecule^{-1}$ s^{-1}]	k_∞ [cm^3 $molecule^{-1}$ s^{-1}	Lifetime [months]	k_{eff} [$months^{-1}$]	Sensitivity [ppt/Tg y^{-1}] Greenland	Antarctica
3.850×10^{-30}	5.810×10^{-13}	0.70	1.44	13.96	6.79
4.125×10^{-30}	6.225×10^{-13}	0.65	1.54	13.08	6.17
4.400×10^{-30}	6.640×10^{-13}	0.61	1.64	12.29	5.65
4.620×10^{-30}	6.972×10^{-13}	0.58	1.72	11.73	5.28
5.500×10^{-30}	8.300×10^{-13}	0.49	2.04	9.92	4.13
1.100×10^{-29}	1.660×10^{-12}	0.24	4.13	5.01	1.48

Table A.18: Acetylene UCI-CTM sensitivities for the tropical biomass burning footprint (30°N - 30°S).

k_0 [cm^3 $molecule^{-1}$ s^{-1}]	k_∞ [cm^3 $molecule^{-1}$ s^{-1}	Lifetime [months]	k_{eff} [$months^{-1}$]	Sensitivity [ppt/Tg y^{-1}] Greenland	Antarctica
3.850×10^{-30}	5.810×10^{-13}	0.68	1.46	2.96	7.00
4.125×10^{-30}	6.225×10^{-13}	0.64	1.56	2.63	6.36
4.400×10^{-30}	6.640×10^{-13}	0.60	1.67	2.34	5.80
4.620×10^{-30}	6.972×10^{-13}	0.57	1.75	2.15	5.42
5.500×10^{-30}	8.300×10^{-13}	0.48	2.08	1.56	4.22
1.100×10^{-29}	1.660×10^{-12}	0.24	4.24	0.38	1.47

Table A.19: Acetylene UCI-CTM sensitivities for the boreal biomass burning footprint (>50°N).

k_0 [cm^3 $molecule^{-1}$ s^{-1}]	k_∞ [cm^3 $molecule^{-1}$ s^{-1}	Lifetime [months]	k_{eff} [$months^{-1}$]	Sensitivity [ppt/Tg y^{-1}] Greenland	Antarctica
3.850×10^{-30}	5.810×10^{-13}	0.78	1.28	112.56	0.07
4.125×10^{-30}	6.225×10^{-13}	0.73	1.37	106.84	0.05
4.400×10^{-30}	6.640×10^{-13}	0.69	1.46	101.68	0.04
4.620×10^{-30}	6.972×10^{-13}	0.66	1.53	97.90	0.03
5.500×10^{-30}	8.300×10^{-13}	0.56	1.80	85.24	0.01
1.100×10^{-29}	1.660×10^{-12}	0.29	3.46	47.09	0.00

Table A.20: Acetylene UCI-CTM sensitivities for the non-boreal biomass burning footprint (50°N-90°S).

				Sensitivity [ppt/Tg y^{-1}]	
k_0 [cm^3 $molecule^{-1}$ s^{-1}]	k_∞ [cm^3 $molecule^{-1}$ s^{-1}	Lifetime [months]	k_{eff} [$months^{-1}$]	Greenland	Antarctica
3.850×10^{-30}	5.810×10^{-13}	0.69	1.45	4.22	7.45
4.125×10^{-30}	6.225×10^{-13}	0.64	1.56	3.81	6.78
4.400×10^{-30}	6.640×10^{-13}	0.60	1.66	3.47	6.20
4.620×10^{-30}	6.972×10^{-13}	0.57	1.74	3.22	5.79
5.500×10^{-30}	8.300×10^{-13}	0.48	2.07	2.48	4.54
1.100×10^{-29}	1.660×10^{-12}	0.24	4.21	0.85	1.62

Table A.21: Acetylene UCI-CTM sensitivities for the Australia biomass burning footprint.

				Sensitivity [ppt/Tg y^{-1}]	
k_0 [cm^3 $molecule^{-1}$ s^{-1}]	k_∞ [cm^3 $molecule^{-1}$ s^{-1}	Lifetime [months]	k_{eff} [$months^{-1}$]	Greenland	Antarctica
3.850×10^{-30}	5.810×10^{-13}	0.70	1.42	0.79	13.19
4.125×10^{-30}	6.225×10^{-13}	0.66	1.52	0.63	12.09
4.400×10^{-30}	6.640×10^{-13}	0.62	1.62	0.52	11.13
4.620×10^{-30}	6.972×10^{-13}	0.59	1.70	0.44	10.45
5.500×10^{-30}	8.300×10^{-13}	0.49	2.03	0.24	8.31
1.100×10^{-29}	1.660×10^{-12}	0.25	4.08	0.01	3.09

Table A.22: Acetylene UCI-CTM sensitivities for the southern hemisphere Africa biomass burning footprint.

				Sensitivity [ppt/Tg y^{-1}]	
k_0 [cm^3 $molecule^{-1}$ s^{-1}]	k_∞ [cm^3 $molecule^{-1}$ s^{-1}	Lifetime [months]	k_{eff} [$months^{-1}$]	Greenland	Antarctica
3.850×10^{-30}	5.810×10^{-13}	0.61	1.64	0.60	7.38
4.125×10^{-30}	6.225×10^{-13}	0.57	1.76	0.47	6.67
4.400×10^{-30}	6.640×10^{-13}	0.53	1.89	0.37	6.05
4.620×10^{-30}	6.972×10^{-13}	0.50	1.99	0.30	5.62
5.500×10^{-30}	8.300×10^{-13}	0.42	2.40	0.15	4.30
1.100×10^{-29}	1.660×10^{-12}	0.19	5.14	0.01	1.39

Table A.23: Acetylene UCI-CTM sensitivities for the southern hemisphere South America biomass burning footprint.

k_0 [cm^3 $molecule^{-1}$ s^{-1}]	k_∞ [cm^3 $molecule^{-1}$ s^{-1}	Lifetime [months]	k_{eff} [$months^{-1}$]	Sensitivity [ppt/Tg y^{-1}] Greenland	Antarctica
3.850×10^{-30}	5.810×10^{-13}	0.86	1.17	0.70	20.34
4.125×10^{-30}	6.225×10^{-13}	0.81	1.24	0.57	18.85
4.400×10^{-30}	6.640×10^{-13}	0.76	1.31	0.47	17.54
4.620×10^{-30}	6.972×10^{-13}	0.73	1.37	0.40	16.60
5.500×10^{-30}	8.300×10^{-13}	0.63	1.60	0.23	13.53
1.100×10^{-29}	1.660×10^{-12}	0.32	3.08	0.02	5.39

Table A.24: Acetylene UCI-CTM sensitivities for the Southern Hemisphere (0-90°S) biomass burning footprint.

k_0 [cm^3 $molecule^{-1}$ s^{-1}]	k_∞ [cm^3 $molecule^{-1}$ s^{-1}	Lifetime [months]	k_{eff} [$months^{-1}$]	Sensitivity [ppt/Tg y^{-1}] Greenland	Antarctica
3.850×10^{-30}	5.810×10^{-13}	0.71	1.42	0.78	11.61
4.125×10^{-30}	6.225×10^{-13}	0.66	1.52	0.63	10.65
4.400×10^{-30}	6.640×10^{-13}	0.62	1.61	0.51	9.80
4.620×10^{-30}	6.972×10^{-13}	0.59	1.69	0.44	9.21
5.500×10^{-30}	8.300×10^{-13}	0.50	2.01	0.24	7.32
1.100×10^{-29}	1.660×10^{-12}	0.25	4.07	0.02	2.70

Table A.25: Acetylene UCI-CTM sensitivities for the Southern Hemisphere to 5°N biomass burning footprint (5°N-90°S).

k_0 [cm^3 $molecule^{-1}$ s^{-1}]	k_∞ [cm^3 $molecule^{-1}$ s^{-1}	Lifetime [months]	k_{eff} [$months^{-1}$]	Sensitivity [ppt/Tg y^{-1}] Greenland	Antarctica
3.850×10^{-30}	5.810×10^{-13}	0.70	1.42	1.05	10.53
4.125×10^{-30}	6.225×10^{-13}	0.66	1.52	0.87	9.63
4.400×10^{-30}	6.640×10^{-13}	0.62	1.62	0.73	8.85
4.620×10^{-30}	6.972×10^{-13}	0.59	1.70	0.64	8.30
5.500×10^{-30}	8.300×10^{-13}	0.49	2.02	0.39	6.56
1.100×10^{-29}	1.660×10^{-12}	0.24	4.08	0.05	2.39

Table A.26: Acetylene UCI-CTM sensitivities for the fossil fuel footprint (*Lamarque et al*., 2010)

				Sensitivity [ppt/Tg y^{-1}]	
k_0 [cm^3 $molecule^{-1}$ s^{-1}]	k_∞ [cm^3 $molecule^{-1}$ s^{-1}	Lifetime [months]	k_{eff} [$months^{-1}$]	Greenland	Antarctica
3.850×10^{-30}	5.810×10^{-13}	0.79	1.26	37.02	2.71
4.125×10^{-30}	6.225×10^{-13}	0.74	1.34	35.27	2.47
4.400×10^{-30}	6.640×10^{-13}	0.70	1.42	33.71	2.26
4.620×10^{-30}	6.972×10^{-13}	0.67	1.48	32.57	2.12
5.500×10^{-30}	8.300×10^{-13}	0.58	1.73	28.81	1.69
1.100×10^{-29}	1.660×10^{-12}	0.31	3.21	17.64	0.73

Table A.27: Acetylene UCI-CTM sensitivities for the biofuel footprint (*Yevich and Logan*., 2000)

				Sensitivity [ppt/Tg y^{-1}]	
k_0 [cm^3 $molecule^{-1}$ s^{-1}]	k_∞ [cm^3 $molecule^{-1}$ s^{-1}	Lifetime [months]	k_{eff} [$months^{-1}$]	Greenland	Antarctica
3.850×10^{-30}	5.810×10^{-13}	0.81	1.24	39.52	3.38
4.125×10^{-30}	6.225×10^{-13}	0.76	1.32	37.71	3.08
4.400×10^{-30}	6.640×10^{-13}	0.72	1.40	36.10	2.83
4.620×10^{-30}	6.972×10^{-13}	0.69	1.46	34.92	2.65
5.500×10^{-30}	8.300×10^{-13}	0.59	1.71	31.02	2.12
1.100×10^{-29}	1.660×10^{-12}	0.31	3.21	19.29	0.91

Table A.28: Acetylene UCI-CTM sensitivities for the geologic footprint (*Etiope and Ciccioli*, 2009)

				Sensitivity [ppt/Tg y^{-1}]	
k_0 [cm^3 $molecule^{-1}$ s^{-1}]	k_∞ [cm^3 $molecule^{-1}$ s^{-1}	Lifetime [months]	k_{eff} [$months^{-1}$]	Greenland	Antarctica
3.850×10^{-30}	5.810×10^{-13}	0.85	1.17	48.69	5.82
4.125×10^{-30}	6.225×10^{-13}	0.81	1.24	46.81	5.45
4.400×10^{-30}	6.640×10^{-13}	0.76	1.31	45.12	5.13
4.620×10^{-30}	6.972×10^{-13}	0.73	1.36	43.88	4.91
5.500×10^{-30}	8.300×10^{-13}	0.63	1.58	39.71	4.20
1.100×10^{-29}	1.660×10^{-12}	0.36	2.81	26.54	2.33

APPENDIX D

CTM perturbations and sensitivity calculations

Perturbation experiments were designed to estimate the response (sensitivity) of ethane and acetylene levels over Greenland and Antarctica to small changes in emissions from various spatial/temporal geographic patterns of major ethane and acetylene sources. These perturbations were done by defining a reference model simulation of the modern atmosphere ("base case") of an ethane-like and acetylene-like tracer species. The "base case" of these species had emissions from fossil fuel and biomass burning. The tracer species reacts in the model with the same OH lifetime and stratospheric loss as ethane and acetylene but does not affect the background chemistry and OH field. Perturbations were carried out whereby the sources of ethane and acetylene tracer were increased by 5% (or some known amount) relative to the "base case" and the sensitivity was calculated as follows:

$$\text{Sensitivity} = \frac{ppt^{-1}_{\text{perturbation}} - ppt^{-1}_{\text{base case}}}{\text{Tg y}^{-1}_{\text{perturbation}} - \text{Tg y}^{-1}_{\text{base case}}}$$

in units of $ppt^{-1}/Tg\ y^{-1}$ of global ethane and acetylene emissions from a particular source. Ethane and acetylene levels (in ppt) were calculated by integrating the mass of the compound up to vertical layer 19 (roughly 500 hPa) and integrating the mass of air up to the same level over the horizontal regions (ex: from 60-90°N).

Sensitives were computed for ethane and acetylene levels over Greenland and Antarctica from perturbations to biomass burning, biofuels, fossil fuels, and geologic emissions. Sensitivities were also calculated from perturbations to biomass burning from different geographic regions. These sensitivities were used in Nicewonger et al. (2018) to develop a

preindustrial ethane budget based on ice core data. Table A.29 shows the resulting model sensitivities for ethane and acetylene from perturbations of each source/geographic region. Table A.30 describes each perturbation run.

Table A.29: UCI-CTM sensitivities for ethane and acetylene for Greenland (GRN) and Antarctica (ANT) from different perturbation simulations. The methane chemical (OH) lifetime in the UCI-CTM is 8.96 years. These sensitivities were used in *Nicewonger et al*. (2018).

			Modeled sensitivities (ppt/Tg y^{-1})			
			Ethane		*Acetylene*	
Source	**Geographic region**	**Fraction of total global emissions (DM %)**	**GRN**	**ANT**	**GRN**	**ANT**
Fossil fuel	Globe	100	9.8	9.2	41.8	2.5
Biofuel	Globe	100	65.4	11.4	32.2	2.2
Geologic	Globe	100	80.9	12.9	--	--
Biomass burning						
	Non-boreal	91	18.4	24.2	4.3	4.7
	Boreal – All	9	190.5	2.4	83.1	0.1
	Boreal - Siberia	7	189.7	2.9	90.8	0.1
	Boreal - Europe	0.2	169.6	0.0	88.0	0.0
	Boreal –North America	2.7	177.9	2.1	85.0	0.0
	Southern Hemisphere Africa	28	10.4	25.5	1.2	4.7
	Southern Hemisphere America	13	7.1	47.8	0.8	13.2
	Australia	7	7.9	35.3	0.9	7.7
	Tropics		13.7	23.3	2.8	4.5
	High southern latitudes	0.9	3.6	99.3	0.5	35.0
	Globe	100	33.2	21.1	11.8	4.3

Table A.30: Description of UCI-CTM perturbation model runs used in *Nicewonger et al*. (2018)

Perturbation	**Description**
Fossil fuel	5% increase in global fossil fuel emissions
Biofuel	Addition of biofuel source of ethane and acetylene with a geographic distribution based on Yevich and Logan (2000). Base case did not have a biofuel source of ethane and acetylene.
Geologic	Addition of a geologic source of ethane with a geographic distribution based on Etiope and Ciccioli (2009). Base case did not have a geologic source of ethane
Biomass burning: non-boreal	5% increase in biomass burning emissions from 50°N to 90°S (all longitudes)
Biomass burning: boreal – all	5% increase in biomass burning emissions from 50°N to 90°N (all longitudes)
Biomass burning: boreal – Siberia	5% increase in biomass burning emissions in the Siberian boreal zone bound by 50-90°N and 45-180°E
Biomass burning: boreal – Europe	5% increase in biomass burning emissions in the European boreal zone bound by 50-90°N and 30°W-45°E
Biomass burning: boreal – North America	5% increase in biomass burning emissions in the North American boreal zone bound by 50-90°N and 45°-180°W
Biomass burning: Southern Hemisphere Africa	5% increase in biomass burning emissions in the southern hemisphere portion of Africa bound by 0-35°S and 13-60°E (includes Madagascar and small islands
Biomass burning: Southern Hemisphere America	5% increase in biomass burning emissions in southern hemisphere America bound by 0-60°S and 35-81°W
Biomass burning: Australia	5% increase in biomass burning emission Australia bound by 9-55°S and 111-168°E
Biomass burning: High southern latitudes	5% increase in biomass burning emissions from 30-60°S (all longitudes)
Biomass burning: Tropics	5% increase in biomass burning emissions from 30°N to 30°S (all longitudes)
Biomass burning: Globe	5% increase in global biomass burning emissions (all latitudes and longitudes)